Fall 2018

Dragline excavation simulation, real-time terrain recognition and object detection

Godfred Somua-Gyimah

Department: Mining and Nuclear Engineering

DRAGLINE EXCAVATION SIMULATION, REAL-TIME TERRAIN RECOGNITION AND OBJECT DETECTION

by

GODFRED SOMUA – GYIMAH

A DISSERTATION

Presented to the Faculty of the Graduate School of the

MISSOURI UNIVERSITY OF SCIENCE & TECHNOLOGY

In Partial Fulfillment of the Requirements for the Degree

DOCTOR OF PHILOSOPHY

in

MINING ENGINEERING

2018

Approved

Dr. Samuel Frimpong, Advisor

Dr. Norbert Maerz

Dr. Kwame Awuah-Offei

Dr. Grzegorz Galecki

Dr. Nassib Aouad

ABSTRACT

The contribution of coal to global energy is expected to remain above 30% through 2030. Draglines are the preferred excavation equipment in most surface coal mines. Recently, studies toward dragline excavation efficiency have focused on two specific areas. The first area is dragline bucket studies, where the goal is to develop new designs which perform better than conventional buckets. Drawbacks in the current approach include operator inconsistencies and the inability to physically test every proposed design. Previous simulation models used Distinct Element Methods (DEM) but they over-predict excavation forces by 300% to 500%. In this study, a DEM-based simulation model has been developed to predict bucket payloads within a 16.55% error. The excavation model includes a novel method for calibrating formation parameters. The method combines DEM-based tri-axial material testing with the XGBoost machine learning algorithm to achieve prediction accuracies of between 80.6% and 95.54%.

The second area is dragline vision studies towards efficient dragline operation. Current dragline vision models use image segmentation methods that are neither scalable nor multi-purpose. In this study, a scalable and multi-purpose vision model has been developed for draglines using Convolutional Neural Networks. This vision system achieves an 87.32% detection rate, 80.9% precision and 91.3% recall performance across multiple operation tasks. The main novelty of this research includes the bucket payload prediction accuracy, formation parameter calibration and the vision system accuracy, precision and recall performance toward improving dragline operating efficiencies.

ACKNOWLEDGEMENTS

I am very grateful to my advisor, Dr. Samuel Frimpong, for his guidance and financial support throughout my study. Thank you for the opportunity to develop my career without restraints. I am also thankful for the guidance offered by my advisory committee members: Dr. Norbert Maerz, Dr. Kwame Awuah-Offei, Dr. Nassib Aouad and Dr. Grzegorz Galecki. Thank you for your contributions towards my development.

Special thanks go to Itasca Consulting Group and the Itasca Education Partnership (IEP) program for the training and free software license. My gratitude also goes to the entire staff of the Mining and Nuclear Engineering department and to the Heavy Mining Machinery Research group, especially to Danish Ali, Bruno Kansake, Mohammed Wardeh and Mohammed Waqas, for their support. I am particularly indebted to Dr. Eric Gbadam and Dr. Wedam Nyaaba, whose presence, selflessness and support allowed me to reach my research objectives much more quickly.

I am very much indebted to my wife, Kyerewaa, for her support, prayers and encouragement throughout my PhD study. I am also grateful to my parents, Mr. Godfried Kwame Gyimah and Mrs. Comfort Seiwaa Gyimah, my brothers, Mr. Clement Saka Gyimah, Mr. Maxwell Boateng-Gyimah, and Rev. William Owusu-Gyimah. I am grateful for your prayers and all the sacrifices you made to enable me to reach this far. Finally, my utmost gratitude goes to my Lord and maker, whose continuous sustenance, grace and provision have brought me this far in life.

TABLE OF CONTENTS

Page

LIST OF ILLUSTRATIONS

Page

LIST OF TABLES

Page

1. INTRODUCTION

This section gives some background information surrounding this research. It summarizes the research problem and highlights the scope and objectives of this study. It provides a high-level summary of the research methodology and also lists the expected contributions of the study to the current body of knowledge.

1.1. BACKGROUND

Coal remains one of the most important sources of energy in the two strongest economies in the world. Currently, the U.S. ranks second world-wide in terms of both coal production and consumption. In the U.S., the EIA [1] projects that coal will contribute at least 20% of annual national energy production through 2040 (Figure 1.1). Coal contribution to China's energy production is expected to be at least twice that figure within the same period (Figure 1.2). The story is no different in the rest of the world as coal contribution to electricity generation is projected to remain above 30% through 2030 (Figure 1.3). In surface mines, coal production is often extracted using the strip mining method. In these mines, dragline mining methods remain the preferred methods for removing overburden. This makes dragline productivity a major factor in coal production. In 1999, about 41% of the total coal production by the United States came from 56 mines dragline operating mines [2]. A dragline system used in surface mines costs anywhere from US$50 to $300 million [3]. The high capital cost of a dragline, coupled with its key role in the coal production chain, has made it an important area of interest to several investigators. Most of the studies in this area have focused on

increasing dragline productivity by improving various aspects of the dragline operating cycle.

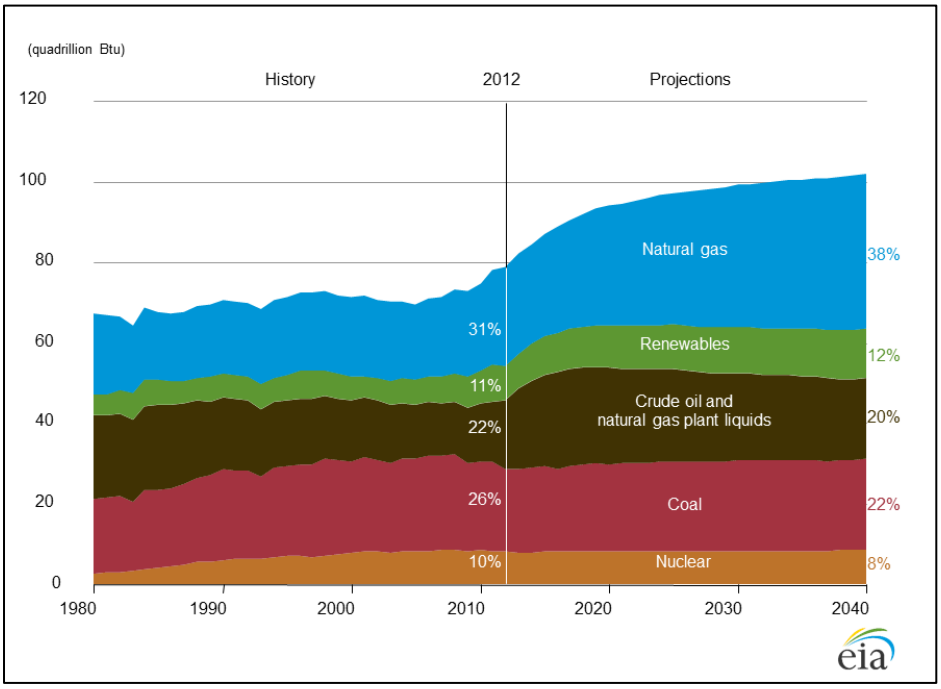

Figure 1.1. Forecast US energy production by source [1]

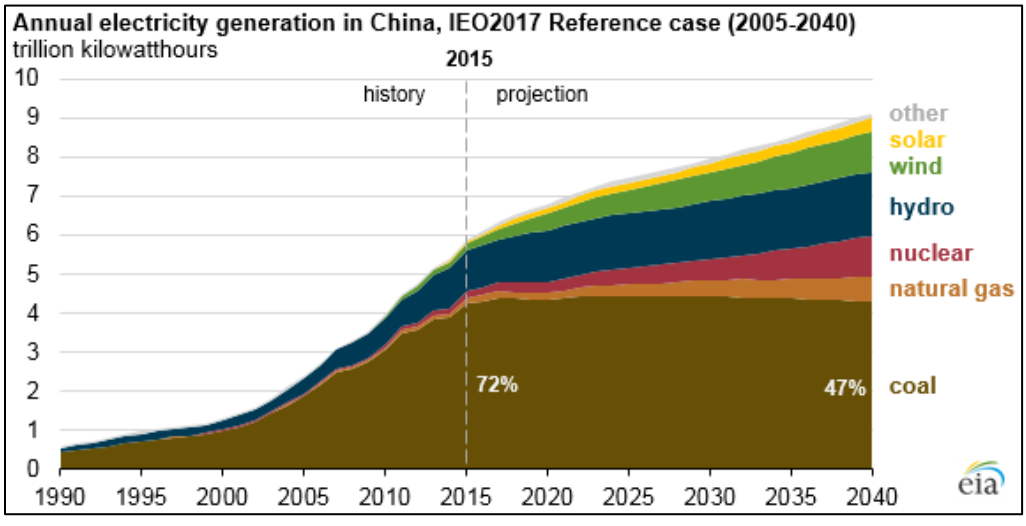

Figure 1.2. Current and projected electricity generation in China [4]

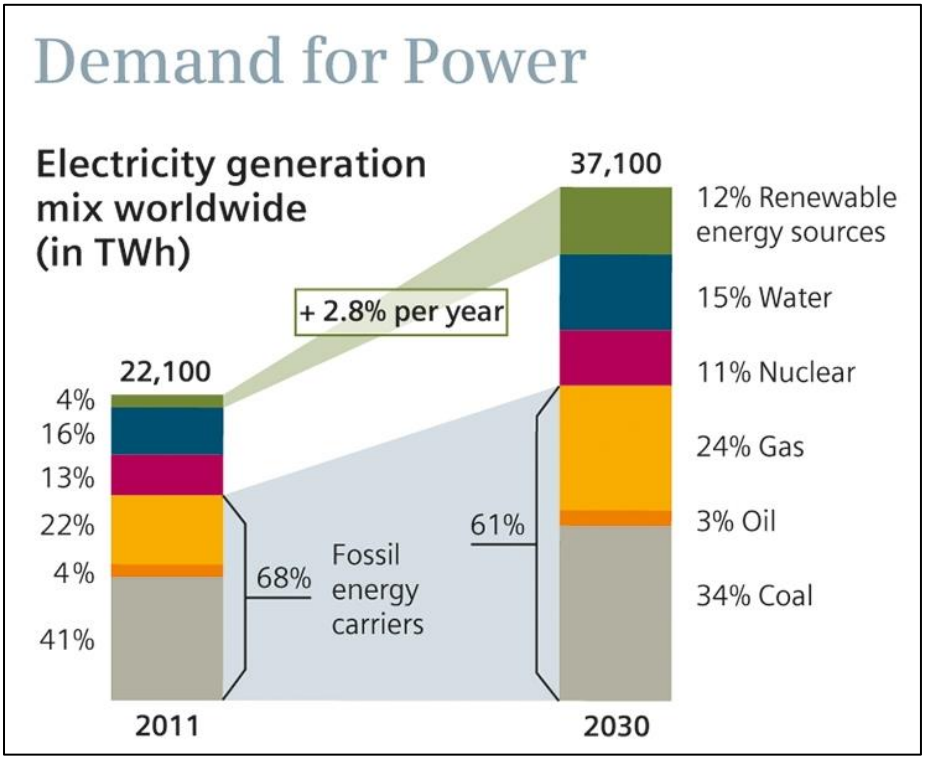

Figure 1.3. Current and projected world electricity generation [5]

Over the years, researchers have concentrated efforts on dragline automation [6-8], kinematics [9, 10], dynamics and rigging [11-14]. The cost of dragline production down time is estimated at AUD 8000 per hour [15]. On the other hand, small improvements in their performance can lead to substantial cost savings. It is estimated that a 1% increase in dragline utilization can contribute an extra $35 million per year in earnings [16]. It is estimated that a 10% improvement in dragline productivity is equivalent to $2,000,000 in savings per dragline per year [17]. Therefore, any study that centers on optimizing dragline productivity (i.e. bucket payload, cycle times, excavation energy) is a step in the right direction.

1.2. PROBLEM SUMMARY

Dragline excavation engineering studies have focused on operating performance. Dragline performance is affected by several factors including operator efficiency, machine availability and material (formation) properties. Dragline excavation technology has improved over the years through the work of several researchers, who sought to optimize different aspects of dragline operations. However, the tasks involved in the work of the dragline operator (swing, hoist, dig, and dump) is an area which has received relatively little attention and therefore remains a bottleneck for production. A study by Lumley [18] found that dragline operator performance on different cycles can be highly variable, even for the best dragline operator teams in the world. Table 1.1 compares the performance of the average dragline operator on key performance indices to best practices. The biggest adverse impacts of operator inefficiency are experienced in reduced payload, hence, increased daily swings and ultimately in reduced productivity. This suggests that current annual dragline production figures are suboptimal and more can be done in this area to improve dragline excavation efficiency.

Over the past couple of decades, there have been efforts to increasingly automate dragline excavation tasks. These efforts have focused primarily on building autonomous systems, which together, will deliver better performance than the average dragline operator. Initial studies and automation trials with hoist, swing and dump tasks gave encouraging results [8, 19, 20]. However, the swing path had to be pre-defined by a human operator, who also monitors the entire swing phase to prevent collisions. Therefore, the unresolved research question in these studies revolved around how the autonomous system will be able to visualize its surroundings and respond to different

situations, without human involvement. This is an even bigger problem during the digging phase, where the excavator cannot follow a pre-defined path, but has to adjust its operations, based on ground conditions. This is a challenge, not only for dragline digging automation but for autonomous excavation in general.

Up to date, the most successful autonomous digging models were all proposed for wheel-loaders and back-hoe excavator operations, where the digging trajectory is slightly more well-defined. Nonetheless, all these models are only successful in completely homogenous material. While some of the models [21, 22] fail completely in the presence of big rocks and other ground obstructions, other models [23, 24] only achieve loading by changing the digging trajectory to avoid these rocks and obstructions. Up to date, the best autonomous digging model [25] uses trial and error to attempt obstruction removal. If obstruction removal is not possible, the bucket disengages and progresses with the excavation elsewhere. The main weakness of all these previous logic-based models is the lack of situational awareness ("blindness") which limits their ability to handle the different, random and complex occurrences of ground obstructions.

Currently, Corke et al. [26] and Hainsworth et al. [27] have proposed the only vision model for dragline operations. However, the model is only able to perform dragline bucket pose estimation tasks. Hence, it requires other dragline vision models to be operational. The model uses an image segmentation technique, which is neither scalable nor suitable for real-time application, and also fails when the bucket approaches full-loading. Therefore, this research will seek to contribute to excavation automation studies by developing a multi-purpose machine vision model, which is scalable, suitable for real-time applications and is capable of addressing all dragline vision tasks. This is an

important step towards improving dragline excavation efficiency through automation as the vision model will enable the dragline to visualize and adjust accordingly to different environments and situations, especially in the digging and swing phases.

Table 1.1. Dragline performance, normalized for Marion 8050 [18]

Key performance indicator	**Average**	**Best practice**	**Impact**
Daily swings (#)	861	957	+13.0%
Payload **(tons)**	88	103.1	+17.2%
Fill time (secs)	15.8	14.9	+1.6%
Swing time (secs)	25.3	25.7	-0.5%
Ret time (secs)	21	20.1	+1.6%
Spot time (secs)	4.7	3.5	+2.2%
Cycle time (secs)	66.8	64.2	+4.8%
Dig time (%)	66.6	72.4	+8.2%
Productivity (BCM/day)	34 440	44 850	+30.2
Productivity (BCM/yr)	12.6 M	16.4 M	

Besides automation, recent dragline excavation efficiency studies have also focused on bucket design improvements. However, this is another area where operator inconsistencies come into play. Currently, the industry standard for bucket design improvements is to build and test the performance of physical scale models of several new designs against conventional buckets. When these new designs are compared with current industry buckets, the differences in performance typically hovers around 10% to 20%. However, the different bucket geometries are not the only variables in these tests. Inconsistencies in operator sequences and techniques alone, can lead to bucket performance variations of over 10% [28].

On the other hand, virtual simulation can provide a control environment, which is repeatable and where the only true variables, are the different bucket geometries. A virtual simulation model will allow for a cheaper and quicker preliminary testing of new designs, while removing opportunity cost to designs that are discarded without testing. Such a model may also be useful in carrying out formation failure analyses and fragmentation studies for efficient excavation. Current dragline simulation models [29, 30] are not able to accurately predict any bucket performance metric, which can be used for comparing different designs. Therefore, this study would also seek to develop a full scale dragline excavation simulation model that is useful for formation failure analyses, fragmentation studies and for testing new bucket designs.

1.3. RESEARCH OBJECTIVES AND SCOPE

The primary goal of this research is to contribute to advances in knowledge and frontiers in dragline excavation and vision. The components of this primary objective include the following:

(i) Develop a scientific method for calibrating the constitutive model of the formation using discrete element parameters.

(ii) Develop a virtual prototype model of a dragline bucket for excavation and bucket payload analysis.

(iii) Develop a dragline vision model to advance excavation efficiency.

This research initiative is limited to dragline excavation technology. Nonetheless, with some modifications where necessary, the derived mathematical formulations and models, as well as the theories and methods employed, may be applied to other excavator

types or tillage equipment. Draglines perform excavations in a cyclic manner. A single operating cycle consists of the (i) bucket filling, (ii) hoisting, (iii) swinging, and (iv) dumping phases. However, all the bucket - formation interactions that are of interest to this study occur during bucket filling. Therefore, the offline simulation portion of this research focuses primarily on the bucket filling (digging) phase processes. In addition, the research is mainly concerned with the development of computer solutions to excavation problems. Consequently, no physical experiments were carried out. Rather, the reported analytical and experimental results of other investigators were used for validating the models.

1.4. RESEARCH METHODOLOGY

A literature review has been undertaken to establish the extent of knowledge in the field. This review includes previous theoretical, experimental and numerical methods employed for various dragline excavation studies. The artificial intelligence model for terrain and obstacle recognition will be developed using a deep learning approach. The convolutional neural network architecture will be used to fit the model. Over 2,000 images collected for different mobile mine equipment, excavation terrains and over-sized particles will serve as data for training the model using the Tensorflow [31] package in Python. The vision model will be verified and validated a portion of the dataset. Application experiments will then be conducted to test the model on publicly-available videos.

For the offline simulation model, interactions between the formation and the dragline bucket will be simulated using the DEM technique [32]. Mathematical models

are used to dynamically measure the required excavation outcomes at pre-determined time intervals. The Hertzian Contact Theory [33] will form the basis for the formation's constitutive model. The discrete parameters of the constitutive model will be calibrated using a machine learning approach, specifically the eXtreme Gradient Boosting algorithm [34]. The data for the calibration will be obtained from virtual laboratory test simulations using a combination of Python and FISH scripting in the DEM framework, Particle Flow Code 5.0 (PFC 5.0). The calibration model will be verified and validated using available overburden property data. The dragline simulation model will also be verified and validated using both qualitative and quantitative comparisons with available experimental data from an Australian mine [35].

Further experiments will be conducted to investigate the following: (i) the performance of the formation calibration model over large-scale testing, (ii) the inter-relationships between formation properties and DEM micro-properties, (iii) the effects of material particle size distribution on simulated excavation performance (payload), and (iv) the material density distribution in a dragline bucket during loading.

1.5. SCIENTIFIC AND INDUSTRIAL CONTRIBUTIONS

Firstly, the dragline excavation model, from this research, expands existing knowledge on the mechanics of formation failure in dragline operations. It confirms existing theories about the formation failure process. It also introduces new knowledge about density variations in the formation ahead of the bucket.

The dragline excavation model is also expected to have immediate industry relevance. It provides an opportunity for parameterized simulation of dragline

excavations under varying control conditions. The simulator will serve as a dependable platform for comparing and evaluating the performance of new bucket designs. It will eliminate operator inconsistencies and scale effects, which are notable improvements on current results obtained through experimental testing. Also, the simulation model will significantly reduce the amount of effort, time and cost that is currently spent on prototype testing for bucket design improvements.

Thirdly, the goal of formation blasting is to achieve good fragmentation for efficient excavation. Poor fragmentation from blasting results in increased cycle times and hence, reduced productivity. Therefore, a clearer understanding of the effects of different material size distributions, on the performance of a particular dragline bucket, holds a lot of promise for optimizing excavation performance. For a given dragline bucket and excavation environment, this can be achieved by observing bucket performance for different fragmentation simulations. When the material size distribution, which guarantees optimum dragline performance is determined from the simulations, it can be used as an input for blast design. The excavation simulation model, from this study, will provide a means for determining the best fragmentation that promises optimum excavation efficiency.

In addition, one challenge with discrete element modeling is that the method requires calibration of model micro-parameters and there is currently no widely-accepted process for calibrating earth materials. The calibration model, from this research, will provide a scientific and generalized process for determining the micro-parameters, which replicate earth material behavior. The model could also be extended for calibrating other granular materials with very little adjustment.

Finally, previous efforts towards autonomous excavation have resulted in a few robotic excavator models that complete digging cycles successfully in homogenous material. However, these models fail when they encounter big rock obstructions. The machine vision model, from this research, will form the basis for future digging control systems. It will enable an autonomous excavator to recognize big rock obstructions and different excavation environments so that the digging strategy may be adjusted accordingly. This study is the first attempt to develop a multi-purpose vision model for any excavator. The study will leverage some significant advances in artificial intelligence, within the last couple of years, to address age-old autonomous excavation challenges, such as bucket pose estimation, boulder identification and terrain recognition.

1.6. STRUCTURE OF DISSERTATION

Section 2 is a comprehensive survey of all relevant literature. It comprises dragline automation studies, machine vision studies in the excavation industry, formation failure theories, processes and resistance models in earthmoving and advances in the evolution of dragline excavation technology.

The first part of section 3 contains details of the proposed geomaterial calibration procedure using machine learning. It discusses the virtual triaxial test simulation process, wrangling of test data and feature engineering, model building and feature selection as well as model verification, validation and experimental design. The second part of the section discusses the methodology behind the offline dragline simulation model. It contains the mathematical modeling for the excavation performance metrics, a discussion

of the distinct element method and simulation modeling in PFC as well as model verification, validation and experimental design.

Section 4 presents the dragline vision modeling approach. It focuses on the theory behind convolutional neural networks, the image data collection and annotation procedure, data augmentation techniques, model training process as well as model verification, validation and experimental design. Section 5 details a discussion of the results from the experiments. Finally, section 6 consists of the research conclusions, contributions and recommendations for future research directions.

2. LITERATURE SURVEY

There has been a significant amount of effort toward dragline excavation research over the past couple of decades, especially by the Australian Coal Association Research Program (ACARP). Since its inception in the early 1990s and as of April 2008, the program had resulted in a 10% improvement in dragline productivity for the Australian coal mining industry. In monetary terms, this is the equivalent of two (2) million USD per dragline per year or 150 million USD for the entire coal industry [36]. Most of ACARP's dragline studies have focused generally on mechanical issues and specifically on dragline productivity and automation [37]. This section will present the seminal literature, which is relevant to dragline excavation research and technology.

2.1. ARTIFICIAL INTELLIGENCE STUDIES IN EXCAVATION

When Orenstein and Koppel presented 'FUTURE' as the first automated excavator in the 1980s at a German science fair, it was considered a sci-fi and fantasy project [38]. The automated component, proposed by Orenstein and Koppel, was an on-line monitor which tracked the actual condition of the excavator's hydraulic system and engine [38]. Since then, various studies have considered the possibility of developing different automated systems for ground excavation. A detailed review of this literature has been presented by Singh [39]. Early studies into autonomous excavation identified some key performance criteria which included the following [25]:

- The autonomous excavator must be able to work in any type of earth material.
- Its excavation accuracy must be within 50mm.

- It should be able to handle different surface and underground obstacles autonomously.
- It should be able to operate at the speed of the average operator in any condition.
- Its operation should be capable of safe integration with other site systems.

One early school of thought held that understanding the soil / rock mechanics and operator behavior during the excavation process is integral to any autonomous excavator model. However, this view was quickly discarded for a number of reasons. Firstly, the excavation process is complex due to the wide range of physical properties of naturally-occurring earth material. This is further complicated by the random occurrence of tree roots, boulders and other such obstructions, which deviate from regular material failure processes. It had however been observed that excavation success depended a lot on the manipulative skills of operators. Therefore, it was concluded that the capability of a controller to detect changes in the operating conditions, adjust its digging strategy and respond in real-time was of utmost importance [25].

Up to date, all the partially-successful models in autonomous excavation adopted classical, rule-based artificial intelligence methods. By observing both experienced and inexperienced operator actions, various investigators have developed rule-based systems which define the digging trajectory. The major difference in these autonomous excavation models is in their response to tree roots, big rocks and other random obstructions in the ground.

The simplest of these systems use pre-set force thresholds to pre-define the excavator response. Gocho [22] presented an autonomous model for the wheel loader. The model was able to achieve loading by driving the bucket into a muckpile until a pre-

defined hydraulic pressure threshold is reached. At that point, the loader scoops the material and moves towards the dumping area. A similar model was proposed by Bullock and Oppenheim [21] for the back-hoe excavator. In their model, Bullock and Oppenheim [21] used strain gauges to monitor strain measurements as the back-hoe travelled through a prescribed trajectory until a preset threshold was exceeded. However, both models fail to successfully complete digging when they encounter big rock obstructions.

Shi et al. [24] Huang and Bernold [40] later extended the digging controls in the previous autonomous wheel loader and back-hoe models to accommodate the presence of big rocks in the ground. However, both models achieve loading by changing the digging trajectory to avoid obstructions, once encountered (Figure 2.1).

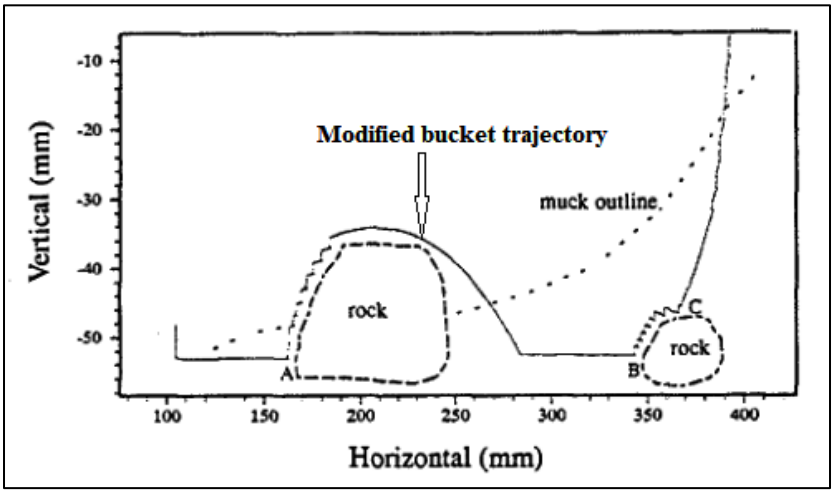

Figure 2.1. Obstacle avoidance wheel loader model [24]

The most successful autonomous excavator model, up to date, was presented by Bradley and Seward [25] for a back-hoe excavator. Their model achieves obstruction removal in some cases, using a trial and error approach (Figure 2.2). In their model, a

boulder is first detected via the force feedback from contact. When this happens, the bucket attack and drag angles are adjusted repeatedly until the bucket completely penetrates the ground underneath the obstruction. If this is not possible, the bucket disengages and progresses with the excavation elsewhere.

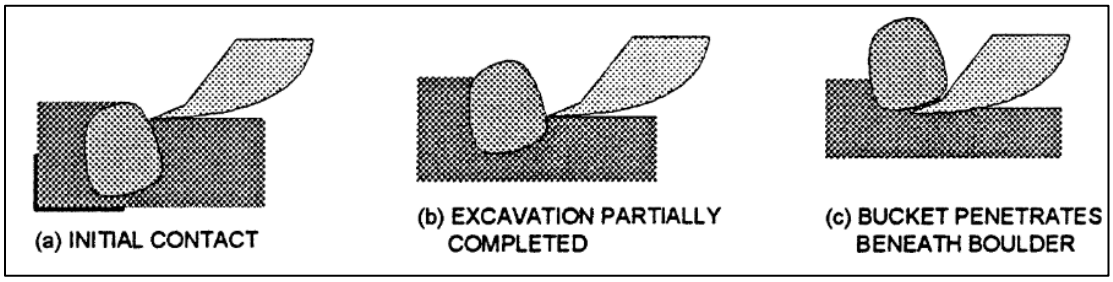

Figure 2.2. Big rock removal by trial and error [25]

The main weakness of all these previous logic-based models is the lack of situational awareness ("blindness") which limits their ability to handle the different, random and complex occurences of obstructions in the ground.

2.2. DRAGLINE AUTOMATION STUDIES

For draglines, initial attempts in automation focused on improving the monitoring of the operating phase. To this end, McCoy and Crowgey [6] developed an automated model for controlling the tightline of dragline buckets. Based on a geometric analysis and the length of the ropes, the model established tightline limits. These limits form part of a control system that monitors the dragline operations and stops or slows down the rope drives when the preset tightline approaches its limits [41].

As scaled physical models grew popular for performance optimization, dragline excavation monitoring also became an essential means of acquiring actual performance data for model validation. By comparing the performance data from fourteen (14) dragline monitors, Lumley and Haneman [42] spotted a high variability in the performance of different draglines. Some of the performance indicators, which were used included idle time, bucket efficiency ratio, return time, swing time, fill time, swing angle and cycle time among others. The high-performance variability was found to be greatly influenced by the differences in bucket design and rigging.

Beyond monitoring, the utmost benefits in dragline automation will be derived from automating the operator's actions, as was revealed in a study by Lumley [18]. Fundamentally, dragline excavation can be considered as the interaction between three main components namely the operator, the dragline excavator, and the ground / formation. Dragline technology improvement studies, in the past, have always focused on one of these areas. Of the three components, operator action is arguably the biggest bottleneck in dragline technology today. Generally, equipment performance is known to be heavily dependent on operator skill, attitude and knowledge [43].

With the aim of investigating variability in dragline operator performance, Lumley [18] studied the team of operators for a dragline that consistently achieved productivity in the top 10% of draglines worldwide. After documenting the productivity and damage impact of each operator on the team (Figure 2.3), Lumley discovered that the average difference between the most productive operators (no. 5 and 23) and least productive operators (no. 14 and 7) is about 35% in productivity and 140% in equipment damage impact. The fact that this study was carried out on one of the best dragline

operator teams in the world makes the results even more disturbing. Interestingly, the study also revealed that even the best operators, are still some way off the optimum performance zone for both productivity and damage impact (Figure 2.3).

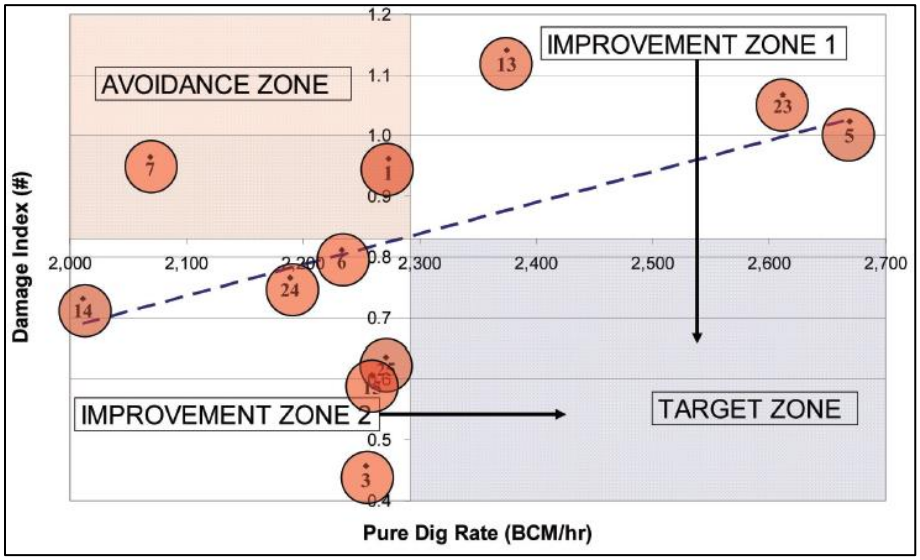

Figure 2.3. Damage versus productivity for dragline operators [18]

Lumley's observations are further supported by Jessett [28], who estimated that inconsistencies in operator sequences and techniques can lead to productivity rate variations of over 10% on any given day. Even for the same operator, Lumley showed that production performance can vary significantly over a six-month period (Figure 2.4), especially for the less-experienced operators. In most industries, people get better with age. The reverse was found to be true in the case of dragline operators. A more recent study by ACARP [17] revealed that the productivity of dragline operators generally declines at an average rate of 0.75% per year of age. The same study also found that operators, on the average, lose about 0.35% of their overall motor skills per year of age.

Earlier solution strategies adopted by most mining companies, involved operator training and performance monitoring. However, these strategies did not sharply improve operator performance or reduce performance variability in the long term. Hence, in the industry's quest for increased productivity, automation has been considered as the next phase in dragline technology evolution for the past couple of decades [44]. Currently, most dragline automation efforts have focused on addressing different aspects of the operation cycle. Advancements in this area have been rather incremental with early studies focusing on remote dragline operation (tele-operation) and semi-automation. Figure 2.5 shows the complete evolution trend for dragline technology. Dunbabin et al. [45] developed one of the first tele-operated dragline models. It was a 1/7 scale model, which was capable of digging, swinging and dumping without direct human operation.

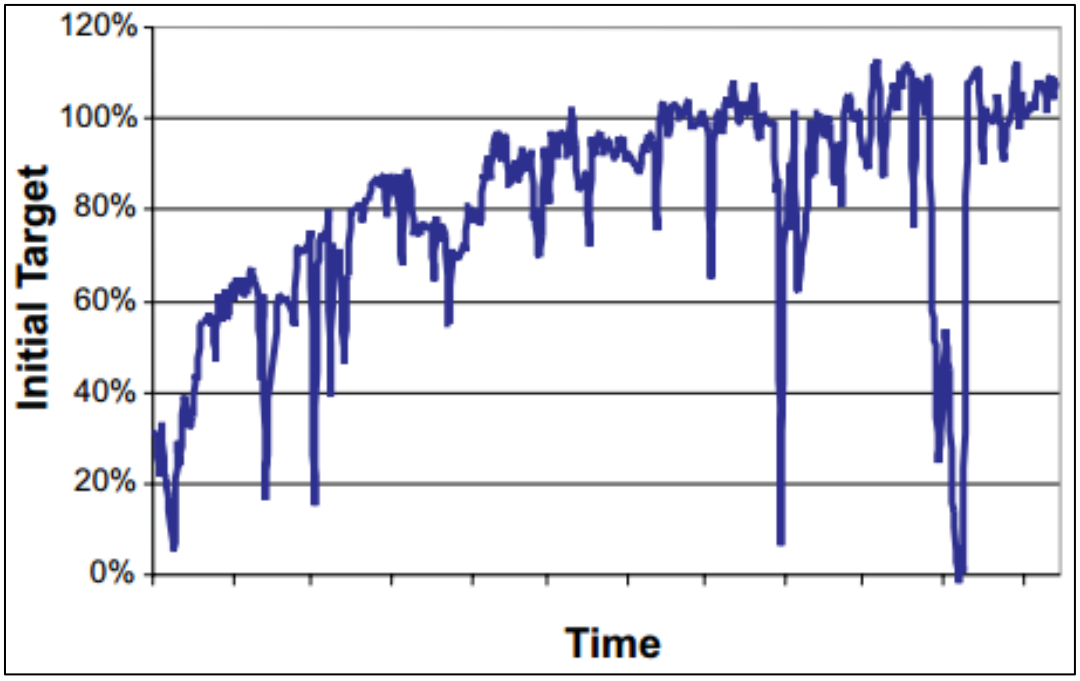

Figure 2.4. Variability in operator digging over six months [18]

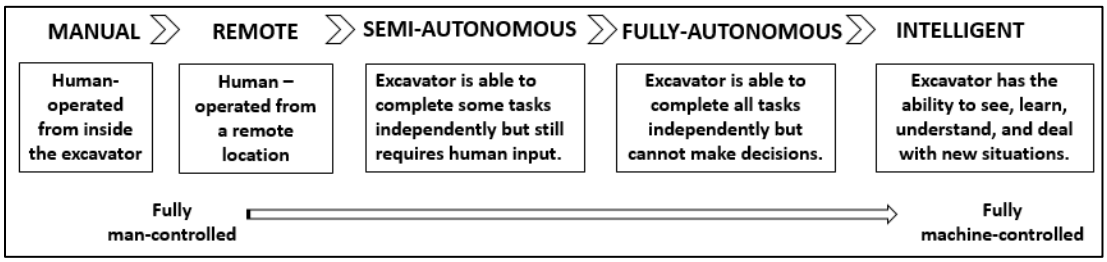

Figure 2.5. Dragline technology evolution

Albeit indirectly, the model still required human control since coordinates for both dig and dump locations had to be pre-defined on an on-board controller prior to every cycle. When tested experimentally, the model was able to complete 50 cycles, moving about 5.1 cubic metres of material in the process. Despite its latency problems, the study is still regarded as an important step towards remote excavation operations, especially for extra-terrestrial mining. Corke et al. [9] presented the first semi-automated mechanical control system for an electric walking dragline. Simulations were performed by using partial manufacturer data to design bucket position control systems. The control model was verified using a 1:10 scale dragline model. Based on this effort, later studies [46-48] led to the optimization and full automation of the dragline dump phase.

For over 20 years, ACARP and the Commonwealth Scientific and Industrial Research Organization (CSIRO) of Australia have spearheaded research efforts on dragline automation. Notably, most of their efforts have centered on automating the swing, dump and return phases of the dragline operation cycle [18]. Corke et al. [26], Corke et al. [46], Winstanley et al. [48], and Winstanley et al. [20] developed a dragline swing automation system to reduce dragline cycle time, consequently reducing excavation costs. One limitation of the study, however, was that the monitoring systems

could not measure the bucket position during the swing phase. Hence, their Dragline Swing Assist (DSA) system was limited by its "blindness" to the excavator's surroundings.

Roberts et al. [49], therefore integrated the three dimensional imaging technology, Digital Terrain Mapping (DTM), with the DSA system for providing situational awareness to swing automation tasks. This was achieved by mounting a DTM laser scanner at the tip of the boom, giving the system an eagle-eye view of the whole excavation environment. This makes it possible to map areas which are obstructed from the operator's view. The result is a short, collision-free path for completing the swing task. However, the model by Roberts et al. [49] still required human interference to avoid swing collisions. Despite all these studies, the complete automation of the entire dragline operating cycle is not yet a reality. A lot of studies have focused on optimizing and even automating other phases of dragline operations but studies on the actual digging phase are relatively limited. The digging phase is, perhaps, the most difficult to automate since it involves forceful interaction with the terrain [50]. Other phases do not involve unpredictable interactions, like in the case of formation interactions. Therefore, autonomy in these phases implied making the excavator complete pre-determined tasks, traveling through pre-determined paths.

On the other hand, the digging phase presents a unique challenge where the bucket – ground interactions may lead to multiple possible outcomes. Therefore, the excavator's subsequent actions must be a direct response to ground interactions and cannot be pre-planned. Hence, full autonomy of the digging phase also requires that the excavator is able to adjust its operations instantaneously, based on the outcome of any

given bucket-ground interaction. Apart from productivity concerns, another risk in autonomous digging is the damage that machines could suffer due to overloading and inappropriate digging routines.

Therefore, for the digging phase, the ability of the excavator to independently complete pre-determined tasks (i.e. automation) is not enough. It must also be able to see, learn, understand and adjust (i.e. intelligent) to constantly changing excavation environments; hence the need for a smart, autonomous excavator. Most, if not all, of a human operator's actions in the digging phase are directly influenced by what he sees. The operator then acts to control bucket movement based on what is happening. Therefore, the entire digging phase can be considered as several cycles of operator action – ground response – operator's adjusted action – new ground response (Figure 2.6), which is guided by the operator's vision.

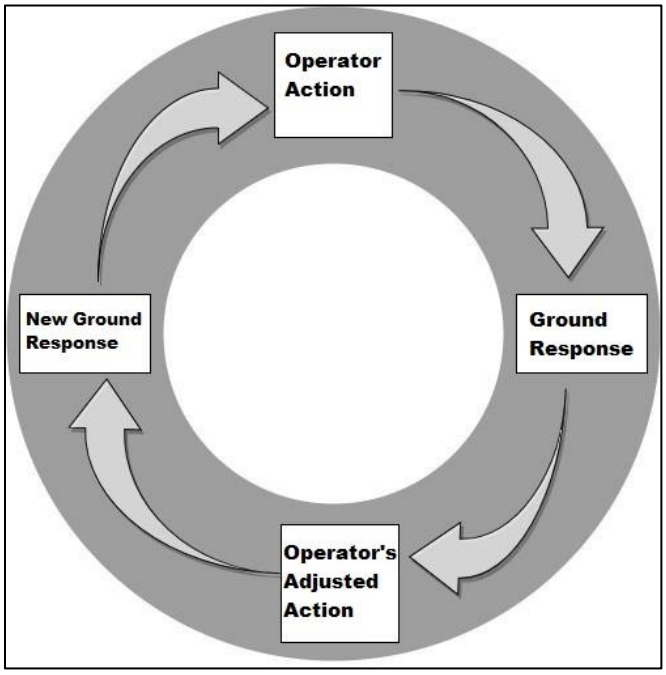

Figure 2.6. Digging phase cycle

Also, for full dragline autonomy, the bucket position must be known, both for stable control of the bucket's movement and for developing path plans to optimize bucket performance [27]. While, there has been very little progress on completely automating the digging phase up-to-date, there has been more interest in solving the machine vision problem. Since an operator's vision influences the entire operating cycle, the development of a fully-functional, multi-purpose dragline vision model is an important step towards full autonomy.

2.3. RECENT VISION-BASED STUDIES IN THE EXCAVATION INDUSTRY

Most of the past vision-based studies in the excavation industry have focused mainly on hydraulic excavators and dump trucks. These studies vary mainly by the feature extraction method used and also by the vision task. Vision tasks typically fall into one of three categories: (i) object recognition, (ii) detection and tracking, and (iii) action recognition. Feature extraction methods used also fall into two main categories: (i) traditional image segmentation using either background subtraction or foreground detection, and (ii) feature extraction using the Histogram of Gradients (HOG).

Chi and Caldas [51] proposed an automated object recognition model for real-time safety monitoring on construction sites. The model first uses a background subtraction and region segmentation algorithm to separate the moving objects from the rest of the image. Image classification is then achieved using both Bayes and Neural Network classifiers. Ji et al. [52] also proposed a model for detecting trucks and excavators using image segmentation. In place of background subtraction, Ji et al. [52] uses a foreground detection algorithm to extract the excavator and dump truck features

from the rest of the image. When tested on actual construction videos, their model achieved detection rates of 73% to 89%.

Bügler et al. [53] presented a novel vision-based method for estimating and monitoring the excavation productivity of construction equipment. The main novelty of their approach is that it combines two data sources (photogrammetry and video analysis) to generate productivity estimates. Photogrammetry algorithms are first used to obtain estimates of excavated material volumes from both ground and aerial images. Video analysis of excavator-dump truck interactions is then used to generate activity statistics, which is later combined with material volume estimates to obtain productivity estimates at specified intervals.

To date, the only vision-based model for draglines was presented by Hainsworth [7] to solve the problem of bucket pose estimation. His study presented a 1:10 scale dragline model which automatically senses bucket position using image segmentation techniques. The machine vision system was achieved by mounting a video camera at a point on the boom to overlook the entire area of bucket motion. The edge outline of the bucket is then colored in green paint. Background subtraction is then used to filter out just the green pigment in the image. Using this approach, the author could locate and track the centroid of the bucket. When tested at full scale, the results on the scaled model could not be satisfactorily replicated on a full-size Tarong dragline. One of the limitations of this model was that the green paint on the bucket edge outline is sometimes covered by the excavated material and this causes the segmentation technique to fail for bucket pose estimation. Generally, image segmentation models do not perform well in active

environments where several different objects need to be recognized within the same image sequence.

In this regard, the HOG method, proposed by Dalal and Triggs [54], outperforms traditional image segmentation approaches. The fundamental idea behind the HOG method is that an object shape and appearance can often be well described by the distribution of edge directions and local intensity gradients in an image. Practically, this is achieved by dividing the image into small regions with each region accumulating a local histogram of edge orientations and gradient directions. The image representation is then formed by a collection of different features, which are defined by the individual local histogram entries.

Most of the recent machine vision models in the excavation industry use the HOG method. Azar et al. [55] developed the server-customer interaction tracker (SCIT), which identifies and measures material loading cycles of dump trucks. The authors used the HOG method for dump truck recognition and Haar-cascade features detection algorithms for tracking the dump trucks. The model detects material loading actions using a combination of pattern recognition and logic-based understanding of spatio-temporal image data, collected from excavator-dump truck interactions. When the SCIT model was tested on real-life construction videos, the results showed that dump truck recognition and tracking were both slow. Also, the SCIT model can only track one operating excavator and hence, is not suitable for construction environments with multiple earthmoving operations.

Memarzadeh et al. [56] also introduced a model to detect excavators, haul trucks and workers in construction environments. Their model combined HOG and color

descriptors with binary Support Vector Machine classifiers to achieve object detection. Golparvar-Fard et al. [57] developed an action-recognition model, which identifies different phases of excavator and truck operating cycles. The model was trained using four classes of excavator action (digging, dumping, hauling, swinging) and three classes of truck action (filling, moving, dumping). The model achieves action recognition by combining the HOG feature extractor with a multi-class Support Vector Machine classifier. The authors tested the model on a construction video dataset and reported model accuracies between 86% and 98%.

Nonetheless, the HOG method is computationally expensive and image processing times are usually very high [55]. HOG method uses a brute force algorithm to search an entire image for target features. Generally, this results in poor scalability and high latency, which limits the suitability of HOG-based models for real-time applications.

2.4. FAILURE MECHANICS IN EARTHMOVING

The failure of earth formations occurs mainly in compression, tension or shear. The most common type of failure in earthmoving operations is shear failure. This section discusses the failure theories and failure processes in earthmoving, as well as the formation resistance models which have been proposed by previous investigators.

2.4.1. Failure Theories in Formation-Excavator Studies. The first attempt at studying formation strength and failure is credited to Coulomb [58]. Coulomb proposed that the resistance of soils to shear failure depends on the soil's internal friction angle, on the cohesive bonds between its particles and on the normal stress, which acts on the failure surface. Mathematically, the relation is expressed as equation 2.1. Rankine [59]

also proposed a theory to address tensile failure of earth materials. The theory assumes that failure occurs when the tensile strength of the earth material is exceeded by the maximum principal stress. However, Rankine's analysis involved several limiting assumptions. Firstly, the earth material was assumed to be both frictionless and cohesionless. Also, the formation failure surface was considered to be planar with the formation-wall (i.e. tool) interface assumed as vertical.

$$\tau_n = c + \sigma_n \, tan \, \emptyset \tag{2.1}$$

Mohr [60] chose to follow Coulomb's approach and later brought more clarity to Coulomb's work by introducing a linear envelope that could predict the failure of a material on its weak surface plane (Figure 2.7). Mohr-Coulomb's failure theory was widely accepted to be true for all isotropic, homogenous materials. However, Karman [61] and Boker [62] performed tests on earth materials and found that, while the theory delivers good accuracy for mid-range compressive stresses, the results are less impressive when the stresses are closer to the extremes. Another criticism of the theory is the assumption of a planar failure surface and a straight line envelope.

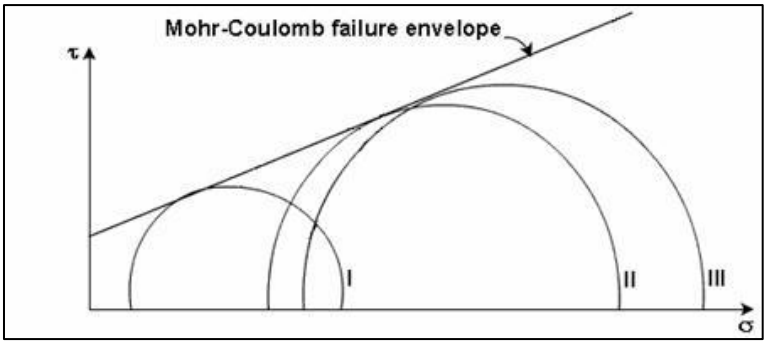

Figure 2.7. Mohr-Coulomb's failure envelope [63]

2.4.2. Formation Failure Processes in Earthmoving. Ohde [64] later developed a logarithmic spiral method that yields a curved envelope. While the method was initially intended for evaluating soil loads, it has been used extensively [65-68] for calculating formation resistance in earthmoving operations. From Ohde's analysis, the earth material that fails, under the action of an excavating tool, is assumed to have two components (Figure 2.8): i) a Rankine passive zone; and ii) a shear zone, which is bounded by a logarithmic curve [69]. The failure surface geometry, proposed by Ohde, was later confirmed through the observations of Selig [70] on the failure mode of different soil types when acted upon by flat blades. However, one limitation of Ohde's method is that it requires a lot of tedious trial solutions in order to obtain the minimum force. Also, the method is not applicable for low rake angles.

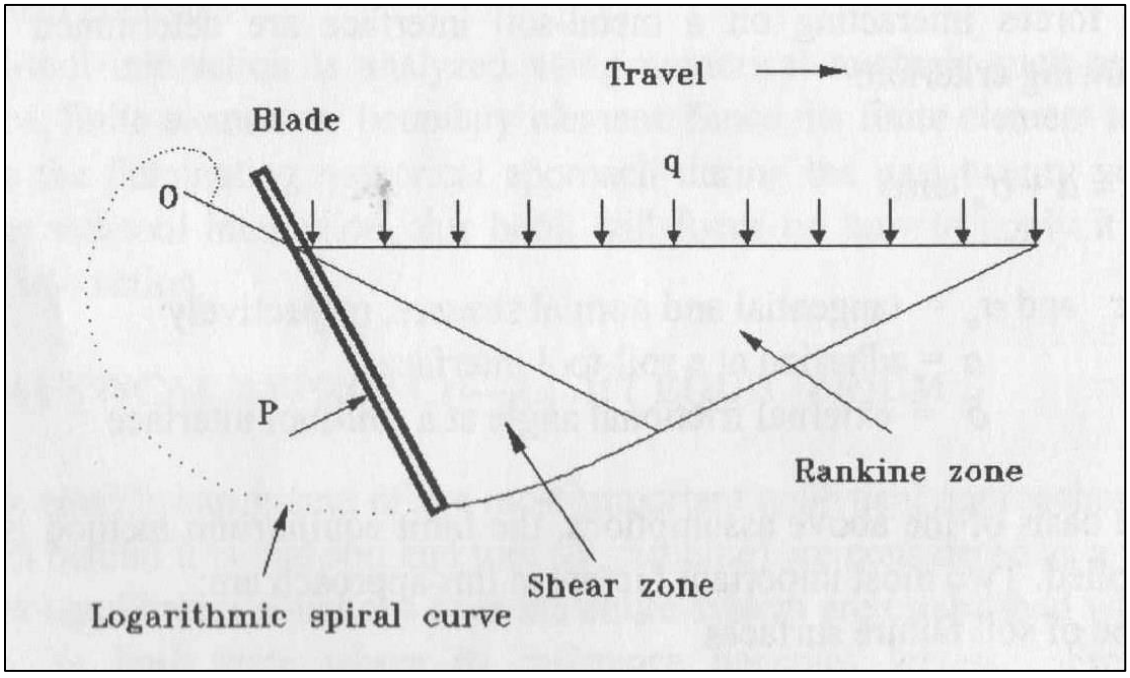

Figure 2.8. Ohde's logarithmic failure theory [69]

After carrying out several experiments on how hard bodies penetrate soft materials, Prandtl [71] observed that the soft bodies underwent plasticity upon failure. Based on these findings, Terzaghi [72] applied Prandtl's plasticity theory to the failure of earth materials under the action of shallow foundations. According to Terzaghi's analysis of the failure mechanism (Figure 2.9), upon failure, the earth material comprises of three (3) zones:

(i) Elastic zone (Zone I), the wedge-shaped area that forms under the surface load;

(ii) Radial shear zones (Zone II), the area bounded by the logarithmic spiral; and

(iii) Rankine passive zones (Zone III)

DeBeer and Vesic [73] later confirmed the nature of the failure surface that Terzaghi assumed in his study. However, their experimental results also showed that the size of the wedge-shaped elastic zone (Zone 1) had been under-estimated, whilst the radial shear zones (II) had been over-estimated in Terzaghi's analysis.

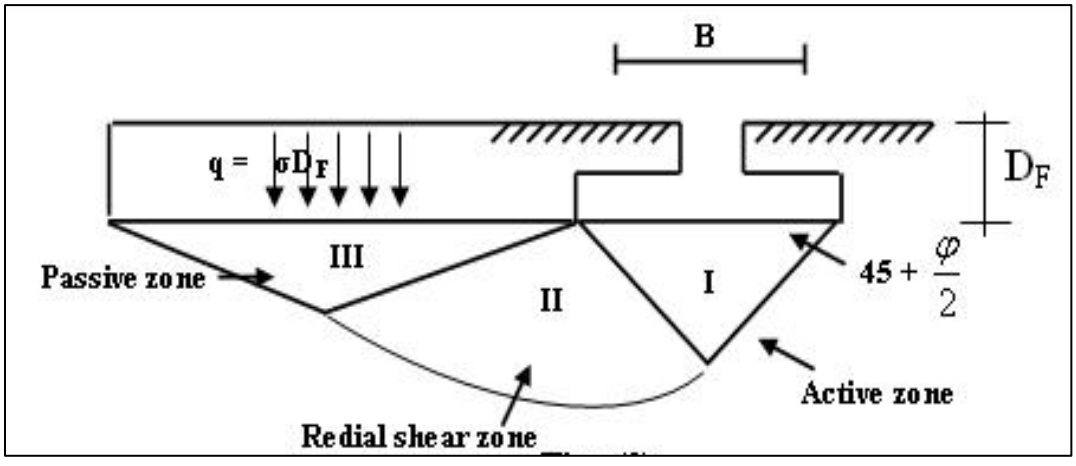

Figure 2.9. Terzaghi's failure theory [74]

Early investigations into formation-tool interactions focused on the formation failure ahead of narrow tools used in agricultural tillage operations. Initial attempts, at better understanding the formation-tool failure phenomenon, were concerned with characterizing the formation and determining the properties, which influence failure patterns. Fountaine and Payne [75] identified these properties to be density, cohesion, soil-metal friction, adhesion and internal friction.

Other studies also focused on fully establishing the various stages involved in the development of formation failure. Payne [76] closely analyzed the mode of soil failure by narrow tools and observed that a wedge-shaped soil block is formed in front of the tool and moves forward with it, acting as a knife in splitting the soil sideways and upwards. O'Callaghan and Farrelly [77] also carried out similar tests on three (3) different types of soil. They observed that the failure zone consisted of two zones: (i) a zone, which resembles Ohde's logarithmic spiral and (ii) a second zone, which satisfies the Prandtl-Terzaghi failure condition.

Osman [78] also tried to assess the applicability of two earth pressure theories (Coulomb's and Ohde's) to excavation processes. Osman concluded that Coulomb's wedge solution only held good for smooth blades of small rake angles, working in cohesionless soils. On the other hand, he found that Ohde's solution gave better accuracy over a wide range of rake angles and soil types [79]. More recent studies by Siemens et al. [80], Bailey and Weber [81], Hettiaratchi and Reece [67], Godwin and Spoor [82], McKyes and Ali [83], Perumpral et al. [84], Swick and Perumpral [85] and Zeng and Yao [86] have resulted in observations that agree either fully or partially with those of Payne, O'Callaghan-Farrelly and Osman.

While formation failure with tillage tools has been extensively researched, relatively little work has been done in earthmoving. The two disciplines have several similarities in their modes of formation failure but there also exist subtle differences. One such difference is the tool orientation, position and trajectory during operation. Most tillage tools merely push and turn the soil. These tools are often vertical or slightly inclined and do not completely undercut the formation during the operation. On the other hand, most earth-movers, such as draglines, consist of near-horizontal components that completely undercut the formation. Therefore, the mechanics of formation failure will differ due to the tool geometry, orientation, trajectory and on the formation properties.

Earthmoving-formation interactions research began in the mid-1900s by the Caterpillar Tractor Company, when Cobb, Cohron and a small team of investigators applied soil mechanics principles to the design of more efficient scrapers [65, 87]. For dragline research, Rowlands [88] carried out the first study on the formation failure ahead of the bucket. Figure 2.10 is a summary of Rowland's observations. By observing the bucket filling patterns of granular materials, he noticed that the failure processes for dragline buckets were quite different from what had been previously presented for other types of excavation equipment. Rowland suggested that, at the initial stages of bucket filling, the granular material can be divided into three different zones: (i) a zone of laminar flow into the bucket, (ii) the active dig zone and the (iii) virgin (undisturbed) material zone. However, as the bucket motion progresses, the number of zones increase to include an active flow zone and a dead load zone.

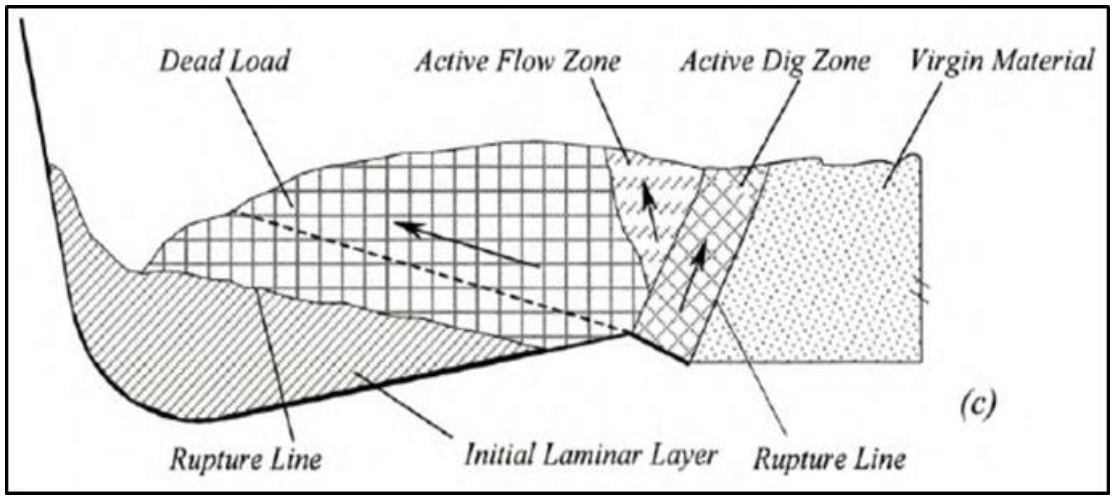

Figure 2.10. Failure regime in Rowland's shear zone theory [88]

Coetzeé [89] later carried out a two-dimensional discrete element experiment, to confirm that Rowland's Shear Zone Theory, holds for other granular material. In his study, Coetzee investigated the flow characteristics of corn and wheat into a bucket-like equipment with a wide blade. By monitoring the ratio of individual particle displacements to blade displacements, he managed to identify the formation of zones at the front end of the blade and found them to be quite consistent with Rowland's theory. Figure 2.11 shows results of the study with the particle displacement ratio (PDR) range for each zone. Fundamentally, the two studies by Rowland and Coetzee suggest that, for dragline bucket filling, the shear zone (active dig zone) follows a Rankine-type failure. Nonetheless, the complex nature of the flow characteristics also warrants some attention. One major limitation of the two models is that they both ignore the effects of the bucket sides, which have been known to also influence formation interactions [90].

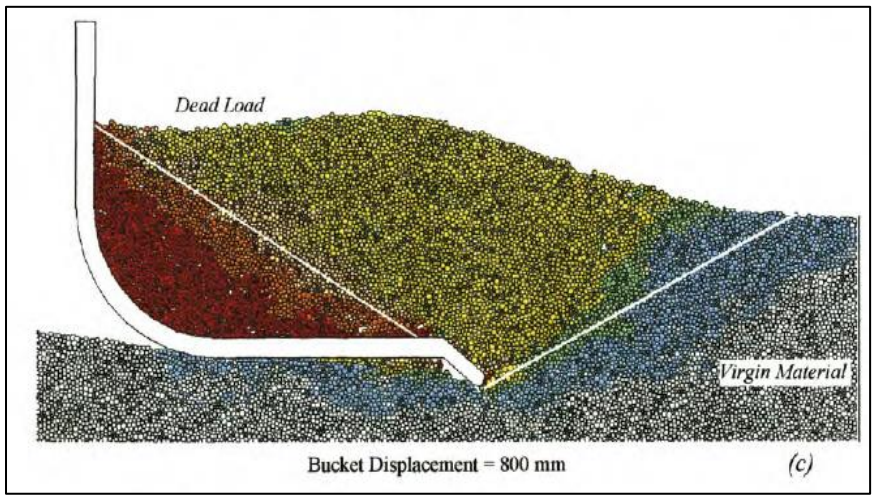

Figure 2.11. Failure regime ahead of a dragline bucket [89]

2.4.3. Formation Resistance Models. The formation resistive forces, which an excavator equipment is required to overcome, have been categorized into three (3) groups by Blouin et al. [91] and Hemami et al. [92]. These groups include:

(i) force required to penetrate the formation (i.e. penetration force);

(ii) force required to move the tool through the formation (i.e. cutting force); and

(iii) total force required to separate, dig out and extract part of the formation (i.e. digging force).

Early records of penetration force studies include the works of Prandtl [71] and Terzaghi [72]. One crucial but perhaps unintended consequence of their work was the discovery that the penetration of a hard body into a softer body also led to shear failure. Having made similar observations, Zelenin et al. [90] noted that the failure pattern of geomaterials were similar for both penetration and cutting forces. Blouin et al. [91] also suggested that, for all practical purposes, the amount of penetration into the material may be used as a measure of its cutting resistance. This is particularly true for situations, such

as dragline bucket filling, where the penetration phase is not completely divorced from the cutting phase.

Formation cutting force theories can be further grouped into (i) those that are derived from fundamental continuum mechanics principles and (ii) those that stem from experimental observations of the cutting process [93]. Reece [65] was one of very few researchers to base their studies on fundamental soil mechanics principles. By comparing formation shear failure in earthmoving to the Prandtl-Terzaghi bearing capacity failure, Reece proposed the fundamental earthmoving equation.

However, Reece's work did not consider the effects of inertia. McKyes [94] later added an inertia term to Reece's work which resulted in equation (2.2) for the resultant cutting force. N_γ, N_c, N_a, N_q, N_{ca} are the weight, cohesion, inertia, surcharge and adhesion factors respectively. Similarly, the horizontal component of the cutting force is given by equation (2.3). Most of the cutting force models were based on experimental studies. From his experiments, Osman [78] proposed one of the first cutting force models for flat blades. His model comprises two main terms: (i) a frictional component and (ii) a second component, which accounts for cohesion and surcharge effects. Gill and Berg [95] also improved Osman's model to account for inertia effects. None of these experimental models considered the effects of the soil-tool interface on the cutting force. Therefore, Swick and Perumpral [85] later suggested a cutting model, which accounts for adhesion effects, as well as surcharge, cohesion and inertia effects.

Goryachkin [96] also proposed equation (2.4) for the cutting force of a plow. m, v, h are the plow mass, plow velocity and the thickness of the cut soil section respectively. The first term of equation (2.4) accounts for 41% of the cutting force, the

second accounts for 56% and the third makes up the remaining 3%. Alekseeva [93] tested Goryachkin's formula on some earthmoving equipment and noted that it yields unacceptable results. Alekseeva attributed these discrepancies to the differences in blade geometry and the type of formation. For excavator buckets, one of the seminal works was presented by Zelenin et al. [90]. Based on the theory of elasticity, Zelenin proposed the following analytical expressions in equation (2.5) for the tangential cutting resistance forces, T_r. C_y, β_0, z, c_b are respectively the number of blows of the dynamic penetrometer, bucket angle co-efficient, cutting depth and the co-efficient accounting for blade effects [93].

$$T = \text{w}\,(\gamma g d^2 N_\gamma + cdN_c + C_a dN_{ca} + qdN_q + \gamma v^2 dN_a) \tag{2.2}$$

$$T_h = T \sin(\beta + \delta) \tag{2.3}$$

$$T = m\delta + kwh + 0.1kwhv^2 \tag{2.4}$$

$$T_r = \begin{cases} C_y z^{1.35}(1 + 2.6l)\,(1 + 0.0075\beta)(1 + 0.03h)\beta_0\mu \;\; \forall \text{ buckets without teeth} \\ C_y z^{1.35}(1 + 0.1h)\left(1 - \frac{90-\beta}{180}\right)\beta_0 \;\; \forall \text{ individual teeth} \\ C_y z^{1.35}(1 + 2.6l)(1 + 0.0075\beta)c_b \;\; \forall \text{ buckets with teeth} \end{cases} \tag{2.5}$$

Within the earthmoving industry, the study of digging forces began with Cobb et al. [97] and Cohron [87], who confirmed that the sides of an excavator bucket tend to increase its excavation force. Osman [78] later observed that the digging force depends on eight (8) parameters which include:

(i) the excavator geometry (i.e. shape and dimension)

(ii) the formation characteristics (i.e. surcharge, density, friction, cohesion)

(iii) the formation-excavator interface properties (i.e. adhesion and friction)

Dombrovskii [98] proposed one of the first expressions for the digging force. He suggested that the tangential resistance to excavation, T_r is given by equation (2.6).

$$T_r = R_c + R_f + P_n \tag{2.6}$$

R_c, R_f and P_n are the formation's cutting resistance, frictional resistance to bucket movement and the resistances to the movement of the failure prism, respectively. The tangential force, T_f, required to overcome this formation resistance was also proposed as equation (2.7). The digging resistance, $k_1$is a function of the cutting resistance, all frictional forces, as well as the bucket trajectory. The shape of the yielded material is also given by the width, w and depth, d. Alekseeva [93] proposed something similar for the formation's tangential resistance and expressed it as equation (2.8).

$$T_f = k_1 wd \tag{2.7}$$

$$T_r = P_f + R_A + P_A \tag{2.8}$$

P_f, R_A and P_A are the penetration force, friction forces and the sum of the cutting force, compression resistance and drag prism resistance respectively. For T_f, he adopted Dombrovskii's expression but introduced a new chart of k_1 values. Zelenin et al. [90] used the same concept to determine the total excavation resistance of bucket excavators (scrapers) from equation (2.9) [91]. P_f, R_p and R_f are, respectively, the penetration-cutting force, the force required to move a filled bucket and the sum of total friction and

compression resistance. Based on the earth pressure theory, Balovnev [99] also determined the total excavation force for a curved dozer blade as the sum of all formation resistance forces on individual components (sides and blade). His proposed horizontal excavation force, H, is given by equation (2.10).

$$T_r = P_f + R_f + R_p \tag{2.9}$$

$$H = P_1 + P_2 + P_3 + P_4 \tag{2.10}$$

P_1 is the surface friction and cutting resistance; P_2 is the extra cutting resistance caused by a blunt blade edge; P_3 is the cutting resistance from the bucket sides; P_4 is the frictional resistance from the bucket sides. Through experimental observations, Zelenin et al. [90] had earlier suggested that the frictional forces on the sides of a bucket typically range from 2% to 3% and up to 6% of the total cutting force and can therefore be ignored [92]. However, a numerical comparison with the formulation of Balovnev [99] showed that frictional forces represented 50% of the total cutting forces in Balovnev's model but only 6% in Zelenin's model. More recently, Bernold [23] performed excavation experiments and concluded that friction accounts for nearly half of the formation resistance, which is consistent with Balovnev's model [91].

Hemami et al. [92] studied the interaction between a shovel dipper and soil formations. They further broke down the total excavation force into six components (Figure 2.12) namely: (i) the payload force, f_1; (ii) the soils resistance to compacting by the base of the bucket in touch with the soil, f_2; (iii) the frictional forces due to material sliding inside the bucket, f_3; (iv) the cutting resistance at the front and cutting edges of the dipper, f_4; (v) the payload's inertia force, f_5; and (vi) the dipper's deadweight, f_6.

Their total excavation force for the dipper is given by equation (2.11). Hemami et al. [92] compared their force components to equation (2.12) from Alekseeva [93], equation (2.13) from Zelenin et al. [90] and equation (2.14) from Balovnev [99].

$$P = f_1 + f_2 + f_3 + f_4 + f_5 + f_6 \tag{2.11}$$

$$P_f = f_4\,, \quad R_A = f_3\,, \quad P_A = f_1 + f_2 + f_5 + f_6 \tag{2.12}$$

$$P_f = f_4\,, \quad R_f = f_1 + f_2 + f_3\,, \quad R_p = f_5 + f_6 \tag{2.13}$$

$$P_1 + P_2 + P_3 = f_4\,, \quad P_4 = f_3 \tag{2.14}$$

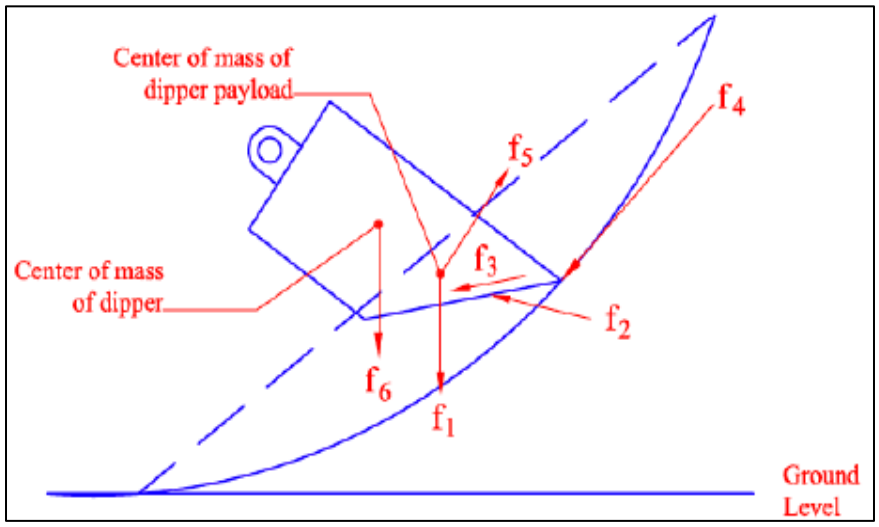

Figure 2.12. Resistance forces in dipper excavation [92]

Takahashi et al. [100] also presented a model, which is quite similar to the one by Hemami et al. [92] except that f_1 and f_6 are combined into a single force component. Also, the bucket in Takahashi's model follows a pre-defined trajectory at zero acceleration to satisfy the assumption of zero inertial force. Moreover, it is assumed that

compression of the formation by the bottom of the bucket is negligible. When compared with experimental data, the model of Takahashi et al. (1998) showed good agreement.

All the force models discussed so far are based on either empirical or analytical methods. Moreover, these models resulted mainly from studies on flat blades, scrapers, excavator buckets and shovel dippers. To date, no analytical or empirical force models have been proposed specifically for dragline bucket operations. Over the years, the practice has been to adopt available models for use in other earth-moving scenarios, which they were not originally intended for. However, these analytical methods cannot satisfactorily address the effects of complex and three-dimensional equipment geometry changes on the results. Similarly, the empirical models for wide blades, scrapers and shovel dippers cannot be extended to explain dragline excavation because they involve different geometries and / or digging trajectories.

2.5. ADVANCES IN DRAGLINE EXCAVATION TECHNOLOGY

This section summarizes some recent seminal advances in dragline bucket design.

2.5.1. Bucket Design Optimization. A typical dragline bucket comprises bucket teeth for engaging the ground, bucket lips for cutting the material and a rear basket for holding the excavated material. The GET component consists of teeth and lip shrouds. Traditionally, dragline buckets were designed as a unit, such that the GET were not detachable. One shortcoming of this traditional design was that whenever there was damage to one component (usually the teeth) from extensive use, the whole bucket needs to be replaced.

Gooch [101] revolutionized the dragline bucket industry by proposing a new bucket design with an easily detachable front-end (teeth and arch). The damaged front-

end could be quickly detached and replacement parts installed relatively cheaply. The main limitation of Gooch's work was that even one damaged tooth requires replacement of the whole front-end component. To address this problem, Bierwith [102] developed a new bucket design, which comes fitted with a connection system for attaching replaceable bucket teeth. Therefore, the bucket tooth, once worn out, could be removed and replaced with a new ground engaging tooth at a reasonable cost. Bierwith's solution introduced a new problem as the detachable teeth become loose with extensive use and fall off. More recently, Smith and Harder [103], Harder and Smith [104], Chenoweth et al. [105], Rimmey [106], Ballinger [107], Campomanes and Lonn [108], Campomanes and Jeske [109], and Jeske [110] have all designed retainer systems to keep the detachable teeth in place.

For a given dragline, its boom is limited by the maximum suspended load that can be carried. This is given by the sum of the bucket deadweight (i.e. mass of empty bucket and rigging) and the mass of the suspended material (i.e. payload). Leslie et al. [111] and Lumley [112] proposed different lightweight bucket designs with geometries that also allow for increased payload. For soft and low-density earth materials, the design by Leslie et al. (2004) showed improvements of 10% increase in payload, 20% reduction in bucket fill time and 30% reduction in drag energy when compared to conventional buckets of similar struck capacity.

Leslie et al. [113] and Leslie et al. [114] later designed multiple buckets with similar performances for hard and high-density earth materials. From experimental scale testing of twelve (12) different bucket geometries, Leslie et al. [115] also found that bucket performance increases considerably for buckets with a 15° side wall inclination

and a bucket front-end with width-to-height ratio of 3.5:1. The authors, however, conceded that further bucket trials with a wider range of geometric variations may result in a more accurate optimization of the bucket dimensions.

2.5.2. Offline Simulation Modeling. One of the earliest dragline simulation models is 3d-Dig 2000 (Figure 2.13), which was developed under ACARP. It is a three-dimensional modeling platform, which provides a graphical interface for integrating topographic simulations with excavation, transport and dump sequence simulations for dragline operation.

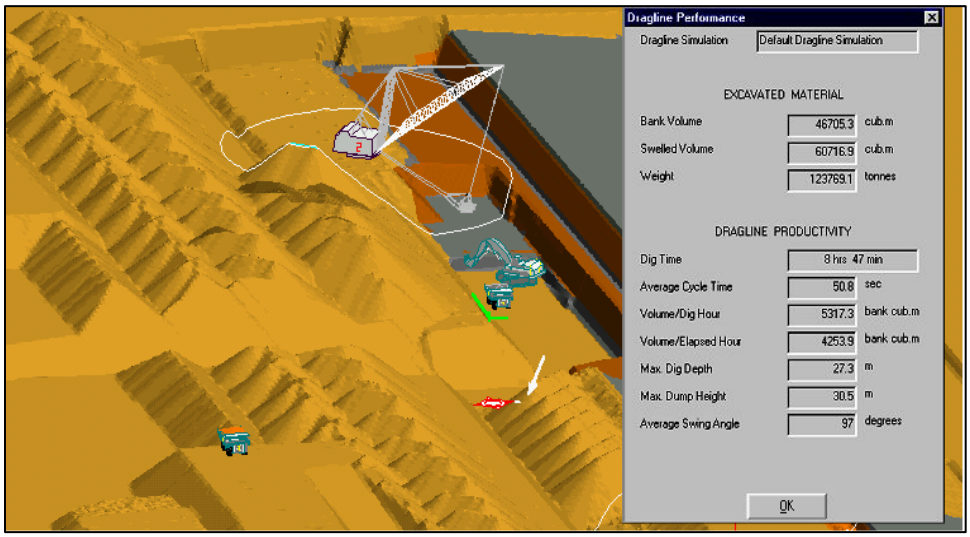

Figure 2.13. 3D-Dig 2000 interface

3d-Dig 2000 compares a Digital Terrain Model (DTM) of the existing pit topography with a user-provided final design topography. To achieve the final design, the model simulates material removal in incremental steps to a user-defined dump area. At each step, a small parcel of material is excavated and dumped numerically. The original

topography is modified accordingly to reflect the excavation and the process is repeated continuously until the desired pit design is achieved. 3d-Dig offers flexibility for simulating operations under variable machine and environmental conditions. In addition to using existing and final DTM maps, it also uses site-specific input data to achieve results. Such input data include spoil material characteristics (swell factor, specific gravity and repose angle), machine characteristics (geometry) and machine-operator performance characteristics (productivity rates, excavated material volume). The model is also able to determine dragline productivity, by considering swelling, excavated material volumes, swing angles, dig times, dig depths, dump heights and average operation cycle times [116]. A more recent version of the software, 3d-DigPlus, offers more flexibility and includes simulation modules for other excavation operations, such as bulldozer and truck and shovel operations.

As a high-level planning tool, 3d-Dig offers a lot of advantages. However, it is not capable as a tool for improving dragline productivity through bucket design optimization. Cleary [29] presented the first dragline bucket simulation model, targeted at comparing the filling behavior and productivity of two competing bucket designs. Cleary's model was based on the Distinct Element Method [117] and it identified six main forces that influence the motion of a bucket (Figure 2.14): the tension in the drag lines, T_1, rigging forces, T_2, collisional forces at lips and teeth, F_c, the force applied to the back of the bucket by the spoil, S_r, the bucket weight, W_b, and the weight of the spoil material in the bucket, W_s.

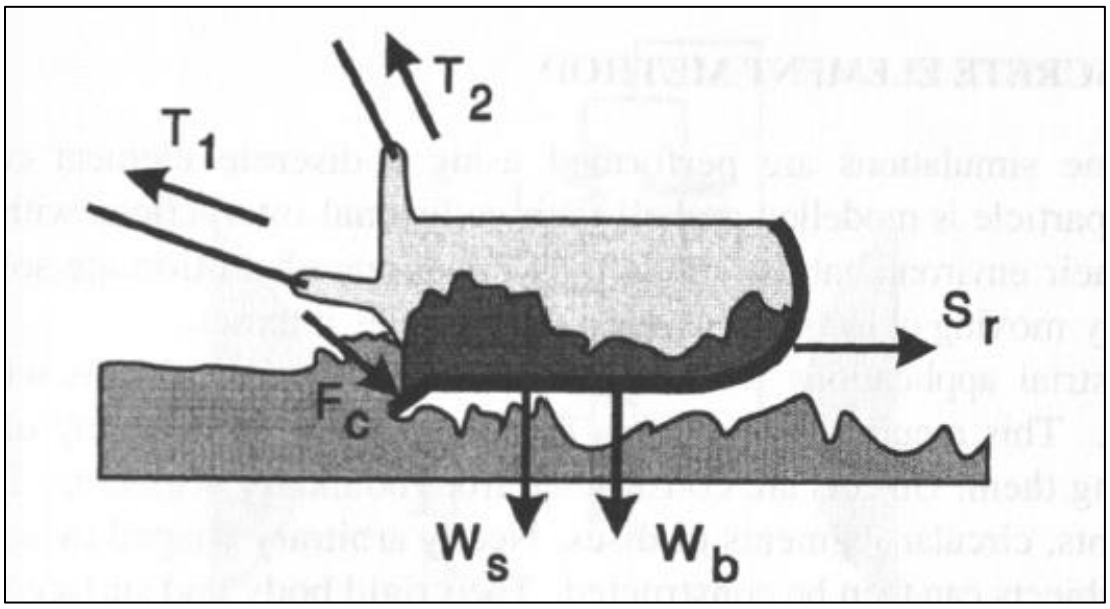

Figure 2.14. Forces acting on a dragline bucket [29]

Cleary [29] demonstrated that the distinct element method can be very useful for evaluating different bucket designs, estimating bucket wear distribution and for evaluating the effects of material characteristics variations. However, the model was only two-dimensional and failed to consider width effects. Coetzee et al. [30] proposed the first three-dimensional dragline simulation model using the Distinct Element approach. In this study, the authors presented a new iterative procedure for calibrating the parameters of the discrete model. However, the iterative process required conducting numerical laboratory experiments repeatedly and varying the value of one parameter in each experiment until the numerical results match the real values for all parameters. The main challenge with this approach is that it is a very tedious process and has to be repeated even for very slight changes in material property. Also, the dragline model from their study over-predicts drag forces by almost five folds.

2.6. RATIONALE FOR PHD RESEARCH

This research is a pioneering effort toward improving dragline technology for efficient and economic excavation. Computer vision research in the mining industry have mainly focused on autonomous dump trucks. To date, the only vision-based model for draglines was presented by Hainsworth [7] who used image segmentation for bucket pose estimation. Hainsworth used a background subtraction technique which fails when the bucket undergoes full loading. In addition, the model only deals with one dragline vision problem (bucket pose estimation) and does not address any others. This study is the first attempt at building a vision-based model for terrain and obstacle recognition during the dragline digging phase, as well as for collision prevention. This research also introduces convolutional neural networks as a better alternative for bucket pose estimation. In short, this study seeks to contribute to vision-based dragline studies by proposing a multi-purpose vision model which is faster, scalable, more accurate and more suitable for real-time application in active construction environments.

In addition, this study contributes to geomaterial calibration methods for numerical modeling in civil engineering and related industries. It introduces a machine learning alternative to the current trial-and-error approach for calibrating distinct element parameters of overburden materials. A better material calibration process results in a more realistic formation model in simulations and consequently, more realistic excavation simulation results.

The mechanics of formation failure differ based on tool geometry, orientation and trajectory. While failure of earth material ahead of tillage and excavation equipment has been the subject of much interest over the years, dragline studies in this area have

received relatively little attention. This study represents the first attempt at investigating the nature of excavator-induced formation failures using the 3-D distinct element modeling (DEM) approach. It also introduces DEM as a cost-effective, time efficient and all-around better alternative to the current scale model technology for initial phase bucket design testing and optimization.

2.7. SUMMARY

In this section, an attempt was made to review the most relevant literature in geomaterial calibration, numerical modeling, dragline automation, machine vision and excavation research. This section captured both early and recent automation studies, related to dragline excavations. Orenstein and Koppel developed the first semi-autonomous excavator. The autonomous component was an on-line monitor for tracking the excavator's condition. Similarly, dragline automation studies started with the initial goal of improving monitoring. McCoy and Crowgey [6] developed the first automated tightline control system for dragline buckets. With time, on-line monitoring became the primary means of obtaining and analyzing dragline performance data. Lumley and Haneman [42] spotted a high variability in dragline performance by analyzing fourteen (14) monitors and found that bucket design and rigging were the biggest contributing factors.

Beyond automated monitoring, dragline studies have also looked into optimizing the operator's actions. It was Lumley [18] who carried out studies to confirm what had been suspected for a very long time: many dragline operators operate at extreme suboptimal levels. After studying the performance of a top 10% global dragline operator

team over six months, he discovered that the average difference between the most productive operators and least productive operators is about 35% in productivity and 140% in equipment damage impact. Lumley's findings were supported by Jessett [28] who also found that inconsistencies in operator sequences and techniques can lead to productivity rate variations of over 10%.

Nonetheless, the shift towards automating the operator's tasks has been rather incremental. Corke et al. [9] presented the first semi-automated mechanical control system for an electric walking dragline. Corke et al. [46], Roberts et al. [47] and Winstanley et al. [48] added improvements which led to the full automation of the dragline's dump phase. Winstanley et al. [19], Winstanley et al. [20], Corke et al. [26], Corke et al. [46] and Winstanley et al. (2003) developed a dragline swing automation (DSA) system to reduce dragline cycle time, consequently reducing excavation costs. Roberts et al. [49] improved the DSA system with the three dimensional imaging technology, Digital Terrain Mapping (DTM), as a means of providing situational awareness to swing automation tasks. However, the improved model still required human interference to avoid swing collisions. Dunbabin et al. [45] developed one of the first tele-operated dragline models, which however, required an operator to input the dig and dump location coordinates.

From the literature, it is obvious that most of the hiccups in dragline automation research concern decision-making, based on what is happening at any given instance. The previous models lack both the vision to see what is happening and the intelligence to learn, understand and deal with new situations based on what is seen. Several studies have focused on vision-based research in excavation. To date, the only vision-based

model for draglines was presented by Hainsworth [7] who used image segmentation to solve the problem of bucket pose estimation. One of the limitations of this model was that the green paint, which was used along the bucket edges to help with background subtraction, was sometimes covered by the excavated material and this causes the segmentation technique to fail. Also, image segmentation models do not perform well in active environments, where several different objects need to be recognized within the same image sequence. This research seeks to contribute to vision-based dragline studies by proposing a deep learning model which is faster, scalable, more accurate and more suitable for real-time application in active construction environments.

In this section, the failure mechanics in earthmoving has also been reviewed. The first attempt at studying formation strength and failure is credited to Coulomb [58] who proposed a shear failure model for soil based on the internal friction angle, the cohesive bonds between its particles and the normal stress, which acts on its failure surface. Mohr [60] improved this model by introducing a linear envelope that could predict the failure of a material on its weak surface plane. However, Karman (1912) and Boker (1915) found that the improved theory only delivers good accuracy for mid-range compressive stresses, and not for very high or very low stresses.

Nonetheless, the Mohr-Coulomb failure theory is still widely accepted to be true for all isotropic, homogenous materials. Rankine [59] proposed the first tensile failure theory for earth materials. However, the theory assumes that the material is both frictionless and cohesionless. Ohde [64] also developed a logarithmic spiral method that yields a curved envelope. A few researchers [65-68] adapted Ohde's model for calculating formation resistance to excavation. Ohde proposed that as soil experiences

failure under the action of a moving, excavating blade, three zones are created within the soil profile: (i) rankine zone, (ii) shear zone, and (iii) logarithmic spiral curve zone.

Up to date, only Rowlands [88] has proposed a failure theory for materials under the action of a dragline bucket. From his experiments, Rowlands observed that the following zones are formed in the material during bucket digging: (i) Initial laminar layer, (ii) Dead load, (iii) Active flow zone, (iv) Active Dig Zone, and (v) Virgin Material. In line with Rowlands experimental work, this research will use three-dimensional bucket excavation simulations to further investigate the material failure process in dragline excavations.

This section also reviewed the most recent advances in dragline technology evolution. Recently, a lot of work in dragline excavation have focused on bucket design improvements. Gooch [101] proposed the first bucket design with an easily detachable front-end (teeth and arch). Bierwith [102] improved this model with a connection system that allowed individual worn-out bucket teeth to be replaced. Later, Smith and Harder [103], Harder and Smith [104], Chenoweth et al. [105], Rimmey [106], Ballinger [107], Campomanes and Lonn [108], Campomanes and Jeske [109], and Jeske [110] all designed different retainer systems to help keep the detachable teeth in place. Leslie et al. [111] and Lumley [112] proposed different lightweight bucket designs with geometries that also allow for increased payload, reduced fill time and reduced drag energy.

However, their models were only suitable for soft and low-density earth materials. Leslie et al. [113] and Leslie et al. [114] later designed multiple buckets with similar performances for hard and high-density earth materials. From experimental scale testing of twelve (12) different bucket geometries, Leslie et al. [115] also found that bucket

performance increases considerably for buckets with a 15° side wall inclination and a bucket front-end with width-to-height ratio of 3.5:1. The authors, however, conceded that further bucket trials with a wider range of geometric variations may result in a more accurate optimization of the bucket dimensions.

All these bucket geometry studies used physical scale models which have huge time, effort and cost constraints. This research will seek to remove these constraints, in addition to opportunity costs, by presenting a three-dimensional numerical model that allows for a wider range of geometries to be tested and compared.

3. DRAGLINE EXCAVATION MODELING

This section discusses the methods for formation parameter calibration and dragline excavation simulation. Both models are based on the Distinct Element Method and are simulated in the Particle Flow Code (PFC) 5.0 environment.

3.1. THE DISTINCT ELEMENT METHOD IN PFC 5.0

The Distinct Element Method (DEM) was developed by Cundall for simulating rock [118] and soil [119] behavior. The numerical simulation is achieved through several series of displacement and contact force calculations. These particle displacements disturb surrounding particles and govern the movement of other particles as this disturbance is propagated through the entire medium with time. The DEM is based on the concept that a single time step is chosen to be very small such that particle disturbances are not propagated beyond immediate neighbors. Therefore, at any given time step, the resultant forces on any particle can be computed from interactions with only the particles that it is in contact with. At each time step, it is assumed that both the accelerations and velocities of all particles are constant. Particle displacements are governed by contact models and are determined through a series of calculations tracing the movements of individual particles at equilibrium. The equations of motion are solved numerically using the Velocity Verlet algorithm to determine the movement of each particle when forces are applied through contact. For a particle, x, which experiences a resultant force, $F_{(x)}$, and moment, $M_{(x)}$ after contact, its linear and angular accelerations ($\ddot{r}$ and $\ddot{\theta}$) are determined via Newton's second law using equations (3.1) and (3.2).

$$m_{(x)}\ddot{r}_i = \sum F_{(x)_i} \tag{3.1}$$

$$I_{(x)}\ddot{\theta}_{(x)} = \sum M_{(x)} \tag{3.2}$$

$$(\dot{r}_i)_{t+\frac{\delta t}{2}} = (\dot{r}_i)_{t-\frac{\delta t}{2}} + \left(\frac{\sum\left[F_{(x)_i} + D_{(x)_i}\right]}{m_{(x)}}\right)_t \delta t \tag{3.3}$$

$$(\dot{\theta}_{(x)})_{t+\frac{\delta t}{2}} = (\dot{\theta}_{(x)})_{t-\frac{\delta t}{2}} + \left(\frac{\sum M_{(x)}}{I_{(x)}}\right)_t \delta t \tag{3.4}$$

$$(r_i)_{t+\delta t} = (r_i)_t + (\dot{r}_i)_{t+\frac{\delta t}{2}}\delta t \tag{3.5}$$

$$(\theta_{(x)})_{t+\delta t} = (\theta_{(x)})_t + (\dot{\theta}_{(x)})_{t+\frac{\delta t}{2}}\delta t \tag{3.6}$$

$m_{(x)}$ and $I_{(x)}$ are the mass and moment of inertia of particle, x, respectively. If the particle accelerations, $\ddot{r}$ and $\ddot{\theta}$, are assumed to be constant over any given time step, δt, the linear and angular velocities ($\dot{r}$ and $\dot{\theta}$) can be derived using the Velocity Verlet algorithm [120] as shown in equations (3.3) and (3.4). $\sum D_{(x)}$ represents the sum of all contact damping forces and $\sum M_{(x)}$ now also includes moments from the contact damping forces. Similarly, the particle linear and angular displacements (r and θ) may be derived through numerical integration as equations (3.5) and (3.6).

The Newton equations (3.1 and 3.2) and Finite-Difference equations (3.3, 3.4, 3.5 and 3.6) above are then repeated for each particle in the collection. Based on the material constitutive model, the force-displacement law is also used to update the forces arising from the relative motion at each contact [121]. This allows the dynamic material behavior

of the entire system to be simulated with moderate memory requirements [32]. The Particle Flow Code (PFC) 5.0 by Itasca is a DEM framework for simulating the mechanical behavior of discrete particles (Figure 3.1).

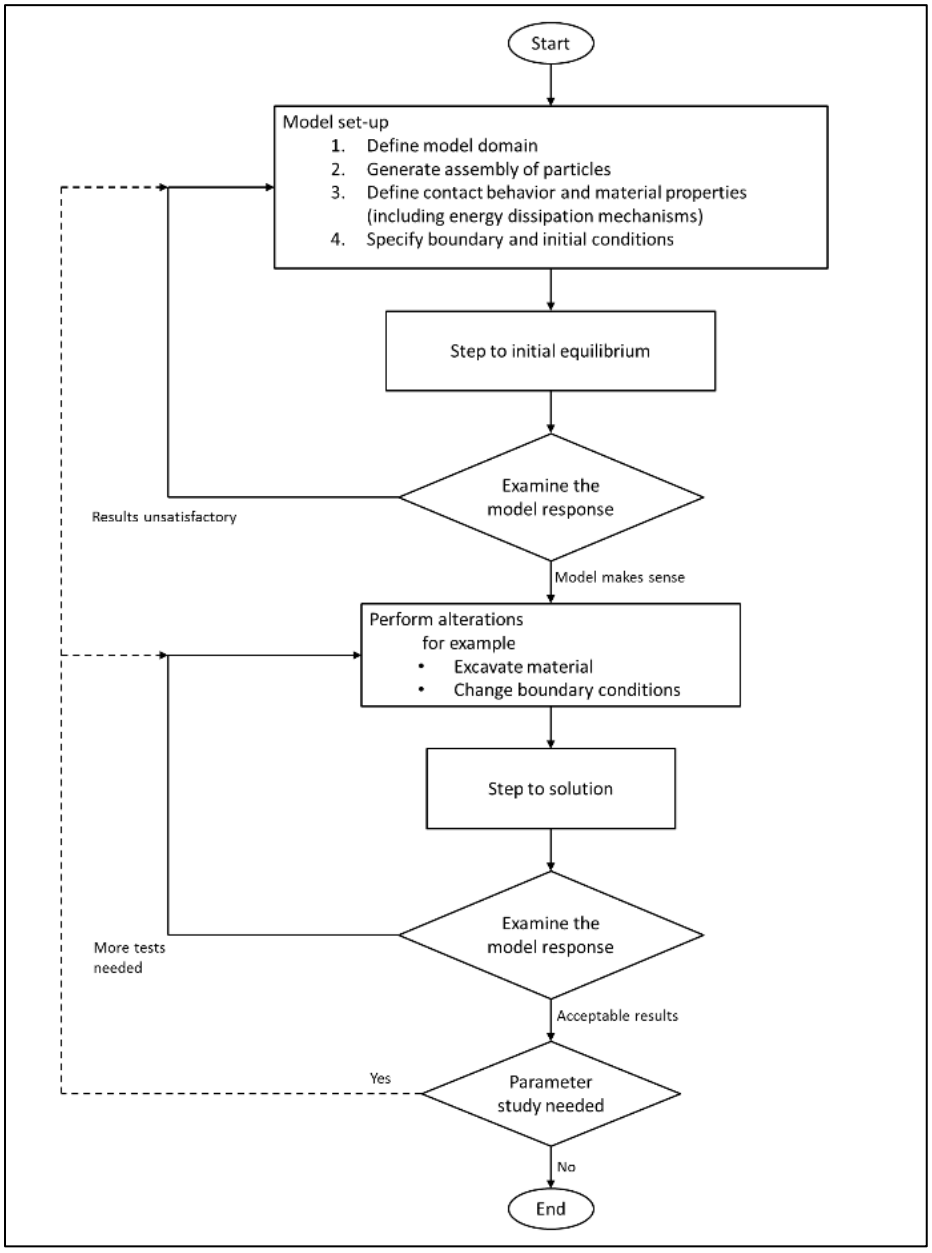

Figure 3.1. General DEM modeling procedure in PFC 5.0

It relies largely on contact mechanics principles for particle movement and interactions. Particles interact at point contacts by means of internal forces and moments with equilibrium established whenever the internal forces balance. Figure 3.1 illustrates the general DEM modeling procedure within PFC 5.0. For every simulation, DEM makes the following assumptions [122]:

- All elements / particles in the simulation behave like rigid bodies.
- Clumps of variable shapes can be formed from a collection of particles but all particles have a base spherical shape.
- Particles overlap one another at contact points and the post-collision behavior is determined by the degree of overlap.
- Particles only interact at a point and the contact force from the interaction relates to the degree of overlap through the force-displacement law.
- A bond may exist between two particles at their contact point.

3.2. THE FORMATION CALIBRATION MODEL

Constitutive modeling of geomaterials is the mathematical description of their behavioral response to various stress loadings. The mechanical behavior of geomaterials plays a vital role in their deformation or failure during ground excavation operations. Traditionally, geomaterials have been modeled at the macro-scale and as a continuum. However, in dragline operations, the earth materials occur as fragmented blocks and distinct particles (i.e. boulders, cobbles, conglomerates, gravels and sand), which only interact at contact points. Therefore, for the purpose of characterizing these earth

materials, a discontinuum model which reflects the particle-to-particle interaction at the micro-scale is more appropriate.

Therefore, constitutive modeling of the formation will follow the Hertzian Contact Theory (Hertz, 1882) which relates contact forces between any two bodies to the stiffnesses of the bodies and to their relative displacements. Numerical simulations with DEM require the selection of constitutive model micro-parameters through a calibration process in which the behavioral response of the physical material has to be replicated in the model. With proper calibration, the linear model proposed by Cundall and Strack [32], has been known to reproduce the stress-strain behavior of granular soil and rock assemblies.

For geomaterials, calibration experiments may be uniaxial, triaxial or tensile testing among others. Most previous studies use iterative simulation processes [30, 123, 124] based on domain knowledge. However, this approach tends to be tedious and the entire process has to be repeated in order to calibrate new material properties. Other studies have proposed calibration charts [125] and curve-fitting methods [126, 127] which seek to define “line of best fit” functions on the original data distribution. To an extent, these calibration charts and simple regression models are able to take advantage of basic hidden relationships between model micro-parameters and macroscopic material behavior. However, these models were developed from few simulation tests (i.e. 10 to 100 tests) and were fitted to those simulation results. Therefore, their performance on calibrating new material properties can be hit-or-miss depending on how these material properties vary from those in the original simulation tests.

This section will describe a novel process for calibrating the linear constitutive model to not only fit the original distribution but also to possess relatively high predictive performance, which makes it very useful for calibrating new material properties. The calibration model is developed from 1,500 triaxial simulation tests and its predictive performance is compared to that of the polynomial curve-fitting technique which has been used for material calibration by previous investigators [126, 127].

3.2.1. The Constitutive Model. Dragline excavation often involves unconsolidated earth and granular material. Hence, the constitutive model for the excavation simulation geomaterial is based on the linear model by Cundall and Strack [32]. The Cundall and Strack model (Figure 3.2) is based on the behavior of an infinitesimal contact surface, which permits relative rotation of the particles in contact, such as in granular materials.

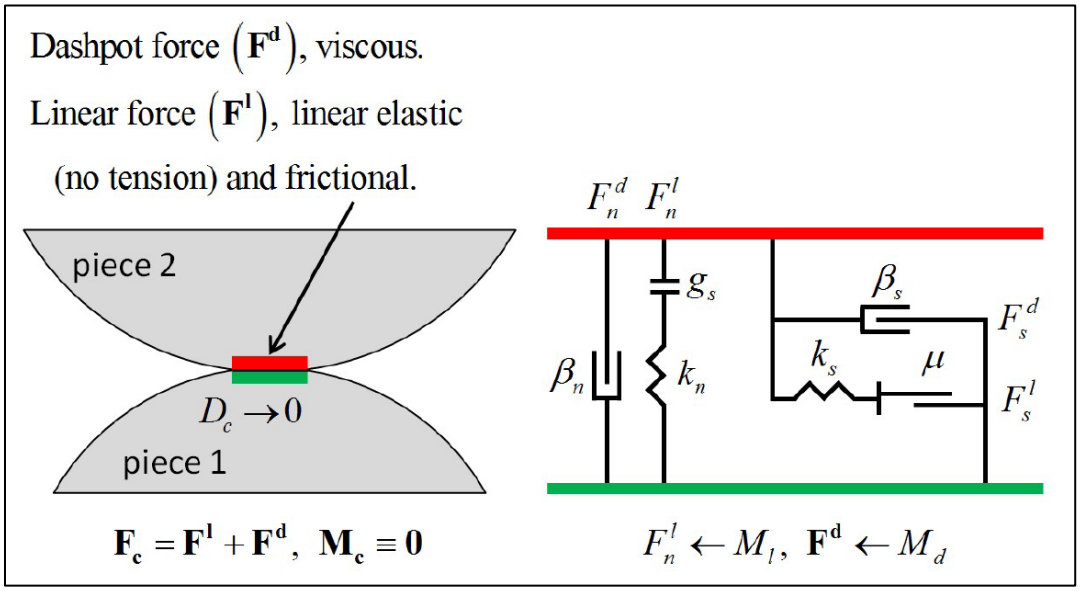

Figure 3.2. Rheological components of the linear model [122]

The contact force which governs the body-to-body interactions of the model is given by equations (3.7) and (3.8). F^l and F^d are the linear elastic and dashpot force components respectively. $\hat{n}_c$ and $\hat{t}_c$ are the unit vectors which define the contact plane. F_n^l and F_s^l are the normal and shear force components of the linear force, F^l. Similarly, F_n^d and F_s^d are the normal and shear force components of the dashpot force, F^d.

$$F_c = F^l + F^d, \quad M_c \equiv 0 \tag{3.7}$$

$$F^l = -F_n^l \hat{n}_c + F_s^l \hat{t}_c \ , \qquad F^d = -F_n^d \hat{n}_c + F_s^d \hat{t}_c \tag{3.8}$$

For visco-elastic, granular earth materials, the model's elastic component represents typical tensionless, frictional behavior while the viscous behavior is reflected in the dashpot component. The linear force component is expressed in terms of the normal and shear stiffnesses (k_n and k_s), the friction coefficient (μ), the effective modulus (E^*), and the normal-to-shear stiffness ratio (k^*). The model's dashpot force component, F^d, is expressed in terms of the normal and shear critical-damping ratios (β_n and β_s), which act in parallel to k_n and k_s, respectively (Figure 3.2). When two moving particles come into contact, the relative normal ($\Delta\delta_n$) and shear ($\Delta\delta_s$) translational displacement increments at that timestep, Δt, are adjusted using the initial $(U_n)_o$ and final (U_n) body-body overlaps as shown in equations 3.9, 3.10 and 3.11 [128].

The adjusted increment is then used according to the force-displacement law to update the linear normal force (F_n^l), linear shear force (F_s^l), damping normal force (F_n^d) and the damping shear force (F_s^d) as shown in $Equations$ (3.12), (3.13) and (3.14). $(F_n^l)_o$ and $(F_s^l)_o$ are the initial linear normal and shear forces. $\dot{\delta}_n$ and $\dot{\delta}_s$ are the

relative normal and shear translational velocities. m_c is the contact mass whereas $m^{(1)}$ and $m^{(2)}$ are the masses of the two particles. During particle-particle interactions, the strain energy from the linear springs (E_k), the total frictional slip energy dissipated (E_μ), and the total damping energy (E_β) are updated according to Equations. (3.15), (3.16), (3.17) and (3.18). $\Delta\delta_s{}^{\mu}$ and $\Delta\delta_s{}^{k}$ are the components of the relative shear displacement increment, $\Delta\delta_s$.

$$\Delta\delta_n = \alpha\Delta\delta_n \tag{3.9}$$

$$\Delta\delta_s = \alpha\Delta\delta_s \tag{3.10}$$

$$\alpha = \begin{cases} \dfrac{U_n}{U_n - (U_n)_o}, & (U_n)_o > 0 \; and \; U_n < 0 \\ 1, & otherwise \end{cases} \tag{3.11}$$

$$F^l = \begin{cases} F_n^l = \begin{cases} \begin{cases} k_n U_n, & U_n < 0 \\ 0, & U_n \geq 0 \end{cases} & \text{; (absolute)} \\ \min\left((F_n^l)_o + k_n\Delta\delta_n, 0\right), & \text{(incremental)} \end{cases} \\ F_s^l = \begin{cases} F_s^* = (F_s^l)_o + k_s\Delta\delta_s, & \|F_s^*\| \leq F_s^{\mu} \\ F_s^{\mu}\left(\dfrac{F_s^*}{\|F_s^*\|}\right), \; F_s^{\mu} = -\mu F_n^l; & \|F_s^*\| > F_s^{\mu} \end{cases} \end{cases} \tag{3.12}$$

$$F^d = \begin{cases} F_n^d = \begin{cases} F_n^* = \left(2\beta_n\sqrt{m_c k_n}\right)\dot{\delta}_n & \text{(full normal)} \\ \min(F_n^*, -F_n^l), & (no-\text{tension normal}) \end{cases} \\ F_s^d = \begin{cases} F_s^* = \left(2\beta_s\sqrt{m_c k_s}\right)\dot{\delta}_s, & \text{(full shear)} \\ 0, & (\text{slip}-\text{cut}) \end{cases} \end{cases} \tag{3.13}$$

$$m_c = \begin{cases} \dfrac{m^{(1)}}{m^{(1)} + m^{(2)}}, & ball - ball \\ m^{(1)}, & ball - facet \end{cases} \tag{3.14}$$

$$E_k = \frac{1}{2}\left(\frac{\|F_n^l\|^2}{k_n} + \frac{\|F_s^l\|^2}{k_s}\right) \tag{3.15}$$

$$E_\mu := E_\mu - \frac{1}{2}((F_s^l)_o + F_s^l).\Delta\delta_s{}^\mu \tag{3.16}$$

$$\Delta\delta_s{}^\mu = \Delta\delta_s - \Delta\delta_s{}^k = \Delta\delta_s - \left(\frac{F_s^l - (F_s^l)_o}{k_s}\right) \tag{3.17}$$

$$E_\beta := E_\beta - F^d.\left(\dot{\delta}\,\Delta t\right) \tag{3.18}$$

The Cundall and Strack model can be fully defined by specifying the following parameters: μ, k_n and k_s, β_n and β_s. However, specifying fixed values for k_n and k_s is considered a "hard-wiring" approach since the same stiffness values have to be used for materials, which may be comprised of particles of variable sizes. A material size agnostic approach and perhaps, better alternative is to rather define E^* and k^*. In the course of

simulations, the k_n and k_s values are then computed automatically for the different particle sizes in the formation using equations (3.19) and (3.20).

$$k_n = \frac{A * E^*}{L} \tag{3.19}$$

$$k_s = \frac{A * E^*}{L * k^*} \tag{3.20}$$

For any given particle-particle or particle – facet (wall) interation (Figure 3.3), the particle surface area, A and body-body distance, L are given by equations (3.21) and (3.22). The damping co-efficients, β_n and β_s, vary based on the nature of the interaction. Hence, they will not be calibrated using triaxial test simulations. Instead, a sensitivity analyses will be carried out on the entire range of possible β_n and β_s values (from 0.0 to 1.0) using bucket filling simulations. The values that best reflect actual excavation outcomes will be selected as optimum.

$$A = \pi r^2 \begin{cases} r = \min\left(R^{(1)}, R^{(2)}\right), & \text{ball} - \text{ball} \\ r = R^{(1)}, & \text{ball} - \text{facet} \end{cases} \tag{3.21}$$

$$L = \begin{cases} R^{(1)} + R^{(2)}, & \text{ball} - \text{ball} \\ R^{(1)}, & \text{ball} - \text{facet} \end{cases} \tag{3.22}$$

On the other hand, k^*, μ and E^* can each range in value from 0.0 to +∞, which makes parameter calibration by sensitivity analyses almost impossible. Therefore, over

1000 triaxial test simulation experiments were performed in FISHTank to generate enough data for the development of a predictive calibration model.

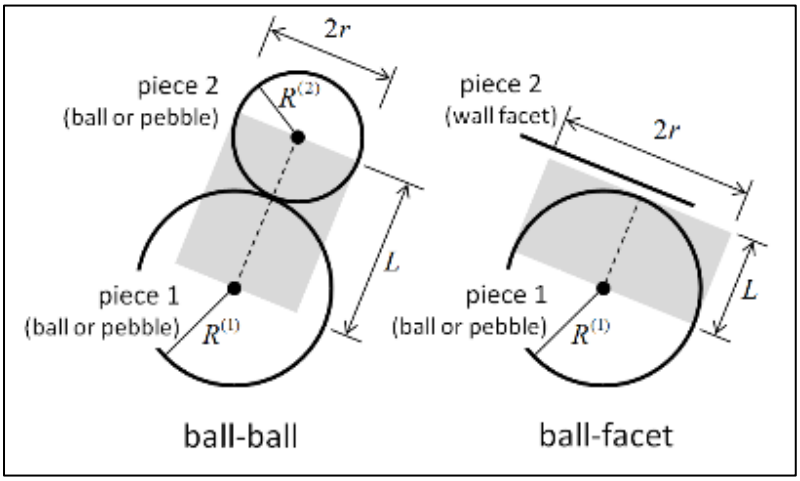

Figure 3.3. Contact interactions of the linear model [122]

3.2.2. Numerical Simulation of Triaxial Tests in PFC 5.0. Triaxial compression tests were simulated in the PFC 5.0 FISHTank virtual environment to provide experimental data for model calibration. The compression tests were performed in rectangular vessels (Figure 3.4) of standard triaxial test specimen dimensions of 38mm x 38mm x 76mm under polyaxial loading conditions. To simulate typical confining pressures in laboratory triaxial tests, pressures of 1.0 MPa were applied at the vessel boundaries in all directions for each test. All the tests were then repeated at 2.0 MPa and 3.0 MPa confining pressures. For each specimen, typical axial loading was achieved by moving the axial walls at pre-defined strain rates while keeping the confining pressure (p_c) constant [129].

For each test, the deviatoric stress (σ_d), axial stress (σ_a), and radial strain (ε_r), were recorded for increasing axial strain (ε_a) at 0.1mm strain intervals. The axial stress at failure (σ_f) was also recorded for each test. The original PFC 5.0 FISH code was modified to compute the actual geomaterial properties which correspond to the chosen model parameter values. The Young's modulus (E_{ym}), resilient modulus (E_{rm}), poisson's ratio (υ_{pr}) and co-efficient of friction (μ_f) of the material were computed from the simulation results using the concept in Figures 3.5 and 3.6 and according to $Equations$ 3.23, 3.24, 3.25 and 3.26. In order to set up experiments for a wide range of pre-defined k^*, μ and E^* values, the original PFC code was modified to automate and repeat the test simulation and material property computation processes.

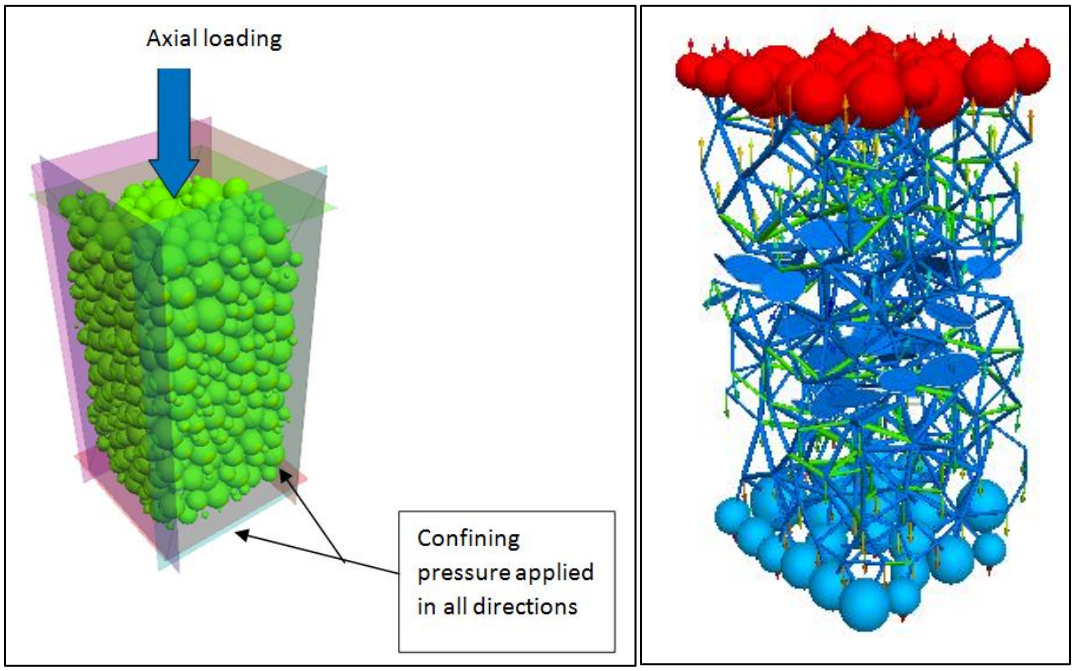

Figure 3.4. Triaxial test simulation in Itasca's FISHTank environment

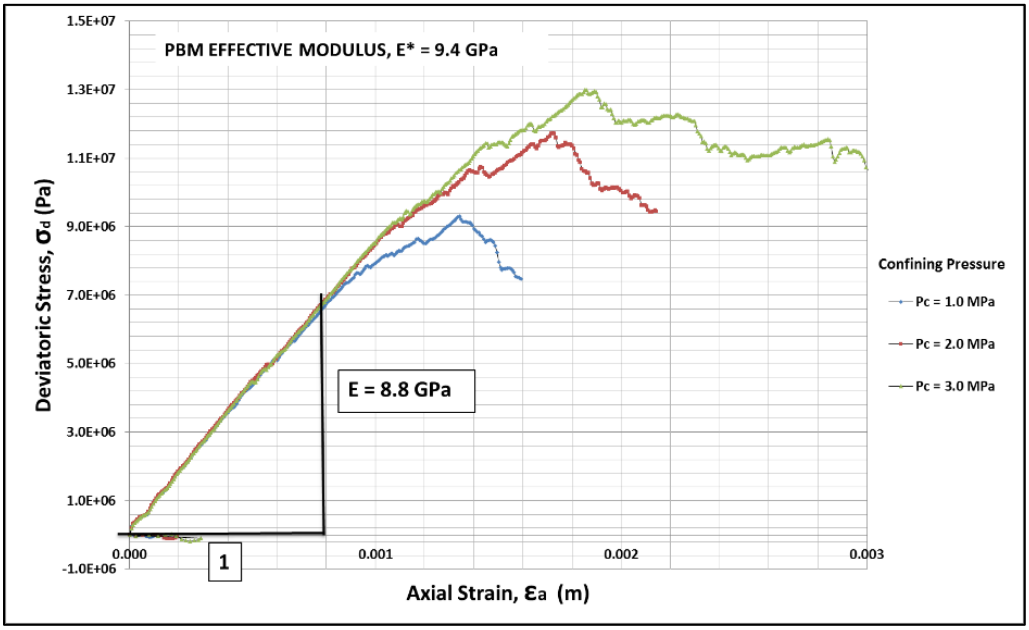

Figure 3.5. Derivation of Young's modulus from simulation results

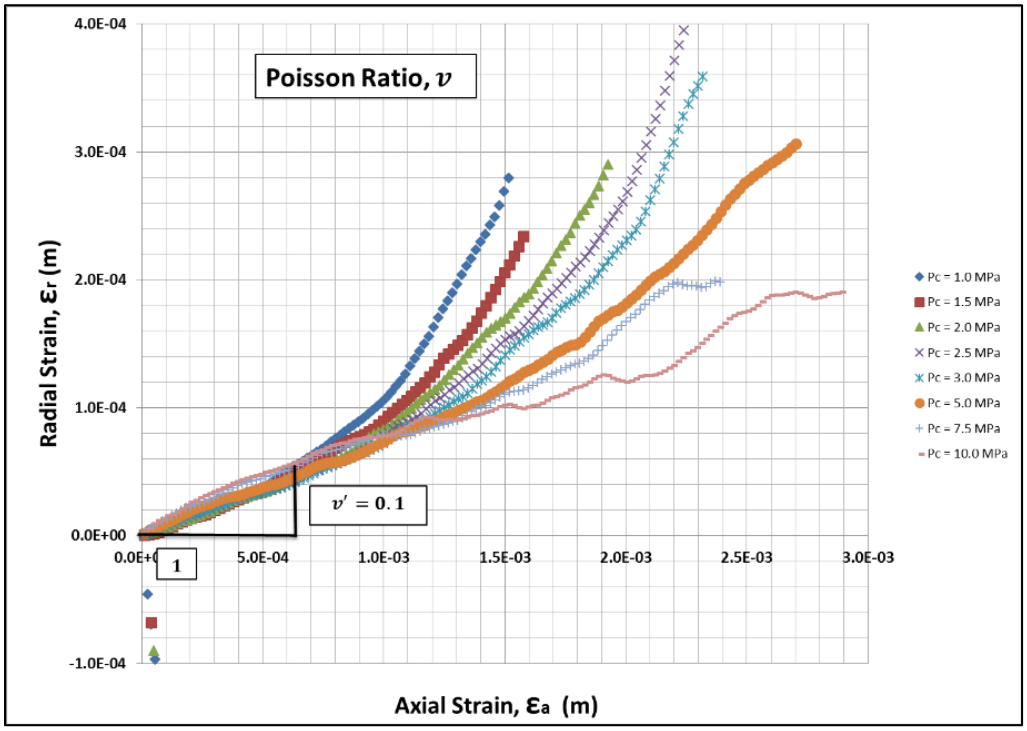

Figure 3.6. Derivation of poisson ratio from simulation results

$$E_{ym} = \left|\frac{\Delta\sigma_a}{\Delta\varepsilon_a}\right| \tag{3.23}$$

$$E_{rm} = \left|\frac{\sigma_d}{\Delta\varepsilon_a}\right| \tag{3.24}$$

$$v_{pr} = -\left(\frac{\Delta\varepsilon_r}{\Delta\varepsilon_a}\right) \tag{3.25}$$

$$\mu_f = \left(\frac{\sigma_f}{2(0.5\sigma_f + p_c)}\right) \tag{3.26}$$

3.2.3. Triaxial Simulation Test Results. A total of 1500 triaxial tests were conducted in a three-stage experiment to generate the PFC material's macroscopic property data (E_{ym}, E_{rm}, v_{pr} and μ_f), which correspond to a wide range of the model's micro-parameters (k^*, μ and E^*). The first stage of the experiment involved 500 triaxial test simulations. Since k^*, μ and E^* all range from 0 to $+\infty$, the main objective of the stage one simulations was to establish the range of model micro-parameter values, which produce typical E_{ym}, E_{rm}, v_{pr} and μ_f values for earth materials. For stage one testing, 71 E^* values were selected from the 100 MPa to 100GPa range. Similarly, 20 k^* values and 43 μ values were chosen from 1 to 5 and 0.36 to 57.3, respectively. These values were considered to be enough for the stage one experiments. The number and value of later parameters were then decided based on the generated data distribution.

For naturally-occuring geomaterials, E_{ym} and E_{rm} values typically range from 0.01 to 10.0 GPa. v_{pr} and μ_f values also range from 0.1 to 0.5 and 0.26 to 3.7, respectively. This information was used to prune the stage 1 results and to fine-tune the

selection of k^*, μ and E^* values for the subsequent stages of the experiment. Once the target k^*, μ and E^* ranges had been established, stage two and stage three experiments were conducted within the target ranges to generate more data and to obtain a good data distribution for predictive model training. Figures (3.7), (3.8), (3.9), (3.10), (3.11), (3.12) and (3.13) show the frequency distribution plots of both the inputs and outputs of the experiment after stage three.

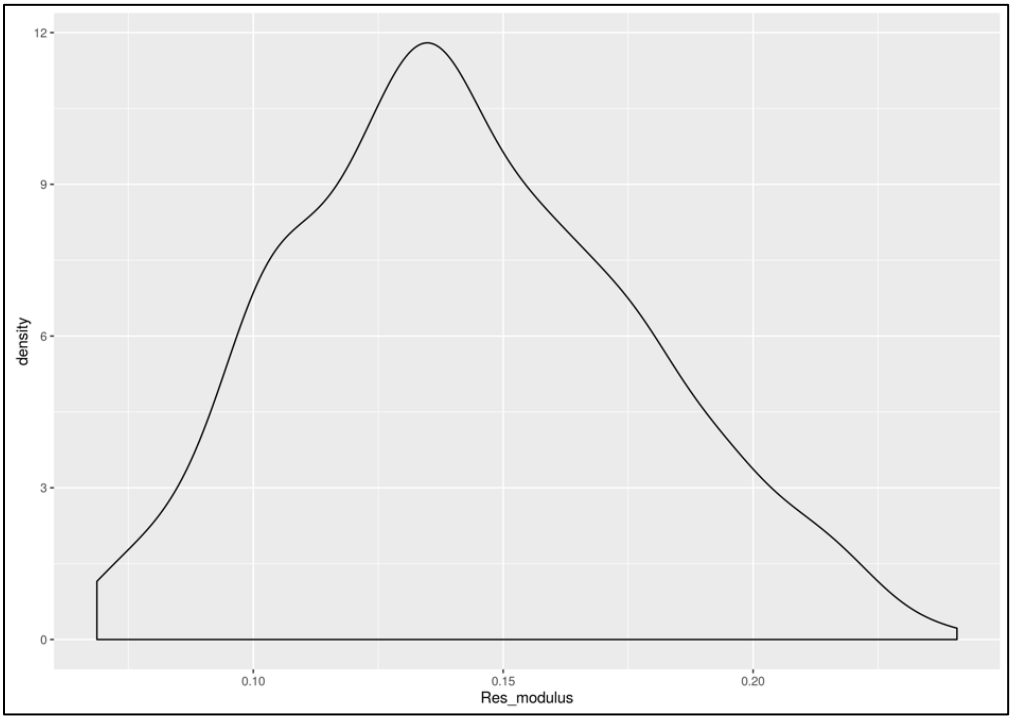

Figure 3.7. Distribution of resilient modulus after stage three tests

For elastic bodies making elliptical contacts, Mindlin [130] showed that k_s/k_n (i.e. k^*) usually ranges from 0.67 to 1.0. Hence, most of the previous granular earth material flow studies, which adopted the Cundall and Strack model [29, 30, 32, 131, 132] assumed a value of 1 for k^*. Although k^* ranged from 0.1 to 5.0 in the triaxial test

simulations, Figure 3.13 illustrates that most of the best results which produced realistic geomaterial macroscopic properties, were obtained with k^* in the 0.5 to 1.5 range and over 70% of the k^* values being exactly 1.0.

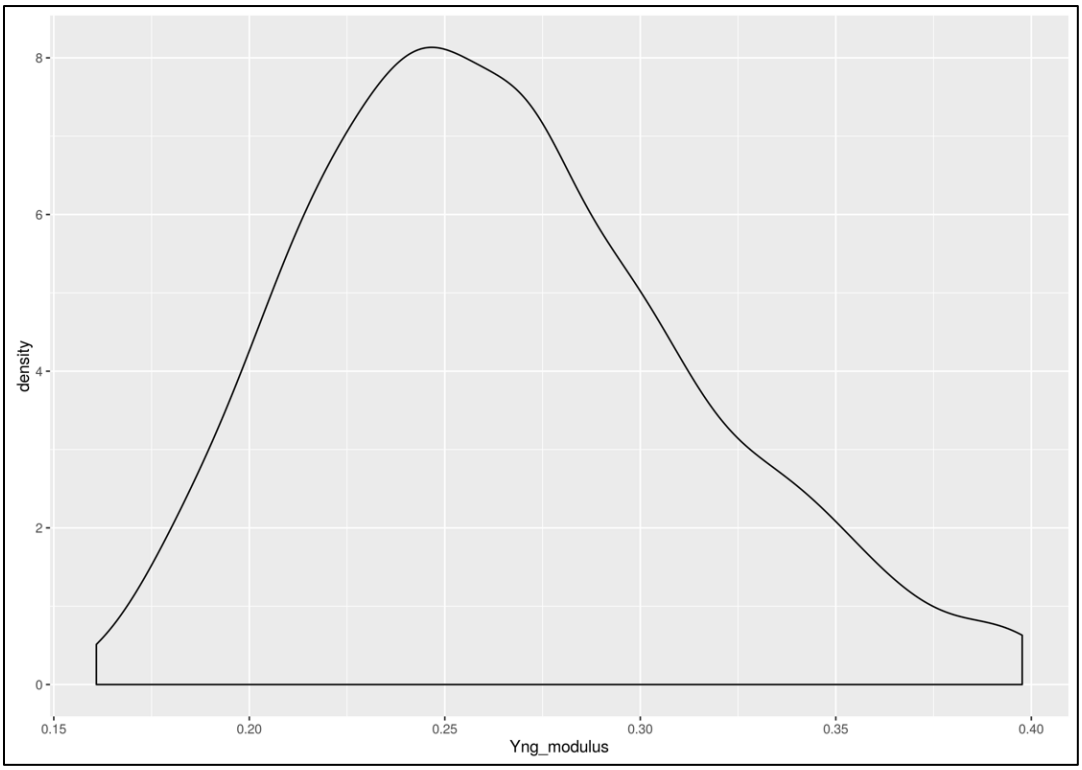

Figure 3.8. Distribution of Young modulus after stage three tests

This creates a high data imbalance, which will skew the results of any predictive calibration model, involving k^*. Also, the empirical evidence, up to date, suggests that previous studies, which assumed k^* to be 1.0 for granular earth materials achieved acceptable results [29, 30, 32, 131]. For these reasons and for the sake of model simplicity, this study will follow convention and assume k^* to be 1.0.

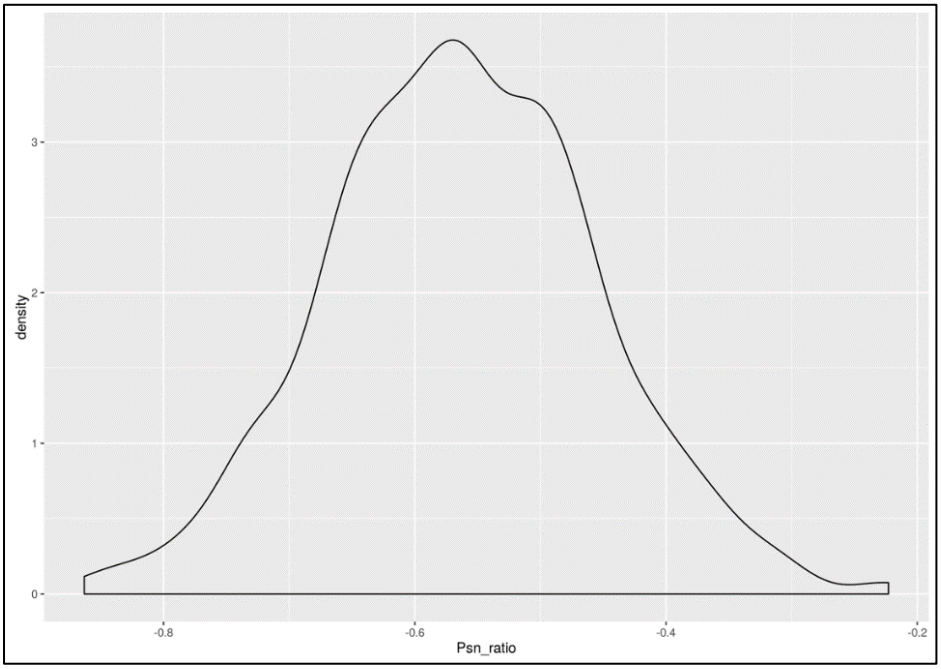

Figure 3.9. Frequency distribution of poisson ratio after stage three tests

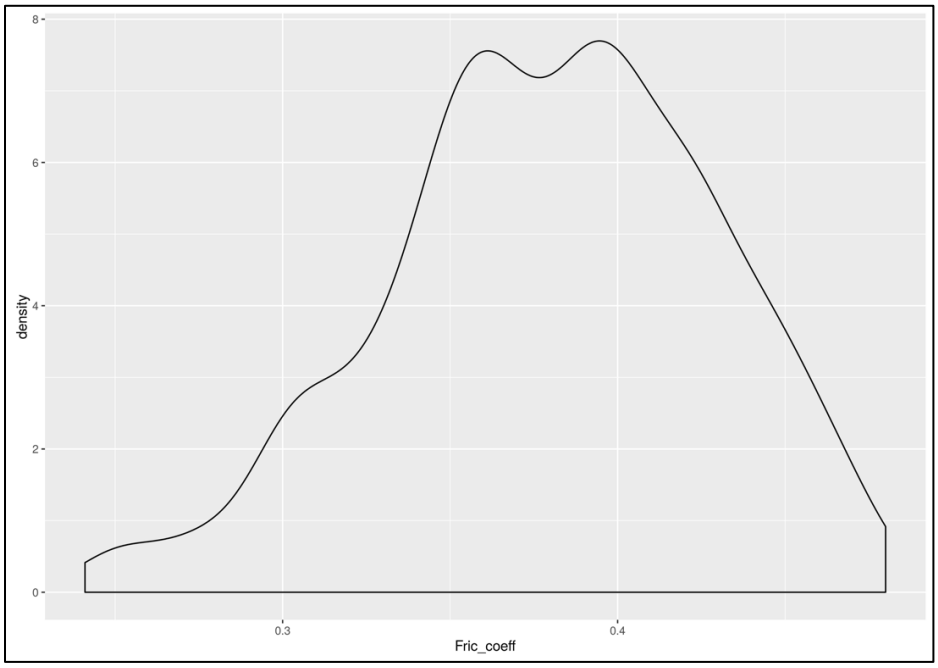

Figure 3.10. Frequency distribution of friction coefficient

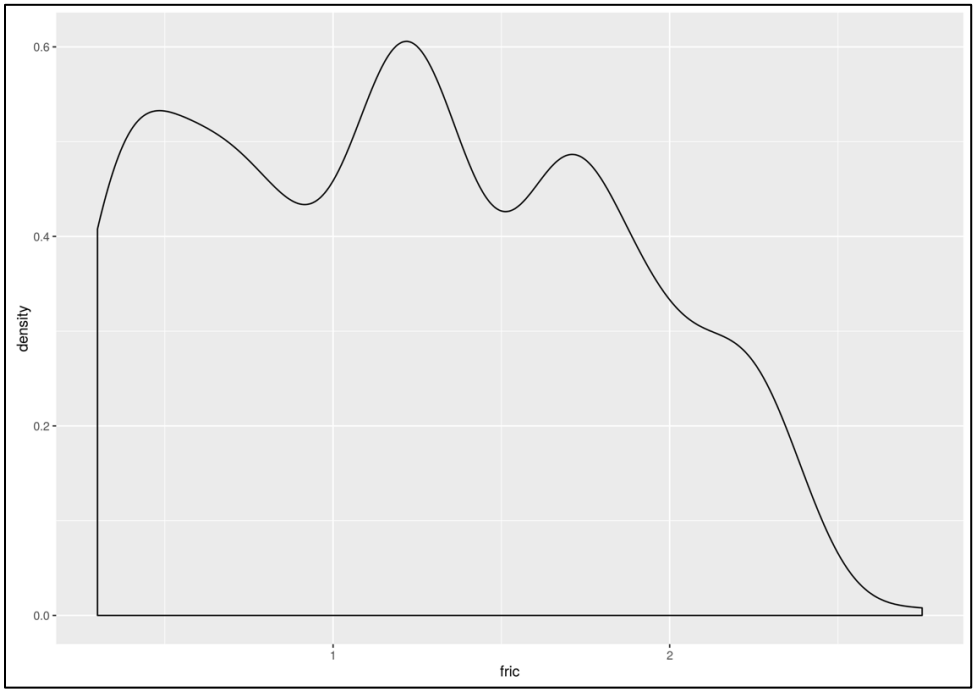

Figure 3.11. Frequency distribution of fric, μ, after stage three tests

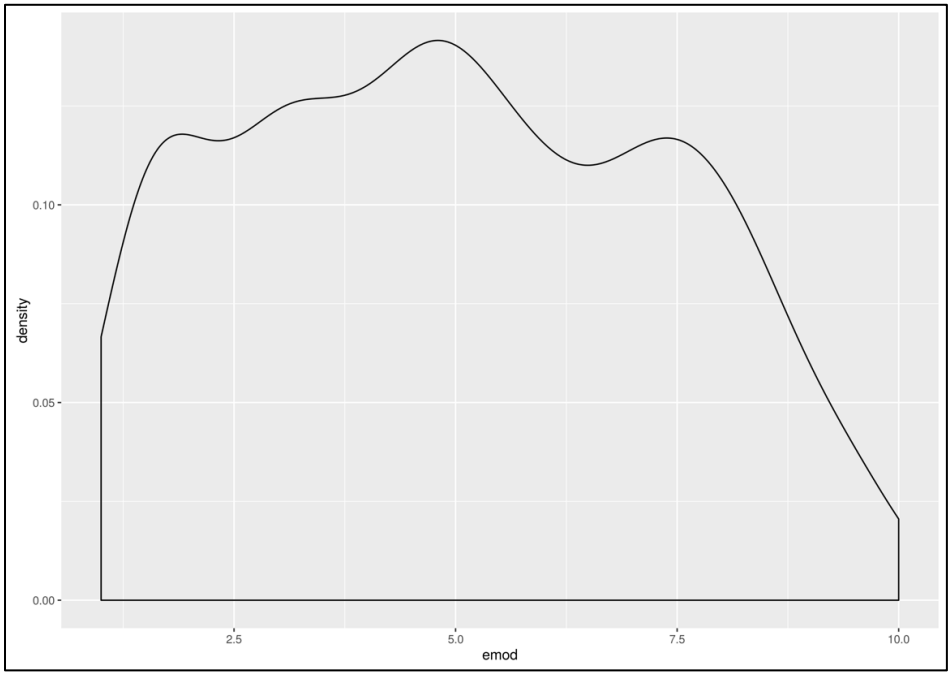

Figure 3.12. Frequency distribution of emod, E*, after stage three tests

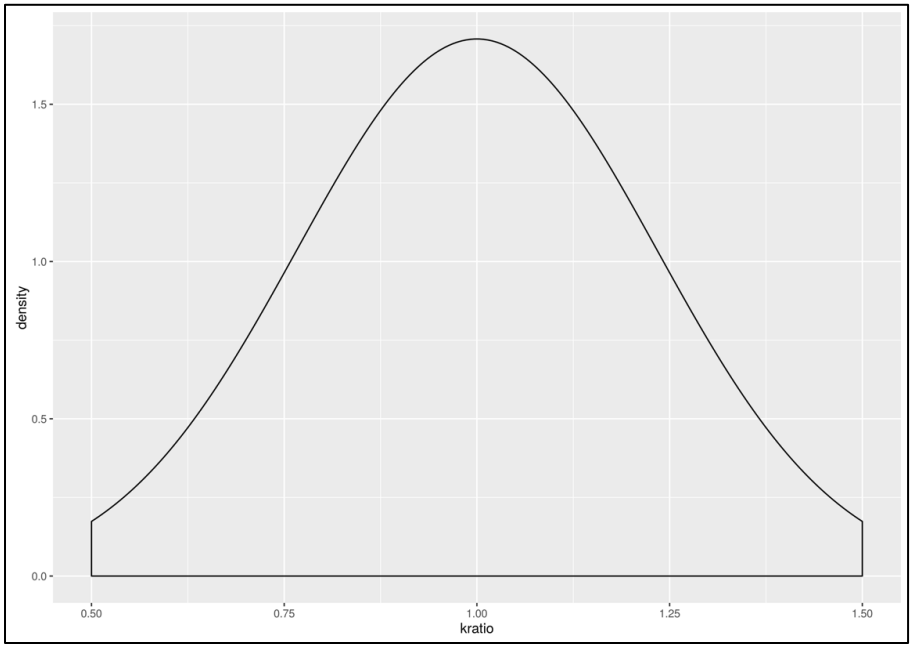

Figure 3.13. Frequency distribution of kratio, k*, after stage three tests

3.2.4. Model Training. After initial analysis of the simulation results, the data for the predictive model was reduced to 849 observations, 2 target variables (E^* and μ) and 4 predictor variables (E_{ym}, E_{rm}, υ_{pr} and μ_f). This was done to remove all data points where k^* was not 1.0 and to also remove outliers in the data, which typically reduce model performance. A new feature, shear modulus (E_{sm}), was added to the data using Equation (3.27). The following 5 higher-order feature transforms were also added to the feature set: $(E_{ym})^2$, $(E_{rm})^2$, $(E_{sm})^2$, $(\mu_f)^2$ and $(\mu_f * E_{rm} * E_{ym} * \upsilon_{pr})$. The predictive calibration model was trained on the data set using the XGBoost machine learning algorithm, proposed by Chen and Guestrin [34]. XGBoost is a tree-based ensemble method which uses additive functions to make output predictions. For a data set with n observations and m features, the prediction output, $\hat{y}_i$, is given by Equation (3.28). A regularization term is added to the optimization objective, equation (3.29), to penalize

model weights and reduce the risk of overfitting the data. Cross-validation is also run at each iteration to further reduce the risk of overfitting.

$$E_{sm} = \frac{E_{ym}}{2(1 + v_{pr})} \tag{3.27}$$

$$\hat{y}_i = \phi(x_i) = \sum_{k=1}^{K} f_k(x_i) \tag{3.28}$$

$$\mathcal{L}(\phi) = \sum_i l(\hat{y}_i, \quad y_i) + \sum_k (\gamma T + \lambda \|w\|^2) \tag{3.29}$$

T is the number of leaves, λ is the L2 norm regularization co-efficient and y_i is the actual target. The method uses a greedy search approach to iteratively determine the best split candidate to add to the tree up to a limiting maximum depth. Parameters of the XGBoost model include: the number of boosting iterations ($nrounds$), the maximum tree depth (max_$depth$), the learning rate, which determines the step size of weight shrinkage (eta), the minimum loss reduction needed to partition a leaf node ($gamma$), the number of variables that can be randomly sampled at a given iteration ($colsample\_bytree$) and the minimum weight of a child node (min_$child_weight$). For model training, it is typical in machine learning to use 80% of the data. The remaining 20% is then used for further model evaluations. Therefore, the 849 observations were split into 80% training and 20% test data. The training data was used for both training and parameter tuning via a ten-fold cross-validation. During model training, 200 different combinations of the 7 model parameters were tested in a parameter tuning process (Figure

3.14) and the combination with the best performance was selected. Table 3.1 shows the final parameter values, which resulted in the lowest RMSE score.

Table 3.1. Final parameter values for XGBoost model

Parameter	eta	max_ depth	gamma	colsample _bytree	min_child _weight	subsample	nrounds
emod	0.5325723	9	0.3462468	0.3800338	4	0.9995035	892
fric	0.1745362	9	0.1604142	0.6762885	7	0.7747859	724

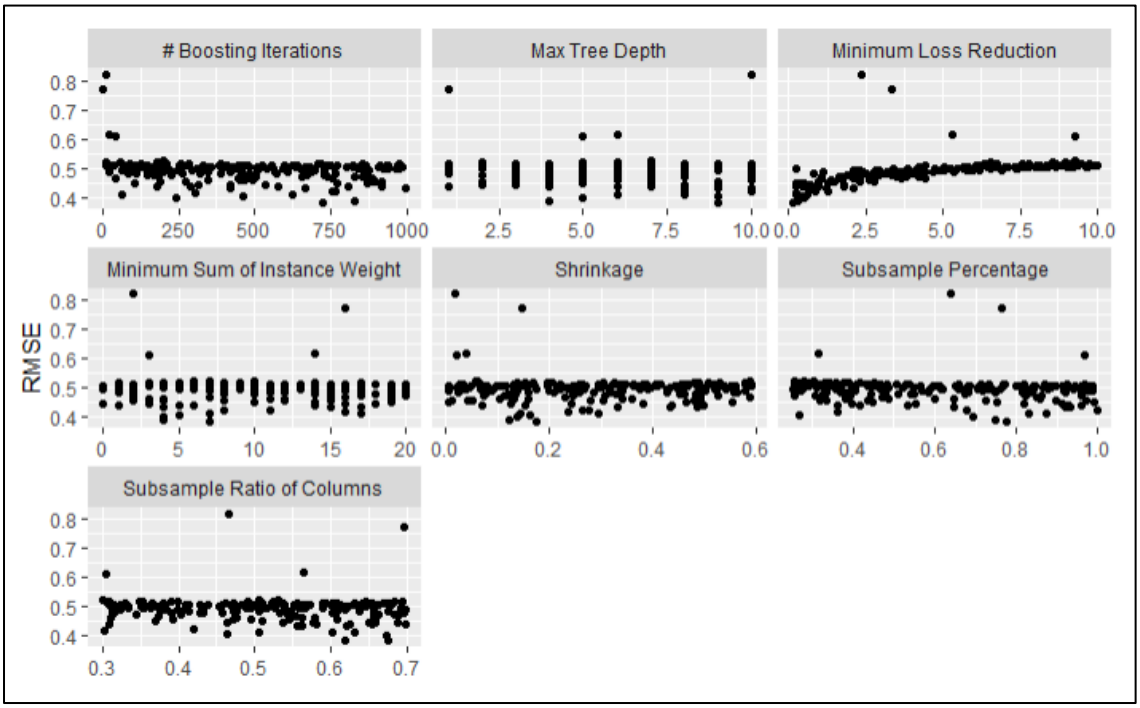

Figure 3.14. XGBoost model parameter tuning via cross-validation

For comparison, a polynomial regression model was also used to fit the same train data set. The loss function of this non-linear curve-fitting model is given by equation

(3.30). w and b are the model weights (parameters) and bias, respectively. y_i is the true output and $(w^T x_i + b)$ is the predicted output of the model. At each iteration, the Stochastic Gradient Descent (SGD) algorithm is used to update the model weights as shown in equation (3.31). The final parameter values of the polynomial regression model is shown in Table 3.2. Figures 3.15 and 3.16 show the results from model training. Both plots show an improvement in model training (reduction in model error) as more data points are added. For comparison, the results of the polynomial curve fitting model is also shown in both plots. As a convention, previous methods for discrete element geomaterial calibration [30, 124-126, 133] always involved few simulation tests (< 100 tests).

Table 3.2. Final parameter values for polynomial regression model

Model Feature	**NL Regression Model**	
	Emod (E^*) **weight**	**Fric** (μ) **weight**
Intercept	2.938	2.938
Res_modulus (E_{rm})	-122.39	-122.39
Yng_modulus (E_{ym})	38.744	38.744
Psn_ratio (v_{pr})	-2.525	-2.525
Shear_modulus (E_{sm})	-25.23	-25.23
Fric_coeff (μ_f)	-13.881	-13.881
Fric_coeff2 $(\mu_f)^2$	97.779	97.779
Res_modulus2 $(E_{rm})^2$	-468.726	-468.726
Yng_modulus2 $(E_{ym})^2$	138.455	138.455
Shear_modulus2 $(E_{sm})^2$	12.692	12.692
Fric_Res_Yng_Psn $(\mu_f * E_{rm} * E_{ym} * v_{pr})$	612.959	612.959

$$Loss_{NL\_Reg} = \frac{1}{n}\sum_{i=1}^{n}(y_i - (w^T x_i + b))^2 \tag{3.30}$$

$$w_{i+1} \leftarrow w_i - \eta\left(\frac{\frac{1}{n}\sum_{i=1}^{n}(y_i - (w^T x_i + b))^2}{\partial w}\right) \tag{3.31}$$

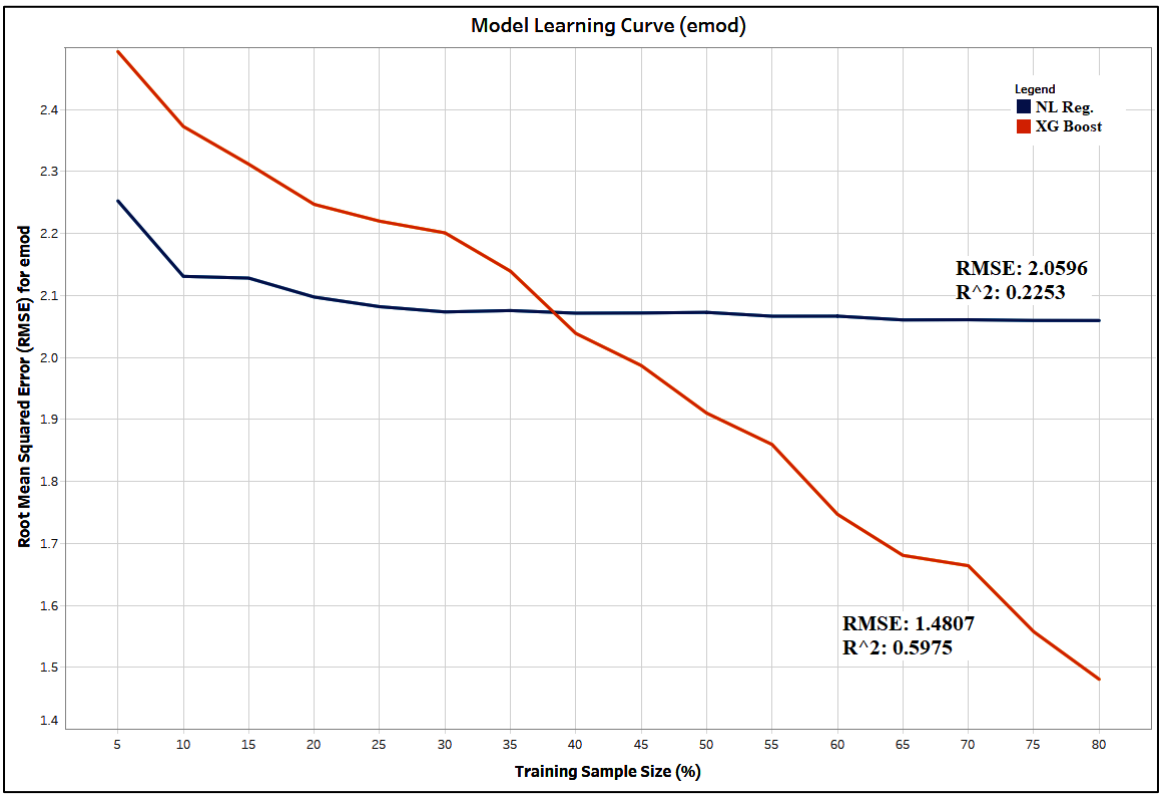

Figure 3.15. Model learning curve for emod (E^*) using train data set

However, Figures 3.15 and 3.16 both indicate that with more data points, and a more powerful learning algorithm, such as XGBoost, it is possible to build a calibration model, which performs significantly better than a conventional polynomial curve-fitting method. When up to 20% (i.e. 170 data points) and 38% (i.e. 323 data points) of the data

points were used for training emod, E^* (Figure 3.15) and fric, μ (Figure 3.16) respectively, the polynomial curve-fitting method performed better than the XGBoost model. However, with the addition of more data, the XGBoost calibration model continued to improve its parameter tuning whilst the performance of the polynomial curve-fitting model remained fairly constant. At each iteration during model training, the XGBoost model also uses the concept of cross-validation to evaluate the overall accuracy of its parameter tuning by testing different hypotheses on 10% of the training data, which was not used in the parameter tuning process.

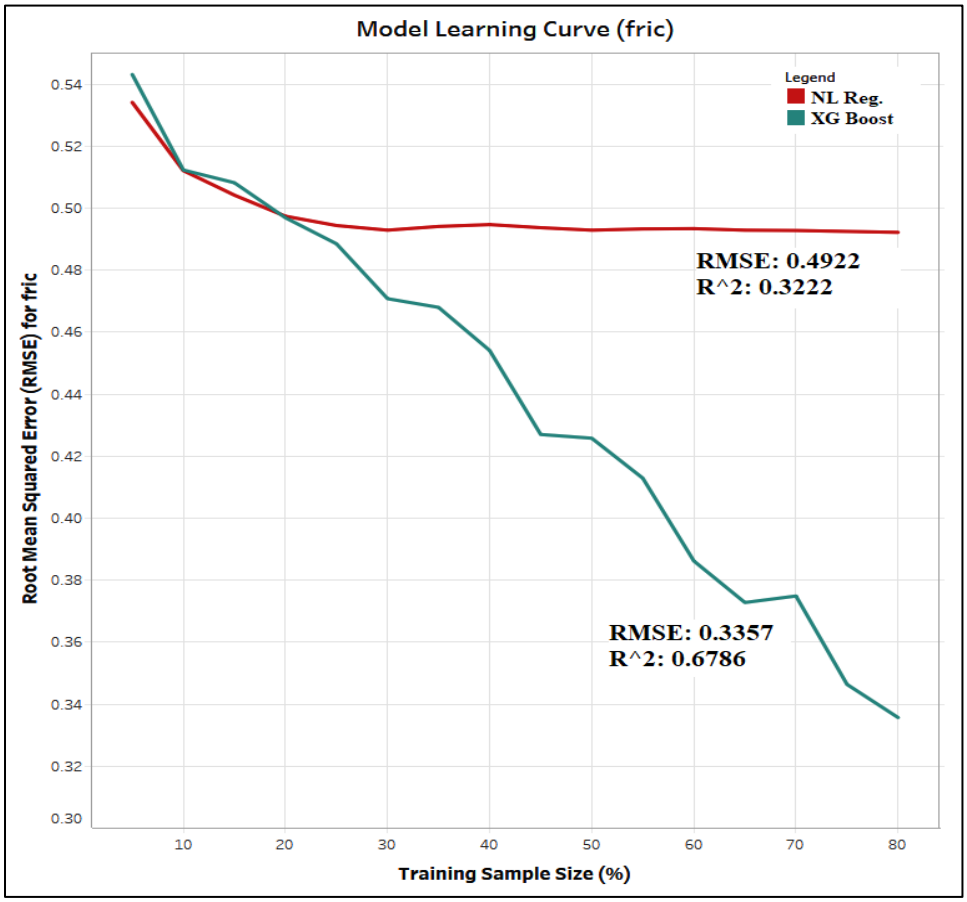

Figure 3.16. Model learning curve for fric (μ) using train data set

Finally, when all 680 train data samples were used, the XGBoost model produces a much lower error (RMSE) and a significantly better R^2 value. These results suggest that the XGBoost calibration model is able to match, and in some cases, outperform conventional non-linear curve-fitting models in reducing errors between actual material properties and model predictions (i.e. material property matching).

3.2.5. Model Verification and Validation. A DEM model of earth material was formulated using Cundall and Strack's viscoelastic constitutive model and calibrated from virtual triaxial experiments in PFC 5.0 using the XGBoost algorithm. The XGBoost calibration model was verified and validated using the formation properties from the Newlands Mine dragline bucket loading experiments, reported by O'Beirne [35]. At the Newlands Mine, the main overburden to the Newlands Upper coal seam is the Rangals formation, which is a mixture of mudstone and siltstone with small to moderate sandstone content. Table 3.3 shows the reported material property values [35, 134, 135], the generated features as well as the XGBoost model's predicted DEM parameters. For model verification and validation, the formation macro-properties were first used to generate the input parameters of the XGBoost Calibration model. The XGBoost model was then used to predict DEM micro-parameters for the formation (Table 3.3). Then using the predicted DEM micro-parameters, triaxial testing in PFC was conducted to generate model estimates of the formation macro-properties (Table 3.4).

The goal of the verification process was to evaluate how well the predicted DEM parameters are able to replicate typical material behavior under triaxial loading. The simulation results from the triaxial loading phase (Figure 3.18) were therefore compared to typical experimental results for mudstones (Figure 3.17) in the literature [136]. Figure

3.18 shows that the model is able to sufficiently replicate the initial gradual rise in deviatoric stress, the distinct peak failure and the post-failure strain-hardening behavior. Hence, the XGBoost calibration model was able to meet the verification criteria.

Table 3.3. Material parameters from XGBoost calibration

Model Input	
E_{rm}	0.235
E_{ym}	0.280
v_{pr}	-0.360
E_{sm}	0.215
μ_f	0.870
$(\mu_f)^2$	0.757
$(E_{rm})^2$	0.055
$(E_{ym})^2$	0.078
$(E_{sm})^2$	0.046
$(\mu_f * E_{rm} * E_{ym} * v_{pr})$	0.020
Model Output	
Emod, E^* (GPa)	28.29259
Fric, μ	0.871712
Kratio, k^*	1.0

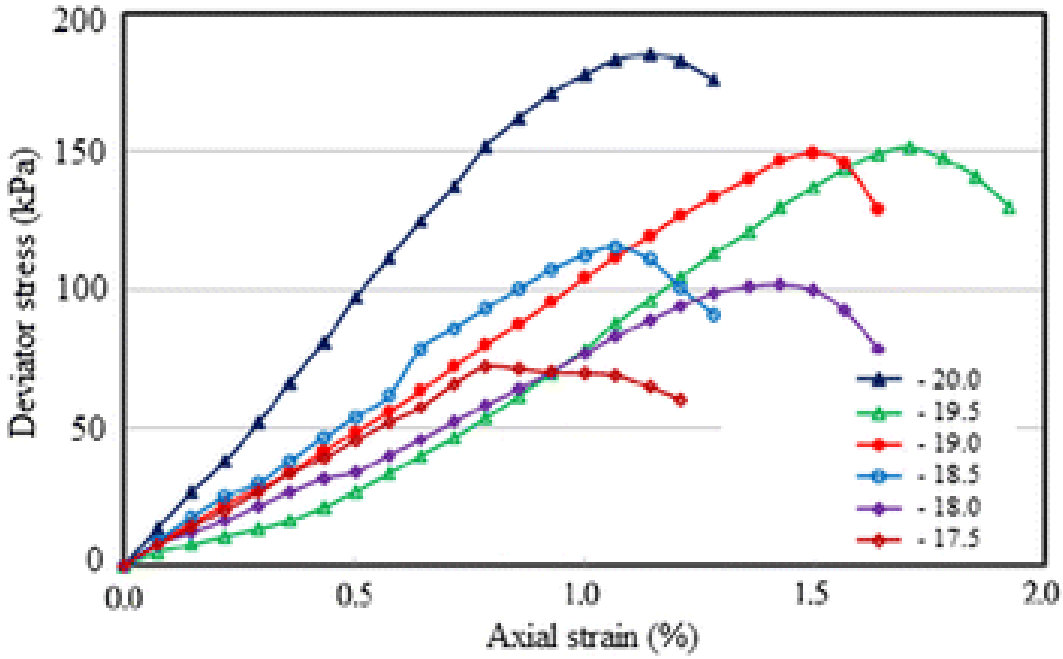

Figure 3.17. Experimental triaxial loading results for mudstone [136]

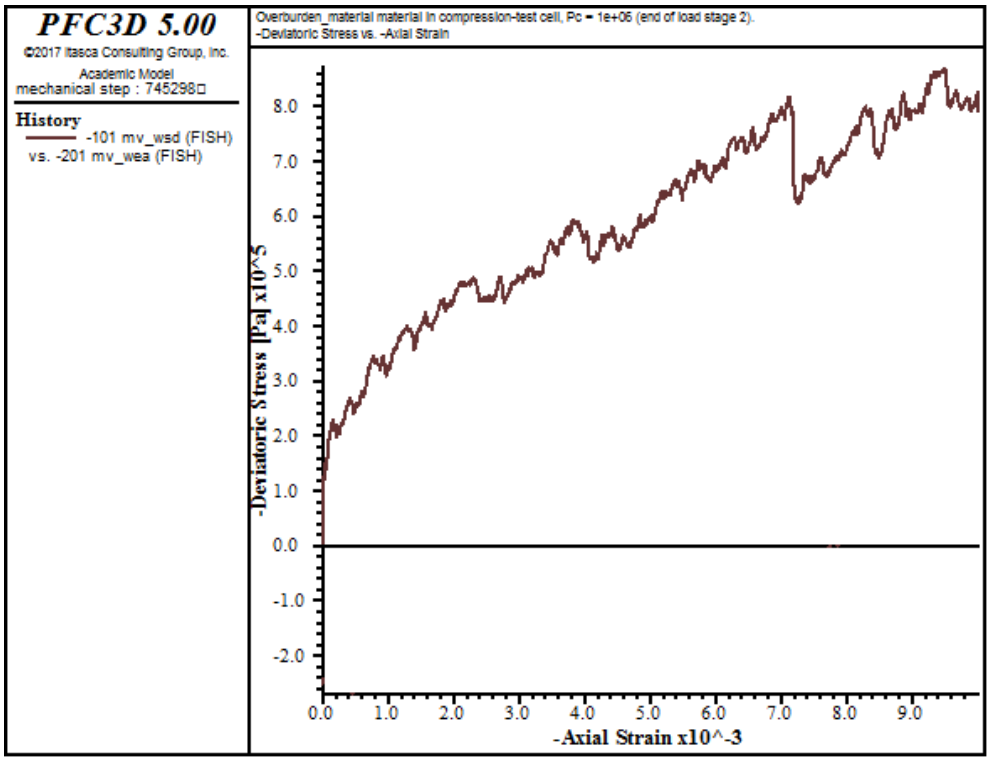

Figure 3.18. Triaxial test loading phase simulation in PFC 5.0

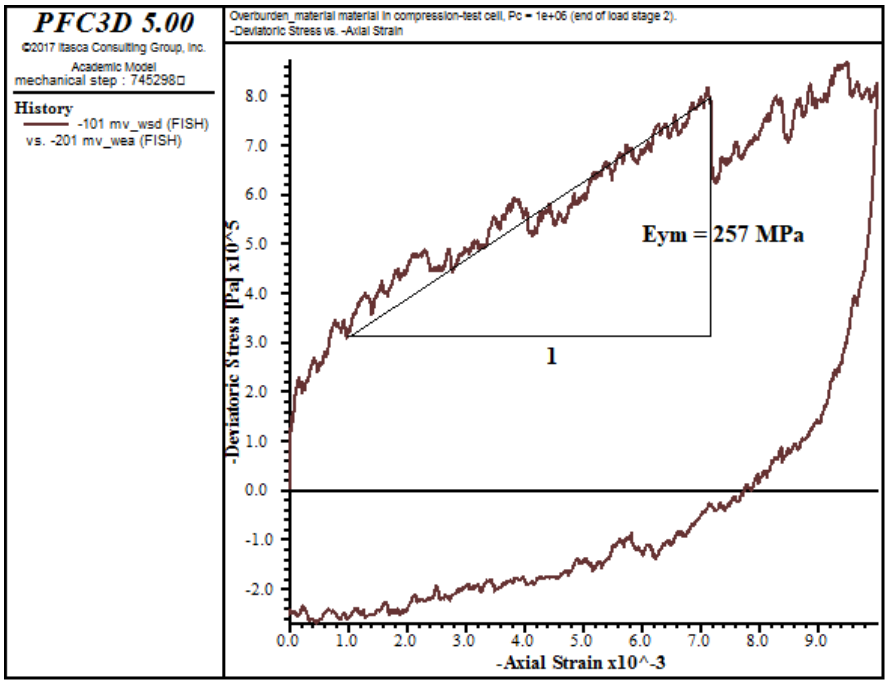

Figure 3.19. Eym result for PFC material parameters

The goal of the validation process was to evaluate how well the model-generated formation macro-properties matched the actual macro-properties. The E_{ym} and v_{pr} values were determined from the plots of the simulation results, as shown in Figures 3.19 and 3.20, respectively. The μ_f and E_{sm} values were also determined from the triaxial simulation using equations (3.26) and (3.27), respectively. Table 3.4 shows the comparison between the reported material properties and the corresponding properties from DEM parameters, determined with the XGBoost material calibration model. From the results, the XGBoost model shows good predictions for E_{ym}, E_{sm} and μ_f with less than 10% error in all cases. The only exception is the predicted v_{pr} value, which shows an error of almost 20%. This can be attributed to the initial modeling assumption that k^* is 1.0. Potyondy and Cundall [124] showed that v_{pr} correlates strongly with k^*.

Therefore, fixing k^* at 1.0 partially accounts for the larger error in v_{pr} prediction, compared to the other properties.

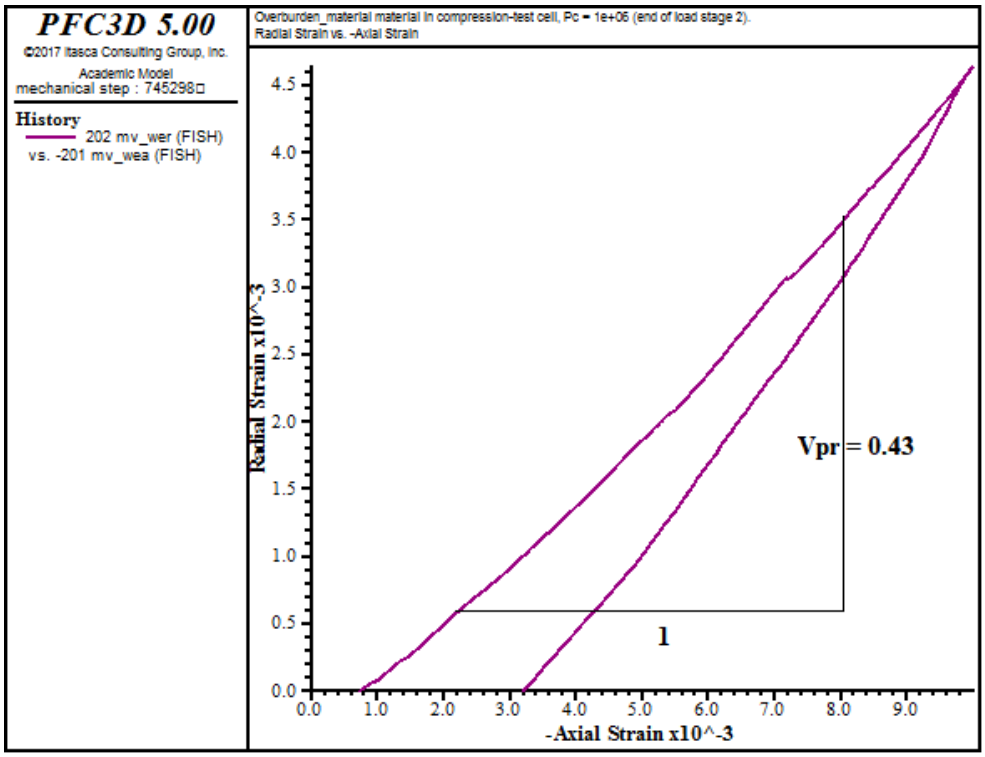

Figure 3.20. Vpr result for PFC material parameters

Nonetheless, the model simplification, which is made possible by this assumption, is desirable since it partially accounts for the small error predictions in the other properties. Also, the model-predicted v_{pr} value of 0.43 is acceptable since it falls in the range of typical values (0.1 to 0.5), for shale and mudstone [137]. Generally, the XGBoost calibration model meets the validation criteria as it sufficiently predicts the actual formation properties.

Table 3.4. XGBoost model evaluation

	Actual material properties	**Material properties from XGBoost-predicted parameters**	**% Error**
E_{ym} **(GPa)**	0.280	0.257	8.21
E_{sm} **(GPa)**	0.215	0.225	-4.46
v_{pr}	-0.36	-0.43	-19.4
μ_f	0.87	0.81	7.24

3.3. DRAGLINE EXCAVATION MODELING

This section discusses the development of a simulation model for dragline bucket – formation interactions. The simulation model is verified and validated using typical bucket loading behavior and actual, full-scale dragline bucket-loading experiments at the Newlands Mine in Queensland, Australia.

3.3.1. Excavation Performance Metrics. As shown in Figure 3.21, the forces which act on a dragline bucket during excavation may be broken down into the following components: (i) payload, f_1; (ii) frictional force generated between bucket floor and the formation, f_2 ; (iii) frictional force generated between payload and bucket floor, f_3; (iv) cutting force at bucket lips and teeth, f_4; (v) inertia force of payload, f_5; (vi) deadweight of the bucket, f_6; (vii) fictional force generated between payload and bucket sides, f_7; (viii) hoist force, F_h; and (ix) drag force, F_D. During dragline excavation simulation in PFC 5.0, the payload at any time step, is given by the total weight of all particles (i.e. earth material) in the bucket. For *n* particles of mass, *m,* and occupying volume, *V,* in a bucket, the payload, f_1 is given by equation (3.32). γ_f and V_i are the unit weight of earth material and the volume of particle, i, in the bucket, respectively. The maximum

suspended load, M_{SL} is given by the sum of the bucket deadweight and the payload in equation (3.33). V_b and γ_b are the volume and unit weight of the bucket respectively. The frictional forces, f_2 and f_3 are then given by equation (3.32) and (3.35), respectively. μ_{sm} is the soil-metal friction. α_f is introduced as a limiting factor because the value of f_3 is high when the bucket is near-empty but reduces with time as the material loading progresses.

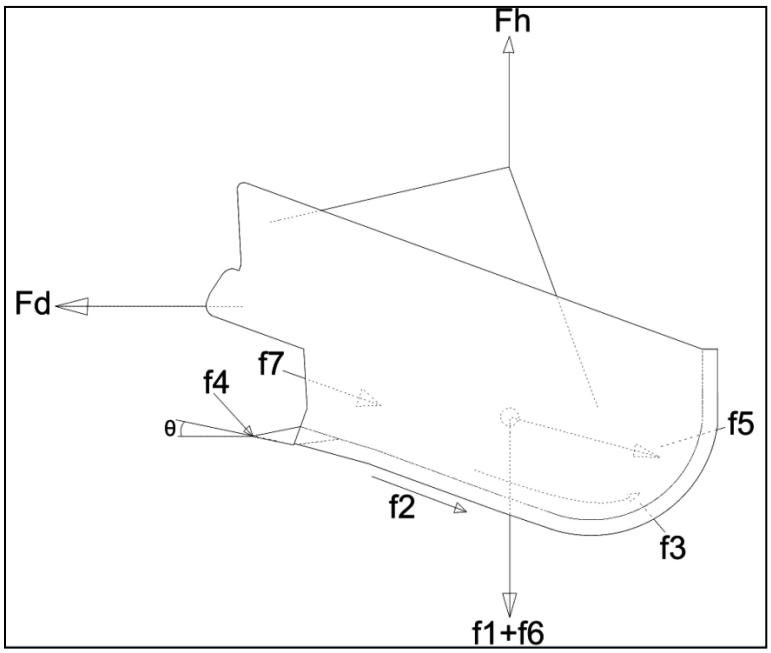

Figure 3.21. Forces on a dragline bucket during excavation

$$f_1 = \sum_{i=1}^{n}(m_i * g) = \sum_{i=1}^{n}(\rho_f * V_i * g) = \gamma_f \sum_{i=1}^{n} V_i \tag{3.32}$$

$$M_{SL} = \frac{1}{g}(f_1 + f_6) = \left(\rho_f \sum_{i=1}^{n} V_i + \rho_b V_b\right) \tag{3.33}$$

$$f_2 = \mu_{sm}\left(\gamma_f \sum_{i=1}^{n} V_i + \gamma_b V_b\right) Cos\ \theta \tag{3.34}$$

$$f_3 = \mu_{sm}\left(\alpha_f \gamma_f \sum_{i=1}^{n} V_i\right);\ 0 < \alpha_f < 1 \tag{3.35}$$

The cutting force, f_4, may be expressed as the sum of all contact forces at the bucket lips and teeth. Its magnitude depends on material stiffness, bucket geometry and the drag velocity. It is assumed that the bucket dragging occurs with minimal changes in bucket velocity. The resistance forces, f_2, f_3 and f_4, are far greater than the force generated between the payload and the bucket sides, f_7. Therefore, f_7 is also assumed to be negligible. The drag force, F_D is given by equation (3.36). $\ddot{x_b}$ and $\ddot{y_b}$ are the bucket acceleration in the x- and y- directions, respectively. At any given time during the simulation, the drag energy of the bucket, E_D can be determined as the sum of the kinetic energy and the work done in dragging the bucket through a horizontal distance, x_b at velocity, $\dot{x_b}$ [138], as given by equation (3.37).

$$F_D = \rho_f \ddot{x_b}\left(\sum_{i=1}^{n} V_i + \rho_b V_b\right) + \mu_{sm}\left(\gamma_f \sum_{i=1}^{n} V_i + \gamma_b V_b + \alpha_f f_1 + f_4\right) Cos\ \theta \tag{3.36}$$

$$E_D = \left(\rho_f \sum_{i=1}^{n} V_i + \rho_b V_b\right)\left(\frac{1}{2}\dot{x_b}^2 + g * x_b\right) \tag{3.37}$$

3.3.2. Dragline Simulation Modeling. In PFC 5.0, simulation modeling begins with first defining the spatial extent of the simulation domain. The material assembly is then generated and the material properties are also defined by the user. Gravity is introduced into the simulation and the system is stepped to equilibrium through a number of cycles until satisfactory initial conditions are achieved after equilibrium. The complete pipeline for DEM dragline simulation in PFC 5.0 is summarized in Figure 3.22.

3.3.3. Experimental Setup. A major difficulty which was encountered in this study was the unavailability of experimental data for dragline bucket loading. In order to replicate physical bucket-formation interactions in a simulation model, specific experimental data on bucket properties (i.e. geometry, weight, velocity), formation properties (i.e. density, porosity, poisson's ratio, elastic modulus, friction coefficient, particle size disstribution), and excavation outcome (i.e. payload or forces) are all required.

The setup for the simulation model followed the experiment by O'Beirne [35] at the Newlands Mine in Australia, since the reort contained enough information for model validation. The bucket used in the experiment wa the $47m^3$ capacity Esco Mark IV dragline bucket. For the simulation, a full scale CAD model of te bucket was developed using Solidworks 2014 and Rhinoceros 5.0 (Figure 3.23). The CAD model was then converted into a STL (stereolithography) file and transferred into the PFC 5.0 virtul environment using FISH codes. A full scale, three dimensional (3-D) bucket - foration interaction model was not found in the literature. Both full scale and 3-D DEM models tend to be computationally expensive. Figure 3.24 shows a close view of the bucket – formation setup.

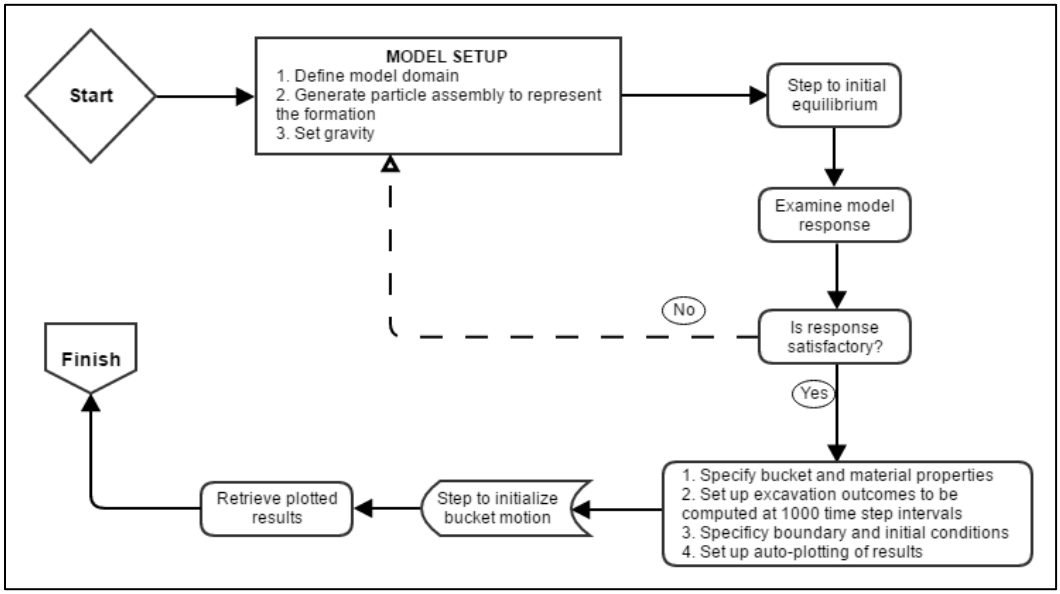

Figure 3.22. Flow chart for the simulation of dragline bucket-filling in PFC

Therefore, in order to perform a full scale, 3-D bucket analyses at a reasonable computational expense, some features of a standard dragline bucket were omitted. Caution was taken to restrict omissions to areas that would have very little to no impact on material flow pattern and payload measurements. These omissions include the bucket rigging and arch. Typically, draglines achieve a 70 – 90 % fill factor in three to six bucket lengths of dragging [29, 30]. Therefore, the required material bin needs to be long and wide enough to allow for bucket-loading behavior without unrealistic boundary effects.

3.3.4. Boundary and Initial Conditions. Boundary conditions were achieved using the material bin, which is bounded by fixed walls at the bottom and on all four sides. These walls act together to restrict material movement. The particles in the material can flow freely within the bin but they lose their velocity and come to a stop at the fixed walls. The setup was designed to ensure that the fixed boundary conditions do

not affect the bucket loading process unrealistically. This was achieved by allowing a gap of at least one bucket width between the bucket path and the side walls. In PFC 5.0, the initial conditions of the material assembly are inherited from the applied boundary conditions and the packing history [139]. After the material assembly was generated, gravitational force was introduced into the system before cycling.

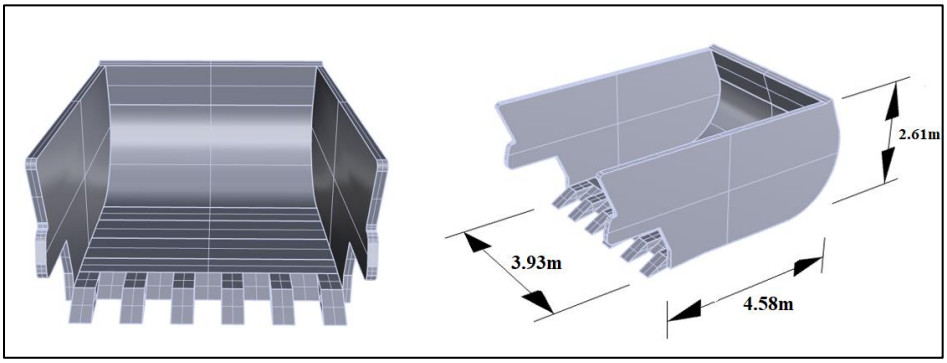

Figure 3.23. Full scale CAD model of dragline bucket

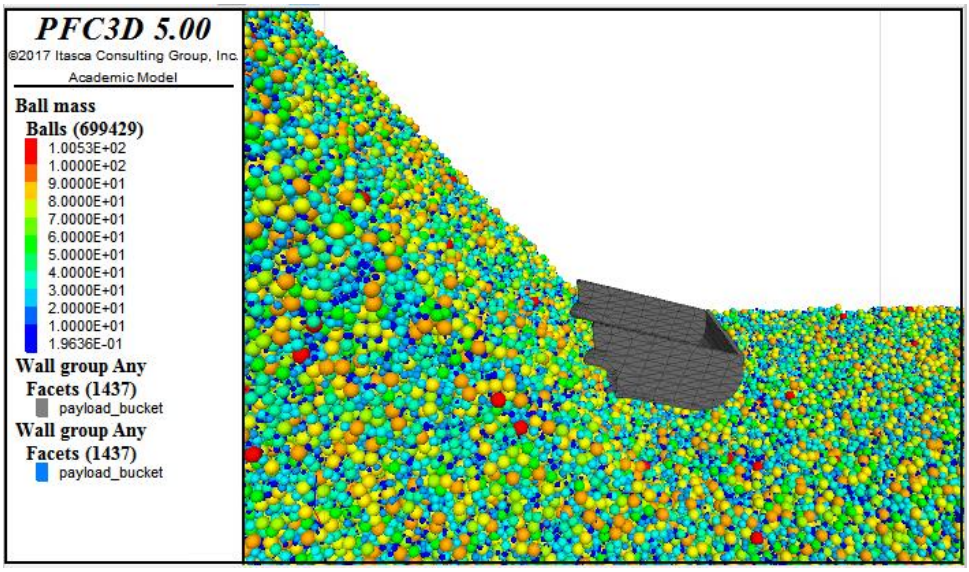

Figure 3.24. Close view of dragline bucket and the formation

3.3.5. Bulk Density Calibration. At the beginning of material simulation in PFC 5.0, the user defines a particle density for the material. PFC uses particle density, rather than bulk material density, which can be determined experimentally. For any physical material, particle density is different and often greater than the material bulk density. Since the bulk density of the virtual material is required to match that of the physical material, a fast, iterative calibration method was proposed.

During material generation, the initial bulk density of the material assembly was determined by writing FISH functions to measure the material mass in three measurement regions, each of volume 1 m^3. The measurement regions were chosen at the left, mid and right sections of the bin. The initial bulk density was then determined from the average of the densities in the three regions. Depending on the difference between this initial bulk density and the actual bulk density of the physical material, new parameter values are then selected for the packing arrangement (material porosity) and the particle density. The two values are then varied iteratively until the bulk densities matched. By using this approach, the bulk densities were typically matched within 3 to 5 iterations.

3.3.6. Payload Measurement. PFC 5.0 has no module for measuring the excavation performance. Hence, a FISH function was defined to measure the payload using the measurement region, shown in Figure 3.25. The measurement region was extended beyond the bucket's struck capacity by about 50% of the bucket height. This was to allow for accurate measurements in case of material heaping during bucket loading. An extension of 50% of the bucket height was deemed sufficient because realistically, material heaping does not reach that height. After every 10,000 cycles

during the simulation, the payload function loops through all the particles within the measurement region and updates the total weight accordingly.

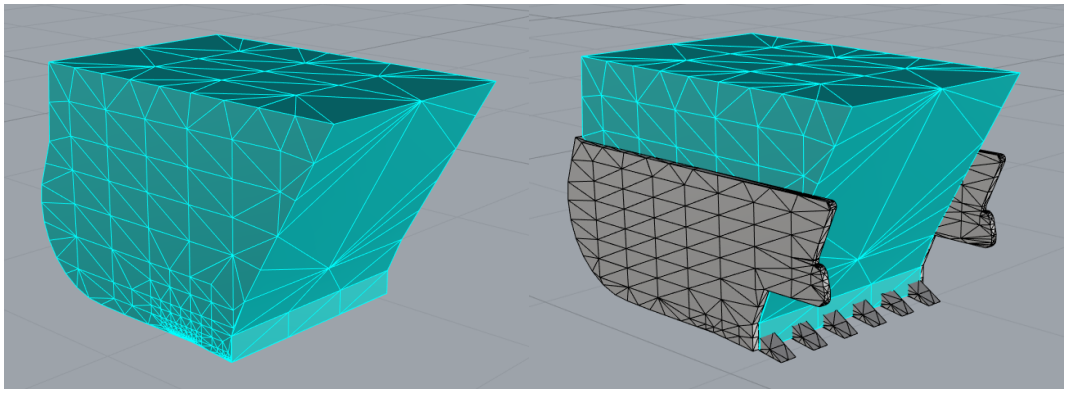

Figure 3.25. Payload-measuring region in dragline bucket

3.3.7. Model Verification and Validation. The simulation model is verified and validated using typical bucket loading behavior and experimental data from the Newlands Mine in Queensland, Australia, which has been reported by [35]. The Newlands Mine lies within the Bowen Basin, where the Rangal formation acts as overburden to the 6.5m thick Upper Newlands coal seam under development [135]. The overburden formation consists mainly of mudstone and siltstone with varying amounts of sandstone content across the basin. Hence, the formation density varies from point to point across the mine [140], depending on local conditions. The overburden was calibrated for DEM simulation using the XGBoost model as previously discussed in section 3.2.

In PFC, a large material bin was used for the simulation to limit unrealistic boundary effects. The bin spans at least ten bucket lengths. Its width was also chosen to be three times the bucket width. Similarly, the material depth was chosen to be at least

twice the height of the bucket. The Bucyrus Erie 1370W (BE 1370) dragline and the Esco Mark IV dragline bucket were used for the Newlands Mine experiments. Figure 3.26 shows the experimental setup in PFC 5.0. Table 3.5 shows both the formation and dragline parameters which were used as input for the simulation model [29, 35, 134, 135, 141].

The model was verified by visual inspection of the bucket loading process. The goal of model verification was to evaluate how well the model simulates typical dragline bucket loading behavior. Figure 3.27 illustrates the bucket-loading process in PFC 5.0. As the bucket interacts with the formation, a check is made after every 1000 time steps to identify material that has moved into the payload-measuring region inside the bucket. These particles turn to green and the bucket payload is updated by iteratively adding the weights of the individual particles, one at a time (Figure 3.27). The green materials in the trail of the bucket represent the heaved material, which fall over as the bucket fills up at the rear. This model behavior is consistent with observations during physical bucket-loading processes.

Two forms of validation were used to evaluate the model. These involved the bucket-filling rate and the payload after four bucket lengths. The bucket filling rate during the simulation was tracked and compared with observed experimental results (Figure 3.29). In PFC 5.0, a measure of the bucket filling rate was achieved by monitoring the bucket payload at 1000 time step intervals and recording the corresponding bucket fill distances. Figure 3.28 shows that the bucket filling behavior during the simulation is similar to the pattern which O'Beirne [35] observed in their field experiments (Figure 3.29). The model was able to correctly capture the slow, initial

build-up in filling, the steady increase in payload with time and distance as well as the reduced filling rate as the bucket approaches full-capacity.

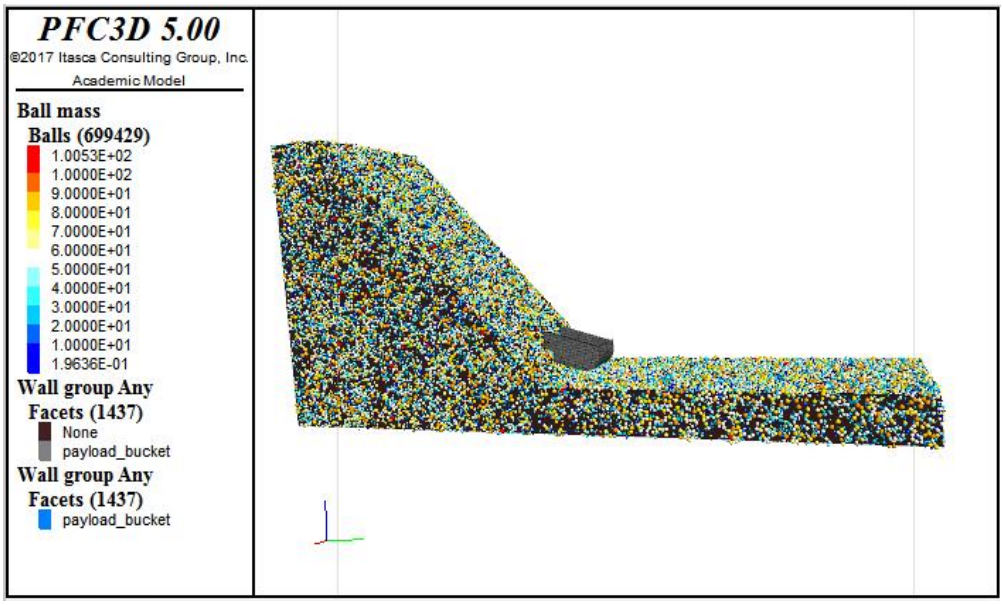

Figure 3.26. Full scale material bin, formation and bucket setup in PFC 5.0

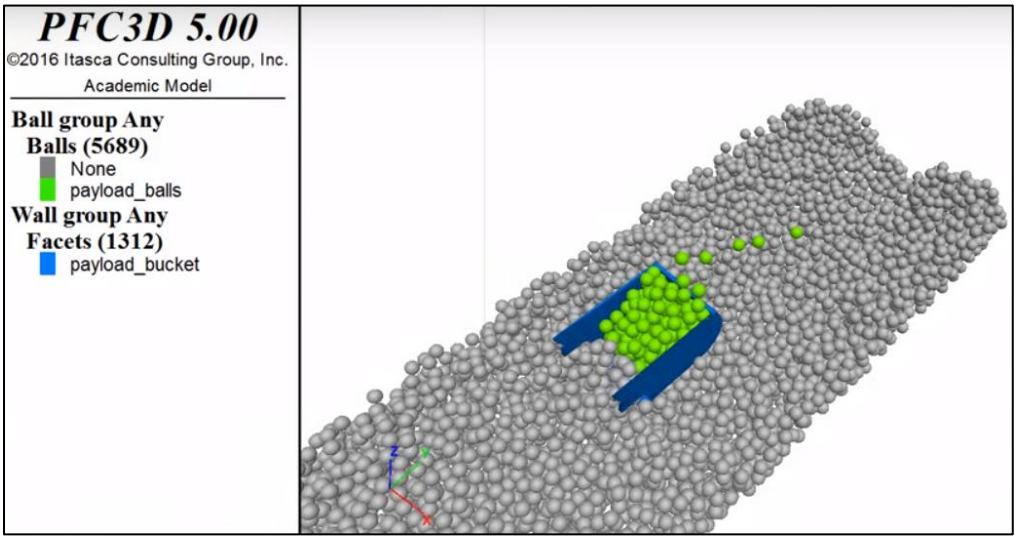

Figure 3.27. Bucket-loading process

Also, while draglines have been known to achieve a 70% to 90% fill factor in less than 3 bucket lengths of dragging [142], it typically takes 3 to 6 bucket lengths in most cases [29]. Figure 3.30 shows a comparison of payload for both simulation and experimental results at different densities for the same $47m^3$ Esco Mark IV bucket. The results show that the simulation model is able to produce excavation outcomes, which fall in the ball park of experimental results. To provide a quantitative evaluation of these results, a linear function was used to fit the experimental data. The mean absolute error of the simulation results was then computed, weighted and then compared with that from the experimental tests. Table 3.6 shows that the experimental results achieve a weighted percentage error of 10.26% about the mean, compared to 16.55% from the model simulation results. Nonetheless, the model is deemed acceptable because even for the same dragline operator, it is typical for payload variations to exceed 16.55% across multiple digging cycles.

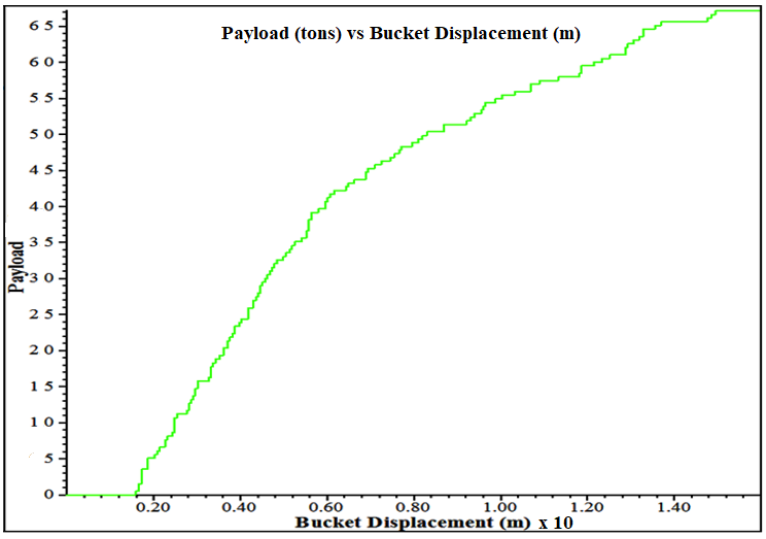

Figure 3.28. Payload tracking during bucket loading in PFC 5.0

Table 3.5. Input parameters for the dragline simulation model

Formation Characteristics	
Formation	Rangal Coal Measures
Bulk Density (kg/m3)	1700 - 2300
Porosity	0.35
fric	0.87
emod (GPa)	2.82
kratio	1.0
Particle size range (m)	0.025 - 0.2
Bucket - Formation friction	0.58
Damping ratio (normal)	0.9
Damping ratio (shear)	0.9
Dragline Specifications	
Dragline model	Bucyrus Erie 1370W (BE 1370)
Dragline weight	3 500 tons
Boom length	97.6 m
Production capacity/hour	3 000 tons
Bucket model	Esco Mark IV
Bucket dimensions: width	4.0 m
Bucket dimensions: height	2.7 m
Bucket dimensions: length	5.2 m
Horse power of drag motor	1045 hp
Bucket weight (empty)	37 ton
Bucket weight (loaded)	73 ton
Rated Bucket Capacity	42.8 m^3
Typical bucket velocities (m/s)	1.5 - 2.0
Max. depth that can be worked	38 m
Typical bucket velocities (m/s)	1.5 - 2.0
Rated Bucket Capacity	42.8 m^3

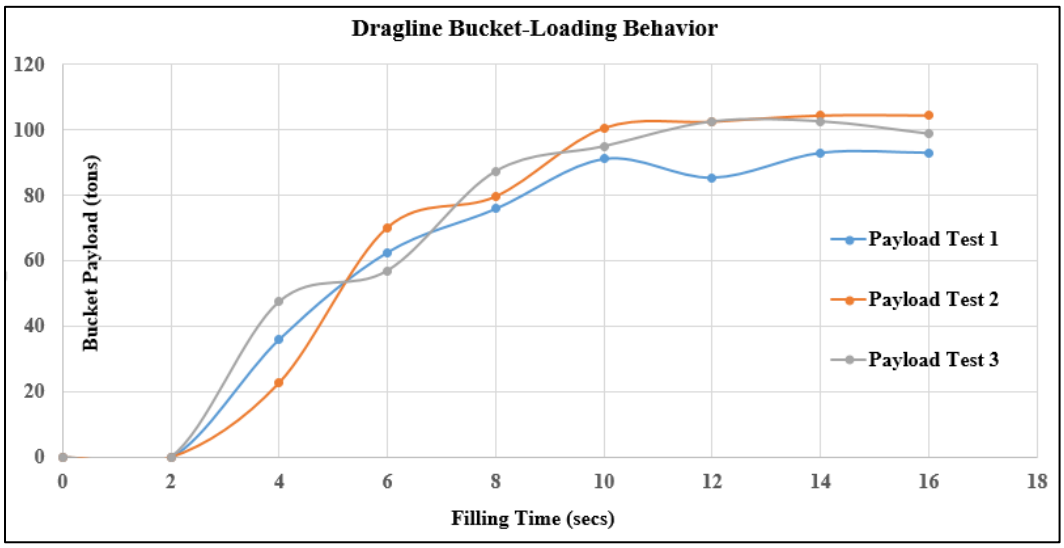

Figure 3.29. Payload tracking during bucket loading [35]

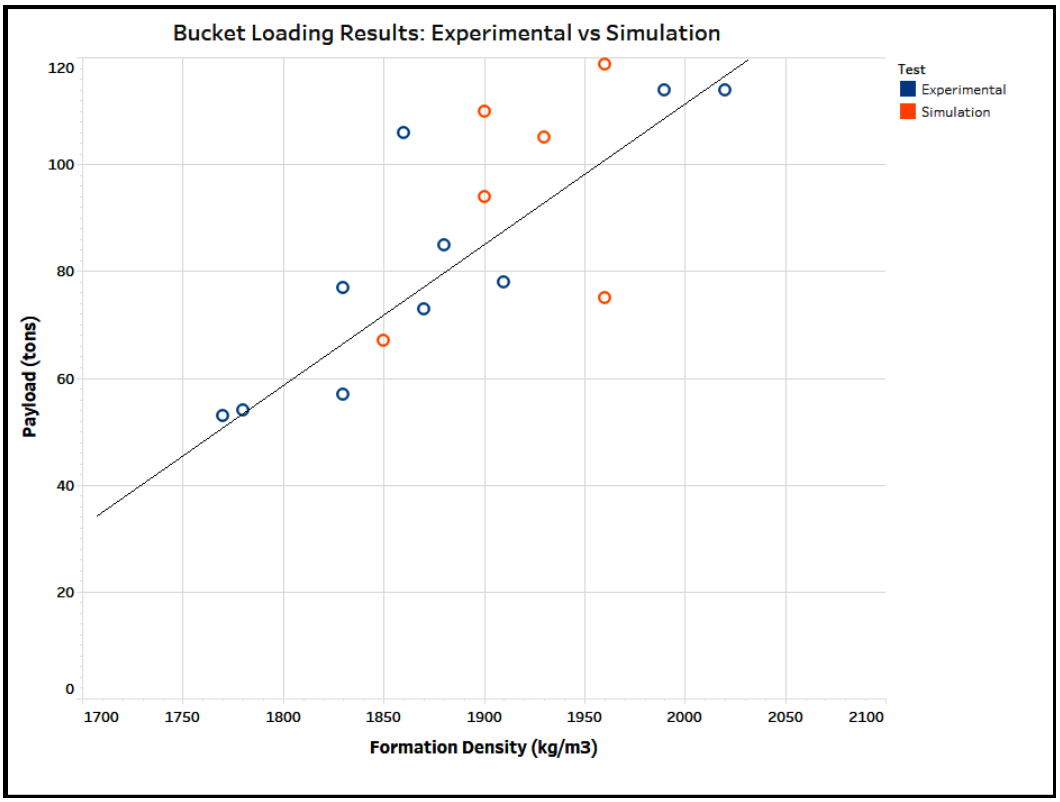

Figure 3.30. A comparison of simulation results and experimental data

Table 3.6. Model validation results

Test	Density (kgm^3)	Payload (tons)	Linear Best_Fit (tons)	Test Mean (Best Fit) (tons)	Standard Error	Absolute Standard Error	Weighted Mean Absolute Standard Error	Weighted % Error
Experimental	2020	114	117.45	81.04	3.45	3.45	8.31	10.26
	1910	78	90.01		12.01	12.01		
	1780	54	57.59		3.59	3.59		
	1860	106	77.54		-28.46	28.46		
	1830	77	70.06		-6.94	6.94		
	1770	53	55.10		2.10	2.10		
	1990	114	109.97		-4.03	4.03		
	1880	85	82.53		-2.47	2.47		
	1830	57	70.06		13.06	13.06		
	1870	73	80.04		7.04	7.04		
Simulation	1960	119	102.48	91.68	-16.52	16.52	15.17	16.55
	1960	75	102.48		27.48	27.48		
	1900	94	87.52		-6.48	6.48		
	1900	110	87.52		-22.48	22.48		
	1850	67	75.05		8.05	8.05		
	1930	105	95.00		-10.00	10.00		

3.4. EXPERIMENTATION

Five experiments were designed for the dragline excavation model. This section discusses these experiments in detail.

3.4.1. XGBoost Calibration Prediction. The convention in DEM parameter calibration of earth material has always been to both calibrate and evaluate the model using a few experiments. In most previous geomaterial calibration models [30, 123-127], the model evaluation process involved only a handful of experiments (< 20 tests). However, without the ability to produce acceptable DEM parameter predictions over a wide range of material properties, a calibration model may not be very useful to other investigators beyond the typically narrow parameter range of the original experiments.

To this end, an experiment was designed to evaluate the predictive performance of the XGBoost calibration model over a wide parameter range. Table 3.7 gives the details of the designed experiment.

Table 3.7. Large scale evaluation of XGBoost calibration model

Experiment IV: Large Scale Performance of XGBoost Calibration Model	
Objective:	To evaluate XGBoost calibration model performance on a wide range of material parameters.
Parameters [Scope]:	(i) Friction coefficient: [0.25 to 0.50] (ii) Poisson ratio: [-0.8 to -0.2] (iii) Young's modulus: [0.15 to 0.40 GPa] (iv) Shear modulus: [0.1 to 1.4 GPa]
Number of experimental tests:	170
Significance:	The convention in DEM parameter calibration of earth material has always been to both calibrate and evaluate the model using a few experiments. This study will seek to determine whether a data-driven calibration process holds more promise for model reliability and extensibility.
Expected results:	The XGBoost model is expected to perform much better than convental calibration methods at large scale testing.

To guard against sampling bias, a test size of 170 samples was used in order to cover a wide, but realistic range of values for both the target micro-parameters (E^* and μ) and the predictor macro-properties (E_{ym}, E_{rm}, v_{pr}, μ_f, E_{sm}, ${E_{ym}}^2$, ${E_{sm}}^2$, ${E_{rm}}^2$, ${\mu_f}^2$ and $[\mu_f * E_{rm} * E_{ym} * v_{pr}]$). Utmost care was taken to ensure that none of the original model training data points were repeated in the 170 test samples. The predictive performance of the XGBoost model is then compared to that of the polynomial regression model. It is

expected that the XGBoost model will outperform the more traditional polynomial regression model.

3.4.2. Effects of Formation Properties on DEM Micro-Parameters. Like most machine learning models, the XGBoost calibration model is a black box. Therefore, beyond new predictions, the model does not improve current knowledge about the nature of the relationships between formation properties and the DEM micro-parameters. Currently, there is no study which has comprehensively investigated the relationship between formation macro- and micro-parameters.

Therefore, an extensive study will be conducted to investigate this relationship using the 20% test data (i.e. 170 samples). From these samples, partial dependence plots will be developed for each formation property and each DEM micro-parameter. Partial dependence plots will reveal the dependence between any given DEM micro-parameter and a formation property, when all other properties are held constant. Table 3.8 summarizes the details of the designed experiment.

3.4.3. Effects of Formation Characteristics on Bucket Filling. Two experiments were conducted to investigate the effects of (i) material fragmentation and (ii) material density on dragline bucket loading performance.

In some situations, blasting is required to improve dragline excavation performance by breaking the formation into sizes that can easily be scooped by the bucket. Good fragmentation during blasting is important for excavation efficiency. When the overburden is poorly fragmented, multiple attempts may be required to remove boulders, thereby increasing cycle time and reducing productivity.

Table 3.8. Formation parameter experiments

Experiment V: Effects of Formation Properties on DEM microparameters	
Objective:	To investigate the underlying relationships between DEM microparameters and the formation properties.
Parameters [Scope]:	(i) Friction coefficient: [0.25 to 0.50] (ii) Poisson ratio: [-0.8 to -0.2] (iii) Young's modulus: [0.15 to 0.40 GPa] (iv) Shear modulus: [0.1 to 1.4 GPa]
Experimentation:	(i) Large Scale experimentation to evaluate the calibration performance of the XGBoost model. (ii) Experimentation to investigate the underlying relationships between DEM micro-parameters and formation properties.
Number of experimental tests:	170
Significance:	There is currently no study that extensively investigates the relationship between DEM microparameters and the properties of the formation. This experiment will seek to explore that space.
Expected results:	The relationships between DEM microparameters and earth material properties have not been previously studied at such a large scale. It is expected that this study will expose some limitations of the current paradigm in material calibration research.

While over-fragmentation will increase the ease of excavation, it is not practical to achieve only fines through blasting. Even if the entire overburden is over-fragmented (powdered) by blasting, the material will flow out of the rear of the bucket without heaping and this reduces the payload [142]. Therefore, it is necessary to establish how large rock fragments can be without adversely affecting excavation performance. The

question about which particle size range (from blasting) guarantees the best excavation outcome is still an open one and the answer may differ from one setup to the next.

No previous studies have explored fragmentation effects on dragline bucket efficiency specifically. However, a clearer understanding of these effects holds a lot of promise for optimum excavation efficiency. For a given excavation environment, this can be achieved by observing bucket performance for different fragmentation simulations. The optimum bucket performance output from model simulations can then be used as input for blast design. An experiment will therefore be carried out to evaluate whether the dragline simulation model provides a suitable platform for investigating the possible excavation outcomes of different fragmentation targets during blast design. Table 3.9 summarizes the details of the designed experiment.

An experiment was designed to evaluate the effects of material densities on dragline bucket excavation performance. Table 3.10 summarizes the details of the designed experiment. This study will investigate whether there is any correlation between material density and bucket performance. The experiment will also explore how different material densities affect bucket fill factors. It is expected that bucket payload will increase with increasing material density. However, it is unclear how this will affect the bucket fill factor in volumetric terms.

3.4.4. Material Density Variations during Bucket Loading. The nature of the formation failure process during dragline bucket excavation has been studied empirically by Rowlands (1992) in what is now accepted as the Shear Zone Theory. Through field experiments, O'Beirne [35] also observed the presence of different density zones in the

dragline bucket during loading (Figure 3.31). However, this observation has neither been studied nor confirmed by other investigators.

Table 3.9. The effects of formation fragmentation on excavation performance

Experiment VI: Formation Fragmentation & Excavation Performance	
Objective:	To evaluate the effects of fragmentation on dragline bucket excavation performance.
Number of Experimental tests:	5 tests
Material Size Distributions (radius):	(i) 2.5 to 25cm (ii) 2.5 to 50cm (iii) 20 to 25cm (iv) 45 to 50cm (v) 95 to 100cm
Significance:	No previous studies have explored fragmentation effects on dragline bucket efficiency specifically. A good understanding of these effects will help to connect the dots between good blast designs and optimum excavation bucket performance.
Expected results:	While no specific studies have been carried out about fragmentation effects on dragline efficiency, available empirical evidence (Lumley, 2014) suggests that a material size distribution from fines to one-third of the bucket width is desirable.

The researcher suspects that the observations in these two separate dragline excavation studies are somewhat connected. Therefore, an experiment will be conducted to explore the development of density zones within both the undisturbed material and the material in the bucket as excavation progresses. Throughout the bucket loading simulations, the material density in nine regions (Figure 3.32) will be monitored continuously after every 1000 iterations.

Table 3.10. The effects of material density on excavation performance

Experiment VII: Material Density & Excavation Performance	
Objective:	To evaluate the effects of material densities on dragline bucket excavation performance.
Number of Experimental tests:	5 tests
Material Densities (kg/m^3):	[1200, 1300, 1400, 1900, 2100]
Significance:	This study will investigate whether there is any correlation between material density and bucket performance.
Expected results:	It is expected that bucket payload will increase with increasing material density. However, it is unclear how this will affect the bucket fill factor in volumetric terms.

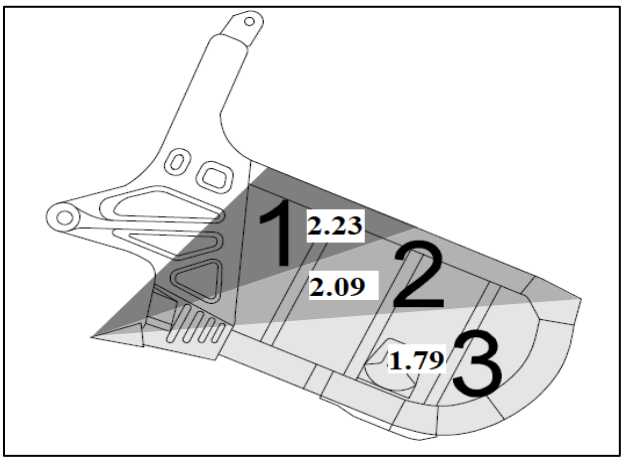

Figure 3.31. Payload zones and densities [35]

These density zones will be tracked to identify whether there are any density variations with time as the bucket progresses. It is expected that a material density distribution will exist within the bucket, as was observed by O'Beirne [35]. However, it is unclear whether this effect extends ahead of the bucket as well. It is also expected that

this study will provide findings that help to further explain the dragline bucket - material failure development processes which have been observed in previous studies (Rowlands, 1992). Table 3.11 summarizes the details of the designed experiment.

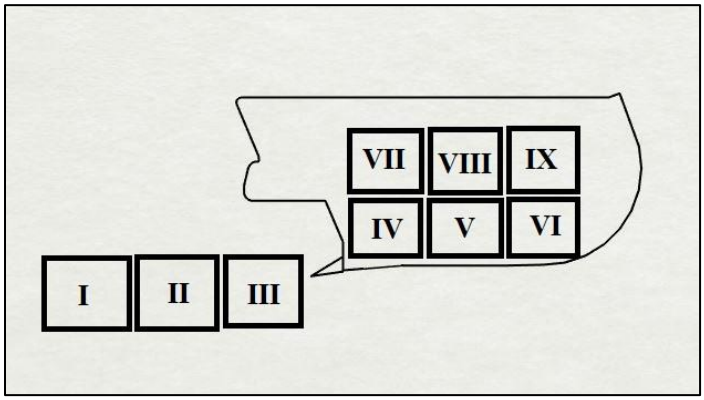

Figure 3.32. Density zone monitoring during dragline bucket loading

3.5. SUMMARY

The first part of this section described the development of a predictive calibration model for determining DEM parameters of earth material. The DEM modeling approach and its implementation in PFC 5.0 was discussed. The Hertzian contact modeling approach was used for constitutive modeling of the earth material. The theory behind the linear model [32], chosen as the constitutive model, was also discussed in detail. Since DEM model parameters do not have any direct relationship with physical material properties, there is the need for parameter calibration.

Virtual simulations were conducted in PFC 5.0 to generate 1500 triaxial test data for model calibration and evaluation. The extreme Gradient Boosting algorithm [34] was used to train a predictive model for material calibration. Initial comparisons with a

conventional curve-fitting method suggests that the XGBoost model is a significantly better calibration model. The XGBoost calibration model was verified and validated using mechanical property data of the Rangal formation at Newlands Mine in Queensland, Australia.

The second part of the section described the development of a simulation model for dragline bucket – formation interactions in PFC 5.0, using the Distinct Element Method. The simulation for model verification and validation was setup like the Newlands Mine experiment, reported by O'Beirne [35]. The model was verified and validated using available experimental data from the Newlands Mine. The Rangal formation was used as the overburden and its DEM parameters were determined using the XGBoost calibration model. The Bucyrus Erie 1370W (BE 1370) dragline and the Esco Mark IV dragline bucket were used in the actual experiment. Therefore, a full-scale CAD model of the $47m^3$ capacity Esco Mark IV dragline bucket was developed for the simulation using Solidworks 2014 and Rhinoceros 5.0.

The PFC 5.0 code was modified by defining FISH functions to calibrate the material's bulk density and to measure the bucket payload at pre-defined intervals. The simulation model was verified by visual impression and its behavior was found to be consistent with typical bucket loading processes. Model validation was achieved by comparing simulation results to typical bucket filling rates as well as payload results from O'Beirne [35]. Further experiments will be carried out to determine the effects of the formation properties, material density distribution and material size distribution on the bucket loading process.

Table 3.11. Investigating material density variations during bucket loading

Experiment VIII: Material Density Distribution	
Objective:	To investigate the formation failure process using material density distribution in different zones, both inside and ahead of the dragline bucket.
Number of density zones:	9
Significance:	The nature of the formation failure process during dragline bucket excavation has been studied empirically by Rowlands (1992) in what is now accepted as the Shear Zone Theory. O'Beirne (1997) also observed the existence of density distributions within the bucket during material loading. The researcher suspects that these two observations are connected and will seek to explore the development of density zones within both the material and the bucket as the material fails.
Expected results:	It is expected that a material density distribution will exist within the bucket. However, it is unclear whether this effect extends ahead of the bucket as well. Also, it is expected that this study will provide findings that help to further explain the dragline bucket - material failure development processes which have been observed by a previous study (Rowlands, 1992).

4. DRAGLINE VISION MODELING

The ideal dragline vision model is one that takes into consideration the most routine operator vision tasks in a typical operation cycle. Among others, common operator vision tasks include:

- detecting and tracking bucket position continuously, especially during fill and dump phases;
- identifying different terrains for digging strategy adjustments;
- identifying big rocks and boulders in bucket path;
- visualizing bucket filling difficulties for digging strategy adjustments; and
- visualizing the entire excavation environment for collision prevention, especially during bucket swing phase and for dragline movements to new working areas.

Generally, operator vision tasks fall largely under two umbrellas, namely: (i) object recognition, and (ii) object detection (localization and tracking). Therefore, the dragline vision portion of this research focuses on developing a deep learning model for simultaneous recognition, localization and tracking of objects in mine environments during dragline operations.

4.1. THE CONVOLUTIONAL NETWORK

Convolutional Neural Networks (CNNs) are unique multi-layer neural network for processing grid-like data, such as pixel data of images. They are able to recognize visual patterns directly from pixel data with very little processing required. Like other neural networks, CNNs are trained with some form of the error back-propagation

algorithm [143]. The concept of convolutional networks was introduced by LeCun et al. [144] as a solution for image recognition problems. It is not entirely clear why CNNs work where artificial neural networks and some other deep neural networks with general back-propagation have failed.

The most widely-accepted notion is that the modeling approach used in CNNs present a unique advantage over other models. For instance, unlike competing deep network models [145, 146], CNNs do not require complex image preprocessing or manual engineering of image feature vectors. Therefore, raw images can be fed into the learning network, which presents endless opportunities in model scalability. This also creates the possibility for real-time applications over a wide range of image recognition problems.

In addition, CNNs use the principle of weight-sharing. This means that all the neurons, in any given feature, share the same parameters. In this way, the same feature can be detected over and over, even when it occurs at different positions in an image. Weight-sharing reduces the number of model parameters, which in turn reduces model complexity, as well as model training time.

Therefore, CNNs are more computationally-efficient than fully-connected networks, which implies that it is easier to run multiple experiments for hyper-parameter tuning [147]. The general CNN model training process is best explained by Figure 4.1. Once a CNN architecture is selected, model weights are initialized and images are randomly selected for training, based on the pre-determined batch size.

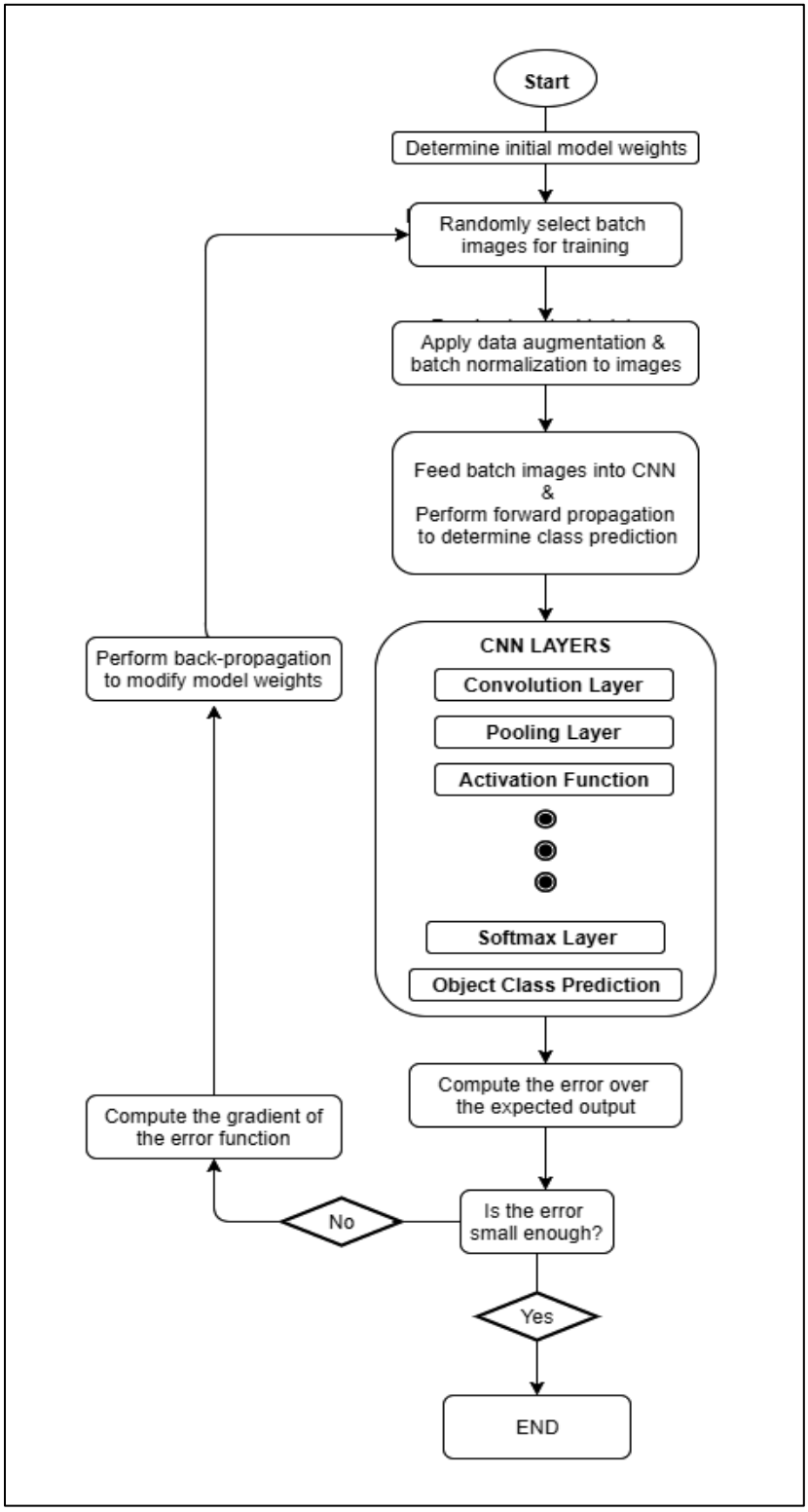

Figure 4.1. Flowchart for model training using ConvNets

Using the initialized model weights, a forward pass is propagated through the neural network to obtain an object class prediction. The model error at the current iteration is computed from the difference between actual object classes and model-predicted classes over the entire batch of images. The gradient of the error function is then computed and the error is propagated backwards through the network from the final layer to the first layer to modify the initial model weights. The process is repeated iteratively to reduce the total error between actual object classes and model-predicted classes over 250,000 epochs. Model training is carried out in Tensorflow [148], which is an open-source python and C++ package for dataflow programming.

4.2. COLLECTION OF INPUT DATA

In training the deep neural network, data has been collected for eighteen (18) object classes, comprising of eight (8) mobile mine equipment classes (Figure 4.3), nine (9) terrain classes (Figure 4.2) and one (1) additional class for site personnel (Figure 4.4). The terrain data was obtained from three Capital Quarries Co. sites and two Lafarge Aggregates Co. sites near the Saint Louis area in Missouri. The equipment data was obtained from the quarry sites as well as from online literature. In all, 2400 images were collected across the 18 object classes. In machine learning, it is typical to use 80% to 90% of the entire data set for model training and the remaining data for model evaluation. Therefore, 2100 images were randomly selected for batch training and cross-validation. The remaining 300 images were used for testing the model.

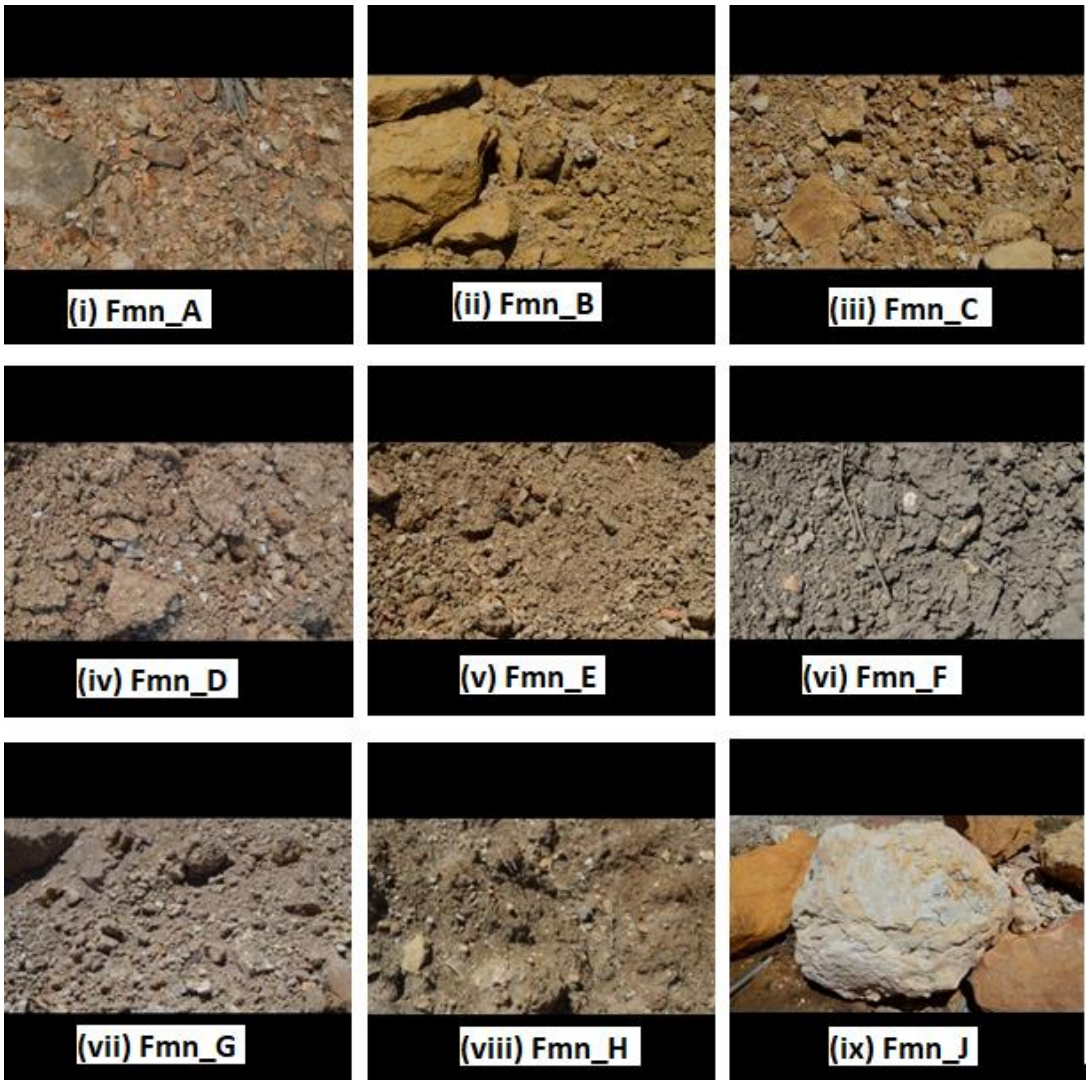

Figure 4.2. Excavation terrain object classes

The main goal of model training is to reduce the total error until model predictions are acceptable. Therefore, a high imbalance of data across object classes during training may result in a relatively-weaker classifier. To prevent such model skewing, the train data was kept fairly balanced across all 18 object classes. For each object class, the train images ranged between 115 and 120. Also, test images ranged between 15 and 20 for each of the 18 object classes.

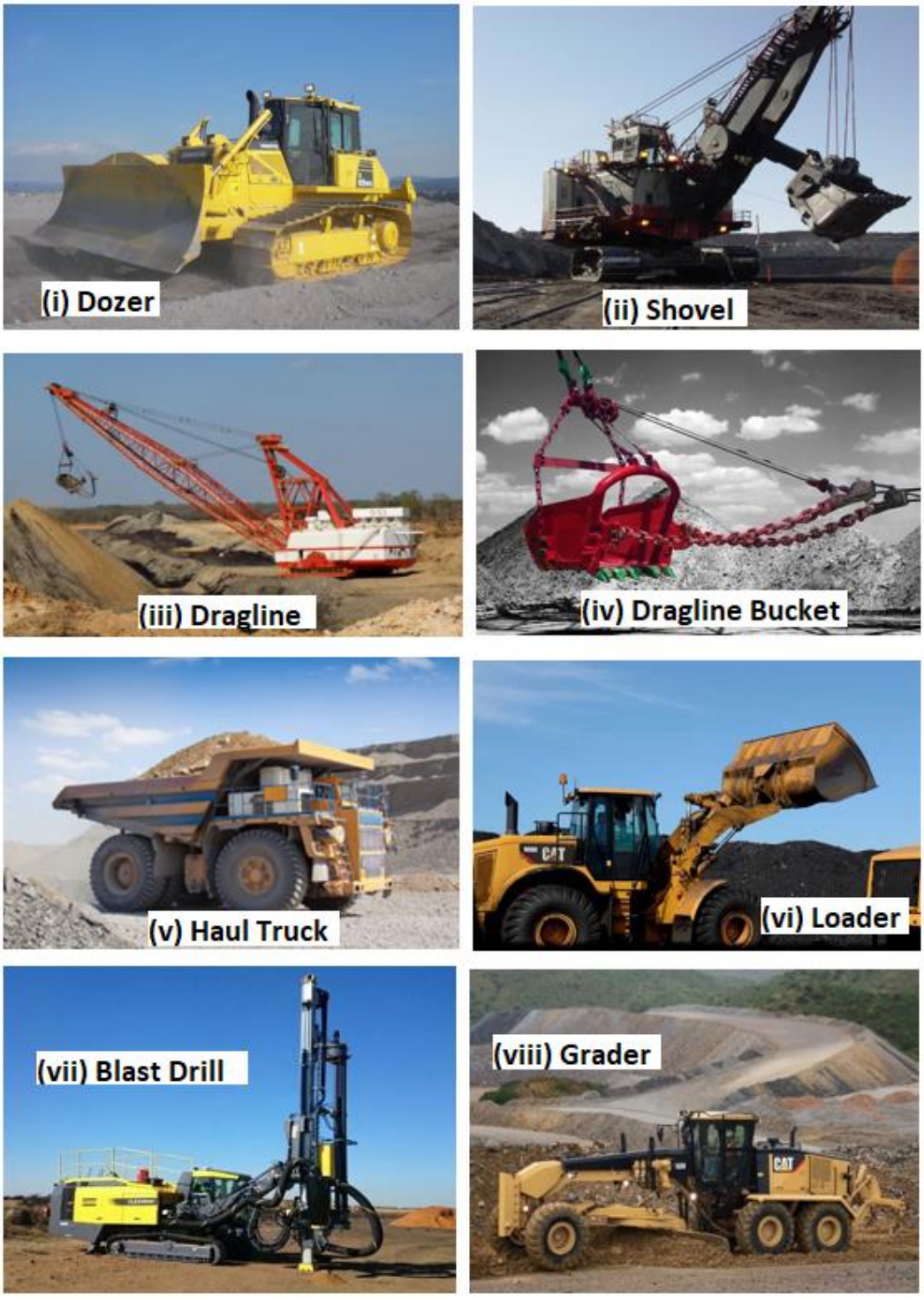

Figure 4.3. Mobile mine equipment object classes [149, 150]

The collected images, which vary in dimensions, are automatically resized during the preprocessing stage of model training. This ensures that the trained deep network model can be used on new images of variable dimension. For very robust CNN models, it is typical to use 5,000 or more images in each object class for network training. Therefore, various data augmentation techniques were used to produce an infinite dataset from the 2100 original training images.

Figure 4.4. Site personnel object class [151]

4.3. IMAGE DATA PROCESSING AND PREPARATION

4.3.1. Image Annotation. Image data was labelled using the LabelImg code by Tzutalin [152]. LabelImg is a python library that uses Qt graphical user interface to help

with image annotations. For each image in the dataset, rectangular bounding boxes are used to identify the position of all object classes within the image (Figures 4.5 and 4.6).

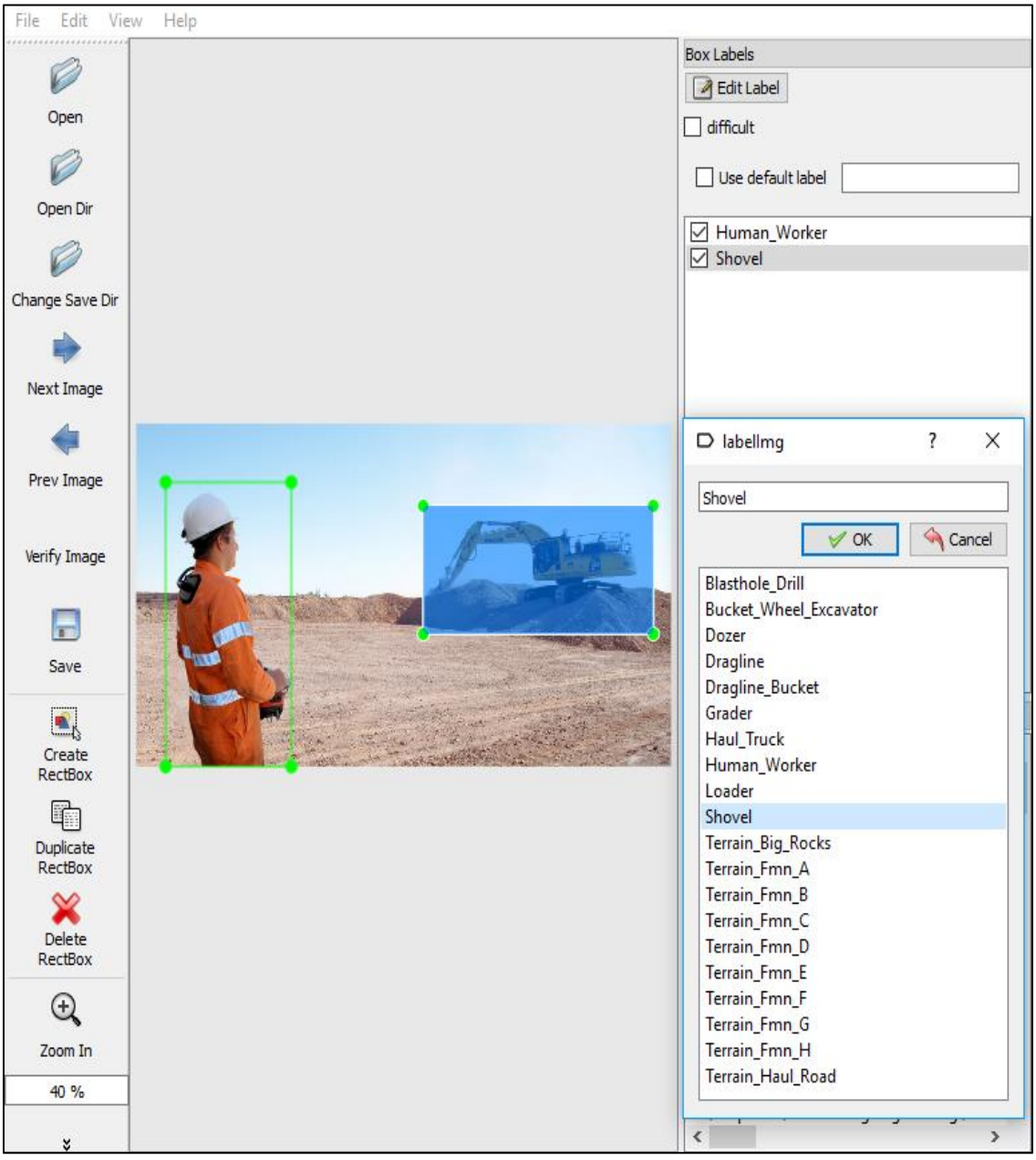

Figure 4.5. The labelImg interface

All annotations and object location coordinates are saved as Extensible Markup Language (XML) files in PASCAL VOC [153] format. Tensorflow uses the Tfrecord file format. Hence, the XML annotation files are first converted into CSV format, and then used to produce Tfrecord files using a modification of the Tfrecord-generation python code by Tran [154].

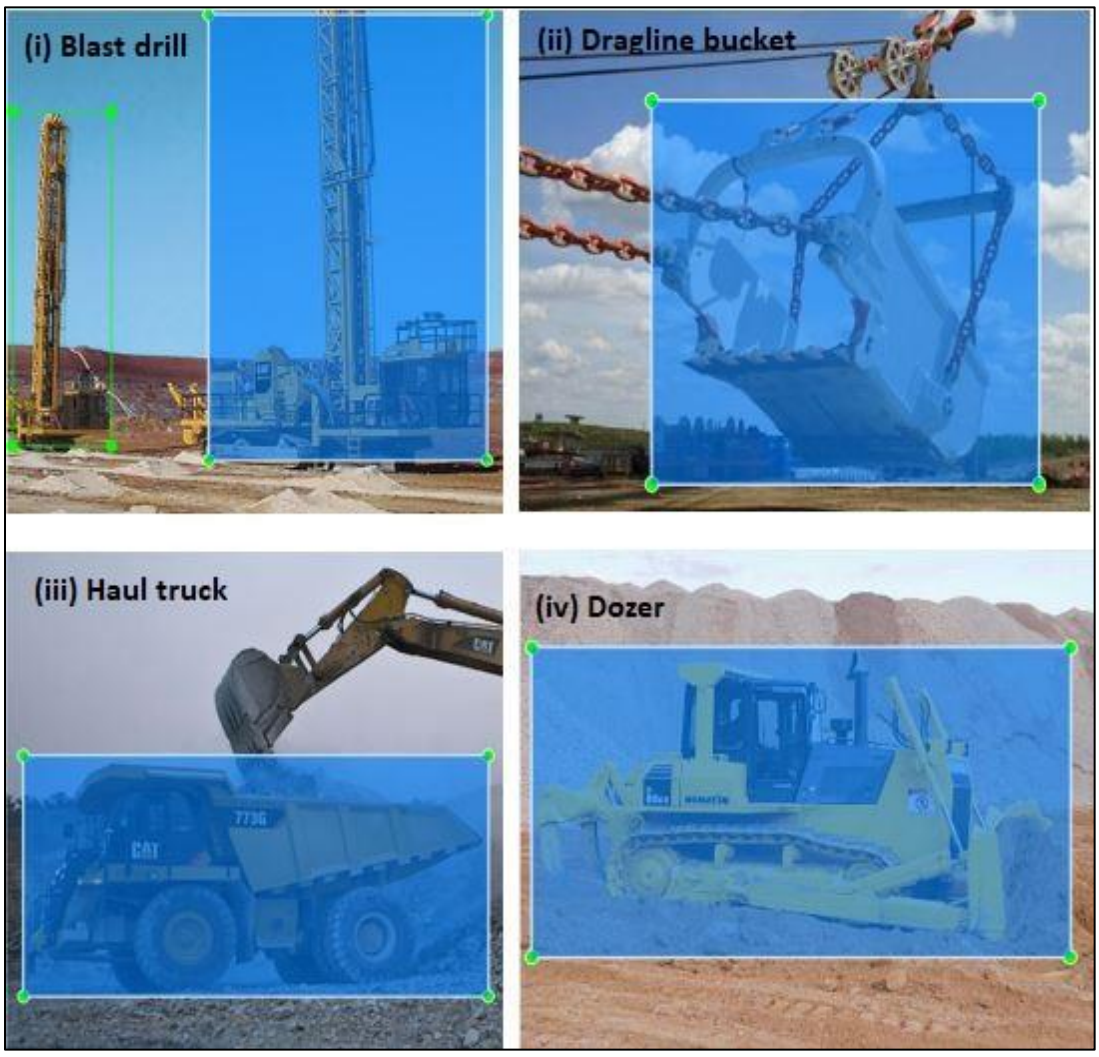

Figure 4.6. Image annotation using labelImg

4.3.2. Data Augmentation Techniques. A good machine vision model should be able to recognize and detect objects of interest under varying conditions. In neural network modeling, it is therefore critical for the training data to include all conceivable scenarios if the model is to be able to generalize well. For excavation environments, this implies that the data set must be diverse enough to capture the objects of interest under varying orientations, sizes, environmental conditions and lighting conditions, among others. Since it is almost impossible to obtain a complete dataset that encompasses all scenarios, data augmentation methods were applied to the 2100 training images as a remedy.

Data augmentation methods are image transformation processes, which are used to generate an infinite set of unique images from a small data set, by constantly and randomly varying the properties of images in the small data set. By implementing random preprocessing, new images are generated, which vary slightly from the original (Figures 4.7 and 4.8). At each iteration during model training, a random number (0, 1 or 2) of augmentation methods are picked from a finite set of augmentation techniques and randomly applied to all batch images to varying extents. The randomness of the process ensures that no two sets of input batch images are exactly the same. This augments the size of the training data infinitely and also prevents the problem of overfitting, where the network simply memorizes the data from all training scenarios.

The applied augmentation methods include image rotation, scaling (resizing), translation, horizontal flipping, vertical flipping, lighting and salt and pepper noise. For a 3-channel image, the transformation equation for noise addition is given by equation (3.1) where n_x, n_y and n_z are the noise vectors.

Figure 4.7. Some data augmentation processing

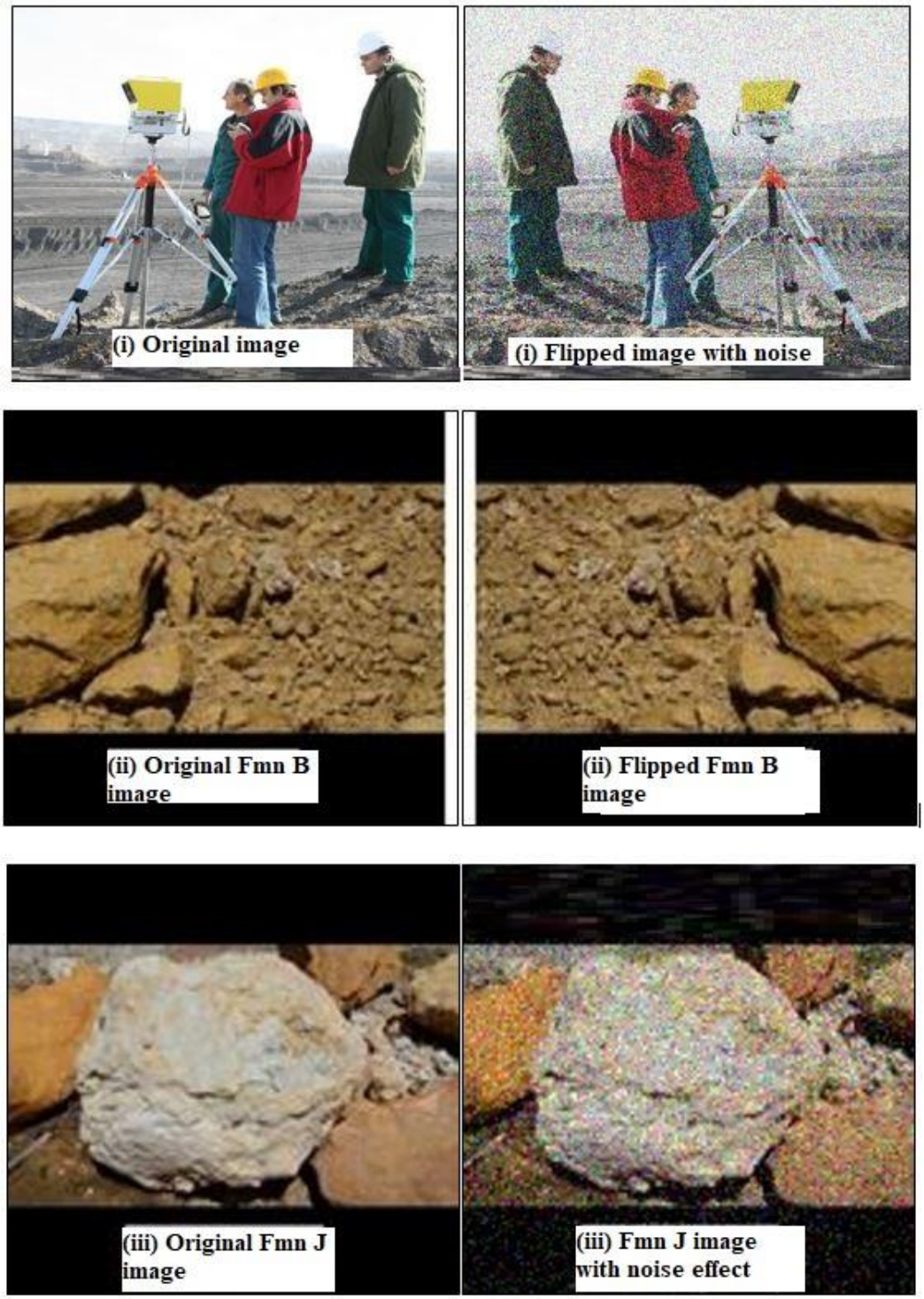

Figure 4.8. More data augmentation processing

Similarly, the scaling transformation is given by equation (4.2) where s_x, s_y and s_z are the scaling vectors. Clockwise rotations of θ degrees about the x-, y- and z- axes are given by equations. (4.3), (4.4) and (4.5), respectively. Shearing transformation is given by equation (4.6) where s_{xy}, s_{yx}, s_{xz}, s_{zx}, s_{yz}, and s_{zy} are the shearing vectors. Translation transformation is also given by equation (4.7) where t_x, t_y and t_z are the translational vectors. Reflection (flipping) transformation is given by equation (4.8).

$$(x_j, y_j, z_j, 3) = (x_i, y_i, z_i, 3) + \begin{pmatrix} n_x & 0 & 0 & 0 \\ 0 & n_y & 0 & 0 \\ 0 & 0 & n_z & 0 \\ 0 & 0 & 0 & 1 \end{pmatrix} * \sqrt{var(x_i, y_i, z_i, 3)} + mean(x_i, y_i, z_i, 3) \tag{4.1}$$

$$(x_j, y_j, z_j, 3) = (x_i, y_i, z_i, 3) * \begin{pmatrix} s_x & 0 & 0 & 0 \\ 0 & s_y & 0 & 0 \\ 0 & 0 & s_z & 0 \\ 0 & 0 & 0 & 1 \end{pmatrix} \tag{4.2}$$

$$(x_j, y_j, z_j, 3) = (x_i, y_i, z_i, 3) * \begin{pmatrix} 1 & 0 & 0 & 0 \\ 0 & cos(\theta) & -sin(\theta) & 0 \\ 0 & sin(\theta) & cos(\theta) & 0 \\ 0 & 0 & 0 & 1 \end{pmatrix} \tag{4.3}$$

$$(x_j, y_j, z_j, 3) = (x_i, y_i, z_i, 3) * \begin{pmatrix} cos(\theta) & 0 & sin(\theta) & 0 \\ 0 & 1 & 0 & 0 \\ -sin(\theta) & 0 & cos(\theta) & 0 \\ 0 & 0 & 0 & 1 \end{pmatrix} \tag{4.4}$$

$$(x_j, y_j, z_j, 3) = (x_i, y_i, z_i, 3) * \begin{pmatrix} cos(\theta) & -sin(\theta) & 0 & 0 \\ sin(\theta) & cos(\theta) & 0 & 0 \\ 0 & 0 & 1 & 0 \\ 0 & 0 & 0 & 1 \end{pmatrix} \tag{4.5}$$

$$(\mathrm{x_j}, \mathrm{y_j}, \mathrm{z_j}, 3) = (\mathrm{x_i}, \mathrm{y_i}, \mathrm{z_i}, 3) * \begin{pmatrix} 1 & \mathrm{s_{xy}} & \mathrm{s_{xz}} & 0 \\ \mathrm{s_{yx}} & 1 & \mathrm{s_{yz}} & 0 \\ \mathrm{s_{zx}} & \mathrm{s_{zy}} & 1 & 0 \\ 0 & 0 & 0 & 1 \end{pmatrix} \tag{4.6}$$

$$(x_j, y_j, z_j, 3) = (x_i, y_i, z_i, 3) * \begin{pmatrix} 1 & 0 & 0 & 0 \\ 0 & 1 & 0 & 0 \\ 0 & 0 & 1 & 0 \\ t_x & t_y & t_z & 1 \end{pmatrix} \tag{4.7}$$

$$(x_j, y_j, z_j, 3) = (x_i, y_i, z_i, 3) * \begin{pmatrix} 1 & 0 & 0 & 0 \\ 0 & 1 & 0 & 0 \\ 0 & 0 & -1 & 0 \\ 0 & 0 & 0 & 1 \end{pmatrix} \tag{4.8}$$

4.4. DRAGNET MODEL ARCHITECTURE

The CNN is implemented for model training using Tensorflow [148], which provides an interface for executing deep neural networks and other machine learning algorithms. The DragNet model consists of the following types of layers: (i) Convolutional layers (ii) Pooling layers (iii) Fully-Connected layers.

4.4.1. Convolutional Layers. Convolutional networks are deep neural networks, which explicitly assume image inputs and use convolutions instead of general matrix multiplication in one or more layers. Convolutions are a special type of linear operation [147], which transform input images into feature maps of localized regions. Each feature map is computed from the dot product of initialized weights and pixel data in a small,

local region of the image. Therefore, each map stores information about where a specific feature occurs in the image. In a typical deep network, several convolutions are performed in parallel to produce a set of feature maps using convolution filters / kernels. Each kernel detects a specific feature which may occur at multiple regions in the input image. Convolutions use weight-sharing among network neurons to reduce the overall number of parameters, which need to be trained, thereby speeding up the training process. For a two-dimensional image, $I(m,n)$, the convolution operation by a two-dimensional kernel, $K(i,j)$ is given by [147] as Equation (4.9). The i^{th} feature map output, from a convolution layer, l, is given by Equation (4.10). $n,\ {b_i}^{(l)}\ and\ {K_{i,j}}^{(l)}$ are respectively the number of kernels, the bias matrix and the kernel connecting i^{th} feature map in layer, l, and the j^{th} feature map from the previous layer $(l-1)$.

$$S(i,j) = (K * I)(i,j) = \sum_m \sum_n I(i-m, j-n)K(m,n) \tag{4.9}$$

$${O_i}^{(l)} = {b_i}^{(l)} + \sum_{j=1}^{n^{(l-1)}} {K_{i,j}}^{(l)} * {I_j}^{(l-1)} \tag{4.10}$$

4.4.2. Pooling Layers. A pooling function further modifies a layer output by performing downsampling operations along the height and width of the feature map. It shrinks the spatial size of activation maps and this reduces the number of parameters to be trained. It can be considered as the 'summary' of the representation in a small, local region of the image. The most widely used pooling functions include Max pooling, Average pooling and L2-norm pooling. The DragNet model uses the average pooling function, which simply outputs the average of the input activations. One key role of

pooling is that it introduces translational invariance into the model, which helps to prevent overfitting and creates a more robust model.

4.4.3. Fully-Connected Layers. Fully-connected layers map activation volume output from multiple layers into a class probability distribution. Therefore, it is used, together with the softmax activation function to output classification results. In the DragNet model, the fully-connected layer is defined by Tum [155] as Equation (4.11). $m_1^{(l-1)}, m_2^{(l-1)}, m_3^{(l-1)}$ denote the activation volume from the previous layer, f denotes the non-linearity function in the layer and $w_{i,j,r,s}^{(l)}$ is the weight parameter matrix. The output of the fully-connected layer, $y_i{}^{(l)}$, is always a probabilistic representation of the likelihood of each object class based on the final activation volume fed to it.

$$y_i{}^{(l)} = f\left(\sum_{j=1}^{m_1^{(l-1)}} \sum_{r=1}^{m_2^{(l-1)}} \sum_{s=1}^{m_3^{(l-1)}} w_{i,j,r,s}^{(l)} \left(Y_i{}^{(l-1)}\right)_{r,s}\right) \tag{4.11}$$

4.4.4. Activation Functions. Typically, the layers in neural networks would be connected by activation functions, which perform non-linear operations on the feature map output from one layer before it is passed on as input into the next layer. The DragNet model uses two types of activation functions: (i) Rectified Linear Units (RELUs) and (ii) Softmax functions. RELUs are used between the convolutional layers and the softmax function is used at the end of the network to output classifications. A RELU function is a piecewise linear function, which is given by equation (4.12).

$$\mathrm{Y_i}^{(\mathrm{l})} = \max\left(0, \mathrm{Y_i}^{(\mathrm{l}-1)}\right) \tag{4.12}$$

The zero lower threshold solves the cancellation problem, which arises from having both positive and negative activations. Also, RELUs are computationally efficient and result in a sparse activation volume, which increases model robustness to noise. The softmax function normalizes the output from the fully-connected layer into the 0 to 1 range such that the sum of all output units is always equal to 1. The softmax function outputs the equivalence of a categorical probability distribution, which tells you the probability by which a given image is likely to belong to any object class. For an input vector, z, with j neurons, the output of the softmax function is given by Equation (4.13).

$$S(x)_j = \frac{e^{z_j}}{\sum_{k=1}^{K} e^{z_k}} \tag{4.13}$$

4.4.5. Batch Normalization. In training deep neural networks, the distribution of input parameters for each layer relies on the parameters of preceding layers. As the parameters of the previous layer change at each iteration, the input distribution of all successive layers also change accordingly. This phenomenon is known as internal covariate shift and it makes network training tedious. It slows down the training process because each layer has to constantly adjust its parameters to a constantly-changing input distribution after each iteration.

Two ways of dealing with internal covariate shift is by using very low learning rates and by carefully choosing initial parameter values for the network. A much better approach is Batch Normalization (BN), which was proposed by Ioffe and Szegedy [156]. BN is based on the assumption that all input features are independent of one another. Therefore, it is possible to normalize each feature to have unit variance and zero mean.

Also, normalization is performed only for the input batch of a single iteration and not across the entire training data set [157].

For any given layer with n-dimensional input, $x = \left(x^{(1)} \ldots x^{(n}\right)$, each feature can be normalized as follows, using the mini-batch mean and variance Yin et al. [158] as given by equations (4.14), (4.15) and (4.16). $\bar{x}_k, \sigma_k^2 \; and \; \hat{x}_k$ are the respective mean, variance and normalized k-th feature. Similarly, $m, x_{i,k} \; and \; \varepsilon$ are, respectively, the mini-batch size, the k-th feature of the i-th sample in the mini-batch, and a small number to ensure numerical stability.

One issue that arises with BN is that, the original representation of a given layer can be lost in the normalization process. To address this problem, two learnable parameters, γ_k and β_k store the representation power of the network and they are used to scale and shift the normalized feature as given by equation (4.17). When γ_k and β_k are set to $\sqrt{\sigma_k^2 + \varepsilon}$ and $\bar{x}_k$ respectively, the original activations can be recovered.

$$\bar{x}_k = \frac{1}{m} \sum_{i=1}^{m} x_{i,k} \tag{4.14}$$

$$\sigma_k^2 = \frac{1}{m} \sum_{i=1}^{m} (x_{i,k} - \bar{x}_k)^2 \tag{4.15}$$

$$\hat{x}_k = \frac{x_k - \bar{x}_k}{\sqrt{\sigma_k^2 + \varepsilon}} \tag{4.16}$$

$$y_k = \gamma_k \hat{x}_k + \beta_k \tag{4.17}$$

4.4.6. Distance Measurement Model. The distance of objects from the dragline can be determined using the triangulation method in Figure 4.9. The method involving two cameras, fitted on the dragline. In the past, tilt sensors have been used on cranes to determine boom angle. Therefore, the inclined angles, θ_1 and θ_2, are measured from tilt sensors, which are fitted at Cam 1 and Cam 2 positions respectively. If the two cameras are a fixed distance, $\boldsymbol{x}$, apart, then the distance, $\boldsymbol{S}$, from the mid-point of $\boldsymbol{x}$ to any object of interest is given by equation (4.18).

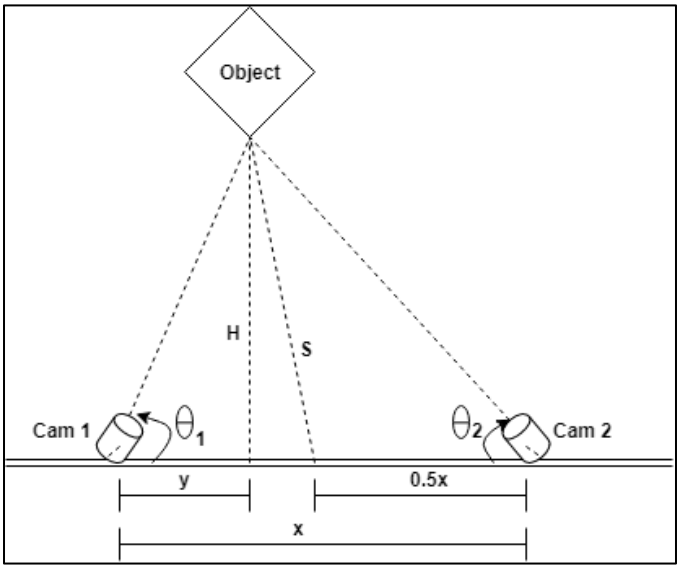

Figure 4.9. Distance measurement using triangulation

The object distance, S, is only measured when both Cams 1 and 2 are focusing at the same area on the object. This is detected using the Jaccard Index [159], also known as Intersection over Union (IoU). IoU (Figure 4.10) is used to measure the similarity between the two images within a pre-defined similarity score threshold. Mathematically, the Jaccard Index is given by Equation (4.19).

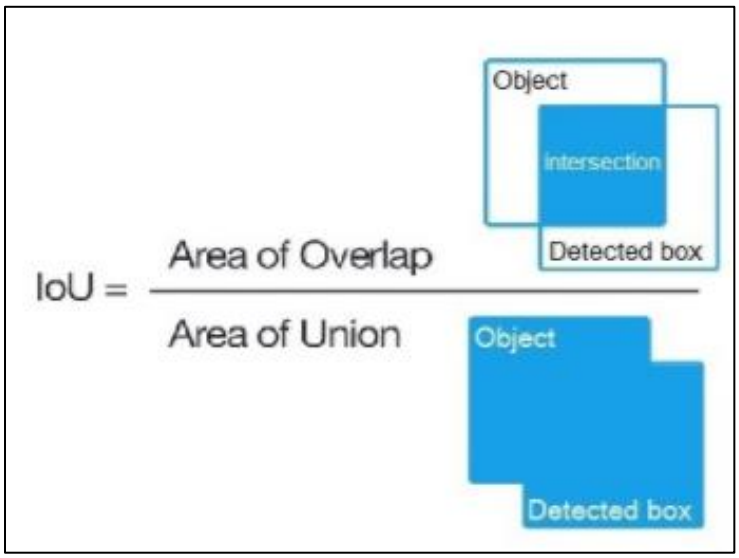

Figure 4.10. Jaccard's index [159]

$$S = \begin{cases} \sqrt{H^2 + \left(0.5x + \frac{xtan\theta_2}{\tan(180 - \theta_1) - tan\theta_2}\right)^2} & \forall\ (\theta_1 > 90^0, \theta_2 < 90^0) \\ \sqrt{H^2 + \left(0.5x - \frac{xtan\theta_2}{\tan\theta_1 + tan\theta_2}\right)^2} & \forall\ (\theta_1 < 90^0, \theta_2 < 90^0) \\ \sqrt{H^2 + \left(0.5x + \frac{xtan\theta_1}{\tan(180 - \theta_2) - tan\theta_1}\right)^2} & \forall\ (\theta_1 < 90^0, \theta_2 > 90^0) \end{cases} \quad (4.18)$$

$$J(A,B) = \frac{|A \cap B|}{|A \cup B|} = \frac{|A \cap B|}{|A| + |B| - |A \cap B|}\ for\ 0 \leq J(A,B) \leq 1 \quad (4.19)$$

4.4.7. DragNet Base Architecture. The architecture used for the DragNet model in Figure 4.12 combines the first fourteen (14) layers of the Howard et al. [160] feature extraction method in Table 4.1 with the object detection method of Liu et al. [161]. The feature extraction system consists of fourteen (14) alternating convolution, batch

normalization and Rectified Linear Unit (RELU) layers. The convolution kernels / filters are mainly $3 * 3$ in size with variable depths of 3 to 1024 and strides of 1 or 2. Where necessary, zero padding was also used to control the size of the output. The size of the feature map from any layer is computed as in equation (4.20). W, S, P, K are the input dimension, stride, padding and filter size respectively. P takes a value of 1 when there is zero padding and a value of 0 otherwise.

For a convolutional layer with filter size, $n * m$, if the input image and expected layer output have l and k feature maps, respectively, the number of learnable parameters in the layer is given by Equation (4.21). Similarly, the number of learnable parameters in the fully-connected layer is given by equation (4.22). DragNet's object detection system is based on the Single Shot MultiBox Detector (SSD) method by Liu et al. [161], which is currently one of the fastest algorithms in the field of object detection.

$$O = \frac{W - K + 2P}{S} + 1 \tag{4.20}$$

$$p_c = \big((n * m * l) + 1\big) * k \tag{4.21}$$

$$p_{fc} = (l + 1) * k \tag{4.22}$$

The SSD method uses feed-forward CNNs to generate bounding boxes and scores for the presence of object class instances. The feature extractor predicts the class labels and the object detector predicts anchor boxes at multiple scales (Figures 4.11 and 4.12). Finally, a non-maximum suppression step is used to select only anchor box detections

that achieve a pre-defined loss threshold. The DragNet model has a total of over 3.0 million parameters, which need to be properly tuned during model training.

Table 4.1. Feature extraction system

Depth	Layer Type	Stride	Filter Shape	Input Size	Parameters
1	Convolution	2	3 x 3 x 32	224 x 224 x 3	864
2	D/w Convolution	1	3 x 3 x 32	112 x 112 x 32	2336
3	D/w Convolution	2	3 x 3 x 64	112 x 112 x 64	8768
4	D/w Convolution	1	3 x 3 x 128	56 x 56 x 128	17536
5	D/w Convolution	2	3 x 3 x 128	56 x 56 x 128	33920
6	D/w Convolution	1	3 x 3 x 256	28 x 28 x 256	67840
7	D/w Convolution	2	3 x 3 x 256	28 x 28 x 256	133376
8	D/w Convolution	1	3 x 3 x 512	14 x 14 x 512	266752
9	D/w Convolution	1	3 x 3 x 512	14 x 14 x 512	266752
10	D/w Convolution	1	3 x 3 x 512	14 x 14 x 512	266752
11	D/w Convolution	1	3 x 3 x 512	14 x 14 x 512	266752
12	D/w Convolution	1	3 x 3 x 512	14 x 14 x 512	266752
13	D/w Convolution	2	3 x 3 x 512	14 x 14 x 512	528896
14	D/w Convolution	2	3 x 3 x 1024	7 x 7 x 1024	1057792
15	Avg Pooling	1	Pool 7 x 7	7 x 7 x 1024	-
16	Fully-Connected	1	1024 x 18	1 x 1 x 1024	-
17	Softmax	1	Classifier	1 x 1 x 18	-
					3185088

4.4.8. Model Training. The model training process combines two tasks: (i) classification of images into object classes and (ii) regression of bounding boxes for the correct localization of the images [160]. The objective cost function is the weighted sum of the confidence loss (conf) and the localization loss (loc). For a default bounding box with center (cx, cy), width (w) and height (h), Liu et al. [161] gives the overall objective loss function, $L(x, c, l, g)$, as Equation (4.23), Equation (4.24), Equation (4.25) and Equation (4.26). α and N are localization weight and the number of matched default boxes, respectively. The first term of the cost function is the confidence error from the classification task, which is the softmax loss over confidences (c) of multiple object classes. The second term is the localization error from the regression task, which is a Smooth L1 loss between the ground truth box (g) and the predicted box (l). The localization error is determined using the Jaccard Index in Figure 4.10, which matches the default boxes with ground truth detection for similarity measurements. The optimization method, RMS Prop, by Hinton et al. [162] was used to minimize the objective cost function. Hinton et al. [162] proposed this gradient-based method as a solution to Adagrad's diminishing learning rate problem. RMS Prop uses a quotient of an exponentially decaying mean of squared gradients to produce an adaptive learning rate. The RMS Prop optimization algorithm is shown in Figure 4.13.

$$L(x, c, l, g) = \frac{1}{N}\left\{\left(-\sum_{i \epsilon Pos}^{N} {x^p}_{ij} \log(\hat{c}^p{}_i) - \sum_{i \epsilon Neg} \log(\hat{c}^0{}_i)\right) + \alpha\left(\sum_{i \epsilon Pos}^{N} \sum_{m \epsilon \{cx,cy,w,h\}} x_{ij}^k \, \text{smooth}_{L1}({l_i}^m - \hat{g}_i{}^m)\right)\right\} \tag{4.23}$$

$$\hat{c}_i^p = \frac{\exp(c_i^p)}{\sum_p \exp(c_i^p)} \tag{4.24}$$

$$\hat{g}_j^{cx} = \frac{(g_j^{cx} - d_i^{cx})}{d_i^w}, \qquad \hat{g}_j^{cy} = \frac{(g_j^{cy} - d_i^{cy})}{d_i^h} \tag{4.25}$$

$$\hat{g}_j^w = log\left(\frac{g_j^w}{d_i^w}\right), \qquad \hat{g}_j^h = log\left(\frac{g_j^h}{d_i^h}\right) \tag{4.26}$$

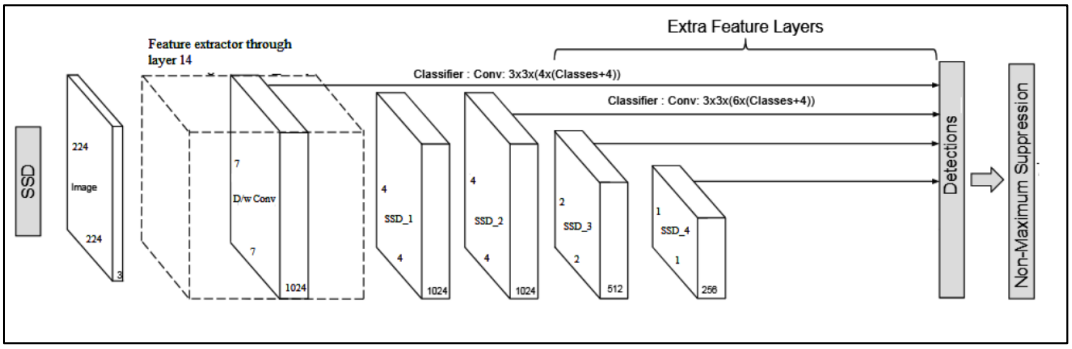

Figure 4.11. DragNet architecture

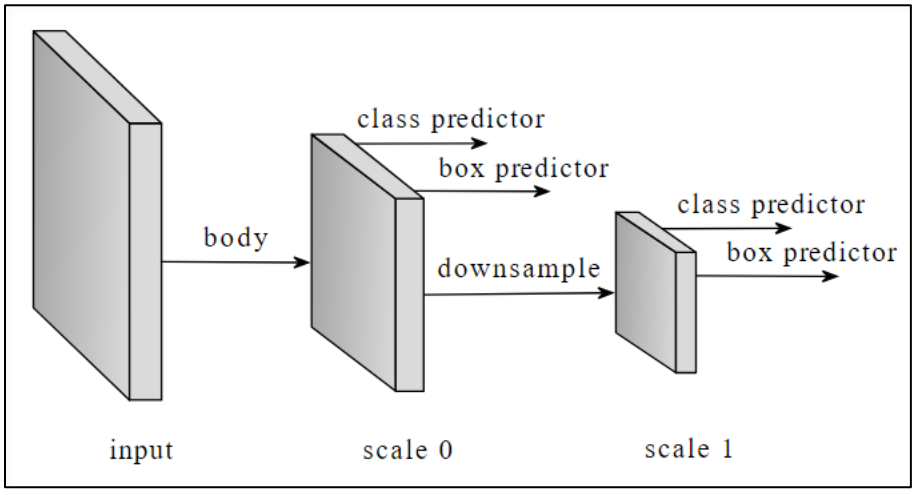

Figure 4.12. SSD principle

Require: Global learning rate ϵ, decay rate ρ
Require: Initial parameter $\boldsymbol{\theta}$
Require: Small constant δ, usually 10^{-6}, used to stabilize division by small numbers
Initialize accumulation variables $\boldsymbol{r} = 0$
while stopping criterion not met **do**
Sample a minibatch of m examples from the training set $\{\boldsymbol{x}^{(1)}, \ldots, \boldsymbol{x}^{(m)}\}$ with corresponding targets $\boldsymbol{y}^{(i)}$.
Compute gradient: $\boldsymbol{g} \leftarrow \frac{1}{m} \nabla_{\boldsymbol{\theta}} \sum_i L(f(\boldsymbol{x}^{(i)}; \boldsymbol{\theta}), \boldsymbol{y}^{(i)})$.
Accumulate squared gradient: $\boldsymbol{r} \leftarrow \rho \boldsymbol{r} + (1 - \rho) \boldsymbol{g} \odot \boldsymbol{g}$.
Compute parameter update: $\Delta \boldsymbol{\theta} = -\frac{\epsilon}{\sqrt{\delta + \boldsymbol{r}}} \odot \boldsymbol{g}$. ($\frac{1}{\sqrt{\delta + \boldsymbol{r}}}$ applied element-wise)
Apply update: $\boldsymbol{\theta} \leftarrow \boldsymbol{\theta} + \Delta \boldsymbol{\theta}$.
end while

Figure 4.13. RMS prop algorithm [147]

4.5. MODEL VERIFICATION AND VALIDATION

The experiments for model verification and validation use the data in Table 4.2 and Table 4.3. These initial parameter values were chosen based on what has been observed to perform well on other object detection tasks. A model fine-tuning experiment was later designed to further optimize the model, based on the most significant parameters. An initial model (Model 1) was developed using all the data augmentation techniques in section 4.2.2. However, the best model (Model 2) was obtained from using only a combination of horizontal image reflections (flipping), random image cropping and pepper and salt noise addition. The main idea in the model verification process was to establish that the patterns-of-interest, within the data, was being learned by the model. This was achieved using the optimization problem in equation (4.15). In order to establish that the proper model weight training was taking place, the error function was tracked over 1000 epochs and 200,000 iterations of training.

Table 4.2. Model input parameters

INPUT PARAMETERS	VALUE
Batch Normalization	
batch_norm_decay	0.9997
batch_norm_epsilon	0.001
Feature Extractor	
minimum_depth	16
depth multiplier	1.0
regularizater	L2_norm
regularization_weight	0.00004
activation	RELU
classification loss weight	weighted_sigmoid
Multi-box Detector	
similarity calculator	IOU
dropout probability	0.8
unmatch threshold	0.5
match threshold	0.5
kernel size	1
number of layers	6
minimum scale	0.2
maximum scale	0.95
aspect ratios	0.33, 0.5, 1.0, 2.0, 3.0

Table 4.3. More model input parameters

INPUT PARAMETERS	VALUE
Losses	
classification weight	1.0
localization weight	1.0
classification loss weight	weighted_sigmoid
localization loss weight	weighted_smooth_L1
Non-Max Suppression	
iou threshold	0.6
score converter	sigmoid
score_threshold	1x10**-8
max_total_detections	100
max_detections_per_class	100
Training Configuration	
train batch size	10
Training epochs	1000
optimization	RMS_Prop
learning rate	0.004
decay steps	800720
decay factor	0.95
training steps	250000
test data size	120
momentum_decay	0.9
momentum_epsilon	1.0
momentum_optimizer_value	0.9

For binary problems, random classification will achieve a loss reduction rate of about 50% on average. However, the dragline vision model is an eighteen (18) object-class problem, which places random classification performance at about 5.56% loss reduction rate. Therefore, if the minimum loss reduction rate from the model is significantly higher than 5.56%, this implies that the model is not “guessing” image classes but is actually “learning” through the training process. This would imply that the model is behaving the right way. A threshold of 70% is significantly higher than 5.56%

from random classification. Therefore, the model was considered to be sufficiently verified if the initial training error is reduced by at least 70%. For comparison, Figure 4.14 shows the training speed of both models. Model 2 trained slightly faster at about 3.0 iterations per second, as compared to 2.1 iterations per second for Model 1.

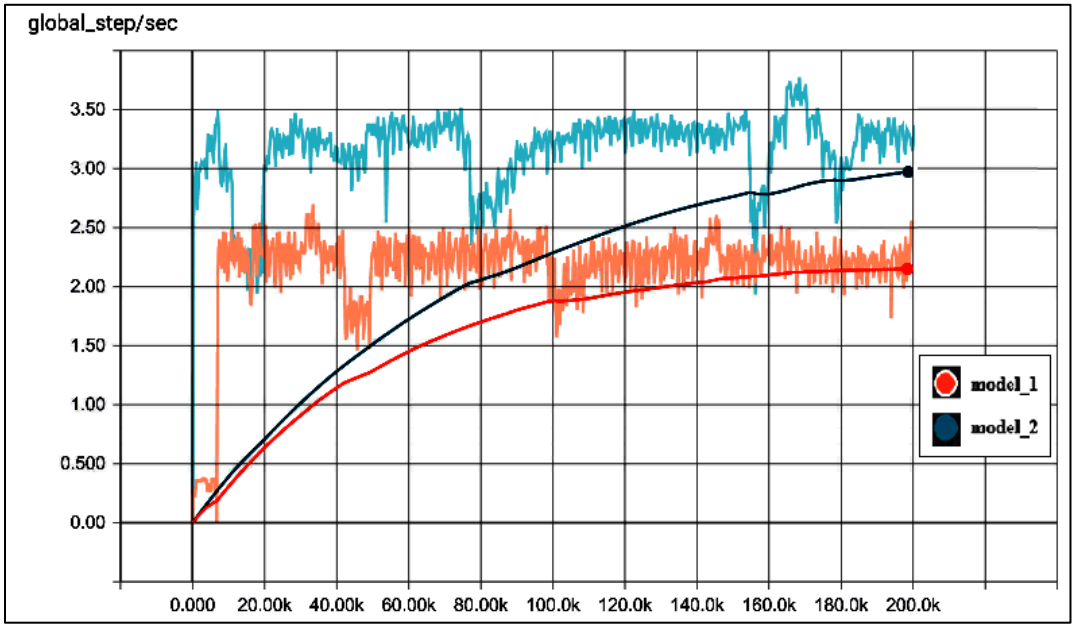

Figure 4.14. Model training speed over 200,000 epochs

From the training results in Figure 4.15, the loss function of the final model, Model 2 (as well as Model 1) dropped from an initial 75.0 to below 10.0 within the first 20,000 iterations. It then tapered off to under 1.0 over 200,000 iterations, signifying a loss reduction rate of over 98.7%, which is well above the 5.56% naïve classification rate as well as the 70% verification threshold. Therefore, the model was considered verified and acceptable.

The model validation process involved testing Model 2 on new image data sets to evaluate how well it performs using both object recognition and object detection tasks on unseen data. Figure 4.16 shows the confusion matrix from the evaluation of Model 2. In machine learning, a confusion matrix (or error matrix) is a tabular layout that is used to describe and visualize the performance of a classification model. The error matrix results shows that the model averages 82.6% classification accuracy across all 18 object classes with only 2 class accuracies falling below 70%. Also, there were only 25 no-detection cases out of a total of 288 test cases, giving the model a 91.3% detection accuracy. Generally, the model performs both classification and detection tasks considerably well. Further experimentation will investigate its suitability for real-time applications, as well as its sensitivity to certain hyper-parameters.

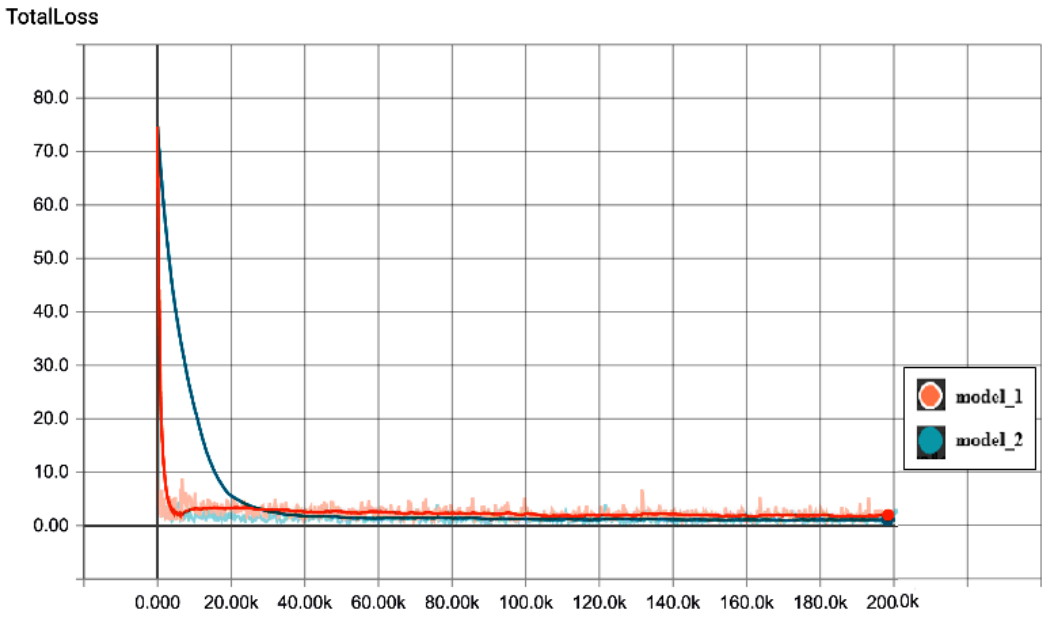

Figure 4.15. Model training results

GROUND TRUTH	MODEL PREDICTIONS																				
		Blast Drill	Dozer	Dragline	Dragline Bucket	Fmn_A	Fmn_B	Fmn_C	Fmn_D	Fmn_E	Fmn_F	Fmn_G	Fmn_H	Fmn_J	Grader	Haul Truck	Human	Loader	Shovel	Undetected	Model Accuracy (%)
	Shovel	-	-	-	-	-	-	-	-	-	-	-	-	-	-	-	-	1	22	2	88.0
	Loader	-	-	-	-	-	-	-	-	-	-	-	-	-	-	-	-	13	1	1	86.7
	Human	-	-	-	-	-	-	-	-	-	-	-	-	-	-	-	4	-	-	1	80.0
	Haul Truck	-	-	-	-	-	-	-	-	-	-	-	-	-	1	8	-	-	-	2	72.7
	Grader	-	-	-	-	-	-	-	-	-	-	-	-	-	13	-	-	-	-	2	86.7
	Fmn_J	-	-	-	-	-	-	-	-	-	-	-	-	10	-	-	-	-	-	3	76.9
	Fmn_H	-	-	-	-	-	-	-	-	-	-	1	11	3	-	-	-	-	-	4	57.9
	Fmn_G	-	-	-	-	-	-	-	-	-	-	20	-	-	-	-	-	-	-	-	100.0
	Fmn_F	-	-	-	-	-	-	-	-	-	19		-	-	-	-	-	-	1	-	95.0
	Fmn_E	-	-	-	-	-	-	-	-	10	-	5	-	-	-	-	-	-	1	-	62.5
	Fmn_D	-	-	-	-	-	-	-	12	-	-	-	-	2	-	-	-	-	-	2	75.0
	Fmn_C	-	-	-	-	-	-	19	1	-	-	-	-	-	-	-	-	-	-	2	86.4
	Fmn_B	-	-	-	-	-	8	-	-	-	-	-	-	-	-	-	-	-	1	2	72.7
	Fmn_A	-	-	-	-	23	-	-	-	-	-	-	-	4	-	-	-	-	-	-	85.2
	Dragline Bucket	-	-	-	8	-	-	-	-	-	-	-	-	-	-	-	-	-	-	1	88.9
	Dragline	-	-	8	-	-	-	-	-	-	-	-	-	-	-	-	-	-	-	3	72.7
	Dozer	-	17	-	-	-	-	-	-	-	-	-	-	-	-	-	-	-	-	-	100.0
	Blast Drill	16	-	-	-	-	-	-	-	-	-	-	-	-	-	-	-	-	-	-	100.0
																			Average:		82.6

Figure 4.16. Confusion matrix from model 2 tests

4.6. EXPERIMENTATION

Three experiments were conducted on the DragNet vision model to fine-tune some hyper-parameters and to investigate its usefulness for real-time application.

4.6.1. DragNet Hyper-parameters. The 39 input parameters, used to train the DragNet model are given in Tables 4.2 and 4.3. The values for these parameters were chosen based on domain knowledge and on parameter choices which have been

successful for similar image classification and detection problems. An experiment was designed to fine-tune three of the DragNet parameters, that typically have the most impact on performance for image detection problems. Table 4.4 shows a summary of this experiment.

Table 4.4. DragNet hyper-parameters experiment

Experiment I : DragNet Parameters	
Objective:	To investigate the effects of three model hyper-parameters on model performance.
Parameters [Scope]:	(i) Localization weight: [0.5, 1.0, 2.0] (ii) Transfer function: [RELU, RELU_6, NONE] (iii) Similarity Calculator: [IOU, IOA]
Number of experimental tests:	6
Model Training time (epochs):	50,000
Significance:	The proposed DragNet model is based on an arbitrary choice of localization weight (1.0), transfer function (RELU_6) and similarity calculator (IOU). This experiment will help to determine whether model performance will benefit from further optimization of these parameters.
Expected results:	Based on domain knowledge and previous image recognition studies, the base DragNet model is expected to perform well. However, it is unclear whether a different combination of these three parameters will yield better performance.

4.6.2. Bucket Pose Estimation. The study of dragline bucket pose estimation is significant for multiple reasons. It has been used to prevent bucket collisions on dragline swing-automated systems using image segmentation [7] as well as for quantifying payload by reducing digital images to digital terrain models in real-time during bucket

loading [35]. As previously discussed, both image segmentation and digital terrain modeling methods have major limitations in active environments where multiple objects need to be recognized in the same image sequence. Therefore, a bucket pose estimation experiment was conducted to test the performance of the DragNet perception model on a single loading cycle of dragline excavation. The model was tested on a publicly-available dragline excavation video and the video output saved. The model was evaluated based on its detection performance in the following five phases: (i) Swinging (pre-loading), (ii) Bucket loading, (iii) Hoisting, (iv) Swinging (post-loading), and (v) Dumping. The model's detection rate was then evaluated by retrieving images from the video results at 0.2 frames per second. Table 4.5 gives a summary of this experiment.

Table 4.5. DragNet bucket pose experiment

Experiment II: DragNet Application - Bucket Pose Estimation	
Objective:	To evaluate the performance of the DragNet model on bucket detection tasks
Experimental tests:	Bucket Pose Estimation: 1 test video
Significance:	The bucket pose estimation video test will evaluate the capability of the DragNet model for real-time bucket position detection through all the phases of a dragline operation cycle. Over 99.0% model performance is required for low collision / accident risk, especially during the bucket swing phase.
Expected results:	The DragNet model is expected to perform well on the bucket detection task. However, it is unlikely to meet the over 99.0% performance threshold. A more expansive data collection and extended model training will be required to exceed the performance threshold for safe operation.

4.6.3. Terrain Recognition. Up to date, the most comprehensive study involving automated terrain recognition was reported by Kim et al. [163]. However, their automated system requires a pre-planning stage during which a 3D laser scanner is used to scan the entire excavation area for obstacles and for terrain analyses. Therefore, the model is incapable of real-time application with an intelligent excavator. An experiment was conducted to evaluate the performance of the DragNet perception model for real-time terrain recognition. The model was tested on a terrain video, which contains all the nine (9) terrain classes used in the development of the model. Both classification performance and detection rate were evaluated by retrieving images from the video results at 0.2 frames per second. Table 4.6 gives a summary of this experiment.

Table 4.6. DragNet terrain recognition experiment

Experiment III: DragNet Application - Terrain Recognition	
Objective:	To evaluate the performance of the DragNet model on terrain recognition tasks.
Experimental tests:	Terrain Recognition: 1 test video
Significance:	The terrain recognition video test will evaluate the ability of the DragNet model to accurately recognize different excavation terrains and environments. The ability to differentiate between terrains, in real-time, will allow an autonomous excavator to adjust its digging strategy accordingly for optimum excavation efficiency.
Expected results:	The DragNet model is expected to perform well on terrain recognition tasks. However, it is unlikely to meet the over 99.0% performance threshold. A more expansive data collection and extended model training will be required to exceed the performance threshold for safe operation.

4.7. SUMMARY

This section describes the development of the DragNet perception model. The Convolutional Neural Network (CNN) was briefly discussed and the general pipeline for model training using CNN was explained. The image data collection, annotation and augmentation procedures were also discussed in detail. The DragNet model combines the feature extraction system of Howard et al. [160] with the Single Shot object detection method of Liu et al. [161]. The final model was verified using the change in error loss over 200,000 iteration cycles. Model evaluation showed good results with the DragNet model averaging over 80% in accuracy. Experiments have been designed to further explore the application of the model to excavation videos.

5. RESULTS AND DISCUSSION

This section discusses the results of all the experiments, outlined in the previous sections. A total of eight experimental programs were carried out, involving five bucket excavation simulation experiments and three dragline vision model experiments. The first ezperiment was conducted to evaluate the performance of the XGBoost model on a wide range of new material properties. This was done to show that the proposed XGBoost model significantly outperforms conventional curve-fitting methods. The new material properties, used in this experiment, were taken from 20% of the original data (170 samples), which had been reserved for model evaluation.

Using the same dataset, a second experiment was carried out to gain some insight into the underlying relationships between formation properties and DEM microparameters. Also, two experiments were carried out, using the bucket simulation model, to determine how some formation characteristics influence excavation performance. The formation characteristics which were considered were the formation bulk density and the material size distribution. Finally, an experiment was carried out to investigate some current theories on formation failure and material density variations during dragline operations.

For the dragline vision model, one experiment was conducted to investigate the sensitivity of model performance to three DragNet hyper-parameters. The hyper-parameters of interest were the localization weight, the activation function and the similarity calculator. Two experiments were also conducted to evaluate the performance

of the DragNet model on actual excavation automation tasks. These included a bucket pose estimation video test and a terrain recognition test.

5.1. LARGE SCALE PREDICTIONS USING THE XGBOOST MODEL

In this study, the predictive power of the XGBoost calibration model was evaluated on 170 triaxial tests. For comparison, the predictive ability of the polynomial regression model was also tested on the same data set. These new data points were not involved in the original model training. Figures 5.1 to 5.6 and Table 5.1 show a summary of the experimental results.

Table 5.1. RMSE and r-squared model evaluation results

Performance Metric	**fric**		**emod**	
	Non-Linear Regression	**XG Boosting**	**Non-Linear Regression**	**XG Boosting**
RMSE	4.0000	0.3462	2.0555	1.6072
R Squared	-43.4603	0.6670	0.2497	0.5413

Figures 5.1 and 5.2 show plots of the actual fric (μ) values from the 170 triaxial tests against fric value predictions of the XGBoost and polynomial regression models respectively. For these plots, the ideal calibration model will have a line of best fit with a slope of 1.0 and very little variance in the spatial position of data points along the line. From Figure 5.1, the results of the XGBoost model predictions demonstrate a lot of the desired outcomes. On the 170 tests, its line of best fit has a slope of 1.04. By comparison, the polynomial regression model has a slope of 0.05 (Figure 5.2).

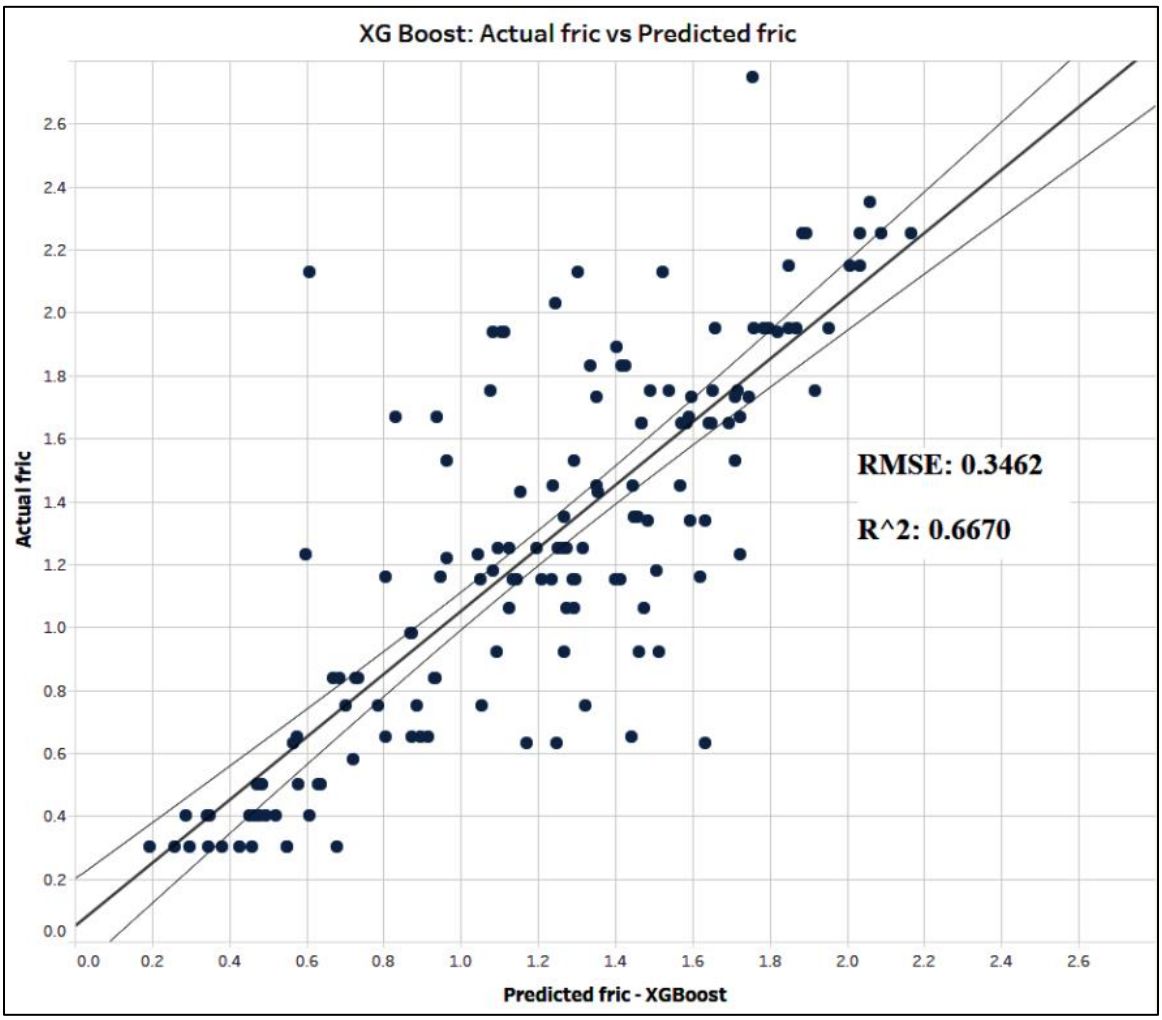

Figure 5.1. XGBoost model: fric (μ) prediction performance on new data set

Generally speaking, the XGBoost model predictions miss the actual fric values only narrowly, which is reflected in the relatively low RMSE score of 0.3462 over 170 tests, compared to an RMSE score of 4.0 in the case of the polynomial regression model. Also, the R^2 value of 0.6670 suggests that the XGBoost model is able to account for 66.7% of the variability in fric values. This is significant because, for the same data set, the more traditional polynomial regression was unable to account for fric value variability (R^2 = -43.46).

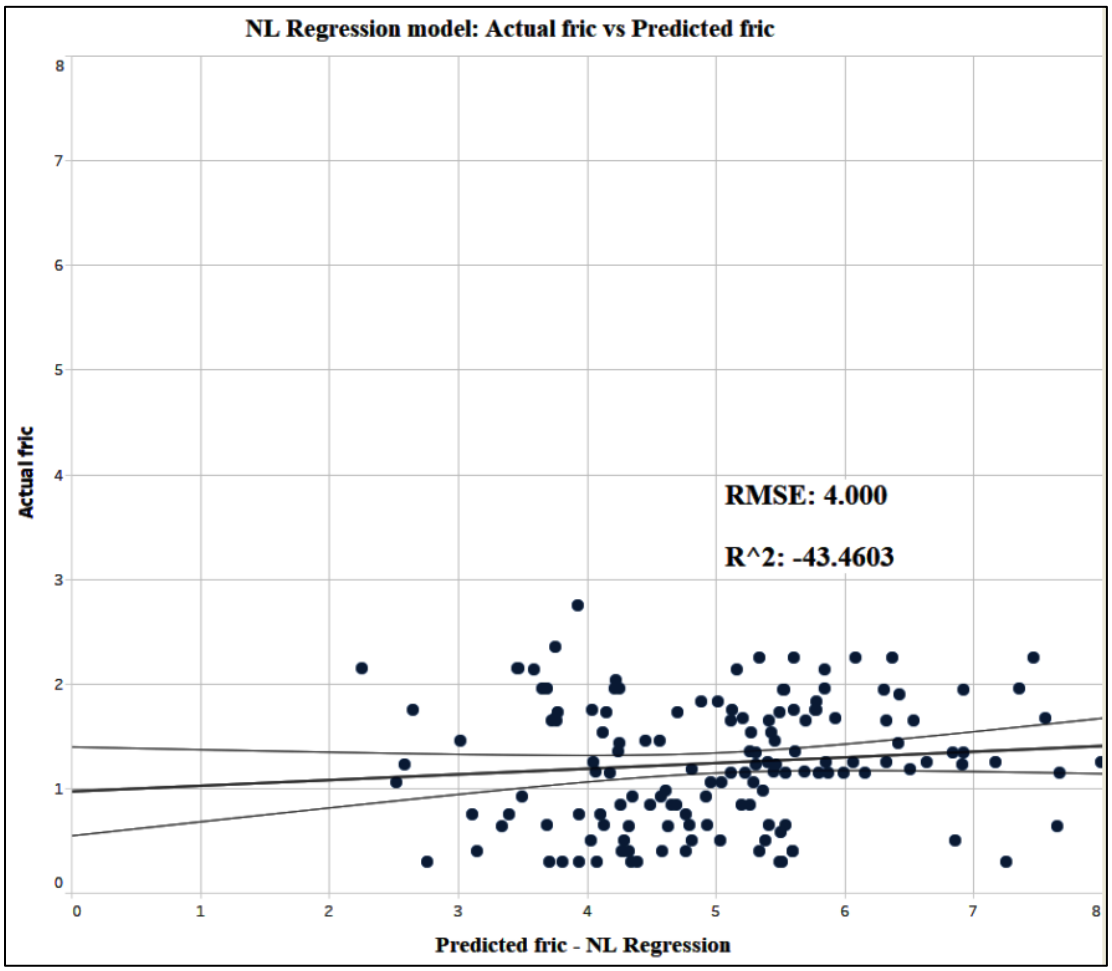

Figure 5.2. Polynomial regression model - fric (μ) prediction performance

To provide a better visual aid of model performance, the cumulative gains chart approach was implemented for both models using the 170 test results (Figure 5.3). Cumulative gains charts paint a better picture of model performance by averaging model results over a number of predictions. The chart was created by first ordering the actual parameter values in ascending order. The results are then grouped into bins of 10 successive data points. For each bin, the mean of the 10 points are plotted as a single point on the graph. This then continues progressively in increasing order up to the bin

containing the 10 largest parameter values. In simple terms, the cumulative gains chart plots the prediction performance of a model by considering the average of its predictions over a number of data points, which are very close in terms of numerical value.

The model prediction plots in Figures 5.1 and 5.2 show the actual model performance for several specific, individual cases. On the other hand, the cumulative gains chart in Figure 5.3 paints a more holistic picture of the kind of model performance which can be expected within any small range of parameter values. From the plot, it can be seen that the XGBoost model predictions closely mirror actual fric values from 0.3 to 0.55 over the first 25 bins. For fric values in the 0.55 to 1.1 range, the model only slightly over-predicts actual parameter values. From 1.1 to 1.4, the model is able to predict near-exact fric values. Finally, from 1.4 to 2.25, the model slightly under-predicts actual fric values. Generally, the XGBoost model performs significantly well across all parameter value ranges.

By comparison, the polynomial regression model significantly over-predicts fric values in all cases. Particularly, the cumulative gains chart does a very good job of exposing the limitations of the polynomial regression model. From the results scatter plot in Figure 5.2, it would seem that the polynomial regression model is able to produce acceptable predictions in some individual cases. However, when its performance in a small value range is averaged over 10 data points, Figure 5.3 shows that the average model prediction is way off the mark in all cases. Figures 5.4 and 5.5 show plots of the actual emod (E^*) values from the 170 triaxial tests against emod value predictions of the XGBoost and polynomial regression models, respectively. From the two plots, both models produce a line of best fit with slope close to 1.0 over the 170 tests. However, the

XGBoost model predictions are much closer to the actual emod values. This can be seen from the low variance in the XGBoost prediction scatter plot (Figure 5.4), relative to the high variance in the polynomial regression results (Figure 5.5).

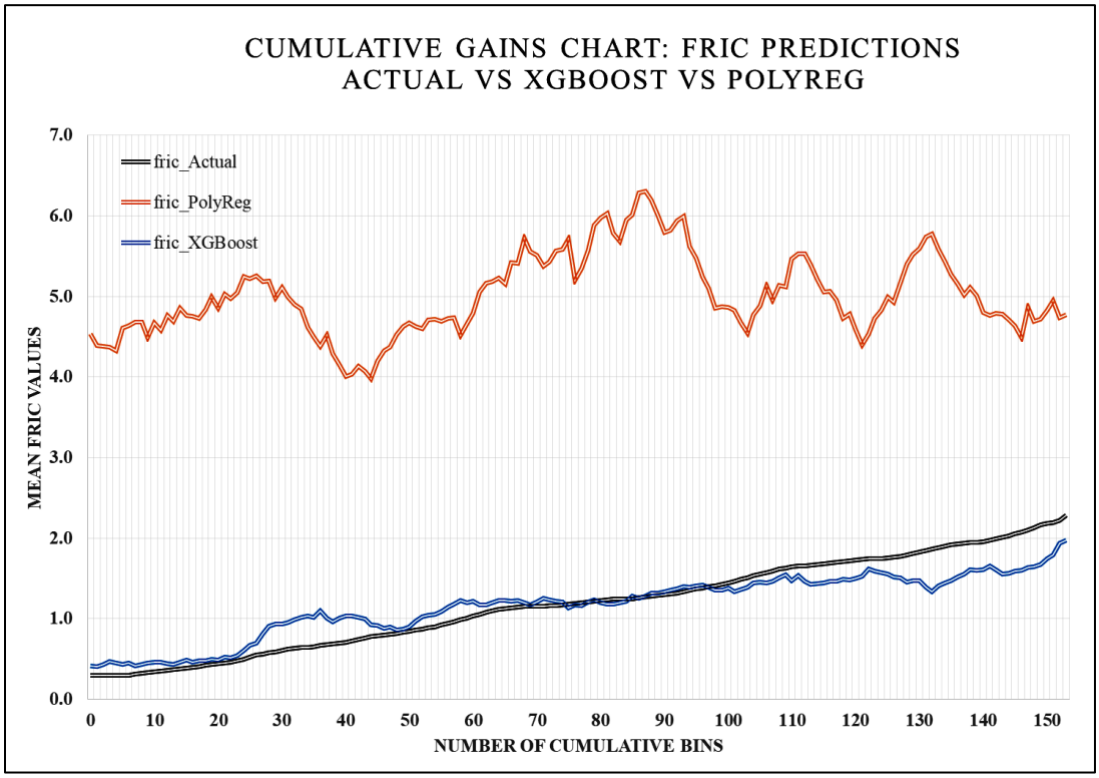

Figure 5.3. Cumulative gains chart for actual and predicted fric values

The superior performance of the XGBoost model is also reflected in the relatively lower RMSE score of 1.6072, compared to 2.0555 in the case of the polynomial regression model. Also, the R^2 value of 0.5413 suggests that the XGBoost model is able to account for 54.13% of the variability in emod values. This is significant because, for the same data set, the more traditional polynomial regression is only able to account for 24.97% of the emod value variability.

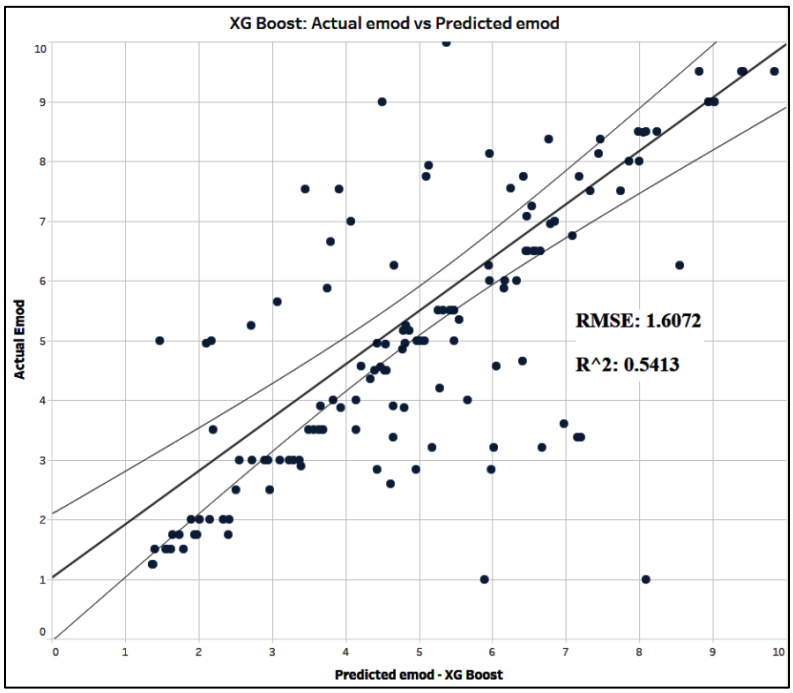

Figure 5.4. XGBoost model: emod prediction performance

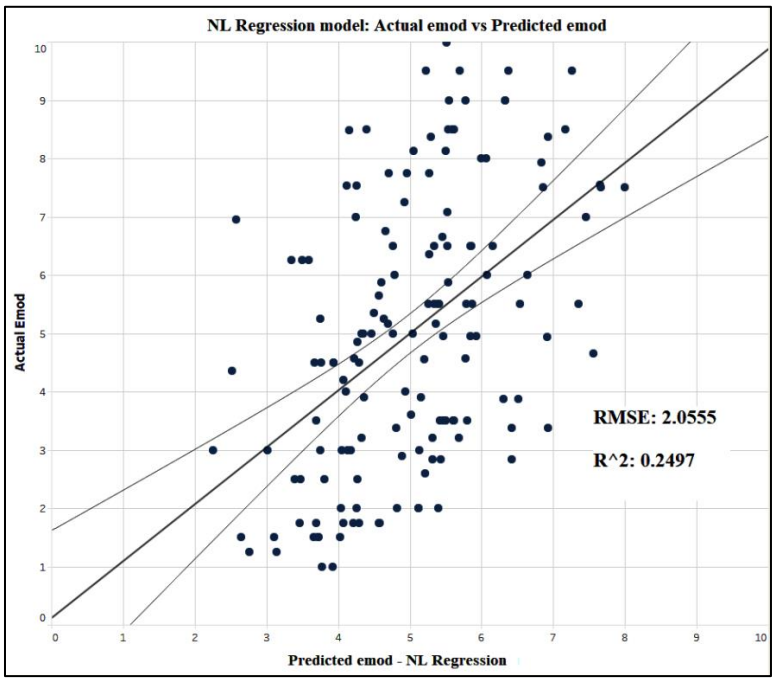

Figure 5.5. Polynomial regression model: emod prediction performance

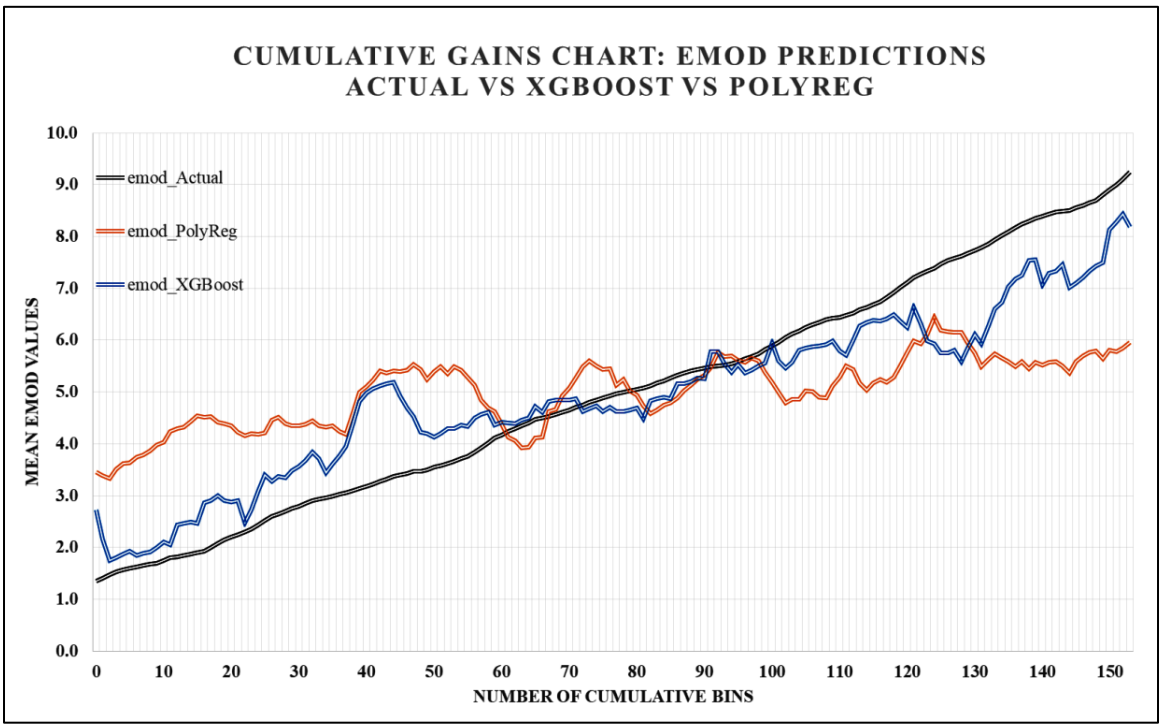

Figure 5.6. Cumulative gains chart for actual and predicted emod values

Figure 5.6 shows a cumulative gains chart, comparing actual and predicted emod values for the two models. From the plot, it can be seen both models perform sufficiently well for emod value predictions. From emod values of 1.2 to 4.2 GPa, both models over-predict actual values. However, the XGBoost model predictions are much closer to the actual values. In the 4.2 to 6.0 GPa emod range, both models closely mirror actual emod values with the XGBoost model, performing slightly better. Finally, for emod values in the 6.0 to 9.2 GPa range, both models under-predict actual parameter values. Again, the XGBoost model performs slightly better than the polynomial regression model in this range.

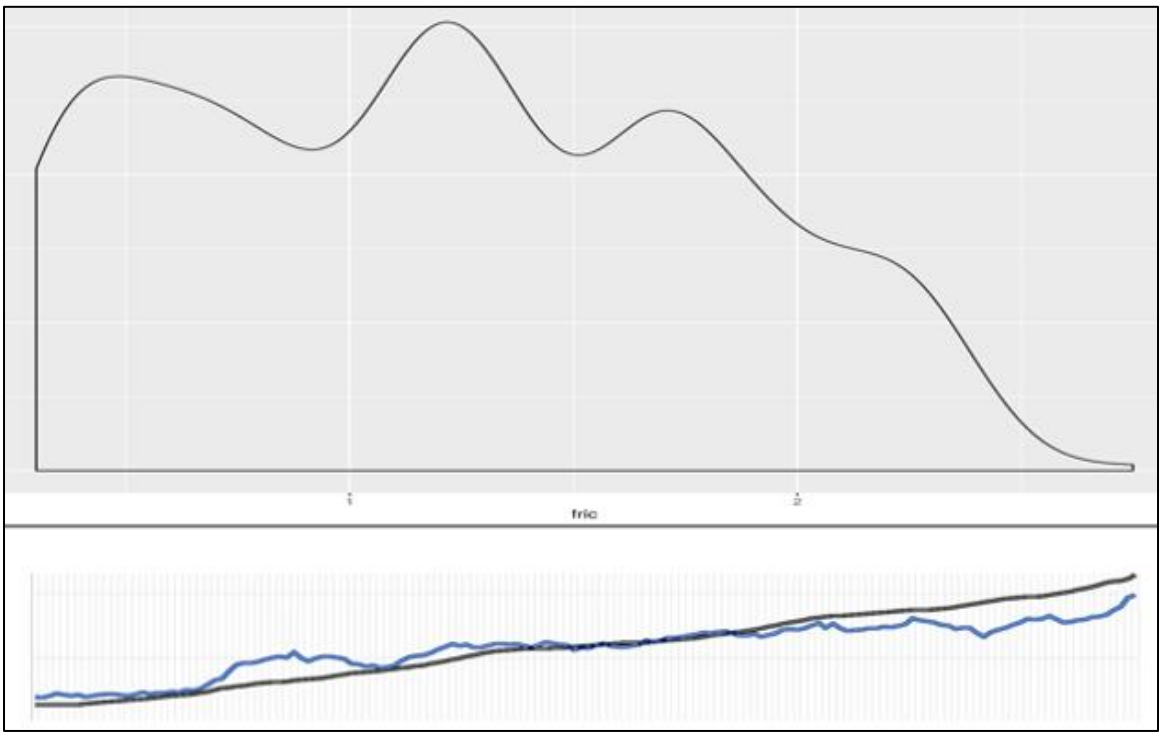

Figure 5.7. Comparison of training data and prediction performance for fric

One significant observation from the two cumulative gains charts was that the XGBoost model generally produced very accurate predictions in the middle portion of both the fric and emod data sets. A comparison between the original training data and the model prediction performance for both fric (Figure 5.7) and emod (Figure 5.8) further revealed that the distribution of the data significantly impacted the results. Generally, the best predictive performance on the test data was obtained in the value ranges, which had a lot of occurrence in the original training data. On the other hand, parameter value ranges with low occurrence in the training data set, also recorded less accurate predictions in the test data. This observation is very encouraging as it suggests that, with significantly more data and a more even train data distribution, the XG Boost algorithm can be used to train a calibration model with even more accurate predictions.

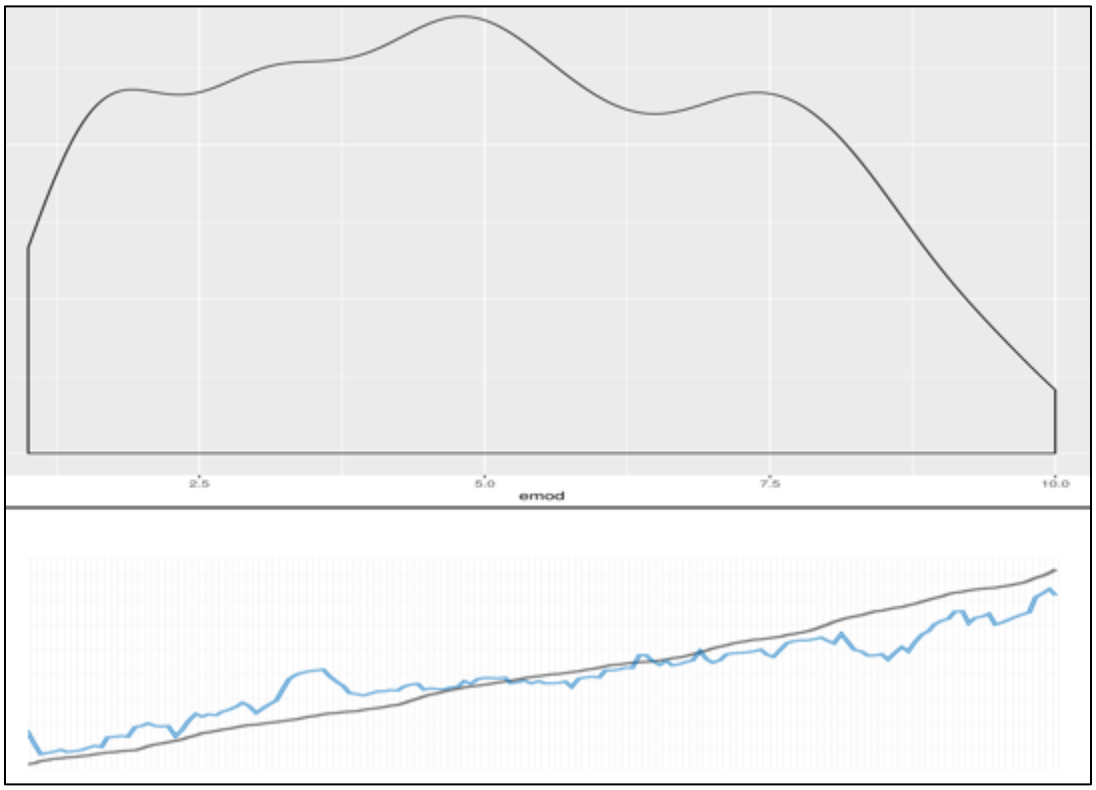

Figure 5.8. Comparison of training data and prediction performance for emod

5.2. EFFECTS OF FORMATION PROPERTIES ON DEM PARAMETERS

An experiment was carried out to investigate the effects of formation properties on the DEM micro-parameters. The relationships between DEM micro-parameters and earth material physical properties have still not been clearly defined by any previous study. While the XGBoost calibration model, proposed in this study, produces quite accurate predictions, it remains a black box approach and therefore, reveals very little about the underlying DEM parameter – material property relationships. One way to investigate these underlying relationships is through the use of partial dependence plots (PDPs). PDPs are graphical visualizations which will reveal the partial effects of a given

material property (E_{ym}, E_{sm}, v_{pr} or μ_f) on a DEM micro-parameter (μ and E^*), when all the other material properties are held constant. The R package, 'pdp', which was introduced by Greenwell [164], was implemented in RStudio to graphically examine these relationships. Figure 5.9 shows the complex relationship between the formation friction coefficient (μ_f) and DEM micro- parameters, emod (E^*) and fric (μ).

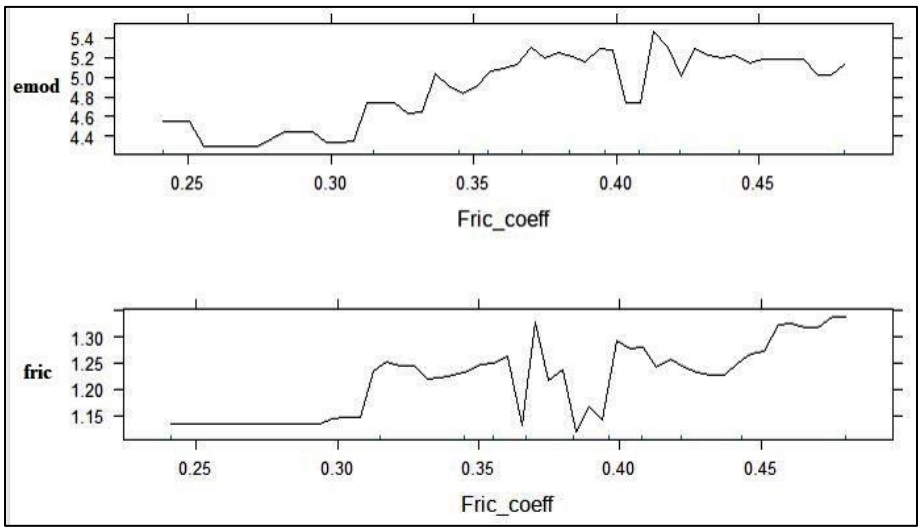

Figure 5.9. The effects of friction coefficient on DEM parameters

From the plot, both E^* and μ remain fairly constant when μ_f is in the 0.25 to 0.30 range. When μ_f ranges from 0.30 to 0.40, both μ and E^* generally rise steadily, with maximum variations of 0.15 and 0.5GPa respectively. Beyond a μ_f value of 0.40, E^* remains fairly constant whilst μ generally continues to rise. Figure 5.10 shows the effects of poisson ratio on DEM micro-parameters. From the plot, E^*rises steadily with increasing v_{pr} up to a value of -0.55, where it begins to decline steadily with some value fluctuations. On the other hand, μ generally declines with increasing v_{pr} up to a v_{pr} value

of -0.4, beyond which it remains fairly constant. Figure 5.11 also shows the relationships between Young's modulus (E_{ym}) and micro-parameters, E^* and μ. Generally, both relationships are very irregular, unpredictable and provide very little insight for future modeling.

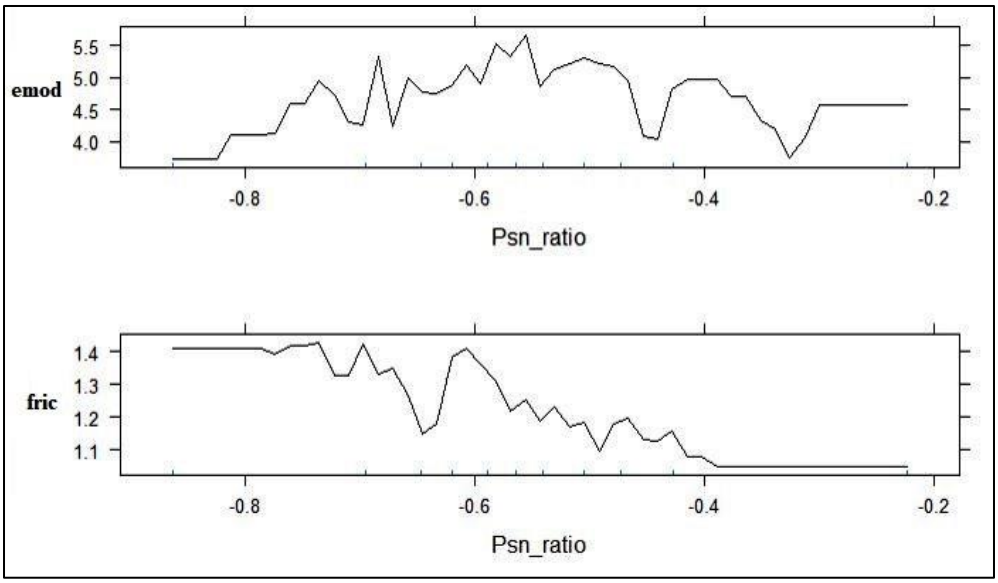

Figure 5.10. The effects of poisson ratio on DEM parameters

On the other hand, there appears to be a more well-defined relationship between E_{sm} and DEM micro-parameters (Figure 5.12). For E_{sm} values below 0.6 GPa, both E^* and μ constantly fluctuate and are unpredictable. However beyond 0.6 GPa, E^* and μ take on fairly constant values with maximum variations of 0.2 GPa and 0.2, respectively. This observation is particularly interesting because it reveals one major limitation of most previous earth material calibration studies. For both E^* and μ, two studies may arrive at different conclusions about their relationships with E_{sm}, depending on the range of E_{sm} values, which are used in each study. For example, if a study only considers E_{sm} values

between 0.8GPa and 1.4 GPa, it will be erroneously concluded that the E_{sm} relationships with E^* and μ are both linear. However, tests over a wider range of values tell a different story. This explains one limitation of the current material calibration paradigm of limited testing.

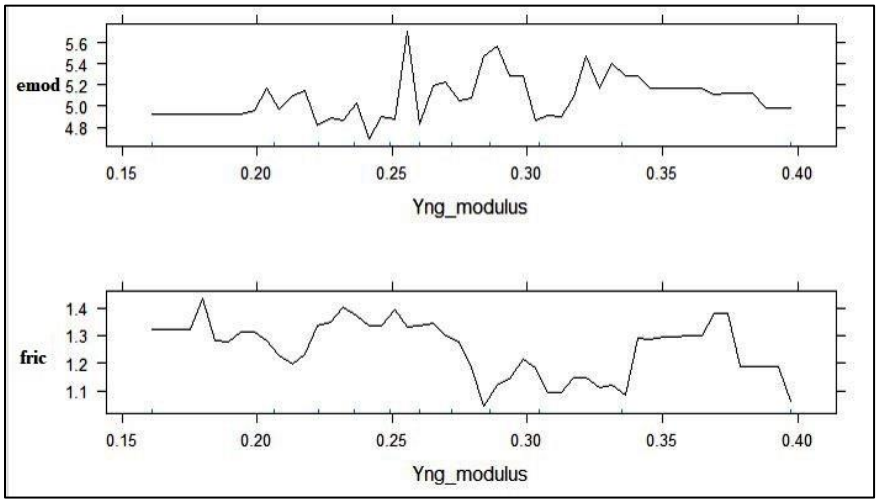

Figure 5.11. The effects of Young's modulus on DEM parameters

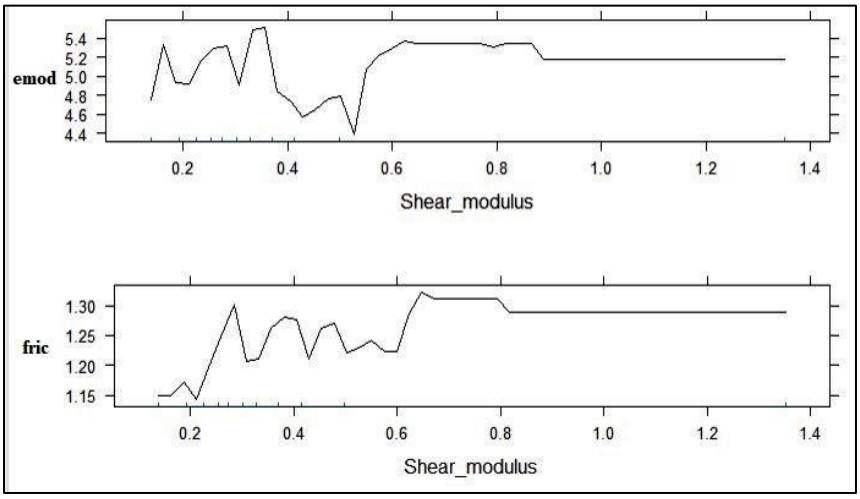

Figure 5.12. The effects of shear modulus on DEM parameters

Overall, the partial dependence plots show that the relationships between DEM parameters and material properties are neither clear nor predictable. This further emphasizes the need for calibration methods, like the XGBoost model, which are able to learn complex, abstract patterns that cannot be revealed from the data by simpler methods.

5.3. EFFECTS OF MATERIAL CHARACTERISTICS ON BUCKET LOADING

Experiments were carried out to investigate the effects of material physical characteristics on bucket loading. Two main material characteristics were considered, namely: (i) material size distribution (ii) material density

5.3.1. Material Size Effects on Bucket Loading. Figure 5.13 shows the results of material size distribution on dragline loading performance for three bucket lengths (15m) of dragging. Generally, the loading behaviors of the various material size distributions follow the expected trends. After about half a bucket length of dragging (2.5m), the formation with the smallest material size range (2.5 to 25cm) recorded the highest payload (42 tons), whilst the formation with the largest material size distribution (95 to 100cm) recorded the lowest payload (5 tons). Similarly, the initial payload for the other three tests decreased with increasing material size distributions (2.5 to 50 50cm, 20 to 25cm, and 45 to 50cm).

For granular earth materials, this observation corresponds to normal behavior. This is because finer discrete particles will generally offer less resistance to excavation, as compared to larger, blocky particles. The same trend was observed at one bucket length (5m). However, after a drag distance of 1.5 times the bucket length (7.5m), the

formation with the largest size distribution only achieves a 34% bucket fill factor (24 tons). By contrast, the other four formations achieve and exceed 100% fill factor within the same drag distance (Figure 5.14). Overall, the observations in this experiment support the theory that bucket loading behavior is strongly influenced by the material size distribution of the formation. Generally, the smaller the material size distribution, the better the loading performance.

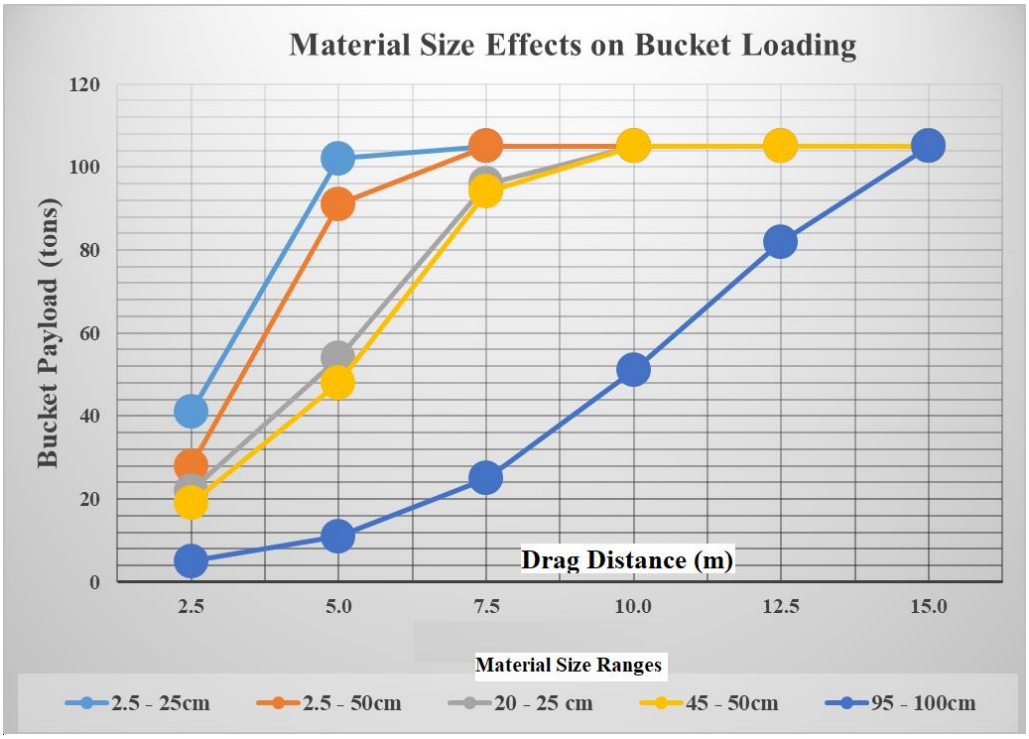

Figure 5.13. Bucket payloads for different material size ranges

For a bucket width of 3.9m, all the formations which had material sizes within 26% of the bucket width (50cm radius) were able to reach full bucket capacity in relatively the same amount of time. On the other hand, the formation with material sizes greater than the 26% threshold required considerably more time to reach full bucket

capacity. In an earlier study, Lumley [142] proposed that good blasting fragmentation is achieved when the formation consists of fines up to about 33% of the bucket width. The observations in this study generally support the assertions of Lumley [142] and show that the threshold may lie between 26% and 33%.

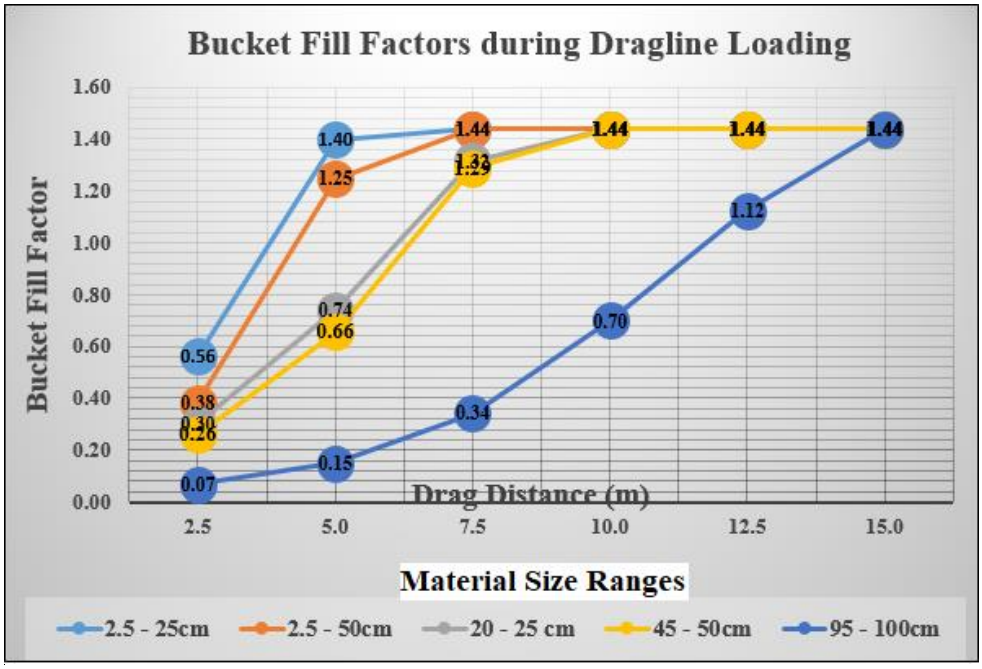

Figure 5.14. Bucket fill factors for different material size ranges

5.3.2. Material Density Effects on Bucket Loading. Figures 5.15 and 5.16 show the results from the material density experiment. From Figure 5.15, the bucket payload is strongly influenced by material density. As expected, the bucket payload, in tons, increases with increasing material density. This effect was very pronounced at lower densities (1200 to 1400 kgm^{-3}) but became less marked at relatively higher densities (1900 and 2100 kgm^{-3}). In contrast, the bucket fill factor appears to have an inverse

relationship with material density. From Figure 5.16, it was observed that the bucket fill factor decreases as the material density increases.

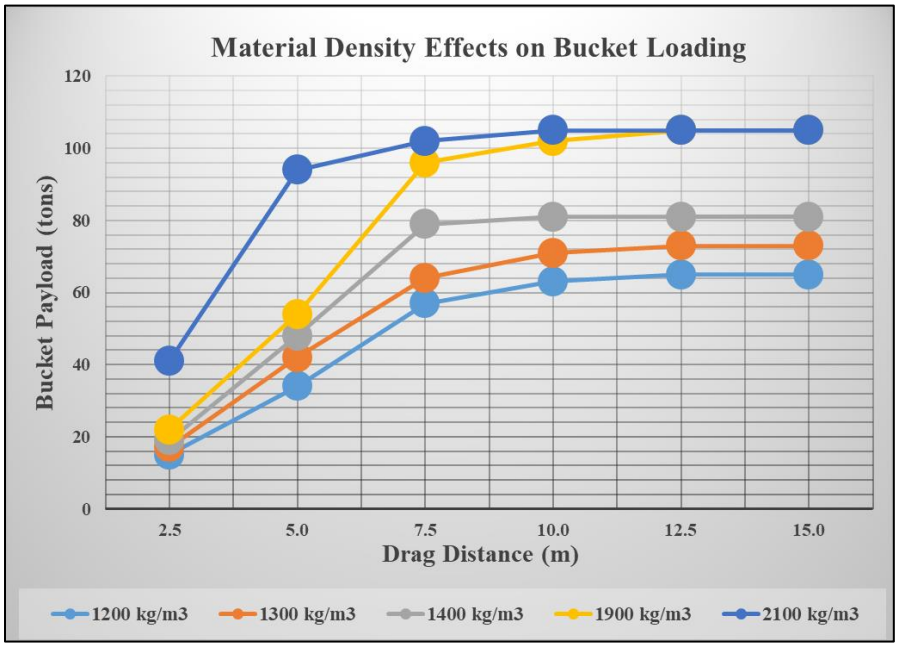

Figure 5.15. Effects of material density on bucket loading

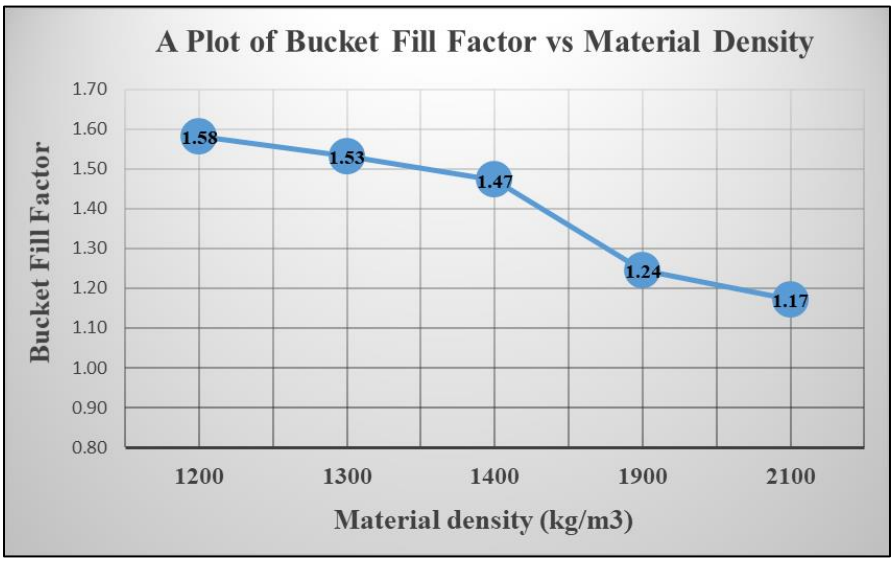

Figure 5.16. Comparison of bucket fill factors for different material densities

5.4. DENSITY ZONE VARIATIONS DURING BUCKET LOADING

An experiment was carried out to investigate the development of density zones during bucket loading, as previously reported by O'Beirne [35]. In this experiment, nine (9) density zones (Figure 5.17), both inside and ahead of the bucket, were tracked for four bucket lengths of simulation (18m). The tracking results are shown in Figure 5.18.

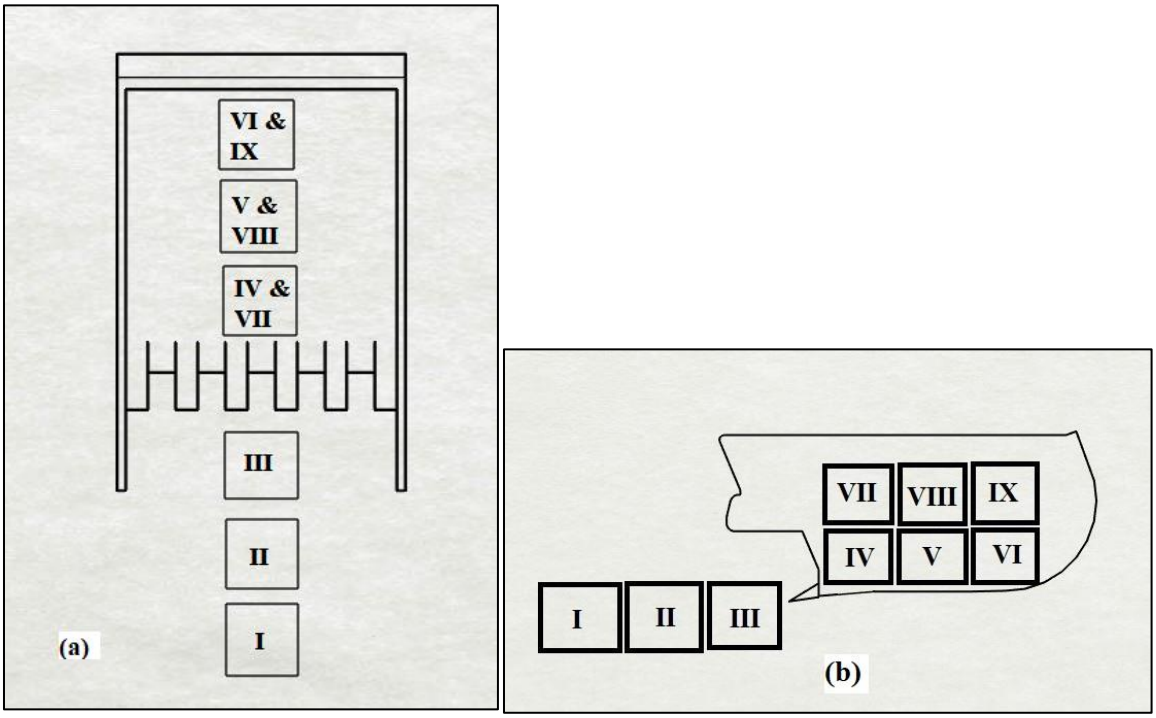

Figure 5.17. Plan and side view of density zones

From Figure 5.18, there appears to be high compression action in the three density regions ahead of the bucket (i.e. Regions I, II and III). Being 5m ahead of the bucket, Region I experiences the least impact of bucket dragging of the three regions. Starting from an initial zone density of 1.01 ton/m^3, the Region 1 density rises quickly to 1.25 ton/m^3 over 1 m of bucket dragging. This is expected behavior as the initial bucket

movement further compresses the material ahead of the bucket, thereby increasing the Region 1 density. However, the compression action reaches a threshold and the zone density is seen to plateau for the rest of bucket dragging.

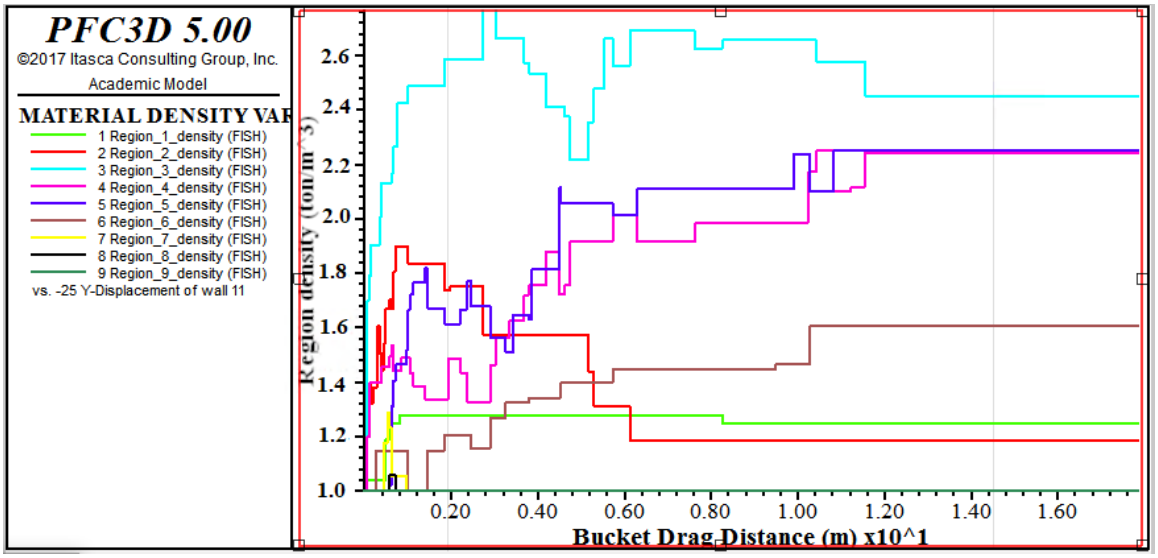

Figure 5.18. Density zones development, observed during simulations

In the case of Regions II and III, the initial material compression at the start of bucket dragging was more drastic as these zones are much closer to the bucket action. From an initial 1.0 ton/m^3 zone density, the Region II and III densities climbed rapidly to 1.9 ton/m^3 and 2.5 ton/m^3 respectively over the first 1m of bucket dragging. For Region II, which is 3m ahead of the bucket, the initial surge in zone density began to fall quickly over the next 5m of dragging, reaching a plateau of 1.2 ton/m^3 after 6m of dragging. Region III, which is 1m ahead of the bucket, experienced the highest impact of bucket dragging with a sustained zone density of 2.2 to 2.6 ton/m^3 throughout bucket dragging. Inside the bucket, the upper zones (VII, VIII and IX) experienced the least

density variations, as expected. This is because these zones are the last to fill during loading. Regions IV and V, inside the bucket, also experienced very high compression, resulting in maximum zone densities of 2.0 and 2.1 ton/m^3, respectively. However, this effect diminishes towards the back of the bucket (Region VI), where the highest density recorded was 1.4 ton/m^3.

In Figure 5.18, there appears to be cyclic changes in material density, especially in the bucket frontend zones (Regions I, II and III). This behavior is best explained by the studies of Payne [76] on wide excavation tools. As the bucket digs through the formation, a wedge-shaped block of material is formed in front of the bucket frontend and moves forward with it. Therefore, material compression increases in these zones, resulting in high local densities. However, when the material failure plane of the wedge-shaped block fully develops, the block of material collapses into the bucket. Consequently, the compression effect diminishes, leading to relatively lower local densities. The process is repeated when the next wedge-shaped block is formed, as the bucket progresses. This explains the fluctuating material densities in Figure 5.18.

During the simulation, the average material bulk density was 1.2 ton/m^3. Therefore, any region which records densities greater than 1.5 times the average bulk density, was considered a high density zone. Figure 5.19 summarizes the highest recorded densities in each zone throughout the bucket dragging. The figure confirms the existence of a material density distribution inside the bucket as initially proposed by O'Beirne [35]. It also shows that a similar density distribution develops ahead of the dragline bucket. From the observations of O'Beirne [35], the density distribution inside a fully-loaded bucket decreases towards the rear of the bucket (Figure 5.20). A similar

observation was made in the 3D simulations as the bucket rear (Regions VI and IX) recorded some of the lowest densities during loading.

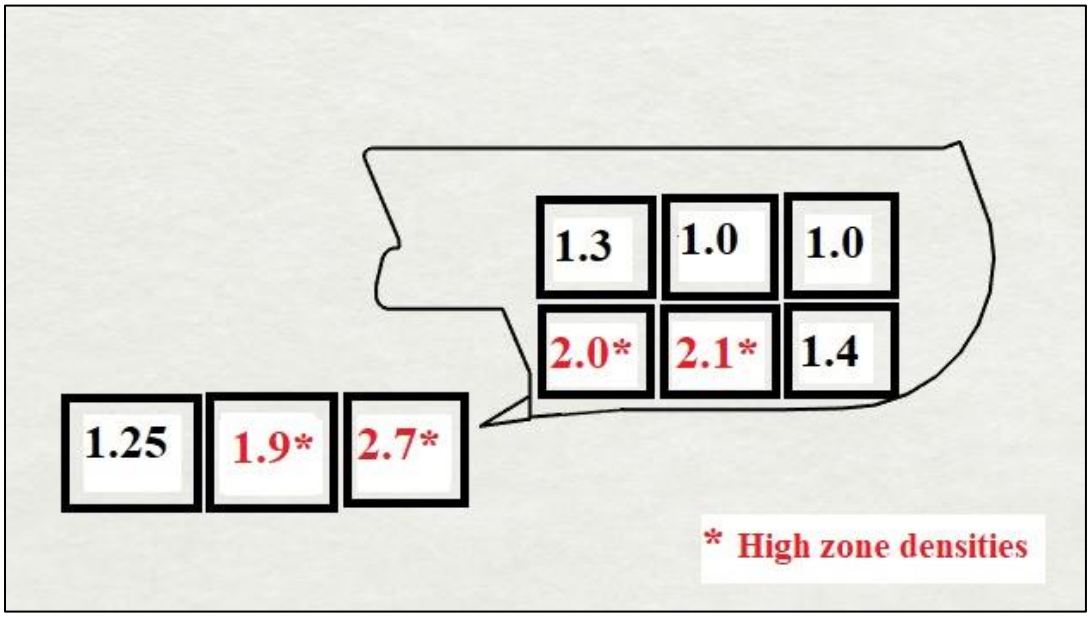

Figure 5.19. Material density variations during loading

Earlier investigators of dragline bucket filling [88, 89] observed the development of shear zones during the loading process (Figure 5.21). The observations in this experiment generally support the existence of very active zones (II, III, IV and V) along with less active zones (I, VI, VII, VIII and IX) inside and ahead of the bucket. The Shear Zone Theory suggests that the virgin and undisturbed material begins at the teeth of the bucket and extends ahead. However, the observations from this study indicate a lot of material disturbance occur ahead of the bucket teeth, especially within a distance equal to two-thirds of the bucket length (Regions II and III).

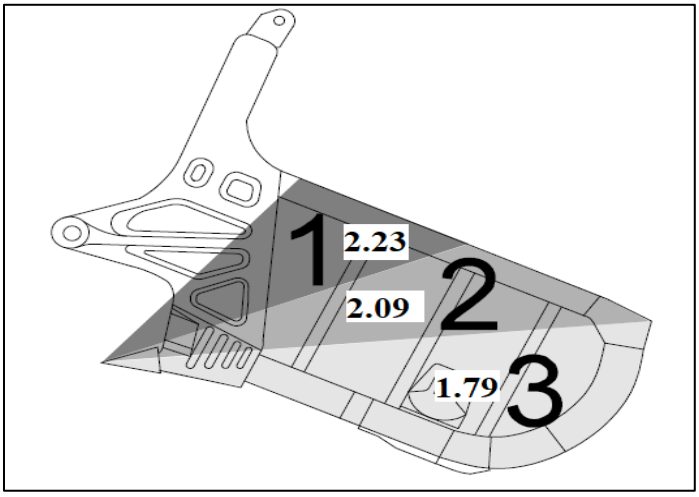

Figure 5.20. Payload zones and densities [35]

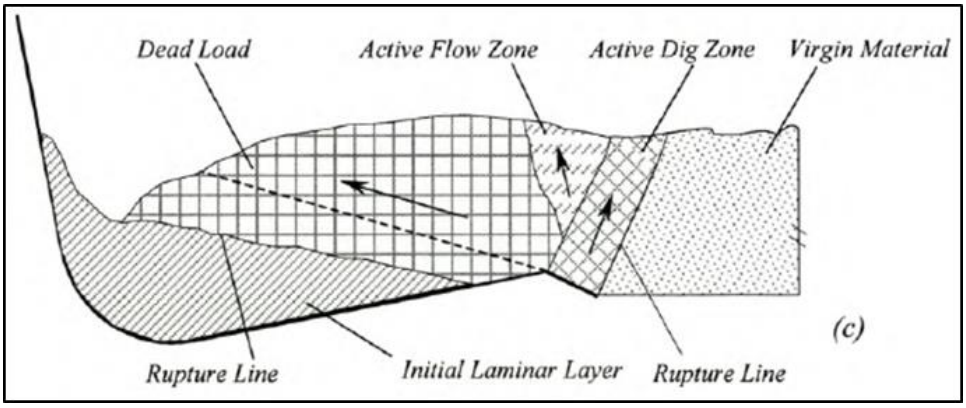

Figure 5.21. The shear zone theory [88]

5.5. INVESTIGATING EFFECTS OF MODEL HYPER-PARAMETERS

An experiment was conducted to investigate the effects of various model hyper-parameters on the performance of the DragNet model using Table 5.2. The experiment investigated the effects of three hyper-parameters: (i) the localization-classification weight ratio, α, (ii) the activation / transfer function (iii) the similarity calculator function. Figure 5.22 shows results of the localization weight experiment. From the three

tests, the highest validation error was recorded for Model_1, where the localization-classification weight ratio, α was kept at 0.5. Model_2, with an α value of 2.0, performed slightly better.

However, the lowest error was obtained in the case of the base model (Model 0), where α was kept at 1.0. This suggests that, for the current dataset, the optimum α value lies between 0.5 and 2.0, converging towards the neighborhood of 1.0. Therefore, future DragNet model improvements may focus on extensive tests within the 0.5 to 2.0 α value range. Figure 5.23 shows the results of the transfer function experiments.

From the graph, the worst model performance was from Model_4, where no activation / transfer function was used. There was very little difference in performance between the models with RELU (Model_4) and RELU_6 (Model_0) activation units. However, both activation units produced better results than when no activation function was used. In terms of the choice of activation function, the graph suggests that the base model (Model_0) is optimum since there was no real difference in performance between the RELU and RELU_6 units.

Table 5.2. Model experiments

	Model 0	**Model 1**	**Model 2**	**Model 3**	**Model 4**	**Model 5**
Localization weight, α	1.0	0.5	2.0	1.0	1.0	1.0
Transfer function	RELU_6	RELU_6	RELU_6	RELU	NONE	RELU_6
Similarity calculator	iou	iou	iou	iou	iou	ioa

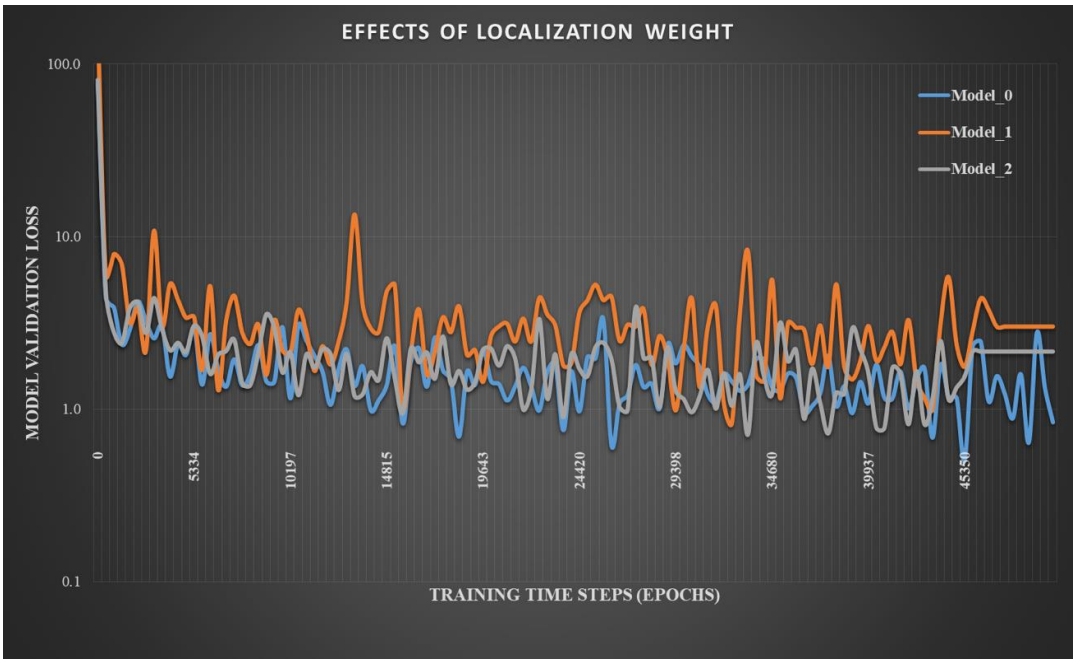

Figure 5.22. Results of localization weight experiment

Figure 5.24 shows the effect of two similarity calculator functions, IOU and IOA, on model performance. From the graph, the base model with IOU (Model_0) outperforms the IOA model (Model_5). Figure 5.25 shows the combined results of the hyper-parameter tuning experiment. Of the three hyper-parameters, the one with the least impact on model performance was found to be the localization-classification weight ratio, α. Within a 0.5 to 2.0 range, the choice of α value only slightly affected model performance. From the graph, the choice of a similarity calculator function is seen to be a bit more significant than the α value. However, the highest difference in performance, relative to the base case (Model_0), occurred with Model_4, where no activation units were used. Very drastic improvements in model performance were achieved with both RELU and RELU_6 activation units. This suggests that, the most significant impact on model performance was the choice of an activation function.

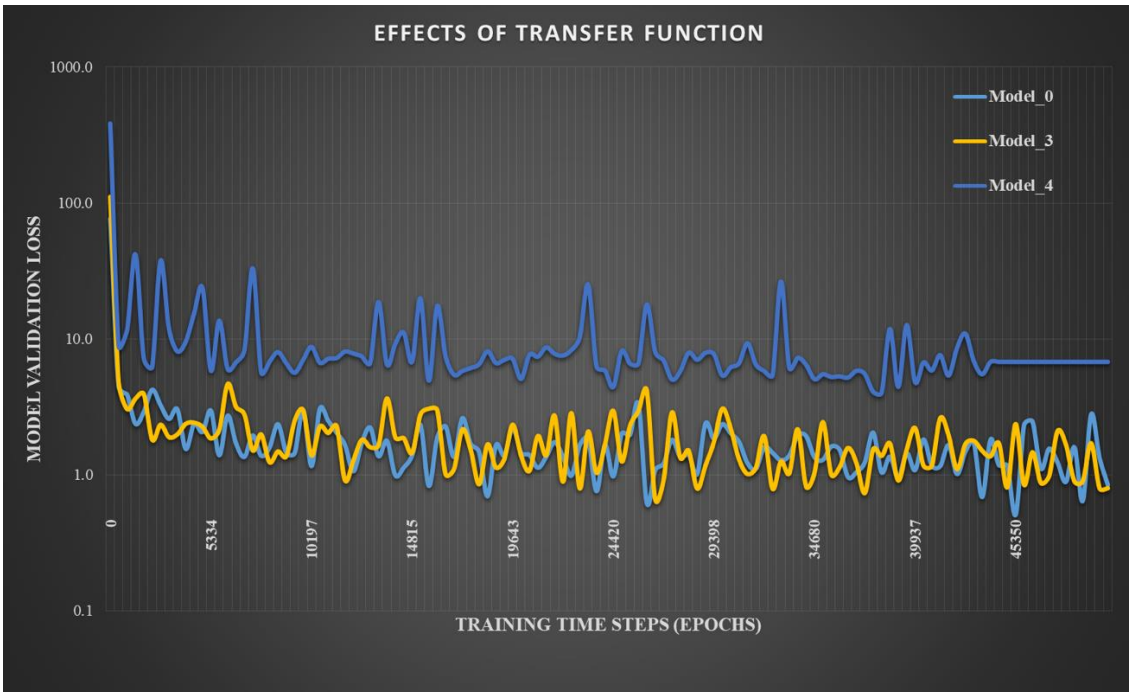

Figure 5.23. Results of transfer function experiment

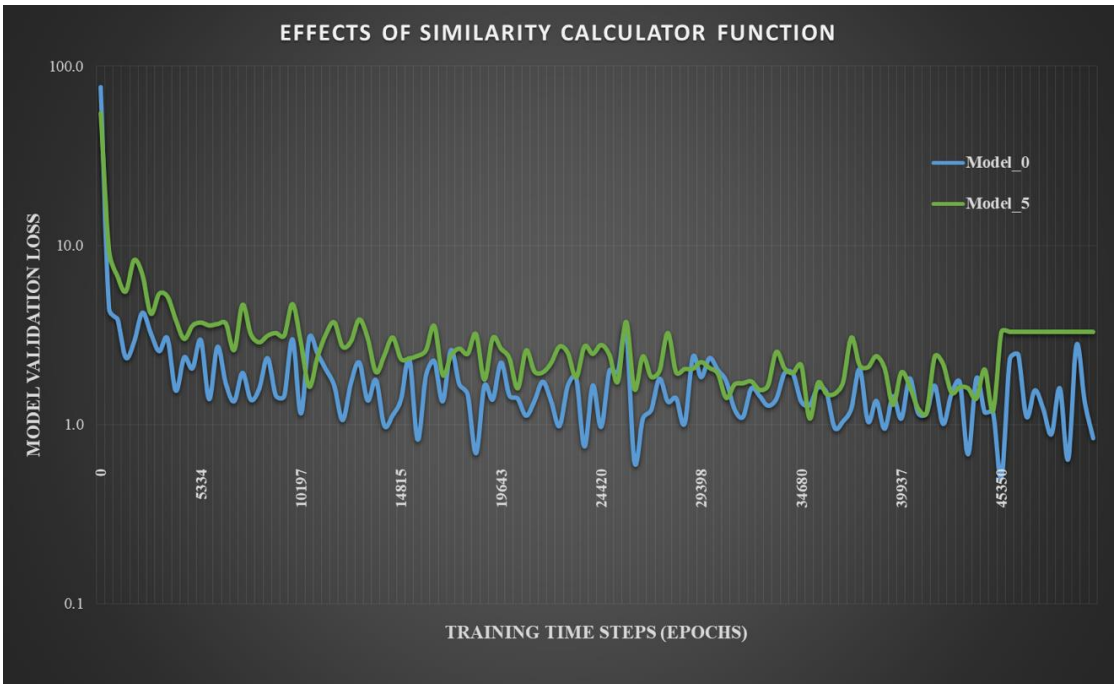

Figure 5.24. Effects of similarity calculator function

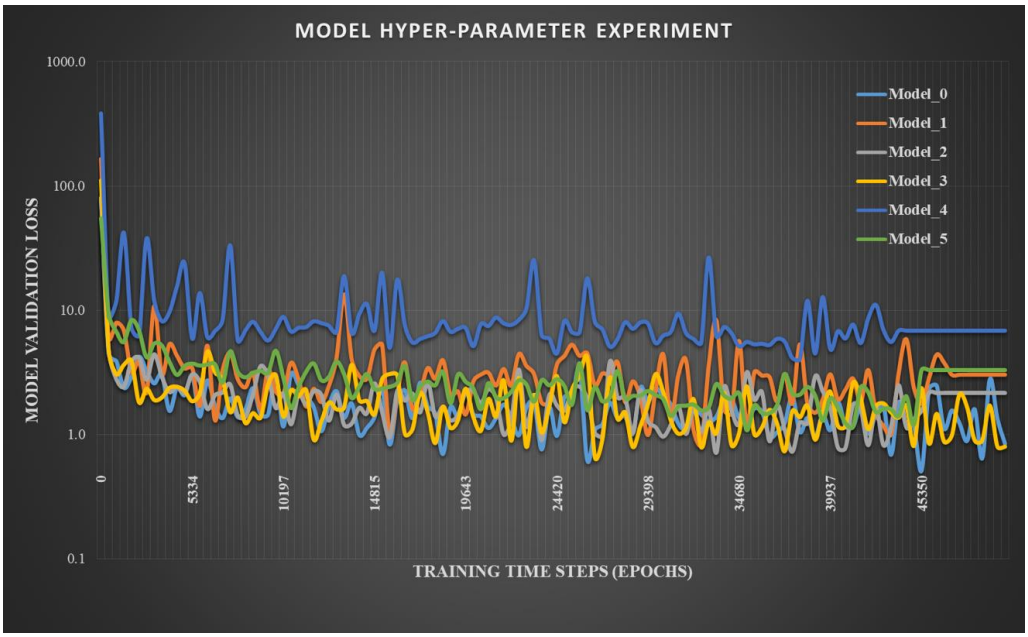

Figure 5.25. Results of model hyper-parameter tuning experiment

5.6. DRAGNET PERFORMANCE ON BUCKET POSE ESTIMATION

An experiment was conducted to investigate the performance of the DragNet model on bucket pose estimation tasks. Figures 5.26 to 5.29 show some detection results for the loading, hoisting, swinging and dumping phases respectively.

Figure 5.26. Some loading phase detection results

Figure 5.27. Some hoisting phase detection results

Figure 5.30 summarizes the detection rate results for the entire video. Perfect detections (100%) were achieved during the hoisting and material dumping phases. The lowest detection rate was recorded during the pre-loading bucket swing phase (72.62%). Interestingly, a relatively high detection rate of 90.63% was recorded in the post-loading swing phase. One possible explanation of this stark difference in swing phases performance is that the pre-loading swing phase is the only phase where the bucket has no payload material. Also, the video quality appears to be relatively poor during the swing phases (Figure 5.28) when the bucket moves a bit faster than in the other phases. From Figure 5.28, it appears that during the swing phases, the dragline bucket blends into the excavation environment and especially so, when the bucket is empty.

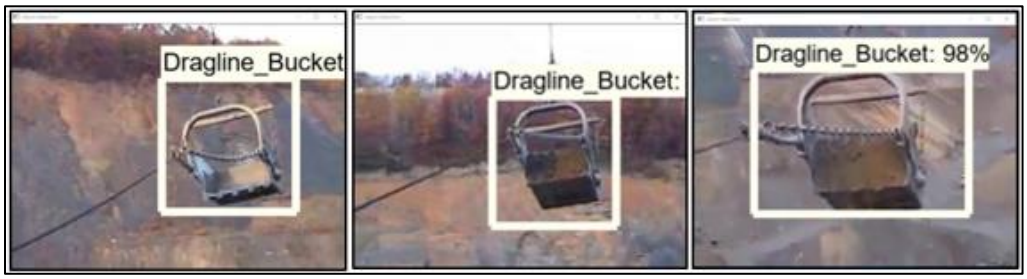

Figure 5.28. Some swinging phase detection results

A better detection rate could be achieved with better video quality and with a sharper contrast in color between the dragline bucket and the excavation environment. The loading phase recorded the next lowest detection rate of 73.33%. To an extent, this can be explained by Figure 5.26 which shows that the bucket is partially covered by the excavation material during bucket loading. From the experimental results, it is clear that bucket detection rates can be greatly enhanced by simply painting the bucket with colors, that highly contrast with the excavation environment / material. With the advent of autonomous excavation, bucket manufacturers may need to consider bucket colors, which would be easier to detect in different excavation environments.

Figure 5.29. Some dumping phase detection results

On the average, the DragNet model achieves an 87.32% detection rate across the entire video. While this can be considered very good performance, a vision model will need to achieve over 99.0% performance across all tasks for safe deployment. Therefore, future model improvements may consider including object images from a wide range of designs, colors, orientations and excavation environments.

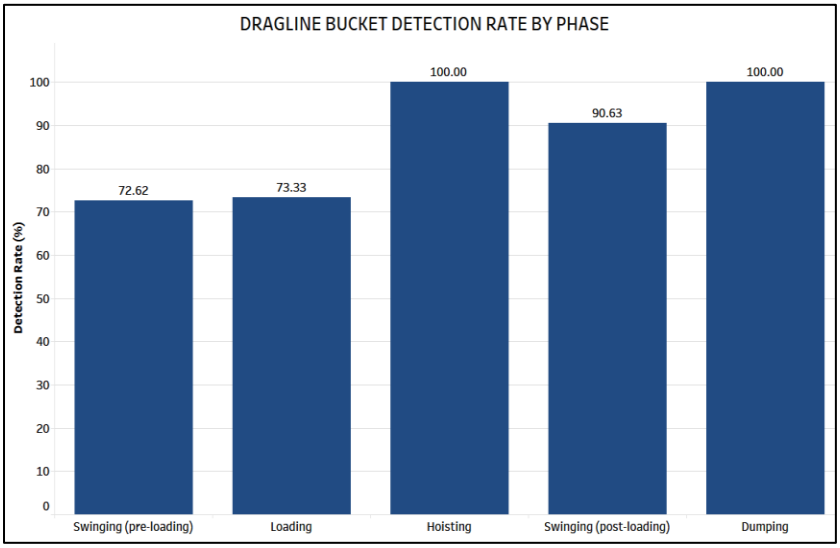

Figure 5.30. Detection rate results from the bucket pose estimation test

5.7. DRAGNET PERFORMANCE ON TERRAIN RECOGNITION

Figure 5.32 shows some correct terrain classification from the DragNet application test. Generally, the DragNet model correctly classified the terrain in most instances with a few wrong classifications. Figure 5.31 shows some of the wrong detections during the terrain recognition test. Figure 5.33 shows the DragNet model detection rate by terrain class. The model achieves very high detection generally, with relatively low rates in only two terrain classes (Fmn_H and Fmn_J). Overall, the DragNet model achieves a high average detection rate of 90.5% across all terrain classes.

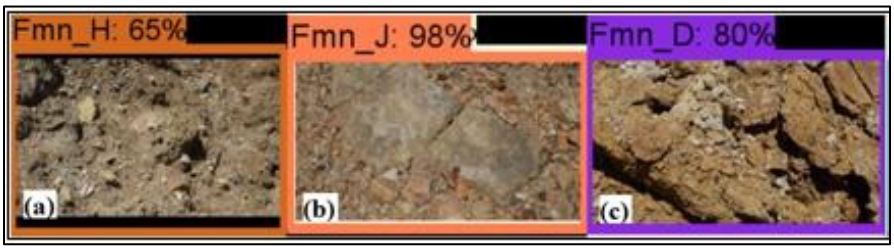

Figure 5.31. Some inaccurate DragNet terrain detections

Figure 5.34 shows a breakdown of the precision and recall performance of the model in the terrain classification task. From the results, the DragNet model achieved 100% precision and 100% recall on terrain F (Fmn_F). In simple terms, this implies that all the Fmn_F image frames in the video were correctly recognized by the DragNet model as belonging to Fmn_F (i.e. recall). Also, the model did not wrongly classify another terrain as being Fmn_F (i.e. precision). For terrains A, B, C, E and H, the model correctly recognized and classified all such image frames in the video sequence, resulting in a 100% recall for each of these classes.

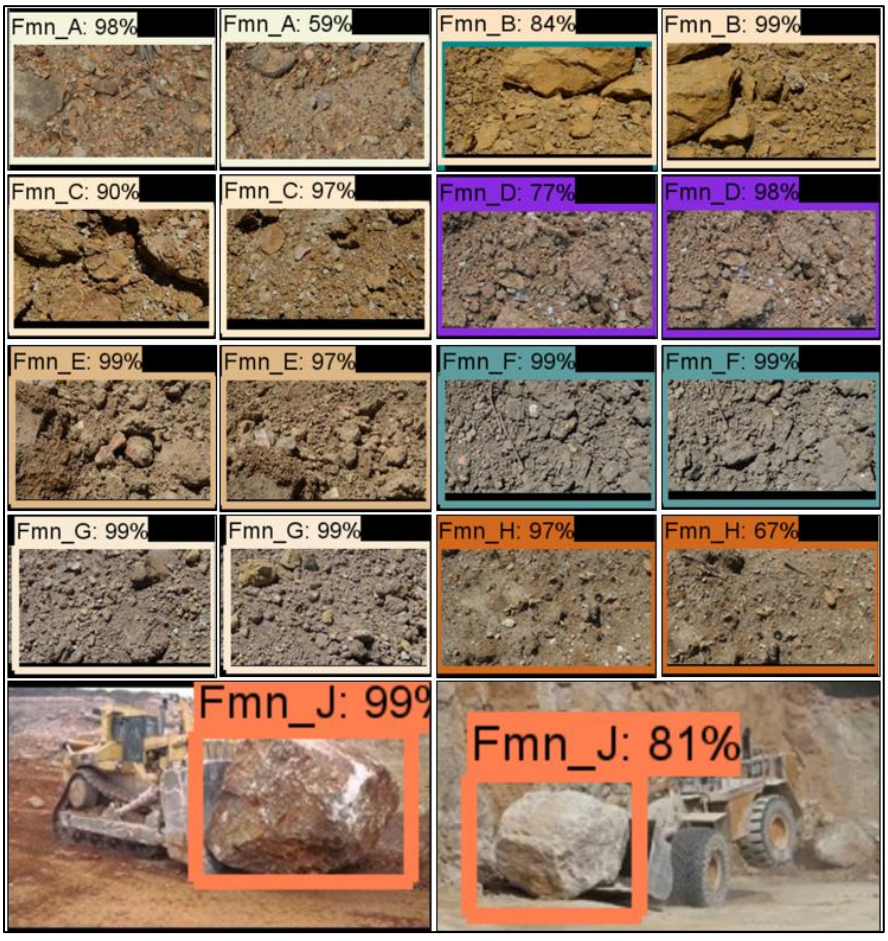

Figure 5.32. Some accurate DragNet terrain detections

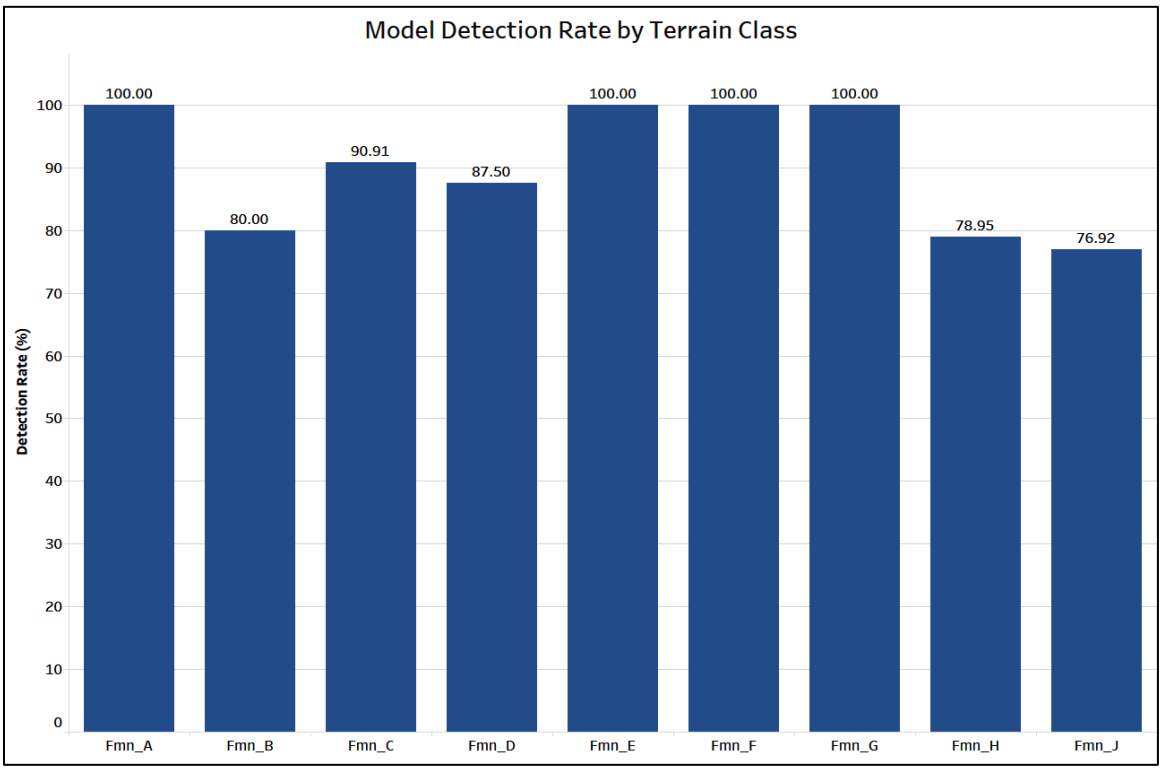

Figure 5.33. DragNet detection rate on terrain recognition video test

However, the model also incorrectly classifies images from other classes as belonging to these classes, resulting in precision rates of 58% to 85%. In the case of terrain G, the model does not correctly recognize all the Fmn_G images in the video sequence (77% recall) but it never misclassifies another terrain as Fmn_G (100% precision). The lowest model performance was recorded for Fmn_J terrain classes with both model precision and recall falling under 80%. On the average, the model performs better in recall (91.3%) than in precision (80.9%) across all terrain class predictions. Model improvement efforts may include increasing the size of the dataset as well as increasing the model training time.

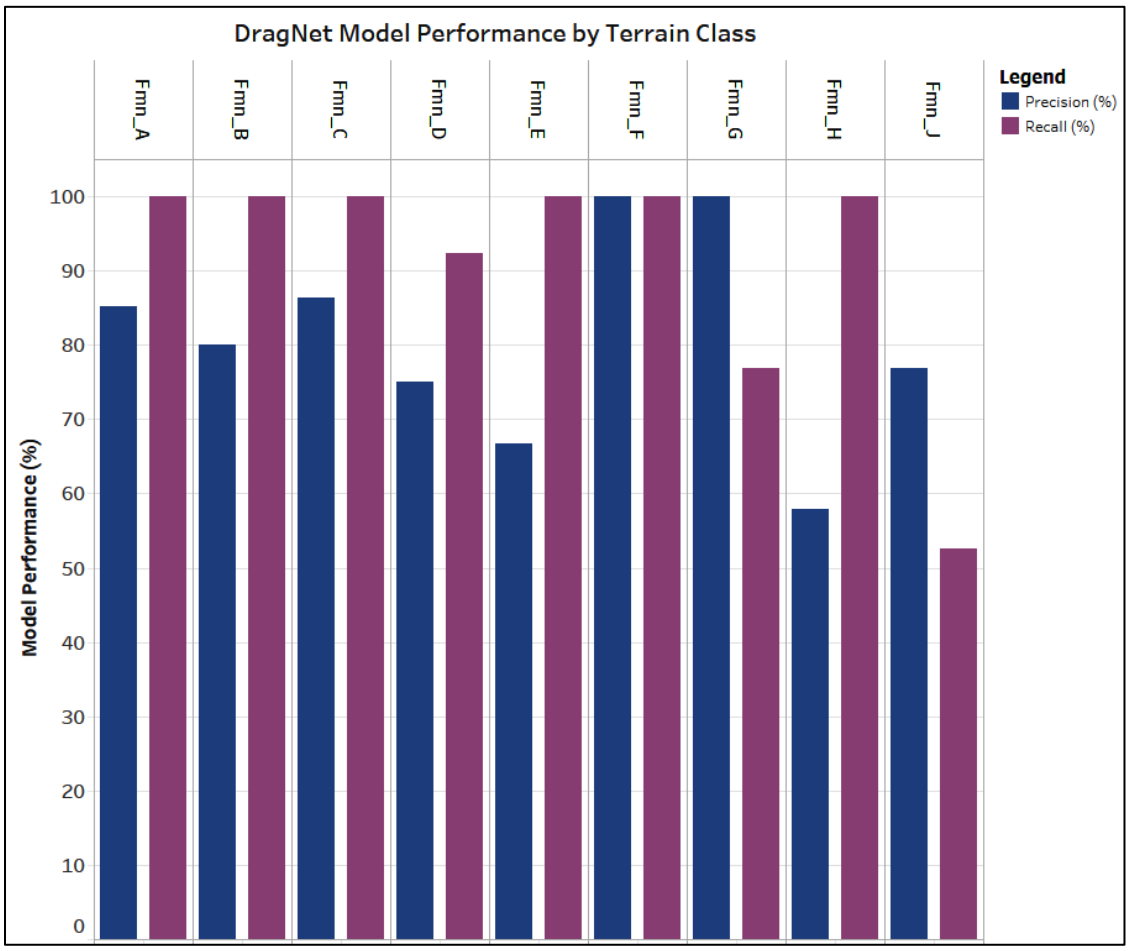

Figure 5.34. DragNet performance on terrain recognition video test

5.8. SUMMARY

This section presented the results of eight experimental programs, involving three dragline vision model experiments and five bucket excavation simulation experiments. The first experiment was conducted to investigate the effects of three DragNet hyper-parameters on model performance. The hyper-parameters of interest were the localization weight, the activation function and the similarity calculator. Of the three hyper-parameters, it was observed that the choice of an activation function had the biggest impact on model performance. On the other hand, the localization weight, α had the least

impact on model performance. Ultimately, the optimum combination of localization weight, activation function and similarity calculator was found to be 1.0, RELU_6 and IOU respectively.

Two experiments were also conducted to evaluate the performance of the DragNet model on actual automation tasks. These included a bucket pose estimation video test and a terrain recognition test. On the bucket pose estimation task, the DragNet model achieved 100% detection rates in the hoisting and dumping phases and 90.63% in the post-loading swing phase. The lowest detection rates were recorded in the pre-loading bucket swing phase (72.62%) and the loading phase (73.33%). On the terrain recognition task, the DragNet model achieves variable performance across all terrains, ranging from 55% to 100% in recall and 58% to 100% in precision. On average, the model achieves an 87.32% detection rate across all the operation phases for the bucket pose estimation task. It also achieves 91.3% average recall and 80.9% average precision for the terrain recognition task. However, further model improvements will be required to achieve the over 99.0% threshold for safe model implementation.

A total of 170 triaxial simulation tests were also conducted to evaluate the XGBoost calibration model performance on a wide range of material parameters. For comparison, the predictive performance of a polynomial regression model was also tested on the same data set. From the results, it was observed that the XGBoost model predictions closely mirror actual DEM parameters. Generally, the XGBoost model performs significantly well across all parameter value ranges. By comparison, the polynomial regression model significantly overpredicts DEM parameter values in most cases.

The 170 test data set was also used to investigate the underlying relationships between formation properties and DEM microparameters. The formation properties, of interest, included the friction co-efficient, Poisson ratio, Young's modulus and the shear modulus. Overall, the relationship between the formation properties and DEM micro-parameters was found to be neither clear nor unpredictable. For each formation property, it was observed that DEM parameter values vary only slightly locally (across a narrow value range) but highly globally (over a wide range of formation property values).

Also, two experiments were carried out to determine the effects of formation characteristics on excavation performance. The formation characteristics which were considered were the formation density and the material size distribution within the formation. Material density was found to correlate directly with bucket performance. It was also observed that bucket loading behavior is strongly influenced by the material size distribution of the formation. Generally, the smaller the material size distribution, the better the loading performance. However, for optimum bucket performance, material size should be kept between 1% to 26%.

Finally, an experiment was carried out to investigate the formation failure process using the material density distribution in nine different zones, both inside and ahead of the bucket. The density distribution inside the bucket was found to decrease towards the rear of the bucket, as initially observed by O'Beirne et al. (1997). In contrast to initial belief (Rowlands, 1992), a lot of material disturbance was found to occur ahead of the bucket, especially within a distance equal to two-thirds of the bucket length.

6. SUMMARY, CONCLUSIONS AND RECOMMENDATIONS

This section highlights the significant results, conclusions and contributions of this research to the existing body of knowledge. It also includes a summary of all methods and procedures, used to achieve the research objectives, as well as recommendations for further research which was not covered in this study.

6.1. SUMMARY

Across the world, coal contribution to energy generation is expected to remain above 30% through 2030. Draglines remain the equipment of choice in most surface mines, where coal production is achieved through the stripping method. Most previous dragline studies have focused on improving dragline productivity. This is justified as a 10% improvement in productivity has been estimated to be equivalent to $2 million in savings per dragline per year [17].

In recent years, the two major areas of interest in dragline productivity research have concerned (i) bucket design improvements and (ii) autonomous excavation, as an improvement on the highly variable human operator performance. Most of the existing research in bucket design have focused extensively on improvements through experiments with physical scale bucket models. However, bucket design testing through computer model simulations presents a cheaper and more time-efficient alternative to physical scale model testing. At the least, computer simulations may be used for preliminary testing of different bucket design ideas before the most promising designs are

built physically. This will help to reduce the current opportunity cost of discarding bucket designs without any form of testing.

Towards autonomous excavation, the efforts by ACARP have already resulted in the development of an excavator that is able to automate hoisting, swinging and dumping tasks [50]. The current efforts towards automating the dragline digging phase have been limited to image segmentation methods for bucket detection during the digging process. However, the method involves a crude means of identifying bucket edges through color filtering. The main weaknesses of the suggested method are:

(i) The model only deals with one dragline vision problem (bucket pose estimation)

(ii) It requires all buckets to be painted in a specific color (green) for the edge detection model to work.

(iii) The detection model fails at full bucket loading when the green paint is covered by the earth material.

(iv) It involves crude color filtering processes which do not allow for scalable, real-time application.

Therefore, the main objective of this research effort was to propose computer models to address these two significant challenges in dragline productivity studies. The components of this primary objective include:

(i) developing a scientific method for calibrating the formation's constitutive model using discrete element parameters.

(ii) developing a virtual prototype of an industry-standard dragline bucket for formation failure analysis and bucket design comparison.

(iii) developing a machine vision model for autonomous dragline excavation.

All three components of the objective have been achieved. Firstly, a machine learning approach to earth material calibration has been proposed in this study. The model, which is based on the eXtreme Gradient Boosting algorithm [34], was verified and validated using laboratory data. It was found to sufficiently predict material properties with 80.6% to 95.54% accuracy.

Secondly, this study has also presented a dragline excavation model, which simulates bucket – formation interactions during material loading and predicts excavation performance (payload). The model has been verified and validated and was found to produce bucket payload, which fall in the ball park of experimental results. Thirdly, a machine vision model, based on the mobilenet convolutional neural network architecture [160] and on fast single shot multibox detection [161], has been proposed for the autonomous dragline. The DragNet model has been verified and validated, with an average of 82.6% classification accuracy and 91.3% object detection rate.

6.2. CONCLUSIONS

From the XGBoost material calibration experiments, the following conclusions are drawn:

1. The XGBoost model significantly outperforms conventional curve-fitting methods.
2. Unlike previous calibration models, the XGBoost model was designed to generalize performance over a wide range of material property values.

3. The relationships between DEM microparameters and formation properties are more complex than can be explained by simple calibration models.
4. The relationships between DEM microparameters and formation properties are not constant. They are unpredictable at worst or vary between finite value ranges at best.

From the dragline excavation simulation experiments, the following conclusions are drawn:

1. The formation particle size distribution has a significant impact on dragline performance. The optimum material size distribution ranges from fines up to about a quarter of the bucket width.
2. Generally, material density has a positive effect on bucket loading. As material density increases, payload typically increases.
3. There is a material density distribution which develops inside and ahead of the bucket during loading. The density distribution decreases towards the rear of the bucket. The “virgin” material ahead of the bucket teeth (i.e. regions II and III), is actually disturbed material because of the compression action of the bucket.
4. The most active material zones during loading are the areas close to the bucket teeth, typically the zones within a distance equal to two-thirds of the bucket length (i.e. regions II, III, IV and V).

From the DragNet vision model experiments, the following conclusions are drawn:

1. For future DragNet model improvements, the choice of an activation transfer function has the most significant impact on performance. Typically, selecting

either RELU or RELU_6 activation units promises high model performance whilst using no activation units usually produce low performance.

2. The optimum localization weight for the DragNet model converges towards 1.0.
3. For the DragNet model, using the Intersection over Union (IOU) similarity calculator usually produces better results than the Intersection over Area (IOA) alternative.
4. The DragNet model is able to achieve perfect bucket pose detection during the hoisting and dumping phases.
5. The DragNet model is able to achieve over 90% detection during the post-loading swing phase.
6. The lowest detection rates for the model occur during the pre-loading swing phase (72.62%) and the loading phase (73.33%).
7. The model is able to achieve an 87.32% average detection rate across all operation phases on bucket pose estimation tasks.
8. The DragNet model is able to achieve 80.9% precision and 91.3% recall performance on terrain recognition tasks.
9. While the DragNet model performs considerably well, future improvements will be required to meet minimum performance thresholds for safe operation.

6.3. CONTRIBUTIONS OF PHD RESEARCH

The following outline the major contributions of this study.

1. This research initiative introduces a novel approach for geomaterial micro-parameter calibration. In this new approach, extensive laboratory test simulation

is first used to generate significant amounts of data. A powerful machine learning algorithm, the eXtreme Gradient Boosting method, is then used to train and evaluate a model on the data set. The new approach has been shown to outperform conventional curve-fitting methods.

2. This is the first study to investigate the predictive performance of a geomaterial micro-parameter calibration model over a wide range of parameter values.
3. This study is the first attempt to investigate dragline bucket loading at both full-scale and in three dimensions using the Discrete Element Method.
4. This study constitutes the first attempt to investigate the material density distribution ahead of the dragline bucket during loading.
5. This study is also the first attempt at investigating the density distribution inside the dragline bucket using the Discrete Element Method.
6. This study represents the first attempt at correlating blast design and fragmentation (material size distribution) to dragline bucket loading performance.
7. The dragline simulation model, developed in this study, complements current bucket design research by providing a cheap and time-efficient tool for comparing different bucket geometries for design improvements.
8. This research effort included over 1500 DEM simulations of typical geomaterial triaxial tests. The experimental results (Appendix A) present the actual DEM parameter values that may be obtained from a given combination of formation property values. This provides a valuable dataset for future material calibration studies.

9. This study represents the first attempt to develop a multi-purpose vision model for the dragline. Earlier models only addressed single and specific vision tasks.
10. This study introduces a scalable and faster solution to bucket pose estimation using the Single Shot MultiBox Detector (SSD) method [161].
11. This study is the first attempt to propose a terrain recognition model using the Depthwise-Separable Convolutional Neural Network method [160].

6.4. RECOMMENDATIONS

The following areas currently present some of the most promising opportunities for research frontier advancement in dragline excavation engineering.

1. The XGBoost calibration model was developed using the same material size distribution and material density. For any given setup, the material bulk density was calibrated iteratively in this study since it is a relatively simple task. Future research should investigate whether a wide range of densities and particle sizes will further improve the model calibration process.
2. One major challenge that was faced in this study was the unavailability of material property data in reported dragline excavation experiments. In order to replicate physical excavator-formation interactions in a simulation model, data on bucket properties (i.e. geometry, weight, velocity), formation properties (i.e. density, porosity, poisson's ratio, elastic modulus, friction coefficient, particle size disstribution), and excavation outcome (i.e. payload or forces) are all required. However, it appears that most mines do not record data on most of the formation properties which influence dragline bucket behavior during excavator

interactions. While such information may not be relevant to the actual excavation operation, its unavailability limits any study that can be made into the material behavior and failure. On the other hand, when material property data is available, an indepth study of formation failure can be carried out with the aim of optimizing excavation efficiency.

3. The dragline simulation model, developed in this study, provides a good tool for future dragline excavation studies. An area of major contribution is in bucket design studies where different bucket geometries are compared. Unlike real life where no two bucket filling tests are exactly the same, this simulation platform provides a very good avenue for comparing bucket performance without bias or operational inconsistencies. Future work should consider the capacity of the model bucket design experiments.
4. Future studies may consider the use of several, smaller density zones to better understand the formation failure, both inside and ahead of the dragline bucket.
5. In this study, it was found that optimum excavation performance is possible when blasting results in fragmentation, ranging from fines up to a quarter of the dragline bucket width. Future work should investigate whether this range changes for different bucket geometries or for different material poperties.
6. Detection of big rocks for secondary blasting: There is a huge research opportunity in improving the DragNet vision model to be able to detect poorly blasted rocks for secondary blasting. The current DragNet model only achieves 55% recall and 78% precision performance on big rocks / boulder detection. Since the current DragNet model was trained with only 120 boulder images, it can be

improved for boulder detection by re-training on a much larger and more diverse set of boulder images.

7. The DragNet vision model only involved 9 different terrains for terrain recognition. As a proof of concept, the model performs well on terrain recognition tasks. Future studies may extend the model to include several different classes of earth materials, which are typically found in surface mine environments.
8. Generally, the current DragNet vision model was only trained for 250,000 epochs over several weeks at a cost of $20/day on a 16GB P5000 GPU. Training the model for magnitudes of epoch higher will significantly improve model performance. This may be attempted when better and more cost-effective model training options become available.

APPENDIX A

HYPER-PARAMETER TUNING FOR XGBOOST MODEL

eta	max depth	gamma	colsample bytree	Min child weight	sub sample	nrounds	Model Performance		
							RMSE	R^2	MAE
0.0013	5	1.7530	0.3789	13	0.970	71	4.723	0.1960	4.103
0.0020	5	7.8238	0.3165	10	0.533	263	3.497	0.1821	2.852
0.0071	4	8.0076	0.4382	5	0.879	424	2.073	0.2745	1.714
0.0076	5	2.6855	0.4754	17	0.575	587	2.057	0.2619	1.694
0.0078	8	6.9895	0.4947	9	0.847	845	1.859	0.3956	1.483
0.0084	7	9.9351	0.6933	4	0.439	337	2.014	0.3225	1.643
0.0158	1	5.4297	0.5475	0	0.294	586	2.218	0.1378	1.851
0.0161	4	2.1963	0.6665	11	0.418	402	2.018	0.2835	1.653
0.0189	3	6.1450	0.4807	1	0.526	821	1.903	0.3658	1.545
0.0225	9	3.7443	0.5980	2	0.811	153	1.766	0.4721	1.368
0.0235	7	7.6862	0.4624	8	0.597	843	1.835	0.4074	1.439
0.0298	2	1.4342	0.3635	19	0.417	375	2.154	0.1854	1.783
0.0315	3	3.7780	0.4786	2	0.388	344	1.980	0.3124	1.617
0.0332	4	9.0799	0.6172	17	0.763	679	1.920	0.3502	1.542
0.0359	7	2.3534	0.6820	1	0.405	204	1.756	0.4560	1.344
0.0388	9	5.2939	0.4665	11	0.828	363	1.827	0.4118	1.402
0.0433	3	8.5885	0.3423	10	0.560	877	1.919	0.3516	1.541
0.0453	7	5.8142	0.4688	12	0.707	539	1.825	0.4112	1.412
0.0458	10	7.8668	0.4773	16	0.967	738	1.860	0.3881	1.462
0.0476	9	7.4355	0.3318	9	0.570	877	1.854	0.3923	1.444
0.0577	8	3.4463	0.3173	6	0.310	772	1.804	0.4298	1.324
0.0610	3	7.7213	0.6445	12	0.361	101	2.126	0.2036	1.759
0.0669	8	6.8467	0.3969	8	0.467	108	1.927	0.3433	1.546
0.0730	6	1.7396	0.6149	8	0.726	499	1.696	0.4962	1.202
0.0736	1	6.6507	0.5549	18	0.885	961	2.121	0.2102	1.761
0.0773	3	3.9079	0.5876	4	0.617	783	1.801	0.4289	1.371
0.0900	1	0.7893	0.3967	10	0.842	506	2.147	0.1887	1.786
0.0952	4	4.0977	0.3010	2	0.319	388	1.808	0.4241	1.368
0.0994	4	5.9284	0.3880	7	0.383	348	1.887	0.3712	1.461
0.0997	6	3.2596	0.6650	3	0.302	871	1.761	0.4590	1.262
0.1005	7	6.9431	0.5493	11	0.442	664	1.840	0.4047	1.402
0.1005	6	9.1073	0.5904	8	0.756	284	1.832	0.4096	1.433
0.1086	6	7.6054	0.4400	19	0.597	373	1.878	0.3755	1.466
0.1123	9	9.1228	0.5793	20	0.385	212	1.982	0.3115	1.592
0.1149	7	4.8610	0.4851	14	0.998	851	1.818	0.4183	1.402

0.1156	10	0.1314	0.6928	11	0.901	197	1.686	0.5117	1.091
0.1165	10	4.7456	0.4509	9	0.602	353	1.774	0.4457	1.333
0.1208	3	8.4466	0.3366	4	0.571	930	1.859	0.3922	1.449
0.1211	9	7.5609	0.5164	8	0.834	498	1.794	0.4304	1.364
0.1232	10	2.2389	0.3494	8	0.435	663	1.813	0.4358	1.271
0.1243	5	5.9867	0.4696	7	0.882	405	1.811	0.4203	1.387
0.1256	7	2.9893	0.6783	16	0.949	967	1.776	0.4472	1.301
0.1274	1	2.7158	0.5753	2	0.785	292	2.145	0.1902	1.789
0.1310	7	9.9099	0.6566	1	0.381	837	1.846	0.4014	1.423
0.1324	8	6.6971	0.3390	13	0.852	284	1.855	0.3929	1.441
0.1339	4	6.0692	0.3405	4	0.323	271	1.850	0.3998	1.438
0.1354	1	8.0175	0.6519	12	0.291	944	2.061	0.2539	1.672
0.1375	5	7.2333	0.4815	3	0.378	869	1.806	0.4267	1.382
0.1430	5	4.7380	0.3544	17	0.739	466	1.826	0.4131	1.397
0.1455	5	8.6275	0.3435	19	0.933	695	1.895	0.3645	1.500
0.1455	7	9.8395	0.3793	15	0.400	352	1.939	0.3371	1.536
0.1463	6	4.8930	0.4919	3	0.550	488	1.792	0.4356	1.332
0.1492	8	3.3214	0.3314	2	0.288	166	1.883	0.3850	1.398
0.1496	4	5.8466	0.4438	16	0.539	515	1.888	0.3765	1.458
0.1498	4	0.5172	0.4593	6	0.391	192	1.825	0.4190	1.355
0.1552	3	2.9623	0.3338	6	0.276	580	1.869	0.3988	1.369
0.1587	4	7.1727	0.3113	15	0.712	126	1.942	0.3357	1.556
0.1627	2	3.2701	0.6684	13	0.619	158	2.003	0.2922	1.633
0.1651	1	6.2443	0.6876	7	0.789	1000	2.043	0.2639	1.684
0.1670	6	4.4459	0.5561	0	0.385	141	1.861	0.3997	1.371
0.1671	2	2.5061	0.6327	19	0.997	256	1.948	0.3319	1.578
0.1679	5	6.9628	0.4994	10	0.486	947	1.800	0.4282	1.373
0.1724	5	0.2544	0.6597	16	0.649	74	1.879	0.3730	1.471
0.1881	6	6.1387	0.3179	6	0.377	85	1.934	0.3452	1.499
0.1914	3	9.3985	0.4916	2	0.715	835	1.847	0.3975	1.458
0.1930	5	5.0940	0.5108	5	0.379	302	1.882	0.3896	1.403
0.1954	6	1.3995	0.6824	12	0.649	422	1.790	0.4574	1.212
0.2021	10	4.4422	0.3581	15	0.437	520	1.823	0.4195	1.360
0.2102	1	1.1423	0.6987	13	0.697	522	2.040	0.2702	1.683
0.2118	10	9.2844	0.5107	2	0.412	69	1.921	0.3530	1.493
0.2136	9	8.5102	0.6337	6	0.530	425	1.860	0.3936	1.406
0.2186	3	3.5211	0.3755	1	0.775	323	1.761	0.4527	1.315
0.2262	3	2.4253	0.6313	13	0.382	107	2.010	0.2908	1.604
0.2299	4	3.2253	0.3361	10	0.749	894	1.835	0.4205	1.326

0.2314	7	4.4475	0.6834	8	0.539	444	1.786	0.4472	1.290
0.2327	3	5.3718	0.5551	15	0.423	74	2.025	0.2753	1.640
0.2337	5	8.2303	0.3887	5	0.390	755	1.944	0.3537	1.479
0.2454	5	3.3691	0.3109	16	0.259	334	1.970	0.3423	1.474
0.2532	4	0.1680	0.5495	6	0.663	295	1.772	0.4761	1.098
0.2537	2	3.9664	0.6569	7	0.535	167	1.957	0.3286	1.545
0.2566	7	3.3328	0.5981	3	0.941	558	1.739	0.4689	1.257
0.2572	2	0.8200	0.6325	4	0.445	458	1.832	0.4212	1.346
0.2573	8	2.2586	0.3176	15	0.776	19	1.949	0.3372	1.567
0.2617	5	6.1002	0.4486	15	0.737	396	1.864	0.3913	1.409
0.2618	9	5.5979	0.4285	19	0.701	634	1.816	0.4215	1.359
0.2651	4	0.7733	0.3256	19	0.350	933	1.884	0.4227	1.229
0.2699	8	2.5242	0.5214	15	0.661	997	1.774	0.4615	1.233
0.2762	3	5.9917	0.3174	10	0.269	722	2.027	0.3251	1.499
0.2785	8	2.5097	0.4478	14	0.765	489	1.796	0.4449	1.269
0.2803	8	1.6006	0.5709	19	0.755	464	1.780	0.4582	1.214
0.2808	7	0.2387	0.5956	20	0.713	604	1.767	0.4811	1.097
0.2810	4	4.7305	0.3338	16	0.570	750	1.859	0.4059	1.358
0.2918	9	9.8884	0.5922	20	0.266	243	2.047	0.2706	1.620
0.2966	9	1.0944	0.6330	20	0.362	969	1.848	0.4388	1.205
0.2990	10	6.8075	0.5376	19	0.712	481	1.845	0.4056	1.385
0.3010	4	3.1232	0.6610	20	0.712	901	1.815	0.4329	1.307
0.3015	9	2.1192	0.3701	3	0.895	250	1.699	0.4924	1.171
0.3017	9	0.7761	0.5775	5	0.628	943	1.697	0.5111	1.077
0.3037	10	2.6167	0.3676	18	0.962	916	1.782	0.4459	1.275
0.3083	3	6.8831	0.4562	15	0.628	517	1.909	0.3690	1.461

APPENDIX B

MODEL PREDICTIONS – XGBOOST vs POLYREG

FORMATION PROPERTIES				DEM PARAMETERS		MODEL PREDICTIONS			
Yng modulus	Psn ratio	Shear modulus (GPa)	Fric coeff	emod (10^9)	fric	emod Poly Reg	emod XGB oost	fric Poly Reg	fric XGB oost
0.261	-0.58	0.312	0.419	1	1.73	3.773	8.088	3.773	1.352
0.256	-0.68	0.403	0.427	1	2.75	3.929	5.891	3.929	1.756
0.188	-0.49	0.184	0.351	10	0.58	5.507	5.375	5.507	0.720
0.252	-0.45	0.231	0.389	3.5	0.3	5.495	4.078	5.495	0.549
0.195	-0.42	0.167	0.241	4.5	0.3	3.937	4.501	3.937	0.382
0.313	-0.22	0.202	0.286	6.5	0.3	5.518	6.166	5.518	0.193
0.199	-0.42	0.171	0.296	8.5	0.3	4.394	7.919	4.394	0.549
0.217	-0.57	0.253	0.366	2.5	0.4	4.271	2.504	4.271	0.342
0.182	-0.39	0.149	0.258	4.5	0.4	4.293	4.537	4.293	0.451
0.219	-0.41	0.186	0.323	5.5	0.4	5.339	5.417	5.339	0.464
0.206	-0.48	0.199	0.357	8.5	0.4	5.598	7.884	5.598	0.609
0.215	-0.46	0.198	0.298	1.5	0.5	4.032	1.550	4.032	0.483
0.216	-0.48	0.207	0.342	5.5	0.5	5.384	5.324	5.384	0.486
0.385	-0.51	0.394	0.435	7.5	0.5	6.854	7.328	6.854	0.631
0.251	-0.69	0.411	0.382	1.75	2.15	3.459	1.741	3.459	2.009
0.303	-0.85	1.001	0.446	2.5	2.15	3.473	2.974	3.473	2.032
0.231	-0.76	0.476	0.358	3	2.15	2.258	2.725	2.258	1.850
0.238	-0.53	0.252	0.369	5.5	0.65	5.411	4.674	5.411	1.443
0.295	-0.52	0.309	0.422	6	0.65	4.792	6.325	4.792	0.896
0.241	-0.49	0.236	0.39	8.5	0.65	5.538	7.985	5.538	0.576
0.181	-0.59	0.220	0.305	1.5	0.75	3.110	2.554	3.110	1.054
0.255	-0.72	0.458	0.367	2.5	0.75	3.399	1.476	3.399	1.324
0.202	-0.46	0.188	0.301	5	0.75	4.770	4.989	4.770	0.700
0.307	-0.60	0.383	0.471	6	1.25	6.640	5.966	6.640	1.317
0.304	-0.61	0.392	0.467	7.5	1.25	7.992	5.369	7.992	1.272
0.273	-0.56	0.307	0.43	8.5	1.25	7.171	8.087	7.171	1.254
0.292	-0.58	0.350	0.449	9	1.25	6.326	8.943	6.326	1.250
0.327	-0.58	0.391	0.393	5.5	1.35	5.263	8.003	5.263	1.269
0.338	-0.72	0.594	0.416	7	1.35	4.246	6.842	4.246	1.449
0.226	-0.64	0.314	0.398	1.75	1.45	4.570	1.942	4.570	1.446
0.243	-0.73	0.456	0.379	3	1.45	3.015	2.941	3.015	1.567
0.310	-0.63	0.416	0.47	3.5	1.15	5.798	3.687	5.798	1.236

0.254	-0.63	0.346	0.413	5.5	1.15	5.871	5.456	5.871	1.209
0.281	-0.43	0.248	0.403	6.5	1.15	6.157	6.474	6.157	1.051
0.331	-0.54	0.361	0.399	8	1.15	5.996	7.856	5.996	1.298
0.302	-0.61	0.383	0.427	9	1.15	5.543	9.019	5.543	1.136
0.229	-0.60	0.288	0.361	1.5	1.95	3.658	1.794	3.658	1.849
0.245	-0.57	0.283	0.354	1.75	1.95	4.212	1.980	4.212	1.869
0.236	-0.66	0.350	0.398	2	1.95	4.256	2.414	4.256	1.758
0.349	-0.56	0.392	0.461	3.5	1.95	3.689	3.697	3.689	1.784
0.241	-0.62	0.315	0.41	1.5	1.65	3.726	1.625	3.726	1.572
0.234	-0.62	0.308	0.393	2	1.65	5.115	2.015	5.115	1.642
0.275	-0.67	0.416	0.438	5.5	1.65	6.537	5.259	6.537	1.648
0.321	-0.66	0.467	0.445	9.5	1.65	5.697	8.818	5.697	1.583
0.199	-0.65	0.288	0.34	1.5	1.75	2.648	1.562	2.648	1.489
0.259	-0.73	0.481	0.397	2	1.75	4.043	5.657	4.043	1.917
0.253	-0.64	0.356	0.392	5.5	1.75	5.785	5.478	5.785	1.652
0.241	-0.51	0.248	0.387	8.5	1.75	5.611	3.088	5.611	1.076
0.370	-0.86	1.352	0.43	7	2.25	7.462	6.849	7.462	2.166
0.302	-0.58	0.356	0.384	8.5	2.25	5.606	8.237	5.606	2.089
0.278	-0.79	0.668	0.406	3	2.35	3.752	2.896	3.752	2.061
0.270	-0.32	0.199	0.308	1.25	0.3	2.766	1.371	2.766	0.345
0.202	-0.47	0.188	0.343	1.75	0.3	4.079	2.197	4.079	0.427
0.212	-0.64	0.296	0.345	2.5	0.3	3.813	2.180	3.813	0.680
0.186	-0.32	0.137	0.252	5	0.3	4.344	5.025	4.344	0.258
0.397	-0.37	0.315	0.3	9.5	0.3	7.256	9.392	7.256	0.297
0.240	-0.36	0.187	0.293	1.25	0.4	3.145	1.386	3.145	0.350
0.236	-0.50	0.234	0.406	3.5	0.4	5.601	3.502	5.601	0.493
0.206	-0.37	0.164	0.316	6.5	0.4	4.765	6.563	4.765	0.519
0.206	-0.48	0.199	0.357	8.5	0.4	5.598	7.884	5.598	0.609
0.201	-0.46	0.186	0.346	1.75	0.5	4.291	1.647	4.291	0.580
0.215	-0.50	0.216	0.371	2	0.5	4.816	2.150	4.816	0.637
0.234	-0.30	0.167	0.28	5	0.5	5.038	4.975	5.038	0.474
0.173	-0.50	0.172	0.252	1.5	0.3	3.711	1.408	3.711	0.459
0.202	-0.47	0.188	0.343	1.75	0.3	4.079	2.197	4.079	0.427
0.212	-0.64	0.296	0.345	2.5	0.3	3.813	2.180	3.813	0.680
0.252	-0.45	0.231	0.389	3.5	0.3	5.495	4.078	5.495	0.549
0.195	-0.42	0.167	0.241	4.5	0.3	3.937	4.501	3.937	0.382
0.313	-0.22	0.202	0.286	6.5	0.3	5.518	6.166	5.518	0.193
0.199	-0.42	0.171	0.296	8.5	0.3	4.394	7.919	4.394	0.549
0.191	-0.47	0.180	0.34	1.75	0.4	4.582	1.971	4.582	0.478

0.191	-0.36	0.148	0.276	5	0.4	4.331	5.074	4.331	0.289
0.210	-0.55	0.234	0.368	1.75	0.65	3.689	2.407	3.689	0.806
0.221	-0.58	0.262	0.363	3	0.65	4.132	3.368	4.132	0.872
0.220	-0.47	0.206	0.329	4	0.65	4.932	4.148	4.932	0.916
0.238	-0.53	0.252	0.369	5.5	0.65	5.411	4.674	5.411	1.443
0.181	-0.59	0.220	0.305	1.5	0.75	3.110	2.554	3.110	1.054
0.255	-0.72	0.458	0.367	2.5	0.75	3.399	1.476	3.399	1.324
0.247	-0.43	0.216	0.348	4	0.75	4.108	3.828	4.108	0.887
0.175	-0.47	0.164	0.298	4.5	0.75	3.938	4.536	3.938	0.785
0.269	-0.65	0.381	0.418	2	1.25	5.401	2.335	5.401	1.267
0.292	-0.65	0.411	0.367	3	1.25	4.054	3.112	4.054	1.096
0.275	-0.50	0.276	0.393	6.5	1.25	5.859	6.460	5.859	1.125
0.304	-0.61	0.392	0.467	7.5	1.25	7.992	5.369	7.992	1.272
0.300	-0.55	0.337	0.433	8	1.25	6.062	7.998	6.062	1.196
0.271	-0.62	0.355	0.432	3.5	1.35	5.617	3.640	5.617	1.457
0.327	-0.58	0.391	0.393	5.5	1.35	5.263	8.003	5.263	1.269
0.279	-0.59	0.340	0.451	3.5	1.45	5.463	3.565	5.463	1.353
0.200	-0.43	0.175	0.326	5	1.45	4.460	5.478	4.460	1.237
0.259	-0.62	0.342	0.409	2	1.15	5.122	1.899	5.122	1.145
0.230	-0.72	0.404	0.379	3	1.15	4.182	3.289	4.182	1.290
0.277	-0.62	0.362	0.458	7.5	1.15	7.668	7.746	7.668	1.401
0.249	-0.57	0.290	0.42	9.5	1.15	5.225	9.841	5.225	1.413
0.241	-0.56	0.271	0.346	4.5	1.95	3.665	4.552	3.665	1.799
0.302	-0.71	0.516	0.467	5.5	1.95	7.356	5.460	7.356	1.951
0.236	-0.52	0.244	0.439	6.5	1.95	5.850	6.654	5.850	1.660
0.305	-0.74	0.583	0.44	3.5	1.65	5.417	4.141	5.417	1.467
0.222	-0.49	0.219	0.324	4.5	1.65	3.761	4.399	3.761	1.469
0.260	-0.68	0.405	0.447	9	1.65	6.324	9.027	6.324	1.695
0.259	-0.73	0.481	0.397	2	1.75	4.043	5.657	4.043	1.917
0.356	-0.78	0.815	0.401	3	1.75	5.127	3.234	5.127	1.718
0.241	-0.51	0.248	0.387	8.5	1.75	5.611	3.088	5.611	1.076
0.298	-0.68	0.463	0.466	9	1.75	5.772	8.937	5.772	1.540
0.379	-0.66	0.563	0.443	6	2.25	6.081	6.164	6.081	1.887
0.367	-0.51	0.372	0.423	6.5	2.25	5.336	6.580	5.336	2.034
0.267	-0.63	0.355	0.447	9.5	2.25	6.370	9.413	6.370	1.895
0.263	-0.67	0.394	0.367	3.9	0.92	4.356	4.646	4.356	1.463
0.296	-0.44	0.265	0.329	5.65	0.92	4.574	3.076	4.574	1.094
0.309	-0.56	0.349	0.354	6.25	0.92	3.500	5.946	3.500	1.514
0.269	-0.65	0.380	0.394	7.25	0.92	4.926	6.541	4.926	1.267

0.220	-0.50	0.220	0.386	3.2	1.16	5.685	6.671	5.685	0.805
0.242	-0.46	0.224	0.351	4.2	1.16	4.073	5.280	4.073	0.948
0.240	-0.67	0.359	0.392	6.65	1.16	5.454	3.802	5.454	1.620
0.217	-0.55	0.239	0.371	3.2	1.23	5.315	6.024	5.315	1.044
0.274	-0.45	0.249	0.391	4.95	1.23	5.470	4.429	5.470	0.599
0.288	-0.73	0.540	0.397	6.95	1.23	2.582	6.787	2.582	1.724
0.309	-0.67	0.471	0.416	3.9	2.13	5.160	3.656	5.160	1.522
0.248	-0.54	0.270	0.393	4.95	2.13	5.842	4.810	5.842	0.607
0.248	-0.66	0.359	0.394	6.25	2.13	3.591	8.547	3.591	1.302
0.351	-0.63	0.477	0.438	7.55	0.63	7.650	6.245	7.650	1.247
0.234	-0.35	0.181	0.329	4.55	0.84	5.199	4.476	5.199	0.684
0.184	-0.38	0.147	0.3	4.85	0.84	4.265	4.775	4.265	0.727
0.211	-0.48	0.204	0.349	5.35	0.84	4.497	5.547	4.497	0.735
0.196	-0.57	0.226	0.363	6.35	0.84	5.269	4.099	5.269	0.933
0.241	-0.63	0.326	0.348	6.75	0.84	4.655	7.084	4.655	0.931
0.246	-0.50	0.248	0.367	7.74	1.06	4.964	5.101	4.964	1.295
0.288	-0.60	0.359	0.372	8.13	1.06	5.046	5.962	5.046	1.475
0.323	-0.66	0.472	0.431	8.37	1.06	5.297	6.763	5.297	1.273
0.234	-0.51	0.240	0.344	2.83	1.34	5.316	5.989	5.316	1.485
0.331	-0.66	0.491	0.405	7.93	1.34	6.836	5.135	6.836	1.634
0.319	-0.68	0.498	0.455	8.37	1.34	6.924	7.463	6.924	1.593
0.287	-0.54	0.313	0.375	2.83	1.53	5.430	4.961	5.430	1.293
0.339	-0.64	0.467	0.41	7.53	1.53	4.124	3.916	4.124	1.711
0.199	-0.51	0.202	0.358	7.74	1.53	5.276	6.416	5.276	0.965
0.267	-0.53	0.284	0.378	2.83	1.43	6.420	4.435	6.420	1.356
0.242	-0.60	0.301	0.386	7.53	1.43	4.257	3.456	4.257	1.154
0.333	-0.61	0.425	0.372	4.57	1.83	5.778	6.051	5.778	1.426
0.344	-0.69	0.551	0.442	3.38	1.89	6.426	7.155	6.426	1.404
0.362	-0.75	0.728	0.443	3.38	1.94	6.926	7.200	6.926	1.819
0.246	-0.59	0.297	0.384	3.87	1.94	6.308	3.938	6.308	1.085
0.284	-0.58	0.340	0.438	5.87	1.94	5.535	3.755	5.535	1.106
0.218	-0.49	0.212	0.317	7.08	1.94	5.526	6.465	5.526	1.111
0.357	-0.54	0.384	0.393	4.57	2.03	4.224	4.210	4.224	1.246
0.299	-0.69	0.481	0.422	3.38	1.18	4.812	4.651	4.812	1.507
0.339	-0.49	0.333	0.39	3.87	1.18	6.508	4.801	6.508	1.082
0.331	-0.42	0.287	0.34	4.93	1.22	6.911	4.542	6.911	0.963
0.211	-0.56	0.237	0.348	5.17	0.98	5.367	4.872	5.367	0.868
0.265	-0.50	0.264	0.411	5.87	0.98	4.608	6.155	4.608	0.872
0.265	-0.54	0.289	0.345	7.74	1.73	4.708	7.176	4.708	1.745

0.236	-0.59	0.285	0.364	8.48	1.73	4.154	8.059	4.154	1.598
0.290	-0.73	0.545	0.415	8.13	1.73	5.500	7.444	5.500	1.711
0.267	-0.43	0.236	0.359	3.2	0.63	4.328	5.177	4.328	1.169
0.319	-0.40	0.267	0.277	5.25	0.63	4.635	4.827	4.635	0.567
0.237	-0.52	0.249	0.321	6.25	0.63	3.343	4.665	3.343	1.633
0.239	-0.59	0.290	0.375	2.6	1.67	5.209	4.610	5.209	1.722
0.288	-0.54	0.316	0.393	4.65	1.67	7.557	6.408	7.557	0.937
0.273	-0.50	0.271	0.404	4.95	1.67	5.928	2.102	5.928	1.592
0.215	-0.57	0.248	0.338	5.25	1.67	3.753	2.715	3.753	0.831
0.255	-0.58	0.307	0.37	2.9	1.83	4.886	3.390	4.886	1.335
0.258	-0.67	0.393	0.424	3.6	1.83	5.013	6.974	5.013	1.417
0.196	-0.57	0.226	0.363	6.35	0.84	5.269	4.099	5.269	0.933
0.195	-0.54	0.211	0.302	5.17	0.84	4.692	4.788	4.692	0.668
0.274	-0.71	0.473	0.364	4.35	1.06	2.520	4.342	2.520	1.124

APPENDIX C

DRAGNET HYPER-PARAMETER TUNING RESULTS

Step	Model_0	Model_1	Model_2	Model_3	Model_4	Model_5
0	76.751	165.703	80.977	111.014	383.684	54.715
425	4.437	5.973	4.815	4.819	8.954	9.351
881	3.899	7.932	2.802	3.059	11.665	6.759
1322	2.369	6.885	2.424	3.648	42.038	5.547
1772	2.901	3.176	3.871	3.949	7.211	8.314
2217	4.217	3.867	4.166	1.823	6.281	6.877
2646	3.245	2.184	2.763	2.346	37.804	4.177
3081	2.571	10.820	4.419	1.904	11.925	5.386
3542	3.027	3.047	2.919	1.994	8.127	5.208
3991	1.546	5.323	2.195	2.383	9.595	3.858
4450	2.370	4.295	2.429	2.431	15.489	3.017
4877	2.062	3.388	2.156	2.265	23.823	3.573
5334	2.963	3.419	3.057	1.859	5.877	3.724
5791	1.388	1.697	2.651	2.149	13.708	3.586
6231	2.720	5.186	1.604	4.675	6.038	3.652
6660	1.695	1.295	2.071	3.173	6.778	3.682
7078	1.349	3.280	2.179	2.797	8.294	2.616
7463	1.946	4.563	2.528	1.519	33.200	4.682
7844	1.375	2.780	1.424	1.994	5.706	3.196
8233	1.585	2.391	1.378	1.243	6.851	2.886
8624	2.352	3.104	2.107	1.494	8.046	3.141
9014	1.451	1.583	3.551	1.374	6.662	3.255
9402	1.443	3.300	2.960	2.523	5.673	3.146
9782	2.992	2.200	1.632	3.011	7.046	4.722
10197	1.154	2.121	2.144	1.397	8.803	2.872
10602	3.057	3.767	1.206	2.278	6.713	1.632
10995	2.487	2.778	2.085	2.040	7.196	2.401
11371	2.033	1.672	1.740	2.289	7.282	3.200
11747	1.649	2.327	2.236	0.916	8.131	3.730
12131	1.059	1.818	2.093	1.285	7.850	2.729
12522	1.705	2.465	1.291	1.819	7.480	2.918
12881	2.224	4.158	2.094	1.606	6.686	3.874
13262	1.365	13.454	1.192	1.652	18.792	3.055
13650	1.772	4.022	1.223	3.664	6.548	1.968
14040	0.988	2.948	1.640	1.891	9.282	2.438
14425	1.127	2.806	1.480	1.871	11.189	3.074
14815	1.379	4.826	2.584	1.458	6.825	2.333
15221	2.324	5.262	1.516	2.794	19.986	2.348

15604	0.825	1.010	0.951	3.078	4.959	2.426
15982	1.880	2.145	2.245	3.005	17.596	2.607
16370	2.266	3.802	1.872	1.015	7.494	3.561
16780	1.349	1.599	2.136	1.107	5.475	1.899
17191	2.607	2.164	1.503	2.169	5.850	2.435
17592	1.679	3.416	2.644	1.523	6.152	2.667
17980	1.467	2.802	1.398	0.857	6.550	2.490
18409	0.692	3.955	1.668	1.684	8.163	3.207
18817	1.646	2.074	1.300	1.135	6.680	1.787
19233	1.381	2.210	1.438	1.313	7.059	3.048
19643	2.219	1.445	2.207	2.348	7.170	2.657
20078	1.454	2.663	2.250	1.392	5.114	2.356
20506	1.397	3.026	1.791	1.077	7.708	1.598
20919	1.121	3.137	2.324	1.941	7.434	2.599
21327	1.353	2.473	1.972	1.402	8.713	1.989
21735	1.738	3.362	0.998	2.742	7.819	1.962
22132	1.356	2.470	1.296	0.894	7.590	2.212
22518	0.982	4.428	3.339	2.858	8.326	2.735
22877	1.649	3.550	1.152	0.798	10.336	2.526
23260	1.837	3.064	2.083	2.094	25.195	1.839
23654	0.755	1.797	0.899	1.041	6.303	2.736
24044	1.655	1.849	2.084	1.676	5.914	2.487
24420	0.971	3.644	1.716	2.973	4.463	2.793
24799	2.002	4.275	1.555	1.260	8.184	2.458
25182	1.966	5.282	2.296	2.309	6.615	1.741
25570	3.301	4.285	2.430	2.962	6.641	3.754
25956	0.617	4.500	1.953	4.178	18.004	1.579
26381	1.077	2.499	1.032	0.667	8.054	2.409
26812	1.205	3.092	0.984	0.921	6.996	1.853
27244	1.803	3.017	3.887	2.896	5.049	1.999
27663	1.344	3.814	1.986	1.339	5.839	3.255
28092	1.403	1.811	1.986	1.514	7.977	1.959
28539	1.010	2.669	1.027	0.797	7.066	2.050
28972	2.384	1.969	2.290	1.178	7.954	2.055
29398	1.843	0.987	1.281	1.750	7.784	2.240
29822	2.355	2.245	1.147	3.079	5.407	2.077
30265	2.018	4.427	0.960	2.214	6.220	1.930
30706	1.747	1.346	1.193	1.304	6.662	1.413
31121	1.218	3.016	1.693	1.019	9.363	1.679

31562	1.101	3.975	1.008	1.127	6.535	1.707
32019	1.591	1.082	1.622	1.938	5.848	1.749
32455	1.446	0.833	1.046	0.794	5.434	1.567
32891	1.275	3.583	1.594	1.259	26.535	1.653
33334	1.385	8.267	0.713	1.032	6.163	2.551
33788	1.940	1.598	2.410	2.178	7.315	2.064
34236	1.925	1.471	1.554	0.825	6.495	1.946
34680	1.341	5.650	1.224	1.037	5.087	2.147
35130	1.282	1.165	3.171	2.455	5.536	1.084
35575	1.612	3.168	1.895	1.010	5.282	1.716
35997	1.524	2.968	2.199	1.143	5.345	1.492
36435	0.959	2.897	0.881	1.586	5.227	1.489
36874	1.041	1.832	1.720	1.228	5.863	1.723
37316	1.229	3.069	1.093	0.738	5.558	3.071
37719	2.039	1.772	0.725	1.552	4.107	2.148
38163	1.041	5.312	1.248	1.382	4.039	2.096
38602	1.356	1.759	1.235	1.710	11.894	2.418
39053	0.948	1.489	2.939	0.913	4.464	2.068
39491	1.438	1.908	2.223	1.545	12.726	1.294
39937	1.080	3.042	1.624	2.224	4.845	1.960
40390	1.813	1.913	0.783	1.177	6.757	1.639
40834	1.163	2.290	0.780	1.178	5.898	1.237
41302	1.153	2.810	1.737	2.628	7.641	1.157
41763	1.650	1.825	1.601	1.962	5.409	2.403
42218	1.009	3.299	0.818	1.108	8.605	2.190
42660	1.477	1.482	1.663	1.698	11.006	1.516
43119	1.722	1.171	0.816	1.790	6.910	1.625
43565	0.683	1.000	1.150	1.512	5.528	1.600
44017	1.813	3.118	2.493	1.374	6.818	1.403
44443	1.172	5.851	1.143	1.716	6.818	2.038
44897	1.161	2.376	1.338	0.813	6.818	1.200
45350	0.507	1.765	1.549	2.376	6.818	3.301
45791	2.319	2.841	2.161	0.849	6.818	3.301
46236	2.470	4.382	2.161	1.476	6.818	3.301
46672	1.107	3.763	2.161	0.877	6.818	3.301
47126	1.553	3.019	2.161	0.988	6.818	3.301
47558	1.228	3.019	2.161	2.111	6.818	3.301
48010	0.884	3.019	2.161	1.671	6.818	3.301
48448	1.594	3.019	2.161	0.903	6.818	3.301

48888	0.640	3.019	2.161	0.903	6.818	3.301
49323	2.778	3.019	2.161	1.717	6.818	3.301
49781	1.334	3.019	2.161	0.802	6.818	3.301
50000	0.840	3.019	2.161	0.802	6.818	3.301

BIBLIOGRAPHY

1. EIA, *Annual Energy Outlook 2014 with projections to 2040*. 2014.

2. Gilewicz, P., *International dragline population matures.* Coal age, 2000. **105**(6): p. 30-32.

3. Mineweb *$100 million Anglo Coal dragline to go under the hammer*. 2013.

4. EIA *Chinese coal-fired electricity generation expected to flatten as mix shifts to renewables*. 2017.

5. Siemens *Facts and Forecasts: Global Support for Renewable Energy Sources*. 2017.

6. McCoy, C.E. and J. Crowgey, *Anti-tightline control system for draglines used in the surface mining industry*. 1980, Pennsylvania State University, Behrend College Graduate Center.

7. Hainsworth, D.W. *Dragline Automation*. CSIRO Exploration & Mining, 1996.

8. Corke, P., et al. *Dragline automation: Experimental evaluation through productivity trial*. in *Field and Service Robotics*. 2006. Springer.

9. Corke, G.J. Winstanley, and J.M. Roberts. *Dragline modelling and control*. in *Robotics and Automation, 1997. Proceedings., 1997 IEEE International Conference on*. 1997. IEEE.

10. Demirel, N. and S. Frimpong, *Case Study: Planar Kinematics of Dragline for Efficient Machine Control.* Journal of Aerospace Engineering, 2009. **22**(2): p. 112-122.

11. Algra, R., P. Corke, and P. Ridley, *Dragline Bucket and Rigging Dynamics.* 2001.

12. Ridley, P. and R. Algra, *Dragline bucket and rigging dynamics.* Mechanism and machine theory, 2004. **39**(9): p. 999-1016.

13. Frimpong, S., Y. Hu, and H. Inyang, *Dynamic modeling of hydraulic shovel excavators for geomaterials.* International Journal of Geomechanics, 2009. **8**(1): p. 20-29.

14. McInnes, C. and P. Meehan, *Trajectory optimization of a mining dragline using the method of Lagrange multipliers.* International Journal of Robust and Nonlinear Control, 2011. **21**(14): p. 1677-1692.

15. Dayawansa, P., et al., *Fracture mechanics of mining dragline booms.* Engineering Failure Analysis, 2006. **13**(4): p. 716-725.

16. CSIRO, *Optimised dragline planning model*, in *Proceedings Of the Mathematics In Industry Study Group*. 1993: Melbourne University.

17. Darnbrough, J., *Dragline R&D hits the bottom line*. 2008, Reed Business Information Ltd. (Australia): Melbourne. p. 20.

18. Lumley, G., *Reducing the variability in dragline operator performance.* 2005.

19. Winstanley, G.J., P.I. Corke, and J.M. Roberts, *Dragline swing automation.* Mineral Resources Engineering, 1999. **8**(03): p. 301-312.

20. Winstanley, G., et al., *Dragline Swing Assist: ACARP C9028—final report*. 2003, Technical report, ACARP.

21. Bullock, D.M. and I.J. Oppenheim. *A laboratory study of force-cognitive excavation*. in *Proc. Sixth International Symposium on Automation and Robotics in Construction*. 1989.

22. Gocho, T. *Automatic wheel-loader in asphalt plant*. in *Proc. of the 9th Int. Symposium on Automation and Robotics in Construction, 1992*. 1992.

23. Bernold, L.E., *Motion and path control for robotic excavation.* Journal of Aerospace Engineering, 1993. **6**(1): p. 1-18.

24. Shi, X., P.J. Lever, and F.-Y. Wang. *Experimental robotic excavation with fuzzy logic and neural networks*. in *Robotics and Automation, 1996. Proceedings., 1996 IEEE International Conference on*. 1996. IEEE.

25. Bradley, D.A. and D.W. Seward, *The development, control and operation of an autonomous robotic excavator.* Journal of Intelligent and Robotic Systems, 1998. **21**(1): p. 73-97.

26. Corke, P., et al., *Automated control of a dragline using machine vision.* 1994.

27. Hainsworth, D.W., P.I. Corke, and G.J. Winstanley. *Location of a dragline bucket in space using machine vision techniques*. in *Acoustics, Speech, and Signal Processing, 1994. ICASSP-94., 1994 IEEE International Conference on*. 1994. IEEE.

28. Jessett, A. *Automated draglines move one step closer to reality.* 2014.

29. Cleary, P., *The filling of dragline buckets.* Mathematical Engineering in Industry, 1998. **7**(1): p. 1-24.

30. Coetzee, C.J., D.N.J. Els, and G.F. Dymond, *Discrete element parameter calibration and the modelling of dragline bucket filling.* Journal of Terramechanics, 2010. **47**(1): p. 33-44.

31. Mart'in, A., A. Ashish, and B. Paul, *TensorFlow: large-scale machine learning on heterogeneous distributed systems.* Preliminary White Paper, 2015.

32. Cundall, P.A. and O.D. Strack, *A discrete numerical model for granular assemblies.* Geotechnique, 1979. **29**(1): p. 47-65.

33. Hertz, H., *On the Contact of Rigid Elastic Solids and on Hardness, chapter 6: Assorted Papers by H. Hertz*. 1882, MacMillan, New York.

34. Chen, T. and C. Guestrin, *XGBoost: Reliable Large-scale Tree Boosting System. arXiv 2016; 1–6.* arXiv preprint arXiv:1603.02754, 2016.

35. O'Beirne, T.J., *Investigation Into Dragline Bucket Filling: Final Report : ACARP Project C3002*. 1997: Australian Coal Association Research Program, Australian Coal Industry Research Laboratories.

36. ACARP *Dragline Productivity Improvements Continue To Improve Mining Company Bottom Lines*. ACARP MATTERS 2008.

37. Humphrey, J., *Dragline Research Review*. 1997.

38. Maciejewski, J. and A. Jarzębowski, *Laboratory optimization of the soil digging process.* Journal of Terramechanics, 2002. **39**(3): p. 161-179.

39. Singh, S., *State of the art in automation of earthmoving.* Journal of Aerospace Engineering, 1997. **10**(4): p. 179-188.

40. Huang, X. and L. Bernold, *Robotic rock handling during backhoe excavation.* Automation and Robotics in Construction, 1993.

41. Costello, M. and J. Kyle, *A method for calculating static conditions of a dragline excavation system using dynamic simulation.* Mathematical and Computer Modelling, 2004. **40**(3–4): p. 233-247.

42. Lumley, G. and D. Haneman *Improved Monitoring of Dragline Operation*. 1994.

43. Mullaney, B. *Immersive Says Case-study Results Meet Simulation Training Goals*. 2015.

44. Lever, P., *Automation and robotics.* SME Mining Engineering Handbook, Society for Mining, Metallurgy, and Exploration, 2011.

45. Dunbabin, M., et al. *Off-world robotic excavation for large-scale habitat construction and resource extraction*. in *AAAI Papers from the 2006 Spring Symposium: To Boldly Go Where No Human-Robot Team Has Gone Before*. 2006. American Association for Artificial Intelligence.

46. Corke, P.I., G.J. Winstanley, and J.M. Roberts, *Modeling and Control of a 3500 tonne Mining Robot*, in *Experimental Robotics V*. 1998, Springer. p. 262-274.

47. Roberts, J.M., P.I. Corke, and G.J. Winstanley, *Development of a 3500-tonne field robot.* The International Journal of Robotics Research, 1999. **18**(7): p. 739-752.

48. Winstanley, G., P. Corke, and J. Roberts, *Dragline Automation Implementation.* 1999(January 1999 Issue).

49. Roberts, J., G. Winstanley, and P. Corke, *Three-dimensional imaging for a very large excavator.* The International journal of robotics research, 2003. **22**(7-8): p. 467-477.

50. Winstanley, G., et al., *Field and service applications-Dragline automation-A dedade of development-Shared Autonomy for Improving Mining Equipment Productivity.* IEEE Robotics & Automation Magazine, 2007. **14**(3): p. 52-64.

51. Chi, S. and C.H. Caldas, *Automated object identification using optical video cameras on construction sites.* Computer-Aided Civil and Infrastructure Engineering, 2011. **26**(5): p. 368-380.

52. Ji, W., et al., *Video-based construction vehicles detection and its application in intelligent monitoring system.* CAAI Transactions on Intelligence Technology, 2016. **1**(2): p. 162-172.

53. Bügler, M., et al., *Fusion of photogrammetry and video analysis for productivity assessment of earthwork processes.* Computer-Aided Civil and Infrastructure Engineering, 2017. **32**(2): p. 107-123.

54. Dalal, N. and B. Triggs. *Histograms of oriented gradients for human detection*. in *Computer Vision and Pattern Recognition, 2005. CVPR 2005. IEEE Computer Society Conference on*. 2005. IEEE.

55. Azar, R.E., S. Dickinson, and B. McCabe, *Server-customer interaction tracker: computer vision–based system to estimate dirt-loading cycles.* Journal of Construction Engineering and Management, 2012. **139**(7): p. 785-794.

56. Memarzadeh, M., M. Golparvar-Fard, and J.C. Niebles, *Automated 2D detection of construction equipment and workers from site video streams using histograms of oriented gradients and colors.* Automation in Construction, 2013. **32**: p. 24-37.

57. Golparvar-Fard, M., A. Heydarian, and J.C. Niebles, *Vision-based action recognition of earthmoving equipment using spatio-temporal features and support vector machine classifiers.* Advanced Engineering Informatics, 2013. **27**(4): p. 652-663.

58. Coulomb, C.A., *Essai sur une application des regles de maximis & minimis a quelques problemes de statique: relatifs a l'architecture*. 1773: publisher not identified.

59. Rankine, W.M., *On the stability of loose earth.* Philosophical Transactions of the Royal Society of London, 1857. **147**: p. 9-27.

60. Mohr, O., *Die Elastizitatsgrenze und Bruch eines Materials.* Z. Ver. Dtsch. Ing., (4): 1524, 1914.

61. Von Karman, T., *Uber den mechanismus des flussigkeits-und luftwiderstandes.* Phys. Z., 1912: p. 49-59.

62. Boker, R., *Die Mechanik der bleibenden Formanderung in kristallinisch aufgebauten Korpern.* Ver. dt. Ing. Mitt. Forsch., 1915. **175**: p. 1-51.

63. Guwahati *Soil Mechanics*. 2009.

64. Ohde, J., *Zur Theorie des Erddruckes unter besonderer Berücksichtigung der Erddruckverteilung*. 1938: Ernst & Sohn.

65. Reece, A. *Paper 2: The Fundamental Equation of Earth-Moving Mechanics*. in *Proceedings of the Institution of Mechanical Engineers, Conference Proceedings*. 1964. SAGE Publications.

66. Hettiaratchi, D., B. Witney, and A. Reece, *The calculation of passive pressure in two-dimensional soil failure.* Journal of Agricultural Engineering Research, 1966. **11**(2): p. 89-107.

67. Hettiaratchi, D. and A. Reece, *Symmetrical three-dimensional soil failure.* Journal of Terramechanics, 1967. **4**(3): p. 45-67.

68. Hettiaratchi, D. and A. Reece, *The calculation of passive soil resistance.* Geotechnique, 1974. **24**(3): p. 289-310.

69. Shen, J. and R.L. Kushwaha, *Soil-machine interactions: a finite element perspective*. 1998: Marcel Dekker Inc.

70. Selig, E.T. and R. Nelson, *Observations of soil cutting with blades.* Journal of Terramechanics, 1964. **1**(3): p. 32-53.

71. Prandtl, L., *Über die härte plastischer körper.* Nachrichten von der Gesellschaft der Wissenschaften zu Göttingen, Mathematisch-Physikalische Klasse, 1920. **1920**: p. 74-85.

72. Terzaghi, K., *Bearing capacity.* Theoretical soil mechanics, 1943: p. 118-143.

73. DeBeer, E. and A. Vesic, *Etude experimental de la capacitie Portante du sable sous des foundations directes etablies en surface Annales des Travaux.* Publics de Belqique, 1958. **59**(3): p. 5-58.

74. Shosha, M. *Bearing Capacity of Shallow Foundation*. 2016.

75. Fountaine, E. and P. Payne, *The Shear Strength of Top Soils*. 1951: British Society for Reasearch in Agricultural Engineering, National Institute of Agricultural Engineering.

76. Payne, P., *The relationship between the mechanical properties of soil and the performance of simple cultivation implements.* Journal of Agricultural Engineering Research, 1956. **1**(1): p. 23-50.

77. O'Callaghan, J. and K. Farrelly, *Cleavage of soil by tined implements.* J. agric. Engng Res., 1964. **9**(3): p. 259.

78. Osman, M.S., *The mechanics of soil cutting blades*. 1964, University of Durham (England).

79. Hettiaratchi, D., *The present state of the theory of soil cutting.* Journal of Terramechanics, 1965. **2**(1): p. 63-76.

80. Siemens, J., J. Weber, and T. Thornburn, *Mechanics of soil as influenced by model tillage tools.* Trans. ASAE, 1965. **8**(1): p. 1-7.

81. Bailey, A. and J. Weber, *Comparison Of Methods Measuring Soil Shear Strength Using Artificial Soils.* Am Soc Agricultural Engineers Trans, 1965.

82. Godwin, R. and G. Spoor, *Soil failure with narrow tines.* Journal of Agricultural Engineering Research, 1977. **22**(3): p. 213-228.

83. McKyes, E. and O. Ali, *The cutting of soil by narrow blades.* Journal of Terramechanics, 1977. **14**(2): p. 43-58.

84. Perumpral, J., R. Grisso, and C. Desai, *A soil-tool model based on limit equilibrium analysis [Mathematical, tillage tool performance in soils]*. Transactions of the ASAE [American Society of Agricultural Engineers], 1983.

85. Swick, W. and J. Perumpral, *A model for predicting soil-tool interaction.* Journal of Terramechanics, 1988. **25**(1): p. 43-56.

86. Zeng, D. and Y. Yao, *A dynamic model for soil cutting by blade and tine.* Journal of terramechanics, 1992. **29**(3): p. 317-327.

87. Cohron, G.T., *The Inception and Evolution of Earth-moving Soil Mechanics.* Journal Of Terramechanics, 1964. **4**.

88. Rowlands, J.C., *Dragline bucket filling.* 1992.

89. Coetzeé, C., *Forced granular flow*. 2000, University of Stellenbosch.

90. Zelenin, A., V. Balovnev, and I. Kerov, *Machines for Moving the Earth: Fundamentals of the Theory of Soil Loosening.* Modeling of Working Processes and Forecasting Machine Parameters, AA Balkema, Rotterdam, Netherlands: p, 1986. **555**.

91. Blouin, S., A. Hemami, and M. Lipsett, *Review of resistive force models for earthmoving processes.* Journal of Aerospace Engineering, 2001. **14**(3): p. 102-111.

92. Hemami, A., S. Goulet, and M. Aubertin, *Resistance of particulate media to excavation: Application to bucket loading.* International Journal of Surface Mining and Reclamation, 1994. **8**(3): p. 125-129.

93. Alekseeva, T.i.a.n.V.e., *Machines for earthmoving work: theory and calculations*. Vol. 30. 1985: Intl Public Service.

94. McKyes, E., *Soil cutting and tillage*. 1985: Elsevier.

95. Gill, W.R. and G.E.V. Berg, *Soil dynamics in tillage and traction*. 1967: Agricultural Research Service, US Department of Agriculture.

96. Goryachkin, V., *Collected works in three volumes 2nd Edition.* TT, 1968. **71**: p. 50087.

97. Cobb, D., G. Cohron, and J. Gentry, *Scale model evaluation of earthmoving tools*. 1962, SAE Technical Paper.

98. Dombrovskii, N., *Excavators.* Mashinostroenie, Moscow, 1969: p. 130.

99. Balovnev, V.I., *New methods for calculating resistance to cutting of soil.* 1983.

100. Takahashi, H., M. Hasegawa, and E. Nakano, *Analysis on the resistive forces acting on the bucket of a Load-Haul-Dump machine and a wheel loader in the scooping task.* Advanced Robotics, 1998. **13**(2): p. 97-114.

101. Gooch, J.E., *Dragline bucket with quick change basket feature*. 2001, Google Patents.

102. Bierwith, R.S., *Excavating bucket with replaceable wedge-locked teeth*. 2002, Google Patents.

103. Smith, M.A. and C.E. Harder, *Ground engaging tool system*. 2010, Google Patents.

104. Harder, C. and M. Smith, *Ground engaging tool system*. 2013, Google Patents.

105. Chenoweth, S.D., G.D. KNIGHT, and M.A. Smith, *Retainer systems for ground engaging tools*. 2015, Google Patents.

106. Rimmey, B.T., *Retainer systems for ground engaging tools*. 2015, Google Patents.

107. Ballinger, C.W., *Retainer systems for ground engaging tools*. 2015, Google Patents.

108. Campomanes, P.S. and A.H. Lonn, *Retainer systems for ground engaging tools*. 2015, Google Patents.

109. Campomanes, P.S. and C.O. Jeske, *Retainer systems for ground engaging tools*. 2015, Google Patents.

110. Jeske, C.O., *Retainer systems for ground engaging tools*. 2015, Google Patents.

111. Leslie, B.A., G. Lumley, and T. Meyers, *Excavator bucket*. 2004, Google Patents.

112. Lumley, G., *Dragline buckets*. 2009, Google Patents.

113. Leslie, B.A., et al., *Heavy duty excavator bucket*. 2011, Google Patents.

114. Leslie, B.A., et al., *Heavy duty excavator bucket*. 2015, US Patent 20,150,292,177.

115. Leslie, B.A., et al., *Heavy duty excavator bucket*. 2014, Google Patents.

116. Murray, P. *Improved Dragline Spoiling Through 3D Simulation*. 1994.

117. Cundall, P.A. *Formulation of a three-dimensional distinct element model—Part I. A scheme to detect and represent contacts in a system composed of many polyhedral blocks*. in *International Journal of Rock Mechanics and Mining Sciences & Geomechanics Abstracts*. 1988. Elsevier.

118. Cundall, P. *A computer model for simulating progressive large-scale movements in block rock mechanics*. in *Proc. Symp. Int. Soc. Rock Mech. Nancy*. 1971.

119. Cundall, P., *A Computer Model for Rock Mass Behavior using Interactive Graphics for the Input and output of Geometrical Data, Report Prepared under Contract Number DACW 45-74-c-006, for the Missouri River Division.* US Army Corps of Engineers, University of Minnesota, 1974.

120. Verlet, L., *Computer" experiments" on classical fluids. I. Thermodynamical properties of Lennard-Jones molecules.* Physical review, 1967. **159**(1): p. 98.

121. Lim, W.L., *Mechanics of railway ballast behaviour*. 2004, University of Nottingham.

122. Itasca, *PFC 5.0 Documentation*. 2013.

123. Cundall, P.A. *A discontinuous future for numerical modeling in soil and rock*. in *Discrete Element Methods@ sNumerical Modeling of Discontinua*. 2002. ASCE.

124. Potyondy, D.O. and P.A. Cundall, *A bonded-particle model for rock.* International Journal of Rock Mechanics and Mining Sciences, 2004. **41**(8): p. 1329-1364.

125. Fakhimi, A. and T. Villegas, *Application of dimensional analysis in calibration of a discrete element model for rock deformation and fracture.* Rock Mechanics and Rock Engineering, 2007. **40**(2): p. 193.

126. Yoon, J., *Application of experimental design and optimization to PFC model calibration in uniaxial compression simulation.* International Journal of Rock Mechanics and Mining Sciences, 2007. **44**(6): p. 871-889.

127. Gbadam, E.K., *Characterization and numerical simulation of the microstructural and micromechanical viscoelastic behavior of oil sands using the discrete element method.* 2017.

128. Itasca, *PFC3D Documentation*. 2008, Itasca Consulting Group

129. Potyondy, D.O., *Material Modeling Support in PFC*. 2015, Itasca Consulting Group, Inc., Minneapolis, MN, .

130. Mindlin, R., *Compliance of elastic bodies in contact.* J. Appl. Mech. Trans. ASME, 1949. **16**: p. 259-268.

131. Coetzee, C. and D. EIs. *Modelling excavator bucket filling with DEM*. in *Fifth World Congress on Computational Mechanics*. 2002.

132. Coetzeé, C., *The Modelling of Bulk Materials Handling using the Discrete Element Method.* 2009.

133. Plassiard, J.-P., N. Belheine, and F.-V. Donzé, *A spherical discrete element model: calibration procedure and incremental response.* Granular Matter, 2009. **11**(5): p. 293-306.

134. Kohli, A.H. and M.D. Zoback, *Frictional properties of shale reservoir rocks.* Journal of geophysical research: solid earth, 2013. **118**(9): p. 5109-5125.

135. Mutton, A.J., *Queensland Coals: Physical and Chemical Properties, Colliery and Company Information*. 2003: Department of Natural Resources and Mines.

136. Phan, V.T.-A., *Improvement in Engineering Properties of Mudstone in Southwestern Taiwan Through Compaction and a Cement Additive.* Geotechnical and Geological Engineering, 2017.

137. Suryakanta *MODULUS OF ELASTICITY & POISSON'S RATIO FOR DIFFERENT ROCKS*. 2015.

138. Leonides, C., *Control and Dynamic Systems V34: Advances in Control Mechanics Part 1 of 2: Advances in Theory and Applications*. 2012: Academic Press.

139. Itasca, *PFC 5.0 Documentation*. 2016.

140. Fielding, C., A. Falkner, and S. Scott, *Fluvial response to foreland basin overfilling; the late Permian Rangal Coal Measures in the Bowen basin, Queensland, Australia.* Sedimentary Geology, 1993. **85**(1-4): p. 475-497.

141. Stafford, J. *Bucyrus Erie 1370W Dragline Specifications*. 1998.

142. Lumley, G., *Dragline Dictionary: PwC – Mining Intelligence and Benchmarking*, P. Coopers, Editor. 2014.

143. Bhiksha, R., *Face Recognition - A Convolutional Neural Netwrk Approach*. 2015.

144. LeCun, Y., et al., *Backpropagation applied to handwritten zip code recognition.* Neural computation, 1989. **1**(4): p. 541-551.

145. Denker, J., et al., *Large automatic learning, rule extraction, and generalization.* Complex systems, 1987. **1**(5): p. 877-922.

146. Denker, J.S., et al. *Neural network recognizer for hand-written zip code digits*. in *Advances in neural information processing systems*. 1989.

147. Goodfellow, I., Y. Bengio, and A. Courville, *Deep learning*. 2016: MIT press.

148. Abadi, M., et al. *TensorFlow: A System for Large-Scale Machine Learning*. in *OSDI*. 2016.

149. Site-K *Cat 7495 shovel loading 795F AC*. 2016.

150. Hyun *Construction Equipment - HL960 Wheel Loader*. 2016.

151. Quantum3D, *Laser scanning* 2017.

152. Tzutalin *LabelImg - A Graphical Image Annotation Tool* 2017.

153. Everingham, M., et al., *The pascal visual object classes (voc) challenge.* International journal of computer vision, 2010. **88**(2): p. 303-338.

154. Tran, D. *Raccoon dataset*. 2017.

155. Tum *Convolutional Neural Networks for Image and Video Processing*. 2017.

156. Ioffe, S. and C. Szegedy. *Batch normalization: Accelerating deep network training by reducing internal covariate shift*. in *International conference on machine learning*. 2015.

157. Hajaj, M.a. and D. Gillies, *Batch Normalization and the impact of batch structure on the behavior of deep convolution networks.* 2018.

158. Yin, Z., et al., *A deep normalization and convolutional neural network for image smoke detection.* IEEE Access, 2017. **5**: p. 18429-18438.

159. Alexey *Windows and Linux version of Darknet Yolo v2 Neural Networks for object detection*. 2017.

160. Howard, A.G., et al., *Mobilenets: Efficient convolutional neural networks for mobile vision applications.* arXiv preprint arXiv:1704.04861, 2017.

161. Liu, W., et al. *Ssd: Single shot multibox detector*. in *European conference on computer vision*. 2016. Springer.

162. Hinton, G., N. Srivastava, and K. Swersky, *Rmsprop: Divide the gradient by a running average of its recent magnitude.* Neural networks for machine learning, Coursera lecture 6e, 2012.

163. Kim, S.-K., J. Seo, and J.S. Russell, *Intelligent navigation strategies for an automated earthwork system.* Automation in Construction, 2012. **21**: p. 132-147.

164. Greenwell, B.M., *pdp: An R Package for Constructing Partial Dependence Plots.* R Journal, 2017. **9**(1).

VITA

Godfred Somua-Gyimah joined the PhD Mining Engineering program at Missouri S & T in Fall 2014. He obtained his Bachelor of Science in Civil Engineering from Kwame Nkrumah University of Science and Technology (June 2010). He also obtained Masters degrees in Engineering Geology from the University of Leeds (August, 2014) and Mining Engineering from Missouri University of Science and Technology (July, 2016). In 2017, he was a Machine Learning and Artificial Intelligence fellow at the nationally-renowned Insight Data Science program in New York.

Prior to graduate school, Godfred spent three (3) years honing his problem-solving skills on multi-million-dollar projects at Huawei Technologies. As a Technical Design Engineer at the world's largest telecom service provider, he quickly gained a reputation for proactively identifying clients' main pain points and developing end-to-end design solutions to client satisfaction.

With a graduate certificate in Data Science and Business Analytics as well as four academic degrees across three different Science and Engineering disciplines, Godfred's main strengths are his advanced problem-solving skills, proven versatility and ability to adapt quickly to new knowledge domains.

In January 2018, Godfred joined the Emerging Leaders in Science (ELS) program at Monsanto Company (now Bayer AG) as a Data Scientist and an Artificial Intelligence expert. In December 2018, he received his PhD in Mining Engineering from Missouri University of Science and Technology.